DESIGN AND SYNTHESIS OF BODIPY-BASED PALLADACYCLES FOR THE DETECTION OF CARBON MONOXIDE

A Thesis Submitted to
the Graduate School of
İzmir Institute of Technology
in Partial Fulfillment of the Requirements for the Degree of

DOCTOR OF PHILOSOPHY

in Chemistry

by
Ahmet EREN

December 2024

İZMİR

We approve the thesis of **Ahmet EREN**

Examining Committee Members:

Prof. Dr. Mustafa EMRULLAHOĞLU
Department of Photonics, İzmir Institute of Technology

Prof. Dr. Ümit Hakan YILDIZ
Department of Chemistry, İzmir Institute of Technology

Prof. Dr. Sinan Balcı
Department of Photonics, İzmir Institute of Technology

Prof. Dr. Derya Gülcemal
Department of Chemistry, Ege University

Assoc. Prof. Dr. Muhammed Üçüncü
Pharmaceutical Basic Sciences, İzmir Katip Çelebi University

05 December 2024

Prof. Dr. Mustafa EMRULLAHOĞLU
Supervisor, Department of Photonics
İzmir Institute of Technology

Prof. Dr. Gülşah Şanlı MOHAMED
Head of the Department of Chemistry

Prof. Dr. Mehtap EANES
Dean of the Graduate School

ACKNOWLEDGEMENTS

Firstly, I would like to thank my advisor, Mustafa Emrullahoğlu, for his unwavering support throughout this challenging doctoral program. He guided me not only in my laboratory studies but also, when necessary, with his life experiences like a brother.

I am deeply grateful to Prof. Dr. Sinan Balcı and Prof. Dr. Ümit Hakan Yıldız for their invaluable suggestions, support, and participation as committee members during my thesis progress seminars and PhD defense seminar. I sincerely appreciate Prof. Dr. Derya Gülcemal and Assoc. Prof. Dr. Muhammed Üçüncü for their time and effort in serving as a committee member and reviewing my work. I want to express my gratitude to Levent Artok, who provided me with laboratory facilities for this study.

During this study, I have worked with many people and made good friendships, including Suay Dartar, Beraat Umur Kaya, Yankı Öncü Yayak, and undergraduate students who worked with me. I would like to thank all of them for their help and cooperation and wish each of them a life full of success.

I would like to thank Beraat Umur Kaya, Mustafa Erdoğmuş, and Dr. Hüseyin Özgener for helping me with NMR analyses throughout my study.

I am profoundly grateful to my parents for their unwavering love, support, and encouragement, which have been with me throughout my life. I would like to express my heartfelt gratitude to our baby, Zeynep, born during this time, and to my beloved wife, Merve, the beautiful woman I have shared my life with, who has supported me through every difficult moment.

ABSTRACT

DESIGN AND SYNTHESIS OF BODIPY-BASED PALLADACYCLES FOR THE DETECTION OF CARBON MONOXIDE

BODIPYs represent a significant class of fluorescent dyes that are esteemed for their remarkable and versatile fluorescence characteristics. Due to their unique chemical structures, these dyes exhibit strong absorption of light in the UV-visible spectrum and emit fluorescence at longer wavelengths. Their exceptional photostability, favorable quantum yields, ease of synthesis, and adaptability in various constructions contribute to their prominence in the scientific literature. BODIPYs are extensively utilized in critical applications, including bioimaging, flow cytometry, fluorescent labeling, and detection.

Heavy atoms within the BODIPY skeleton can inhibit fluorescence by increasing the rate of intersystem crossing. Consequently, the quantum yield experiences a significant reduction, resulting in a loss of BODIPY's essential fluorescence characteristic. However, BODIPY has the capability to specifically react with certain analytes or molecules, which enables the restoration of its fluorescent properties. This intriguing aspect of BODIPY inspired the synthesis of palladium complexes, which have been effectively employed as fluorescence-based detectors for carbon monoxide gas.

Carbon monoxide is an odorless, colorless, and highly toxic gas for both humans and animals. Its detection is crucial due to its significantly higher binding affinity to hemoglobin compared to oxygen. Preclinical studies have also shown that carbon monoxide can have anti-inflammatory effects and offer cellular and tissue protection in living organisms when administered in low doses. In this study, carbon monoxide was detected using fluorescence technique, even at very low concentrations of 187 nM. This capability was further extended to living human cells using fluorescence microscopy, highlighting the remarkable potential for carbon monoxide detection in biological contexts.

ÖZET

KARBON MONOKSİT TESPİTİ İÇİN BODİPY TABANLI PALADASİKLİKLERİN TASARIMI VE SENTEZİ

BODIPY'ler, dikkat çekici ve çok yönlü floresan özellikleriyle takdir edilen önemli bir floresan boya sınıfını temsil eder. Benzersiz kimyasal yapıları nedeniyle, bu boyalar UV-görünür spektrumda ışığı güçlü bir şekilde emer ve daha uzun dalga boylarında floresan yayar. Olağanüstü fotostabiliteleri, elverişli kuantum verimleri, sentez kolaylığı ve çeşitli yapılarda uyarlanabilirlikleri, bilimsel literatürde öne çıkmalarına katkıda bulunur. BODIPY'ler, biyolojik görüntüleme, akış sitometrisi, floresan etiketleme ve tespit dahil olmak üzere kritik uygulamalarda yaygın olarak kullanılır.

BODIPY iskeletindeki ağır atomlar, sistemler arası geçiş hızını artırarak floresansı engelleyebilir. Sonuç olarak, kuantum veriminde önemli bir azalma yaşanır ve bu da BODIPY'nin temel floresan özelliğinin kaybolmasına neden olur. Ancak, BODIPY belirli analitler veya moleküllerle özel olarak reaksiyona girme yeteneğine sahiptir ve bu da floresan özelliklerinin geri kazanılmasını sağlar. BODIPY'nin bu ilgi çekici yönü, karbon monoksit gazı için floresan tabanlı dedektörler olarak etkili bir şekilde kullanılan paladyum komplekslerinin sentezine ilham kaynağı olmuştur.

Karbon monoksit kokusuz, renksiz ve hem insanlar hem de hayvanlar için oldukça zehirli bir gazdır. Oksijene kıyasla hemoglobine bağlanma afinitesinin belirgin olarak daha yüksek olması nedeniyle tespiti kritik öneme sahiptir. Klinik öncesi çalışmalar ayrıca karbon monoksitin düşük dozlarda uygulandığında anti-inflamatuar etkilere sahip olabileceğini ve canlı organizmalarda hücresel ve doku koruması sağlayabileceğini göstermiştir. Bu çalışmada karbon monoksit, 187 nM gibi çok düşük konsantrasyonlarda bile floresan tekniği kullanılarak tespit edilmiştir. Bu yetenek, floresan mikroskobu kullanılarak canlı insan hücrelerine daha da genişletilmiş ve biyolojik bağlamlarda karbon monoksit tespiti için dikkate değer bir potansiyel olduğu vurgulanmıştır.

TABLE OF CONTENTS

LIST OF FIGURES

Figure **Page**

Figure **Page**

Figure **Page**

Figure **Page**

Figure **Page**

Figure **Page**

Figure **Page**

Figure **Page**

LIST OF TABLES

Table **Page**

ABBREVIATIONS

ACN……..Acetonitrile

Au……Gold

BODIPY……4,4-Difluoro-4-bora-3a,4a-diaza-s-indacene

CO……...Carbon monoxide

Cu…….Copper

cm……...centimeter

CORM……..Carbon monoxide-releasing molecule

d……...doublet

DAPI……...4′,6-diamidino-2-phenylindole

DCM……Dichloromethane

DMEM……...Dulbecco's Modified Eagle Medium

DMF……Dimethylformamide

eq……..…equivalent

Et_3N……...Triethylamine

EtOAc……..Ethyl acetate

EtOH……...Ethanol

ex……..……Excitation

Fe……...Iron

g……...gram

H……..Hydrogen

HRMS……..High-resolution mass spectroscopy

Hz……Hertz

ICT……...Intramolecular charge transfer

IUPAC……International Union of Pure and Applied Chemistry

LOD……Limit of Detection

M……Molarity

m……multiplet

MeOH……...Methanol

mg……...…Milligram

MHz……Megahertz

min……...Minute

mL…….Milliliter

mm……..Millimeter

mmol…….Milimole

mV…….....Millivolt

NIR…….Near-infrared

nm…….……..nanometer

nM……..Nanomolar

NMR……..Nuclear Magnetic Resonance

NO……Nitric Oxide

PBS……Phosphate Buffer Saline

Pd…….Palladium

ppb……..parts per billion

ppm……parts per million

Pt……...Platinum

q……quartet

QTOF……...Quadrupole Time-of-Flight

Rf……Retention factor

Rh……..Rhodium

RT……..Room temperature

Ru……...Ruthenium

s…….singlet

t…….time

TBTD……...5-(3-thienyl)-2,1,3-benzothiadiazole)

THF……...Tetrahydrofuran

TLC……Thin Layer Chromatography

UV……...ultraviolet

V……...Volt

v……...volume

CHAPTER 1

INTRODUCTION

BODIPY, an acronym for 4,4-Difluoro-4-bora-3a,4a-diaza-s-indacene, was initially synthesized by Treibs and Kreuzer in 1968. According to the IUPAC numbering system, the carbons numbered 1, 2, 6, and 7 are designated as beta carbons, while those numbered 3 and 5 are referred to as alpha carbons, the carbon labeled as 8 is identified as the meso carbon (Figure 1.1.). BODIPY dyes exhibit absorption of light in the ultraviolet-visible region and emit fluorescence at longer wavelengths with high quantum yields. Variations made at different positions can significantly influence their fluorescence characteristics. Due to their stability in physiological environments, BODIPY dyes are widely utilized in fluorescence imaging of living cells.

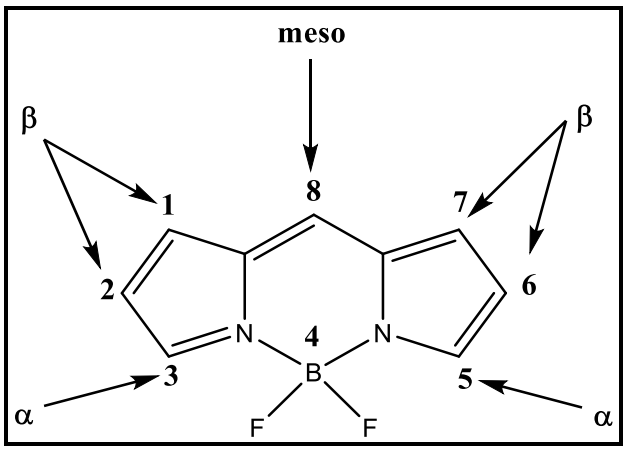

Figure 1.1. Structure of BODIPY

Carbon monoxide (CO) is a colorless, odorless, and flammable gas that poses significant toxicity to humans due to its high binding affinity to hemoglobin, which is approximately 300 times greater than that of oxygen (Wilkinson, 2007), (Steinberg, 2014). This strong affinity disrupts the oxygen transport capacity of hemoglobin and can lead to cellular death. Interestingly, despite its harmful effects, carbon monoxide serves as a gasotransmitter and plays a vital role in cellular messaging (Untereiner et al., 2012). It is also recognized for its anti-inflammatory properties and its function in oxidative

stress defense, contributing to the prevention of cell death (Takagi et al., 2015). In pathophysiological conditions and environments characterized by oxidative stress, the endogenous production of CO increases significantly, as a result of heme catabolism mediated by heme oxygenase (Wang et al., 2007), (Coburn et al., 1967). The application of exogenous CO through carbon monoxide-releasing molecules (CORMs) is being explored as a therapeutic strategy for the treatment of various diseases (Faizan et al., 2019). Enhanced levels of carbon monoxide during episodes of cellular hypoxia, along with alterations in its concentrations, offer valuable diagnostic insights. The recognition of CO within cells has further underscored its significance in cell imaging studies.

Heavy atoms in fluorophores facilitate intersystem crossing, which enhances phosphorescence or thermally activated delayed fluorescence (Lower and El-Sayed, 1966). However, the presence of these heavy atoms increases non-radiative pathways, resulting in a corresponding decrease in fluorescence emission. Palladium, as a heavy metal, can quench the fluorescence properties of fluorophores. Moreover, the proximity of palladium to the fluorophore core is inversely related to the quantum yield of the fluorophore. Additionally, palladium can form palladacycles by bonding with a carbon atom, particularly when that carbon is part of an aromatic or nitrogen-containing functional group. These palladacycles can undergo demetallation or carbonylation reactions in the presence of carbon monoxide.

CHAPTER 2

LITERATURE WORKS

2.1. Electrochemically CO Detection

The first electrochemical detection of CO was documented in 1974 by Blurton and Sedlak. Their study utilized a Pt electrode to perform potentiostatic measurements, enabling the determination of steady-state currents associated with CO oxidation. By approaching steady-state conditions, the researchers were able to evaluate the influence of the Pt oxide surface on the current generated during this process. In Figure 2.1, the variations in electrode potential are presented, which signify the presence of CO in an air/CO mixture (Blurton and Sedlak, 1974).

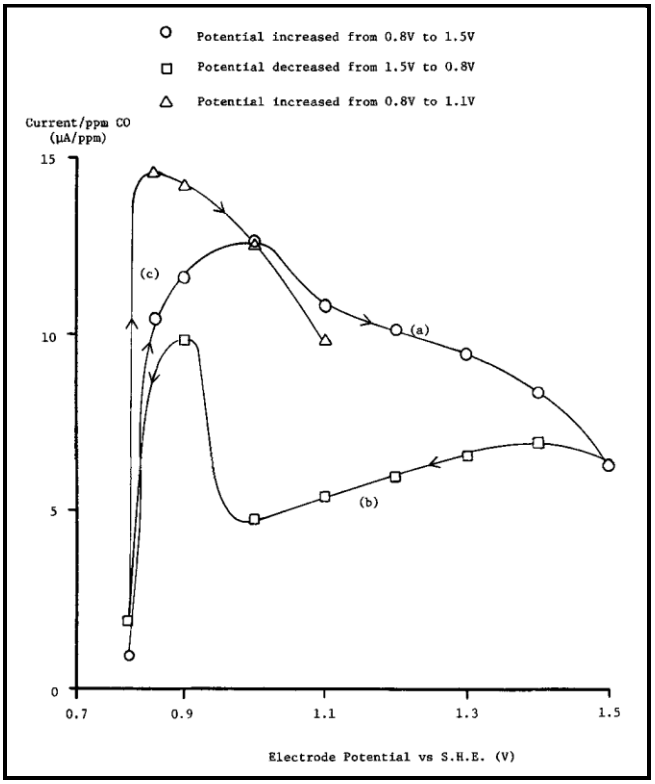

Figure 2.1. The CO oxidation current vs. the potential of the Pt electrode (Source: Blurton and Sedlak, 1974).

Bay and colleagues conducted an analysis of CO concentrations in the air, focusing on a range of 21 to 385 ppm. This investigation utilized Teflon-bonded diffusion electrodes that were catalyzed with Pt. To enhance the sensitivity of the electrodes to CO while minimizing the currents associated with the reduction of O_2 and the oxidation of water, the anode potential was maintained at 1.2 volts. A continuous flow of a CO/air mixture was directed over the reverse side of the sensing electrode at a consistent rate. The electrochemical oxidation of CO generated a current, which was measured by assessing the potential drop across a standard resistor (Bay et al., 1974).

In 1976, Sedlak and Blurton reported a significant study utilizing an electrochemical cell that featured an Au electrode, differing from their previous work, which employed a Pt electrode (Sedlak and Blurton, 1976). The gold electrode demonstrated the capability to respond to and detect CO, NO, and NO_2. At a voltage of 0.8 V, the electrode successfully detected NO_2, as both CO and NO exhibited unreactive behavior at this potential. Additionally, when the voltage was increased to 1.5 V, the electrode served effectively as a sensor for NO, with CO remaining inactive at this level (as illustrated in Figure 2.2.a). For the detection of CO, the electrode operated proficiently within a voltage range of 1.0 V to 1.4 V, as indicated in Figure 2.2.b.

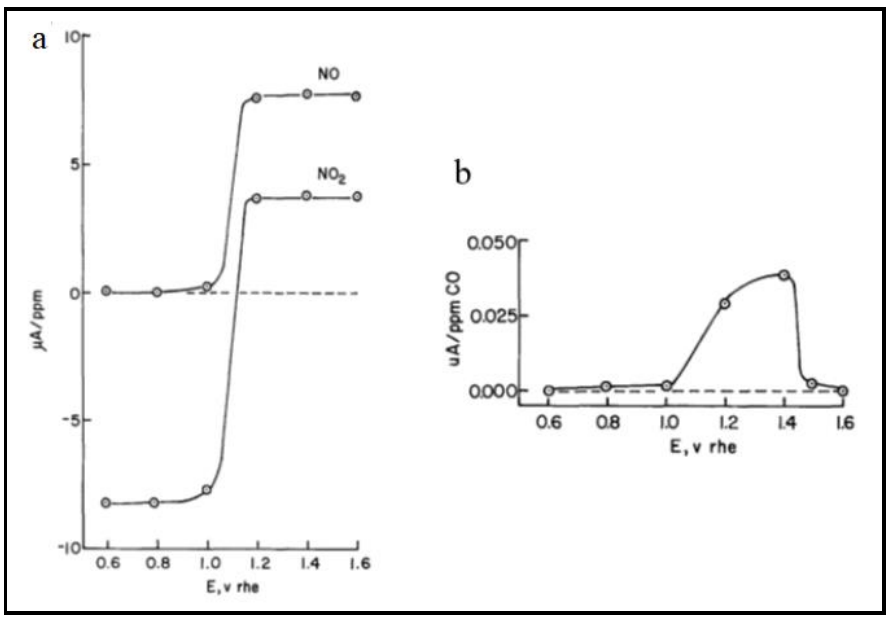

Figure 2.2. a) NO oxidation and NO_2 oxidation-reduction currents; b) CO oxidation currents (Source: Sedlak and Blurton, 1976).

A dynamic coulometric technique was developed for the potential amperometric detection of CO within a concentration range of 18 to 200 ppm, achieving an accuracy of approximately 7% (Zaromb and Stetter, 1983).

In 2003, a tin-supported platinum electrode was innovatively developed to enhance sensitivity towards carbon monoxide (Tsceng and Yang, 2003). The sensitivity of this electrode, Sn-modified Pt/Nafion, is 5.5 times larger than the Pt/Nafion electrodes (Figure 2.3.).

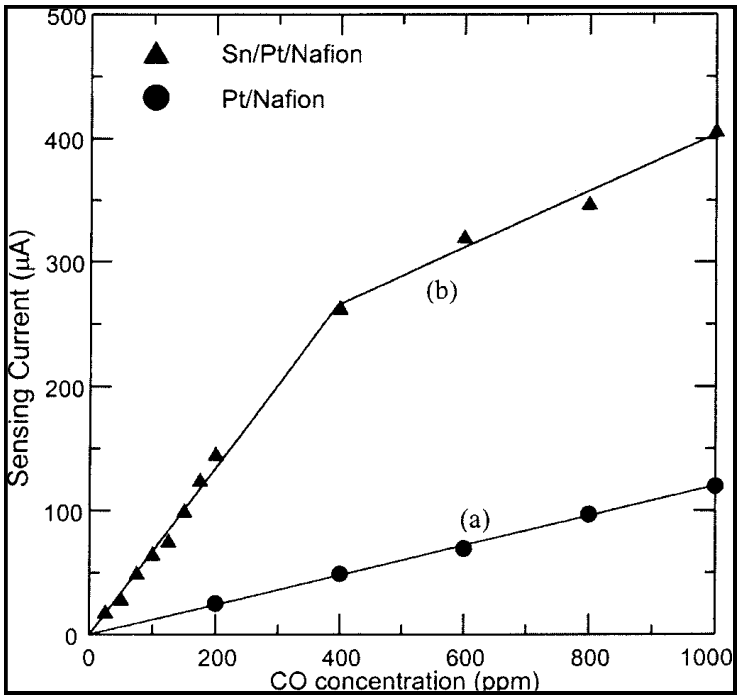

Figure 2.3. CO concentration vs. Current. a) Pt/Nafion at 0.8 V vs. Ag/AgCl; b) Sn/Pt/Nafion at 0.5 V vs. Ag/AgCl (Source: Tsceng and Yang, 2003).

An electrochemical sensor has been developed that incorporates a nano-gold colloid modification on a platinum disk microelectrode for the detection of CO (Chen et al., 2005). The catalytic activation of this electrode was evaluated across various supporting electrolyte solutions. The findings indicate that the electrode demonstrates a significant catalytic effect on the electrochemical oxidation of CO, as illustrated in Figure 2.4.

Lee and Kim developed an amperometric dual microsensor for simultaneous detection of NO and CO (Lee and Kim, 2007). This probe successfully determined CO and NO from living biological tissue surfaces. Measurements taken with the sensor positioned 10 μm away from the tissue surface are depicted in Figure 2.5.

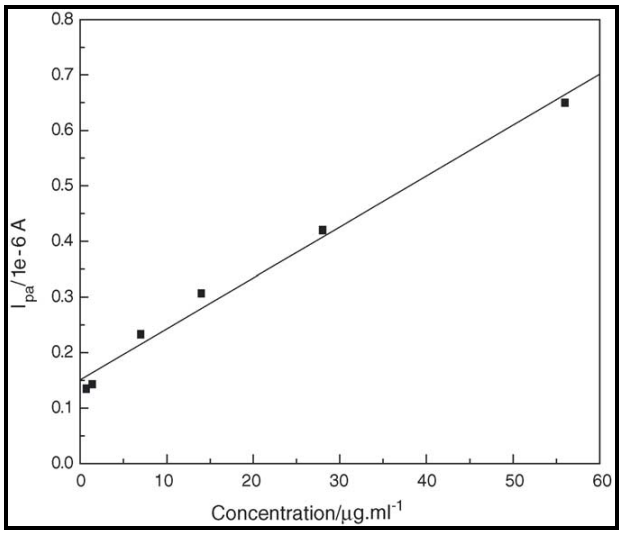

Figure 2.4. The linear relationship between current and the concentration of CO (Source: Chen et al., 2005).

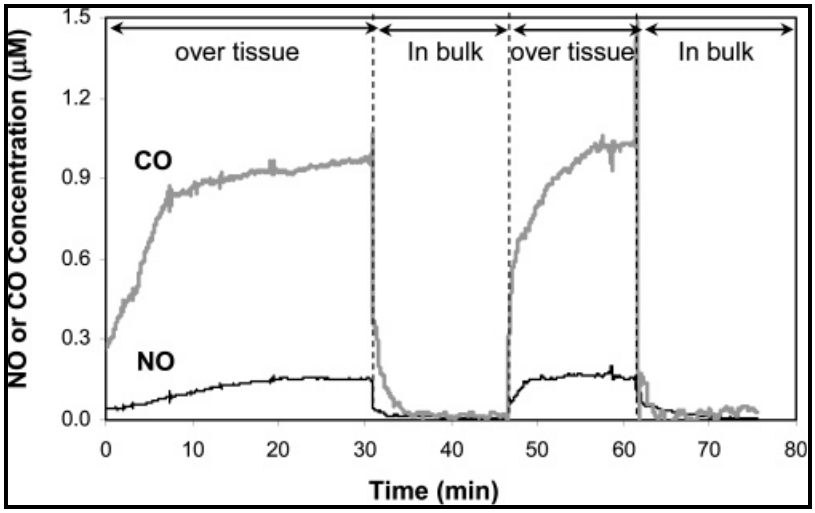

Figure 2.5. Representative simultaneous measurements of NO and CO over time for mouse (c57) kidney tissue (Source: Lee and Kim, 2007).

In 2012, a Pt-Ru electrode was developed that operated effectively under physiological conditions, showing both selectivity and sensitivity to carbon monoxide (Seto et al., 2012). This innovative probe can accurately measure carbon monoxide concentrations in the range of 0.9 to 9 μM. However, it was observed that under physiological conditions, uric acid, ascorbic acid, and hydrogen peroxide also reacted with the Pt-Ru electrode. To address this issue, the researchers implemented a Nafion coating on the surface of the electrode, successfully mitigating the responses from uric

acid and ascorbic acid. Furthermore, a layer of manganese dioxide (MnO_2) combined with chitosan was introduced to eliminate the electrode's response to hydrogen peroxide. Consequently, a Pt-Ru/Nafion/MnO_2 electrode was designed, which enables highly sensitive amperometric detection of CO (Figure 2.6).

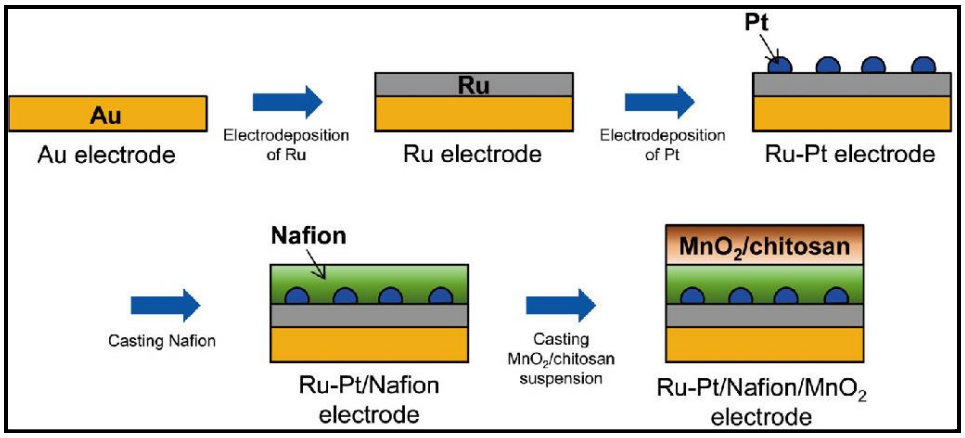

Figure 2.6. Preparation of Pt-Ru/Nafion/MnO_2 electrode (Source: Seto et al., 2012).

Park and colleagues developed an advanced amperometric dual microsensor designed to simultaneously analyze endogenous NO and CO (Park et al., 2012). This sensor exhibited remarkable stability during the analysis of these gases in live C57 mouse kidney cells. The measurements obtained indicated that the introduction of a NO synthase inhibitor, L-NAME, led to a reduction in NO concentration while simultaneously increasing the CO concentration (Figure 2.7).

In 2015, a dual sensor was developed for the in vivo analysis of NO and CO levels on the surface of the living rat brain cortex (Park et al., 2015), (Figure 2.8.). Studies were carried out by adding L-NAME to cells to examine the relationship between endogenously produced CO and NO.

Ha developed a miniaturized sensor that can be placed in living tissues to analyze NO and CO gas (Figure 2.9). The dual sensor is constructed utilizing a dual microelectrode system consisting of an Au-deposited platinum microdisk and a platinum black-deposited Pt disk (Ha et al., 2016).

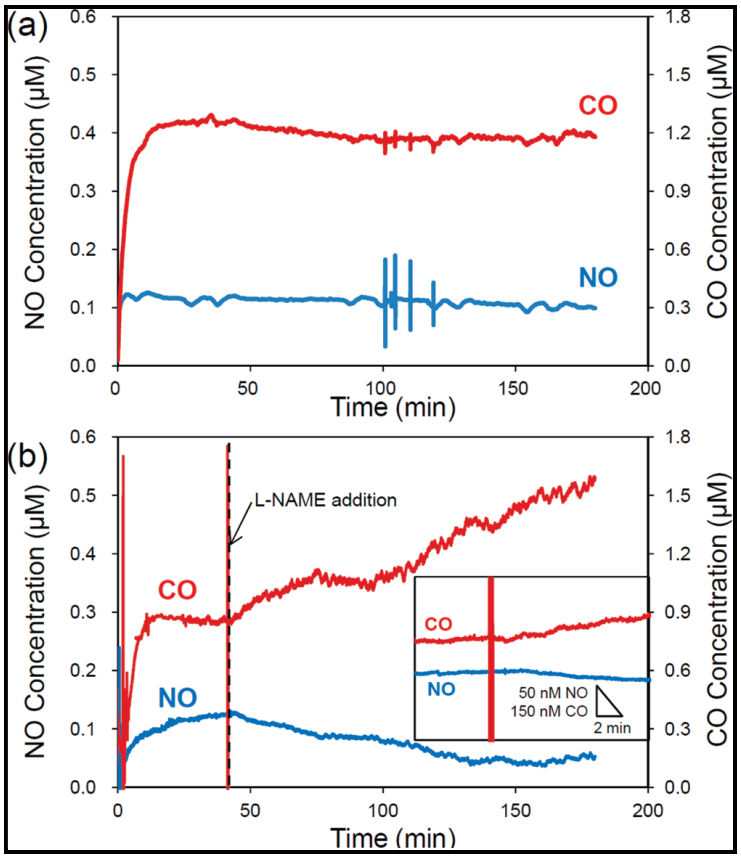

Figure 2.7. NO and CO measurements near the surface of a mouse kidney. a) without and b) with L-NAME (Source: Park et al., 2012).

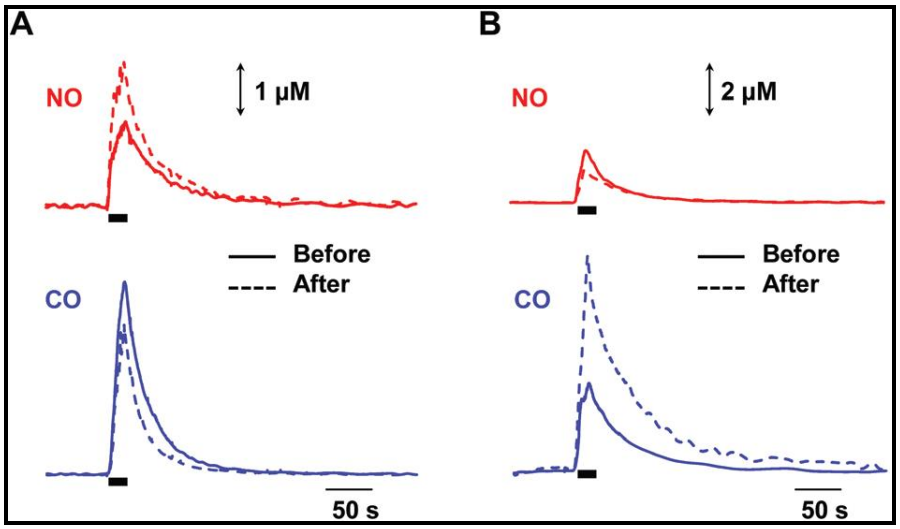

Figure 2.8. NO, CO concentrations vs. electrical stimulation. A) L-arginine treated; B) L-NAME treated (Source: Park et al., 2015).

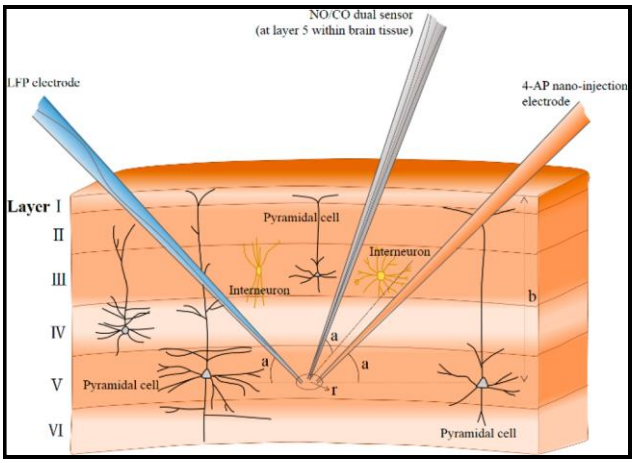

Figure 2.9. Schematic illustration for injecting probe in biological tissues (Source: Ha et al., 2016).

2.2. Colorimetric CO Sensors

The first colorimetric CO sensor was developed by Itou in 2006, utilizing ruthenium complexes coordinated with various ligands (Itou et al., 2006). Following the photosensitized electron transfer, the formal oxidation state of ruthenium changes, facilitating the coordination of CO to the complex. This interaction results in a detectable color change, indicating the presence of CO gas (Figure 2.10.).

In 2010, binuclear rhodium compounds were developed as chromogenic probes (Estaban et al., 2010). It is known that binding to the binuclear rhodium compounds axial site results in color changes. According to this knowledge, when CO gas was bubbled through chloroform containing rhodium complex, a color change from purple to orange was observed (Figure 2.11.).

In 2011, a significant advancement in chromogenic sensors was published by Moragues et al., focusing on the axial coordination of CO with rhodium. This innovative probe, when dissolved in chloroform, exhibits a distinct color change from purple to yellow and orange upon exposure to CO (Figure 2.12). The observed transition between these two colors signifies the formation of two unique structural species, illustrating the probe's sensitivity to CO. Moreover, the sensor demonstrates high selectivity and an impressive low detection limit, capable of accurately detecting CO concentrations as low as 0.2 ppm.

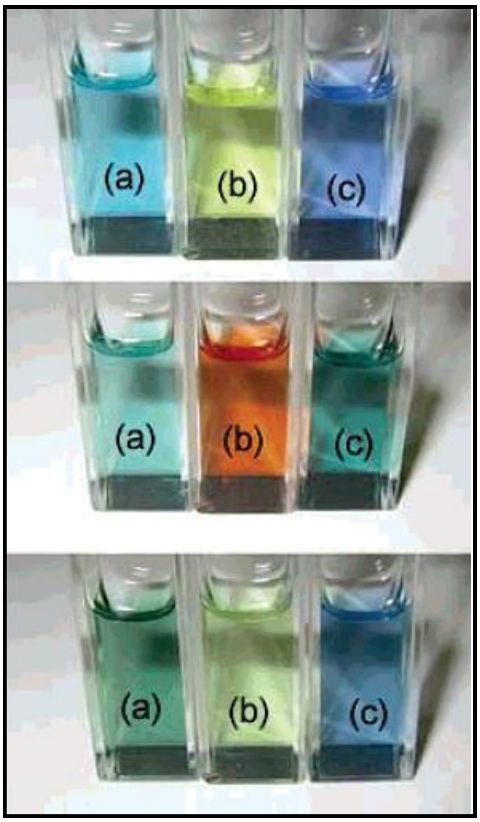

Figure 2.10. Color changes of ruthenium complexes. a) A ruthenium complex; b) One electron reduced ruthenium complex; c) CO exchange ruthenium complex with three different ligands (Source: Itou et al., 2006).

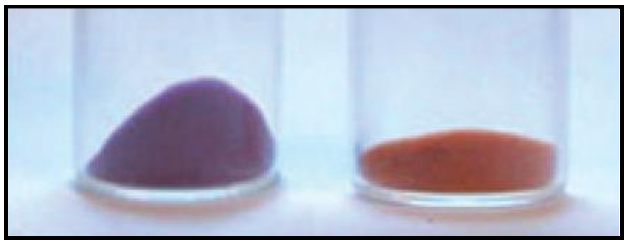

Figure 2.11. Photograph of silica gel containing Rh complex, left is the absence of CO, right is the presence of CO (Source: Esteban et al., 2010).

Courbat et al. (2011) demonstrated that a rhodium complex can transform from purple to yellow in the presence of CO (Figure 2.13). The sensor developed through this process exhibited high sensitivity in both gas cell tests and standardized fire tests. As a result, it can be utilized as a fire detector and for monitoring indoor air quality.

In 2014, a ruthenium(II) compound was developed that exhibits a color change from orange to yellow upon exposure to carbon monoxide CO (Moragues et al., 2014)

(Figure 2.14.). This compound serves as a visual probe that can be easily detected by the naked eye, demonstrating a notable color change at concentrations as low as 5 (ppb) of CO. Furthermore, it is capable of activating fluorescence at 1 ppb concentration. The compound has been found to possess high selectivity and sensitivity in solid-state applications.

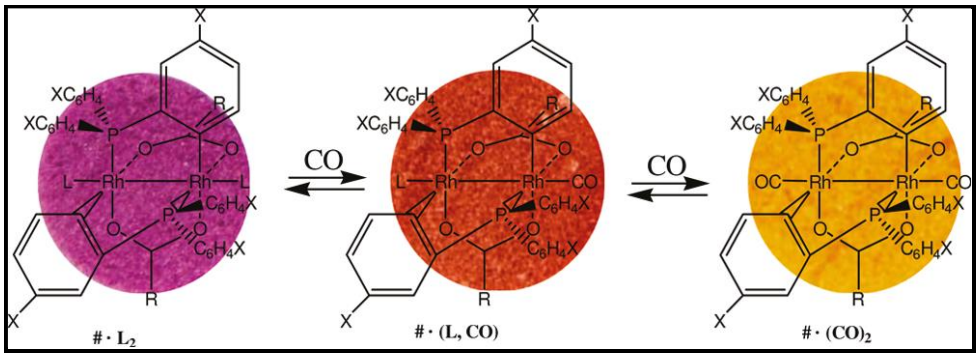

Figure 2.12. Color changes of the complex in the presence of CO (Source: Moragues et al., 2011).

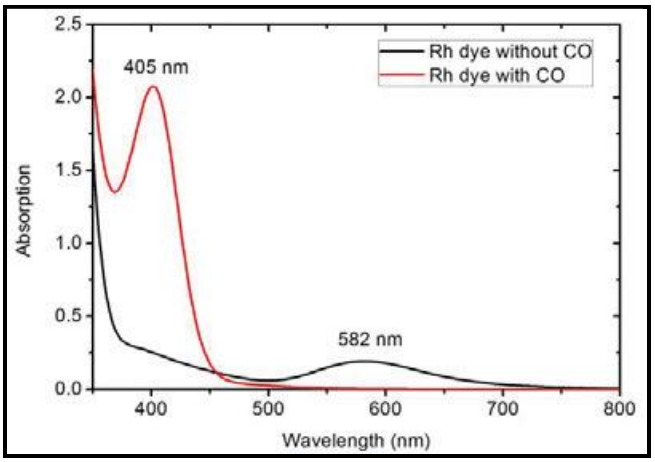

Figure 2.13. Spectrophotometric measurements of probe absence and presence of CO (Source: Courbat et al., 2011).

In 2016, a new sensor for CO was developed, which is colorimetric and near-infrared fluorescent (Yan et al., 2016). The sensor features a synthesized probe that is colorless and non-fluorescent; this was achieved by attaching allyl chloroformate to the hydroxyl groups of the naphthofluorescein structure. The operational principle is based on the Tsuji-Trost reaction. In the presence of CO and Pd(II), the allyl groups are

eliminated from the chromophore, resulting in the reduction of Pd(II) to Pd(0), and the probe exhibits fluorescence (Figure 2.15.).

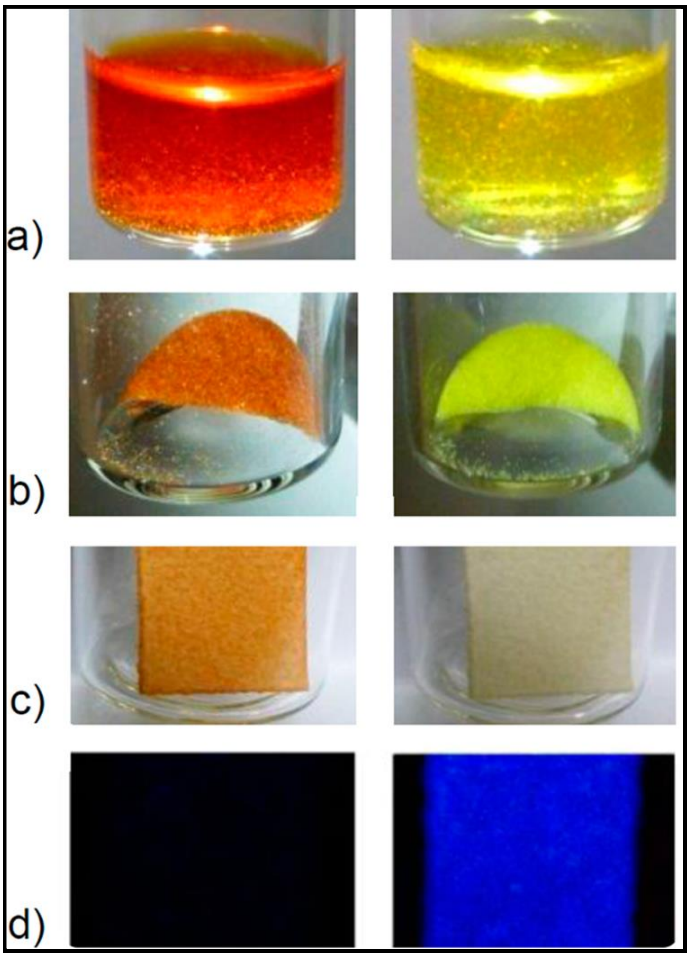

Figure 2.14. Ru complex in the absence (left) and presence (right) of CO. a) dissolved in DCM; b) adsorbed on silica gel; c) deposited on cellulose paper; d) under UV radiation of c (Source: Moragues et al., 2014).

In 2018, Toscani et al. developed vinylic complexes of Ru metal that exhibited remarkable sensitivity and selectivity in the detection of CO in both solution and gaseous environments. The incorporation of the fluorophore 5-(3-thienyl)-2,1,3-benzothiadiazole (TBTD) group into these complexes resulted in phenomena of fluorescence quenching. Notably, in the presence of CO, the TBTD group is released from the complex, leading to an enhancement in fluorescence, which serves as an effective means of CO detection (Figure 2.16). Additionally, when these complexes are adsorbed onto silica, a noticeable color transition occurs from dark red to lighter shades, correlating with increasing concentrations of CO (Figure 2.17).

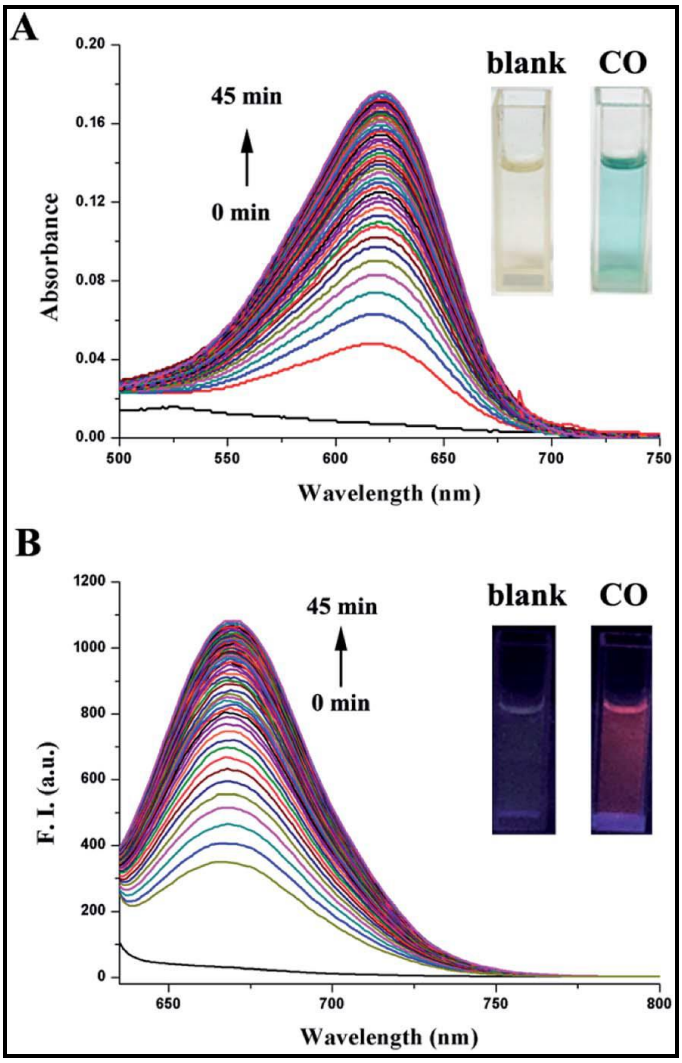

Figure 2.15. A) Absorbance and B) fluorescence spectra of the probe in the absence and presence of CORM (Source: Yan et al., 2016).

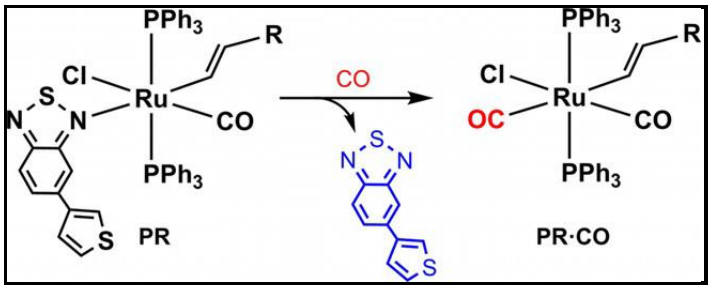

Figure 2.16. Reaction of the probes with CO (Source: Toscani et al., 2018).

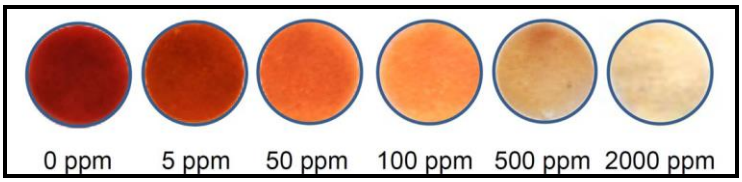

Figure 2.17. Color change of the complex adsorbed with silica according to increasing CO concentration (Source: Toscani et al., 2018).

2.3. Fluorescent CO Probes

In 2012, Wang et al. made a significant advancement by developing the first genetically encoded fluorescent sensor for the selective detection of CO in living cells. This innovative probe was constructed utilizing the strong binding affinity of CO to CooA, a heme-containing regulatory protein known for its CO-sensing capabilities. A fluorescent protein was integrated into CooA, resulting in the replacement of CO with the axial ligand Pro2. This substitution enhances the complex's fluorescent properties, thereby facilitating real-time CO monitoring (Figure 2.18.).

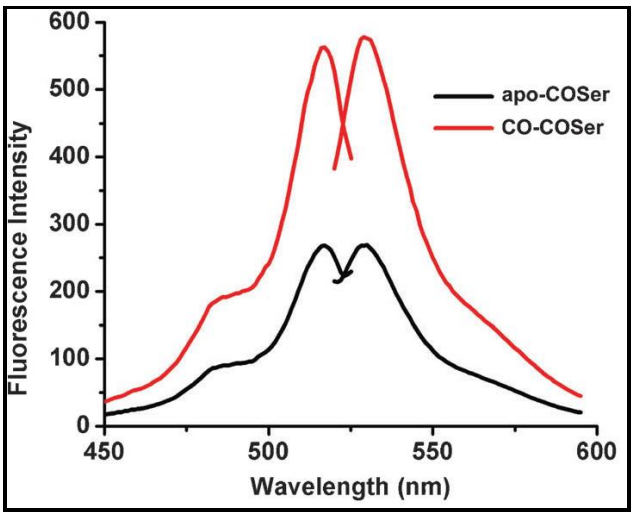

Figure 2.18. Fluorescence emission of the probe before and after CO addition (Source: Wang et al., 2012).

In 2015, Toscani et al. developed vinyl complexes of ruthenium and osmium for the purpose of detecting CO through colorimetric and fluorometric techniques (Figure 2.19.). These probes demonstrate a significant color change in chloroform solution upon

exposure to CO gas, facilitating detection without specialized equipment. Furthermore, when the probes are adsorbed onto silica, they are capable of colorimetric detection of CO gas at concentrations as low as 5 ppb. The incorporation of pyrenyl, naphthyl, and phenanthrenyl functional groups enhances the fluorescent properties of the complexes, enabling effective measurements both in solution and in the air (Figure 2.20.).

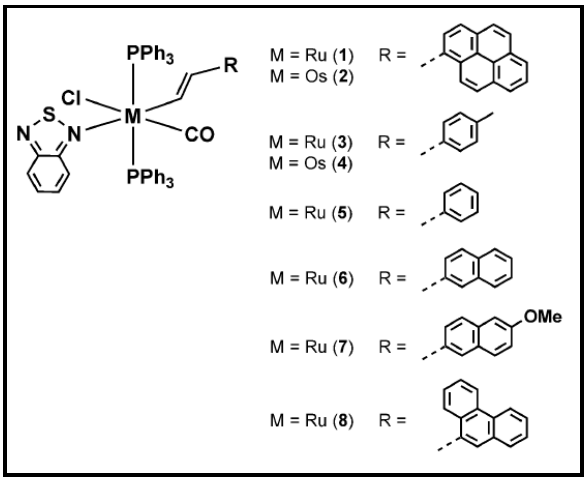

Figure 2.19. Structure of the CO probes (Source: Toscani et al., 2015).

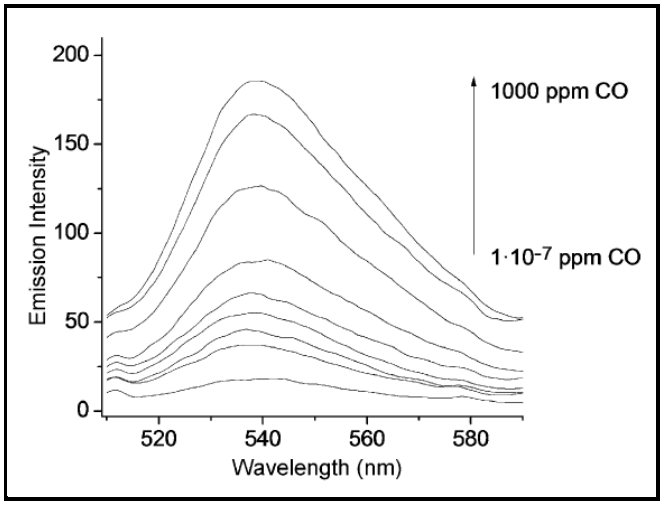

Figure 2.20. Fluorescence intensities of complex 7 vs. increasing CO concentrations (Source: Toscani et al., 2015).

A water-compatible vinylic ruthenium compound has been developed to achieve the first simultaneous measurements of CO levels and viscosity in living cells (Robson et al., 2020) (Figure 2.21). This innovative compound is capable of detecting endogenous

CO in both normoxic and hypoxic environments. Additionally, due to it having a BODIPY fluorophore, it allows for the precise observation of microscopic viscosity changes through fluorescence lifetime imaging microscopy.

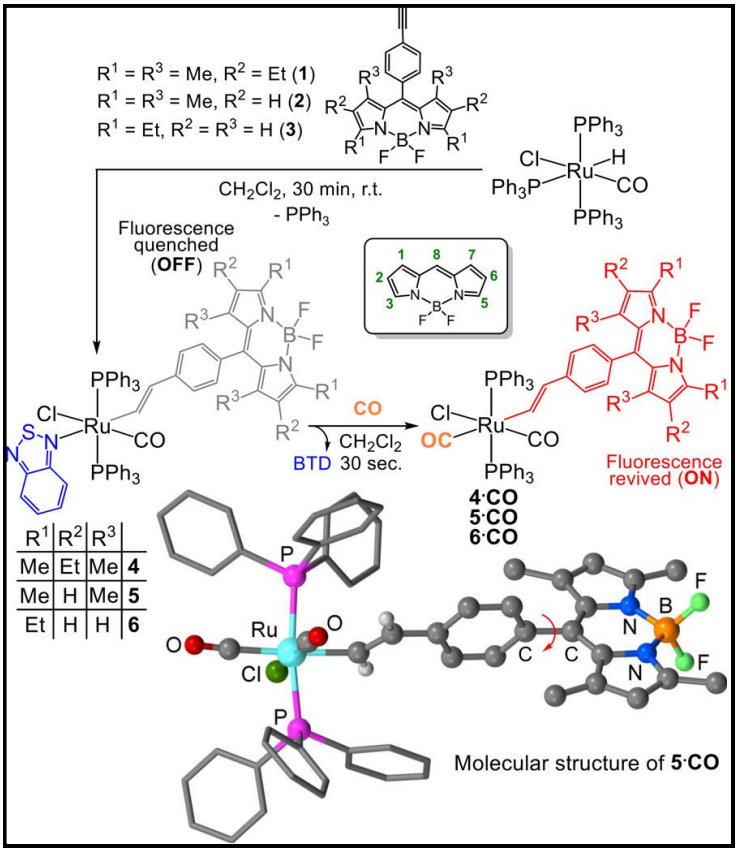

Figure 2.21. Molecular structure of the probes (Source: Robson et al., 2020).

A fluorescent CO probe was developed based on the reduction of Cu(II) to Cu(I) to avoid the production of any leaving groups at the end of the reaction (Bai et al., 2022) (Figure 2.22.). This probe demonstrates high selectivity, rapid detection, and a low limit of detection at 17 nM for CO. It exhibits low cytotoxicity and can effectively measure both endogenous and exogenous CO in HeLa cells. Furthermore, it offers a cost-effective alternative compared to previous methods that utilized Pd.

Drawing on the CO binding properties of heme iron, a novel rhodamine-based iron complex has been synthesized for the fluorescent detection of CO within living cells (Fang et al., 2024) (Figure 2.23.). This innovative method provides a cost-effective and user-friendly alternative to traditional metal-based techniques, such as palladium, ruthenium, and rhodium, while significantly reducing concerns related to toxicity.

Notably, as the concentrations of CORM-3 or CO increase, there is a corresponding decrease in fluorescence intensity, enabling detection sensitivity down to 146 nM.

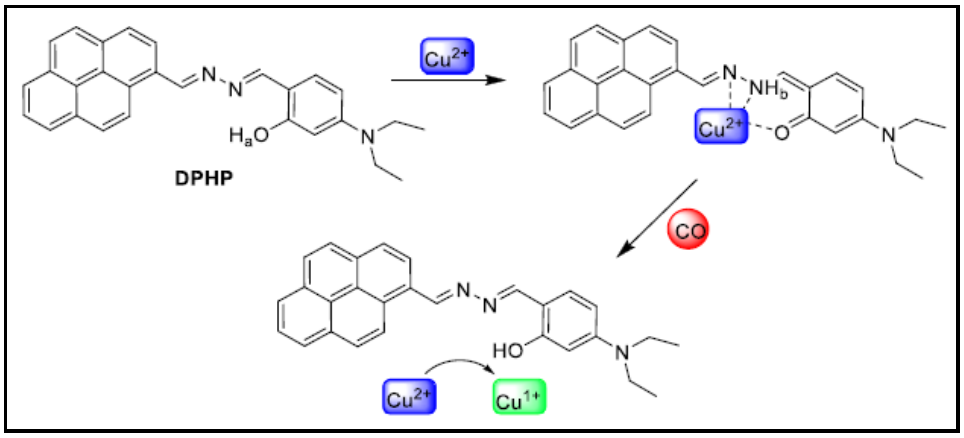

Figure 2.22. Sensing mechanism of the probe (Source: Bai et al., 2022).

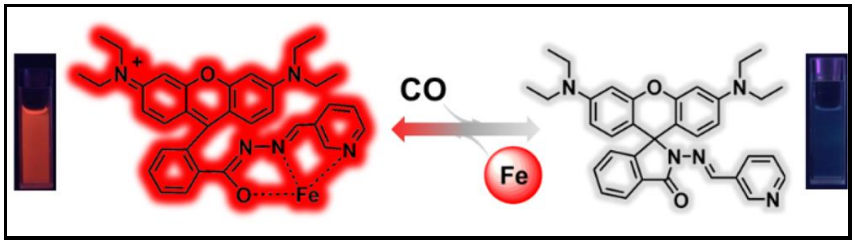

Figure 2.23. Fe-based rhodamine molecule for CO determination (Source: Fang et al., 2024).

2.4. Pd Containing CO Sensors

2.4.1. Based on Tsuji-Trost Reaction

The first colorimetric and NIR fluorescence CO sensor documented in the literature was synthesized by conjugating allyl chloroformate with the naphthofluorescein fluorophore (Yan et al., 2016). This particular fluorophore was selected for its advantageous absorption and emission characteristics at longer wavelengths, which have demonstrated efficacy in detecting intracellular CO during live cell imaging experiments.

In the presence of CO, the reduction of Pd^{2+} to Pd^{0} results in the cleavage of the allylic group from the molecule, leading to the generation of fluorescence properties (Figure 2.24.).

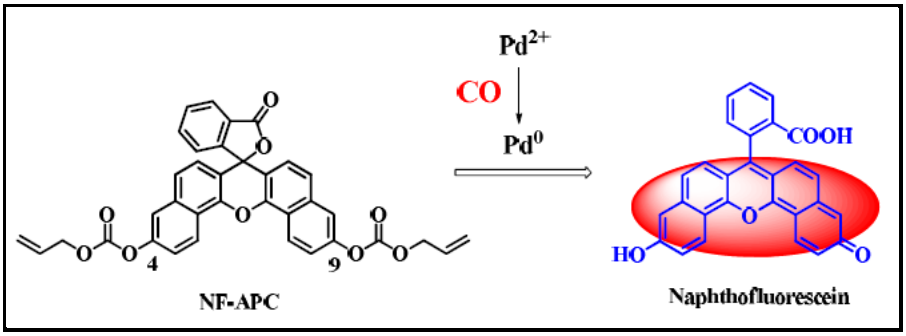

Figure 2.24. Sensing mechanism of the probe (Source: Yan et al., 2016).

Feng et al. reported the first CO probe with an allyl ether in the fluorophore group in 2017. Their work involved the synthesis of two allyl fluorescein ethers in the presence of $PdCl_2$, which exhibited exceptional selectivity and sensitivity toward CO (Figure 2.25.). This probe demonstrates notable stability, high water solubility, rapid sensing capabilities, and effective functionality within living cells, all at remarkably low concentrations.

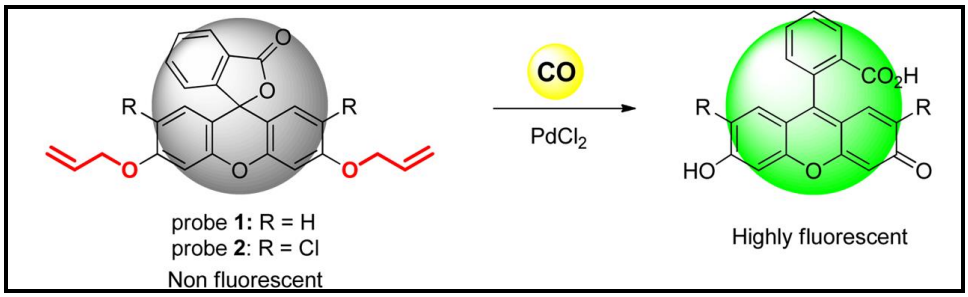

Figure 2.25. Probe 1 and probe 2 sensing mechanisms (Source: Feng et al., 2017).

In 2018, a hemicyanine-based NIR fluorescence probe was synthesized to determine CO (Li et al., 2018). This synthesized molecule is positively charged, so it is easily located in the mitochondria of the cell and easily detects both endogenous and exogenous CO in cells and tissues. The probe shows fluorescence when it interacts with Pd^{2+} and CO (Figure 2.26.).

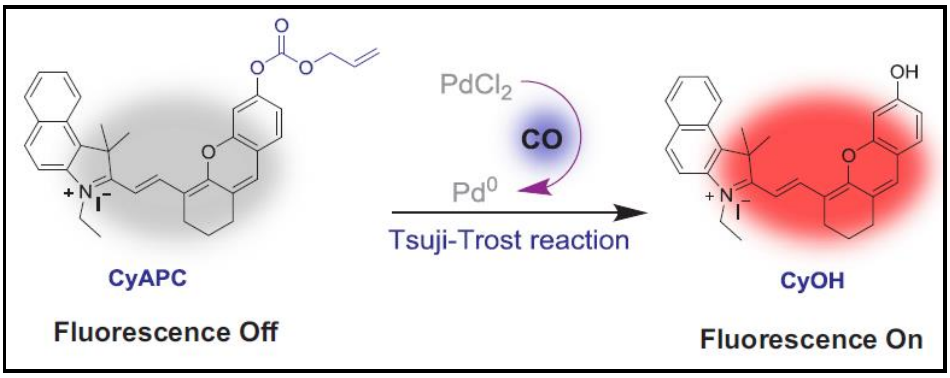

Figure 2.26. Response mechanism of the probe (Source: Li et al., 2018).

A resorufin-based, turn-on probe was synthesized to determine CO in aqueous systems (Biswas et al., 2019) (Figure 2.27.). The resorufin group monoprotected by allyl chloroformate shows weak fluorescence. The probe exhibits high fluorescence when exposed to CO and selectively and sensitively detects as low as 62 nM in cells.

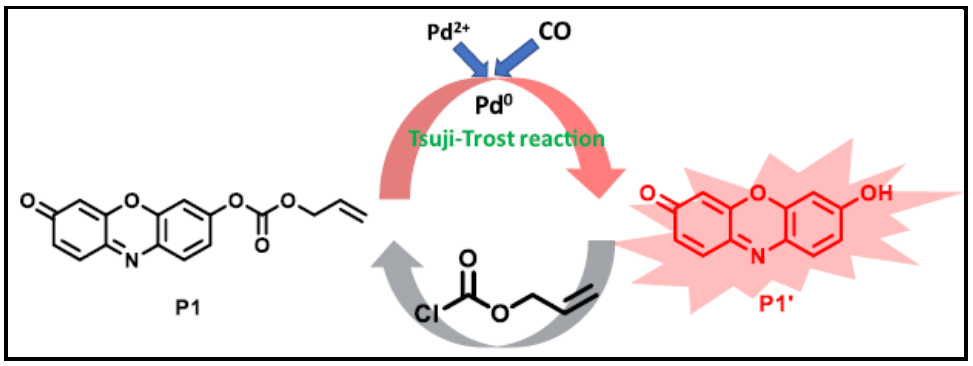

Figure 2.27. Proposed sensing mechanism of the probe (Source: Biswas et al., 2019).

In 2021, a ratiometric probe was developed for the specific detection of CO within mitochondria (Du et al., 2021). This probe features an allyl ether group incorporated into the fluorophore, which facilitates responsiveness to CO. Additionally, a triphenylphosphonium group has been introduced to ensure targeted delivery to mitochondria (Figure 2.28.). In the presence of $PdCl_2$, the fluorescence emission undergoes a change due to the cleavage of the allyl ether. This mechanism enables the sensitive and selective determination of both endogenous and exogenous CO within mitochondrial environments.

Chen and colleagues have developed a novel CO probe by synthesizing a conjugated system that incorporates tetrahydroquinoxaline as an electron donor, a

coumarin fluorophore as the emissive component, and a five-membered pyrrolidine ring to mitigate the effects of twisted intramolecular charge transfer (TICT) (Chen et al., 2021) (Figure 2.29.). The detection limit of this synthesized probe was determined to be 31.2 nM for CORM-3. In addition, the probe exhibited high sensitivity, selectivity, and effective performance in biological assays, including studies conducted in HepG2 cells and zebrafish models. This advancement offers significant potential for applications in the field of biochemical research.

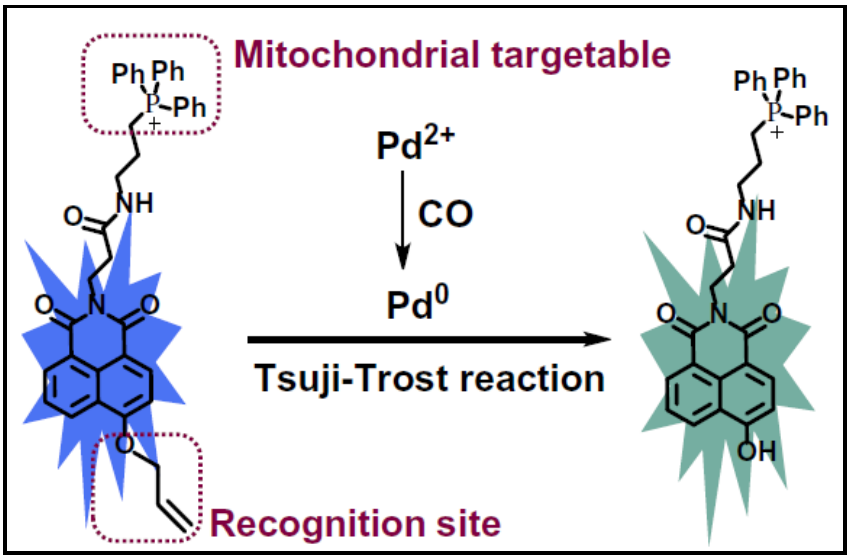

Figure 2.28. The ratiometric sensing mechanism of the probe (Source: Du et al., 2021).

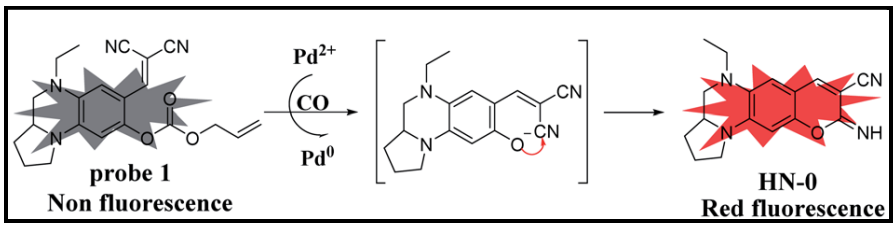

Figure 2.29. Sensing mechanism of the probe (Source: Chen et al., 2021).

A CO probe has been developed incorporating an allyl formate group, which enhances water solubility and facilitates fluorescence quenching (Fu et al., 2022). The probe demonstrates fluorescence emission at 650 nm, attributable to the excited-state intramolecular proton transfer (ESIPT) mechanism, in the presence of both CO and Pd^{2+} ions (Figure 2.30.). Notably, at a CO concentration of 100 µM, the fluorescence intensity

of the probe increases by 29-fold. Furthermore, this probe has been successfully utilized in biological studies, showcasing its efficacy in HepG2 cells and zebrafish models.

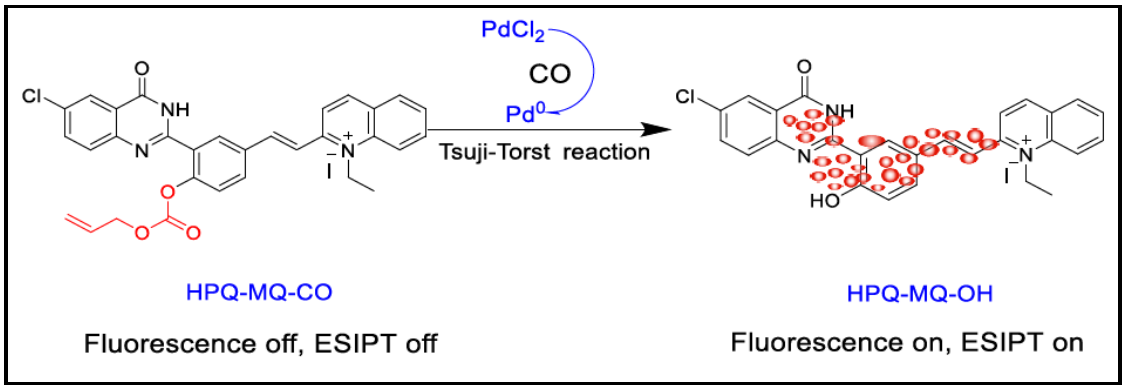

Figure 2.30. Schematic illustration of the probe with CO (Source: Fu et al., 2022).

A ratiometric two-photon fluorescent probe has been developed utilizing 7-(dimethylamino)-4-hydroxycoumarin in conjunction with allyl carbonate as the reactive unit (Tang et al., 2023) (Figure 2.31.). This probe demonstrates fluorescence emission at longer wavelengths, which is facilitated by the intramolecular charge transfer (ICT) mechanism. Following the completion of the Pd^0-mediated Tsuji-Trost reaction, the resulting compound exhibits fluorescence emission at shorter wavelengths. Notably, the probe displays exceptional selectivity and sensitivity for CO within living cells and zebrafish models, while also possessing the capability to image endogenous CO.

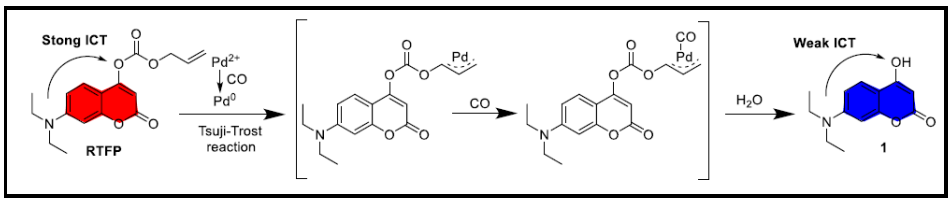

Figure 2.31. Sensing mechanism of the probe (Source: Tang et al., 2023).

2.4.2. Based on Demetallation or Carbonylation Reaction

In 2012, Michel and colleagues introduced an innovative CO sensor based on a palladium-mediated carbonylation reaction. This sensor involves the synthesis of a

cyclopalladated BODIPY compound, which exhibits a significant decrease in fluorescence due to the heavy atom effect of palladium. During the carbonylation reaction in a CO-rich environment, palladium is released from the compound, leading to the formation of a more fluorescent BODIPY molecule (Figure 2.32.). This probe has been shown to effectively and selectively detect CO in aqueous buffer systems as well as in living cells.

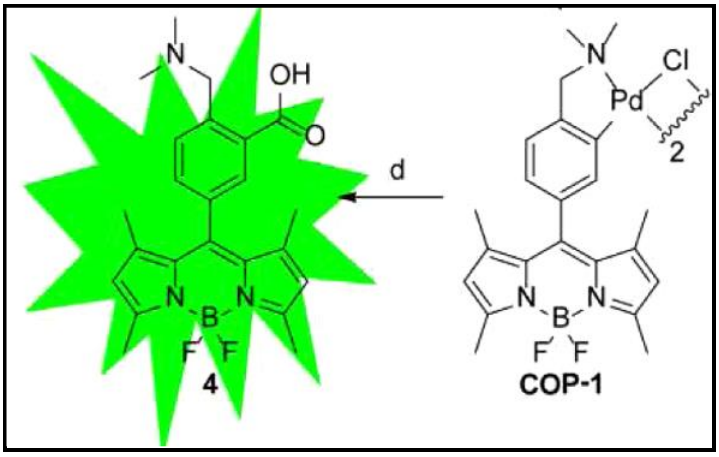

Figure 2.32. Fluorescence mechanism of the probe (Source: Michel et al., 2012).

In 2016, two novel BODIPY derivatives were synthesized incorporating the azobenzene-cyclo palladium moiety, which exhibits sensitivity to carbon monoxide (Li et al., 2016), (Figure 2.33.). CO generated endogenously in response to hypoxic conditions, was quantitatively detected through fluorescence assays conducted in aqueous buffer solutions and living cells in this study.

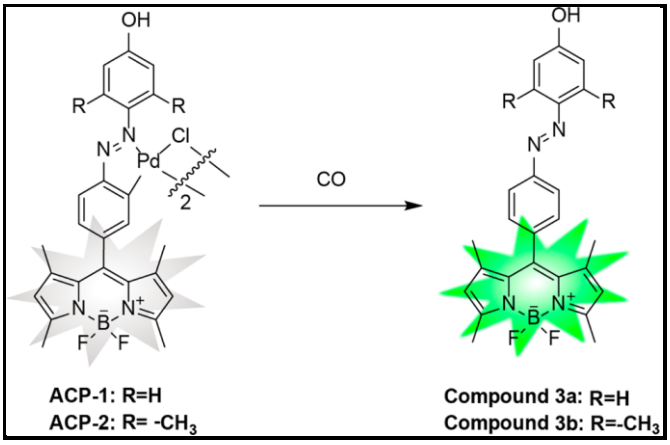

Figure 2.33. Sensing mechanism of the probes towards CO (Source: Li et al., 2016).

Madea et al. (2020) detailed that a palladium-based Nile Red dye displayed a notable activation of fluorescence following CO-induced demetallation (Figure 2.34.). In their investigations involving mouse hepatoma cells, they observed that the probe possessing a hydroxy group at position 2 allowed for efficient permeation across the cellular membrane. This specific derivative demonstrated superior cellular uptake relative to other analogs, thereby enhancing its applicability in intracellular studies.

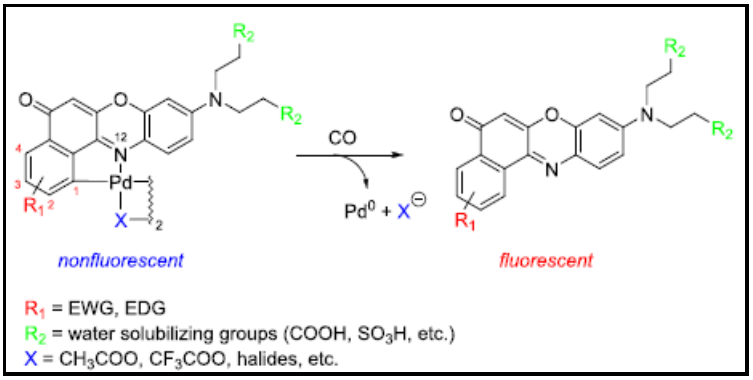

Figure 2.34. Fluorescently CO determination by the probe (Source: Madea et al., 2020).

In 2020, Morstein and colleagues synthesized ligand-activated sensing probes for fluorescent CO detection. Among these probes produced in a palladium ligand environment, COP-3E-Py gave the most successful results in living cells, brain settings, and endogenous CO production in fly brain studies (Figure 2.35.).

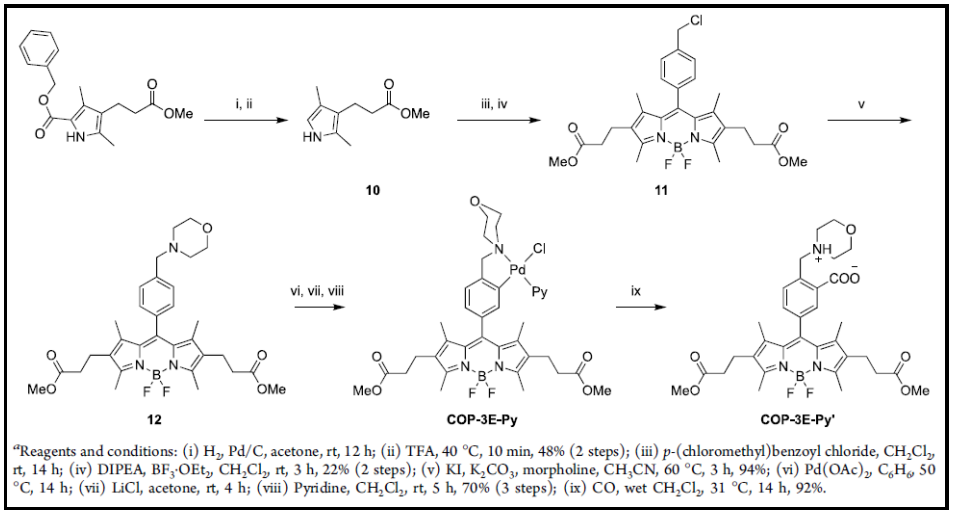

Figure 2.35. Synthetic route of the COP-3E-Py and reaction with CO (Source: Morstein et al., 2020).

In the same year, two researchers developed a fluorescence turn-on probe sensitive to carbon monoxide by synthesizing a naphthalimide-palladium(II) complex (Saha and Saha, 2020), (Figure 2.36.). The LOD value of this probe, which gives a 9-fold fluorescence turn-on due to demetallation in a carbon monoxide environment, was calculated as 1.4 μM.

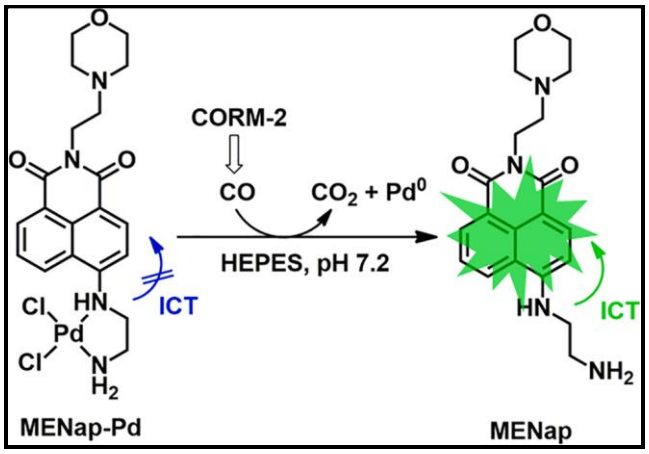

Figure 2.36. Probe response mechanism in CO environment (Source: Saha and Saha, 2020).

Three years later, a sensor employing a Pd complex with triphenylamine as the fluorophore was developed (Fang et al., 2023). This probe features a limit of detection (LOD) of 160 nM and is characterized by low cytotoxicity and high cellular uptake in cell-based studies. Furthermore, it displays exceptional selectivity and sensitivity toward CO. Notably, the supramolecular gel formulated with this probe achieves a 24% reduction of CO in the air, facilitating visible detection (Figure 2.37.).

In 2024, a fluorogenic CO sensor with a NIR BODIPY was produced by applying Pd-mediated carbonylation (Xiao et al., 2024). To enhance the water solubility of this probe, which can detect both endogenous and exogenous CO, conjugation was extended by incorporating two tetra ethylene glycol derivatives of benzaldehyde, and the Pd complex was configured as a monomer (Figure 2.38.).

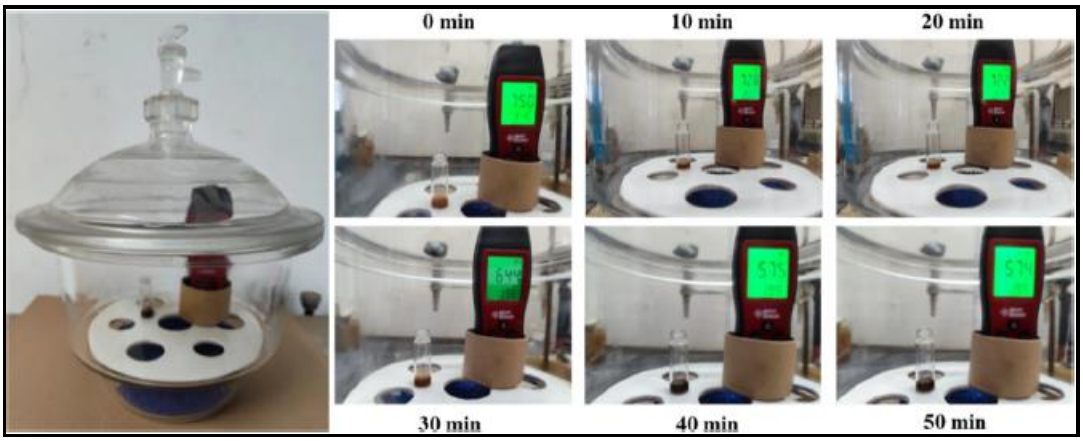

Figure 2.37. Displaying the removal of carbon monoxide in the environment at 10-minute intervals (Source: Fang et al., 2023).

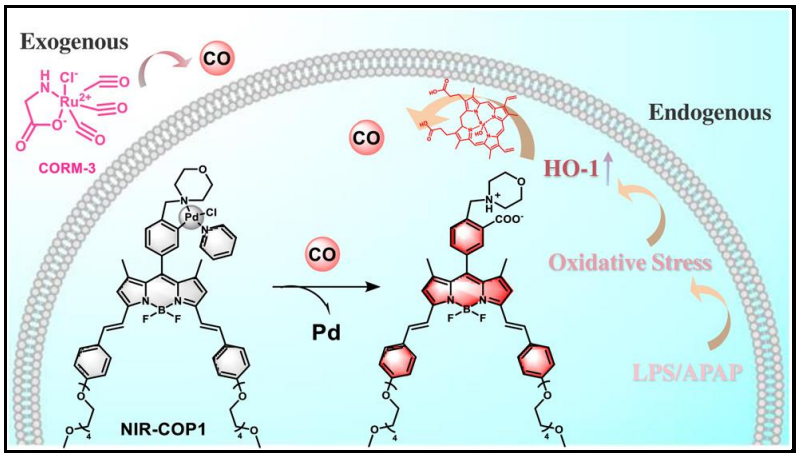

Figure 2.38. Structure of the probe and reaction with CO (Source: Xiao et al., 2024).

2.5. CO Sensors Based on Nitro Group Reduction

Recent advancements in fluorescence sensor technology involve a metal-free reduction process that converts nitro groups into corresponding amine groups in the presence of CO (Table 2.1). In these studies, CORM-2 or CORM-3 are commonly utilized as a source of CO. Initially, the presence of the nitro group inhibits fluorescence through photoinduced electron transfer (PET). However, following reduction by CO, the transformation to an amine group inhibits non-radiative decay pathways, thereby

facilitating the intramolecular charge transfer (ICT) mechanism and resulting in enhanced fluorescence.

Table 2.1. Literature studies of CO sensing probes via reduction of nitro groups.

Year	Author	Fluorophore	*Fl. Enh.	LOD	CO Source
2018	Das et al.	Naphthalimide	33 times	123 nM	CORM-3
2018	Dhara et al.	Naphthalimide	75 times	600 nM	CORM-3
2020	Sarkar et al.	Naphthalimide	55 times	180 nM	CORM-3
2021	Yue et al.	Naphthalimide	280 times	19.8 nM	CORM-3
2022	Xu et al.	Hemicyanine	-	103 nM	CORM-2
2022	Li et al.	Naphthalimide	32 times	350 nM	CORM-3
2023	Zhao et al.	BODIPY	20 times	490 nM	CORM-2
2023	Sarkar et al.	Naphthalimide	11 times	80 nM	CORM-3
2023	Sakla et al.	Naphthalimide	8 times	5940 nM	$Mn(CO)_5Br$
2024	Zhu et al.	BODIPY	100 times	20.3 nM	CORM-2

* Fluorescence Enhancement

CHAPTER 3

EXPERIMENTAL STUDY

3.1. General

Tetrahydrofuran (THF) was dried by refluxing with sodium wire and benzophenone. Dichloromethane (DCM) was dried using molecular sieve 4A. Unless otherwise, all reactions were carried out in an argon gas atmosphere. NMR spectra were acquired using a Varian VNMRJ 400 Nuclear Magnetic Resonance Spectrometer. Fluorescence and absorbance measurements were performed with a Horiba-Duetta, a combined fluorescence and absorbance spectrometer. The samples were measured in a quartz cuvette with a path length of 10.0 mm and a volume of 2.0 mL. Fluorescence imaging was conducted with a Zeiss Axio Observer inverted fluorescence microscope. The pH measurements were recorded using the HI-8014 device manufactured by HANNA. Mass spectra were obtained with an Agilent 6530 Accurate-Mass QTOF LC/MS. All measurements were carried out in triplicate.

3.2. Cell Studies

A549 human lung adenocarcinoma cells were cultured in DMEM with 10% fetal bovine serum (FBS) at 37 °C in a 5% CO_2 environment. Cells were seeded onto 12 mm coverslips within a 6-well- or 12-well plate and allowed to grow for 24 hours. Before experimentation, the cells were rinsed with PBS buffer, treated with probes for 20 minutes at 37 °C, and washed three times with PBS. Subsequently, the cells were incubated with CORM-2, or PBS solution saturated with carbon monoxide gas, for 20 minutes at 37 °C, followed by three PBS washes. DAPI was applied for 10 minutes at 37 °C, after which cells were washed three times with PBS. Fluorescence images were captured using a Zeiss Axio Observer inverted fluorescence microscope.

3.3. Quantum Yield Determinations

The fluorescence quantum yields of the probes were ascertained using optically comparable solutions of fluorescein (Φ_F= 0.925 in 0.1 M NaOH) as a reference standard (Michel et al., 2012). Based on the equation,

$$\Phi_{F(X)} = \Phi_{F(S)} (A_S F_X / A_X F_S) (n_X/n_S)^2$$

where Φ_F is the fluorescence quantum yield, A is the absorbance at the excitation wavelength, F is the area under the corrected emission curve, and n is the refractive index of the solvents. Subscripts S and X refer to the standard and the unknown.

3.4. Determination of Detection Limits

The detection limits were calculated from the fluorescence titration data (Wu et al., 2011). All measurements were taken in triplicate using freshly prepared aliquots. The graphics illustrate the change in fluorescence signal ($\Delta_F = F_1-F_0$) relative to the concentration of CORM-2. They show linear relationships between the CORM-2 concentration and the fluorescence signal changes, expressed by the equations indicating that as the concentration of CORM-2 increases, the fluorescence signal also increases proportionally. The limit of detections was calculated using the equation LOD = 3σ/k, where σ is the standard deviation of blank measurements, and k is the slope of the intensity versus concentration plot.

3.5. Photostability Studies

For photostability studies, absorbance measurements of the probes were conducted over time under suitable illumination conditions within the optimized solvent system. Samples were placed in a 10x10 mm quartz cuvette, positioned 15 cm away from the light sources. Incident radiation intensity was calculated as 3.3 mV/cm^2. The degradation rate was calculated from the equation below:

$\ln(A_t/A_0)=k_{deg} \times t$

where A_t is the absorbance at the irradiation time, A_0 is the absorbance at t=0, and t is time. The half-life is calculated using the formula: $\ln 2/k_{deg}$.

3.6. Filter Paper Experiments Exposed to CO Gas

Filter papers impregnated with the probe solutions were placed in a single-necked, 50 mL round-bottomed glass flask sealed with a septum. The balloon, pre-inflated with CO gas, was securely attached to the syringe and then inserted into the bottom of the flask. The gas was allowed to circulate outwards for one minute, and then the outlet was closed (Figure 3.1.). After remaining in the system for 2 hours under dark conditions, the filter papers were removed and compared with reference filter papers under UV light and daylight.

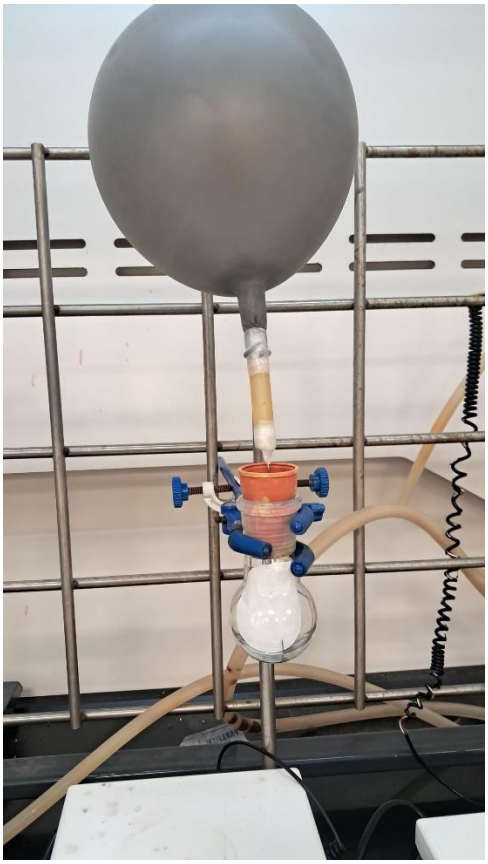

Figure 3.1. Application of CO gas to filter paper in an isolated system.

3.7. Synthesis of the Probes

3.7.1. Synthesis of the Probe 1a

Kryptopyrrole (1.35 mL, 10.0 mmol) was dissolved in THF (10 mL) at room temperature, Et_3N (1.95 mL, excess) and benzoyl chloride (0.86 mL, excess) were added to the solution over a few minutes. The reaction mixture was refluxed for 6 hours and then cooled to room temperature. The resulting triethylamine hydrochloride precipitate was removed by filtration, and the solvent was evaporated under reduced pressure. The residue was purified by column chromatography using a hexane-ethyl acetate (20:1) eluent to yield 4-ethyl-3,5-dimethyl-1H-pyrrol-2-yl(phenyl)methanone. Then, in a stirred solution of 4-ethyl-3,5-dimethyl-1H-pyrrol-2-yl(phenyl)methanone (1.135 g, 5 mmol) in dichloromethane (25 mL) at room temperature in an argon atmosphere, phosphorus oxychloride (0.5 mL, 5 mmol) was added (Çevik Eren et al., 2022). After 30 minutes, 2,4-dimethyl pyrrole (0.5 mL, 5 mmol) in 10 mL DCM was added, and the mixture was then continuously stirred for two hours at 40°C. After that, 3.5 mL of triethylamine (25 mmol) was added. Boron trifluoride diethyl etherate (6 mL, 35 mmol) was added after 15 minutes. After 2 hours, the resulting mixture was purified by column chromatography with hexane-ethyl acetate (30:1) to afford **S1** (1.2 g, 68%) as an orange solid.

S1: ^{1}H NMR (400 MHz, $CDCI_3$) δ=7.42 – 7.38 (m, 3H), 7.22 – 7.19 (m, 2H), 5.87 (s, 1H), 2.48 (s, 6H), 2.23 (q, 2H), 1.27 (s, 3H), 1.23 (s, 3H), 0.91 (t, 3H). ^{13}C NMR (101 MHz, $CDCI_3$) δ=155.54, 153.95, 142.05, 141.01, 139.49, 135.52, 133.60, 131.38, 131.04, 129.20, 128.95, 128.22, 120.67, 17.21, 14.69, 14.62, 14.41, 12.77, 11.83 (Çevik Eren et al., 2022).

To a stirred solution of **S1** (935 mg, 2.79 mmol) in 20 mL DCM, N-iodosuccinimide (1.57 g, 7 mmol) in 20 mL DCM was added dropwise at room temperature. The reaction was followed by TLC; after completion of the reaction, it was extracted with DCM, dried over $MgSO_4$, filtered, and concentrated under reduced pressure. The product was purified by column chromatography using n-hexane-EtOAc (20:1) as eluent and affords **(S2)** (1.067 g, 80%) as dark red crystals (Çevik Eren et al., 2022).

S2: ^{1}H NMR (400 MHz, $CDCl_3$) δ=7.52−7.47 (m, 3H), 7.28−7.25 (m, 2H), 2.62 (s, 3H), 2.56 (s, 3H), 2.31 (q, 2H), 1.35 (s, 3H), 1.30 (s, 3H), 0.99 (t, 3H). ^{13}C NMR (101 MHz, $CDCl_3$) δ=158.17, 153.10, 142.05, 141.09, 140.67, 135.35, 134.83, 131.89, 130.64, 129.37, 129.26 128.17, 17.25, 16.65, 15.85, 14.54, 13.03, 12.05.

S2 (613 mg, 1.28 mmol) was dissolved in a mixture of toluene (50 mL), ethanol (26 mL), and a 2 M solution of potassium carbonate (26 mL). To this solution, 4-formylphenylboronic acid (480 mg, 3.2 mmol) and tetrakis(triphenylphosphine)palladium (135 mg, 0.117 mmol) were added under an argon atmosphere at room temperature. The mixture was stirred for 40 minutes and refluxed at 80 °C for an additional 30 minutes. At the end of the reaction, the solvent was removed under reduced pressure, and the residue was extracted three times with DCM (3 × 30 mL). The combined organic extracts were dried over $MgSO_4$, filtered, and evaporated. The resulting residue was purified by column chromatography using an n-hexane-ethyl acetate (20:1) solvent system and obtained **S3** (409 mg, 70% yield) as an orange solid (Çevik Eren et al., 2022).

S3: ^{1}H NMR (400 MHz, $CDCl_3$) δ=9.94 (s, 1H), 7.83−7.80 (m, 2H), 7.45−7.39 (m, 3H), 7.27−7.23 (m, 4H), 2.52 (s, 3H), 2.46 (s, 3H), 2.26 (q, 2H), 1.25 (s, 3H), 1.22 (s, 3H), 0.94 (t, 3H). ^{13}C NMR (101 MHz, $CDCl_3$) δ= 192.02, 157.50, 150.95, 141.43, 141.10, 140.46, 137.52, 135.47, 134.87, 134.51, 132.25, 131.35, 130.94, 130.52, 129.79, 129.36, 129.18, 128.18, 17.24, 14.60, 13.31, 12.97, 12.72, 12.00 (Çevik Eren et al., 2022).

$NaBH_4$ (32 mg, 0.85 mmol) was added in a single portion to a stirred solution of **S3** (390 mg, 0.85 mmol) in 40 mL THF and stirred at RT for 1.5 hours. The solvent was removed under a reduced vacuum, and the residue was subjected to column chromatography using an n-hexane to ethyl acetate (10:1) solvent system to afford the hydroxylated product (234 mg, 60% yield). ^{1}H NMR (400 MHz, $CDCl_3$) δ=7.44−7.39 (m, 3H), 7.31−7.29 (m, 2H), 7.25−7.23 (m, 2H), 7.08−7.06 (m, 2H), 4.64 (s, 2H), 2.50 (s, 3H), 2.43 (s, 3H), 2.25 (q, 2H), 1.24 (s, 3H), 1.19 (s, 3H), 0.93 (t, 3H). ^{13}C NMR (101 MHz, $CDCl_3$) δ=155.96, 152.22, 141.19, 139.68, 139.48, 138.11, 135.66, 135.15, 133.81, 133.52, 131.73, 131.34, 130.52, 129.96, 129.27, 129.03, 128.23, 127.09, 65.30, 17.23, 14.69, 13.33, 12.84, 12.72, 11.91 (Çevik Eren et al., 2022). To the solution of the hydroxylated product (234 mg, 0.51 mmol) in 25 mL DCM at 0 °C, PBr_3 (51 μL, 0.51

mmol) was added drop by drop over 10 minutes. Upon completion of the reaction, the solvent was removed by evaporation, and the product was purified by column chromatography using n-hexane-EtOAc (20:1) to yield **S4** (174 mg, 65%).

S4: ^{1}H NMR (400 MHz, $CDCI_3$) δ=7.43–7.39 (m, 3H), 7.33–7.31 (m, 2H), 7.25–7.23 (m, 2H), 7.06–7.04 (m, 2H), 4.45 (s, 2H), 2.50 (s, 3H), 2.43 (s, 3H), 2.25 (q, 2H), 1.24 (s, 3H), 1.19 (s, 3H), 0.93 (t, 3H). ^{13}C NMR (101 MHz, $CDCI_3$) δ=156.31, 151.94, 141.24, 139.86, 138.00, 136.29, 135.60, 134.44, 133.97, 132.14, 131.85, 130.72, 129.29, 129.10, 129.06, 128.21, 33.65, 17.24, 14.67, 13.35, 12.88, 12.73, 11.93 (Çevik Eren et al., 2022).

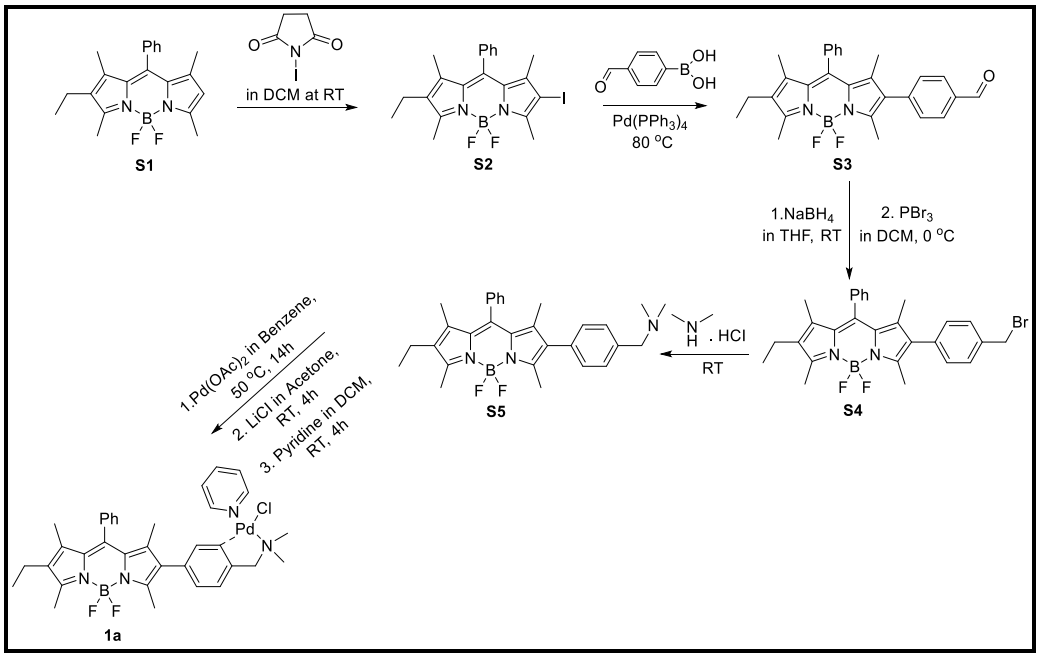

Figure 3.2. Synthesis of **1a**.

Et_3N (250 µL, 1.65 mmol) was added to a stirred solution of dimethylamine hydrochloride (135 mg, 1.65 mmol) in 30 mL DCM and 0.4 mL MeOH at room temperature. To this solution, **S4** (174 mg, 0.33 mmol) in 20 mL DCM was added. After 2 hours, the solvent was removed under reduced pressure, and the residue was purified with column chromatography using DCM-MeOH (20:1) as eluent to produce **S5** (Cinelli et al., 2015).

S5: ^{1}H NMR (400 MHz, $CDCI_3$) δ=7.49–7.44 (m, 5H), 7.31–7.29 (m, 2H), 7.17–7.15 (m, 2H), 3.82 (s, 2H), 2.56 (s, 3H), 2.51 (s, 6H), 2.49 (s, 3H), 2.31 (q, 2H), 1.30 (s,

3H), 1.25 (s, 3H), 0.99 (t, 3H). ^{13}C NMR (101 MHz, $CDCI_3$) δ=156.34, 151.78, 141.26, 139.89, 137.94, 135.56, 134.77, 133.99, 132.05, 131.96, 131.86, 130.74, 130.56, 130.19, 129.27, 129.06, 128.19, 62.60, 43.87, 17.21, 14.62, 13.32, 12.84, 12.70, 11.90 (Çevik Eren et al., 2022).

$Pd(OAc)_2$ (89 mg, 0.4 mmol) was added to a solution of **S5** (179 mg, 0.37 mmol) in 10 mL of benzene. The reaction vessel was wrapped with foil to protect it from light, sonicated for one minute, argon atmosphere applied to the reaction, and stirred for 14 hours at 50 °C. After cooling the reaction mixture to RT, 40 mL of hexane was added to precipitate the acetate dimer product as an orange solid (Çevik Eren et al., 2022). ^{1}H NMR (400 MHz, $CDCI_3$) δ=7.44–7.36 (m, 3H), 7.26–7.22 (m, 2H), 6.81–6.76 (m, 1H), 6.71–6.65 (m, 2H), 3.64 (d, J=14 Hz, 1H), 3.06 (d, J=14 Hz, 1H), 2.72 (s, 3H), 2.49 (s, 3H), 2.38 (s, 3H), 2.24 (q, 2H), 1.93 (s, 3H), 1.23–1.14 (m, 9H), 0.92 (t, 3H). ^{13}C NMR (101 MHz, CDCI3) δ=180.97, 155.25, 152.68, 145.73, 143.82, 140.97, 139.30, 138.22, 135.72, 133.82, 133.60, 133.52, 131.52, 130.65, 130.24, 129.21, 129.17, 128.97, 128.28, 128.23, 126.39, 120.83, 72.33, 52.64, 51.46, 29.83, 24.64, 17.22, 14.70, 13.39, 12.73, 11.85 (Çevik Eren et al., 2022).

In the second step, acetate dimer was dissolved in acetone saturated with lithium chloride. The reaction mixture was stirred in the dark at RT for 4 hours under an argon atmosphere. Then, the solvent was removed, and the residue was dissolved in DCM and filtered through celite. After evaporation of the solvent, the product was crystallized from DCM-Hexane, yielding chloride dimer as an orange solid (Çevik Eren et al., 2022). ^{1}H NMR (400 MHz, $CDCI_3$) δ=7.44–7.32 (m, 3H), 7.27–7.19 (m, 2H), 6.88–6.82 (m, 1H), 6.77 (d, J=7.4 Hz, 1H), 6.65 (d, J=7.5 Hz, 1H), 3.84 (s, 2H), 2.85–2.69 (m, 6H), 2.48 (s, 3H), 2.43 (s, 3H), 2.29–2.17 (m, 2H), 1.22 (s, 3H), 1.18 (s, 3H), 0.92 (t, 3H). ^{13}C NMR (101 MHz, $CDCI_3$) δ=154.74, 153.50, 145.80, 142.75, 140.97, 139.00, 138.59, 135.77, 134.45, 133.73, 133.29, 131.38, 130.75, 130.54, 129.17, 128.90, 128.30, 126.71, 121.13, 73.18, 29.83, 17.23, 14.71, 14.26, 13.56, 12.84, 12.73, 11.81 (Çevik Eren et al., 2022).

In the final step, to a stirred solution of chloride dimer (48 mg, 0.077 mmol) in 9 mL DCM, pyridine (0.093 mmol, 7.5 μL) was added, and the reaction mixture was stirred for 4 hours under argon in darkness. Upon completion of the reaction, the solvent was

evaporated, and the desired product (**1a**) was crystallized using a chloroform-n-hexane solvent system (Morstein et al., 2020).

1a: ^{1}H NMR (400 MHz, $CDCI_3$) δ=8.87−8.79 (m, 2H), 7.80 (tt, J=7.7, 1.6 Hz, 1H), 7.48−7.41 (m, 3H), 7.31 (ddd, J=7.6, 5.1, 1.4 Hz, 2H), 7.24−7.19 (m, 2H), 6.97 (d, J=7.6 Hz, 1H), 6.76 (dd, J=7.6, 1.6 Hz, 1H), 5.74 (d, J=1.5 Hz, 1H), 3.99 (s, 2H), 2.94 (s, 6H), 2.54 (s, 3H), 2.33−2.27 (m, 5H), 1.27 (s, 3H), 1.15 (s, 3H), 0.98 (t, 3H). ^{13}C NMR (101 MHz, $CDCI_3$) δ=155.60, 153.79, 153.61, 152.29, 148.68, 146.18, 146.11, 140.94, 139.49, 138.00, 137.89, 135.67, 133.94, 133.70, 133.26, 131.59, 130.76, 130.55, 129.19, 129.01, 128.21, 126.56, 125.36, 121.27, 74.08, 53.75, 52.96, 31.74, 17.22, 14.68, 13.45, 12.78, 11.87. HRMS: m/z: Calcd. for ($C_{35}H_{38}BCIF_2N_4Pd$) [$M+H^+$]: 705.1954; found, 705.1907) (Çevik Eren et al., 2022).

3.7.2. Synthesis of the Probe 1b

To a solution of 240 mg of zinc oxide in 40 mL of dry DCM, 2,4-dimethylpyrrole (8 mmol, 0.82 mL) and benzoyl chloride (10.4 mmol, 1.2 mL) were added, respectively. The reaction was stirred overnight at room temperature under an argon atmosphere. The polar product was purified by column chromatography (10 DCM:1 MeOH). In the second step, the product was dissolved in 40 mL of DCM, and boron trifluoro etherate (8.5 mL) and triethylamine (6.8 mL) were added. The reaction was stirred for 4 hours at room temperature under an argon atmosphere. At the end of the reaction, the mixture was extracted with DCM-water, and the organic phase was dried with Na_2SO_4, and the solvent was removed in vacuo. The obtained product (**S6**) was purified by column chromatography (10 Hexane: 1 EtoAc), (1.45 g, %56 yields) as orange solid, and the Rf value is 0.6 (4 Hexane: 1 EtOAc).

S6: ^{1}H NMR (400 MHz, $CDCI_3$) δ= 7.54 – 7.42 (m, 3H), 7.33 – 7.24 (m, 2H), 5.98 (s, 2H), 2.56 (t, 6H), 1.37 (d, *J* = 0.8 Hz, 6H).

S6 (2.3 mmol, 750 mg) was dissolved in 80 mL of ethyl acetate. Pyridinium chlorochromate (PCC) (4.6 mmol, 1 g) was added in portions over 5 minutes. It was stirred under an argon atmosphere at room temperature for 3 hours. At the end of the experiment, the mixture was filtered through celite, and the solvent was removed under

reduced pressure. The obtained product (**S7**) was purified by column chromatography (8 Hexane: 1 EtOAc), (428 mg, %55 yields) as dark red crystals, and the Rf value is 0.4 (4 Hexane: 1 EtOAc) (Ramos-Torres et al., 2019).

S7: ^{1}H NMR (400 MHz, $CDCI_3$) δ= 10.20 (s, 1H), 7.48 – 7.45 (m, 3H), 7.23 – 7.21 (m, 2H), 6.70 (s, 1H), 6.16 (s, 1H), 2.59 (s, 3H), 1.40 (s, 3H), 1.32 (s, 3H).

(630 mg, 1.86 mmol) **S7** was dissolved in 40 mL EtOH. To this solution, (155 mg, 2.23 mmol) hydroxylamine hydrochloride was added, and the reaction mixture was refluxed for 10 minutes. After, the solvent was removed, and the crude product was purified with column chromatography by using hexane- EtOAc (6:1) to yield **S8** (%78) as a red powder. The Rf value is 0.4 (4 hexane: 1 EtOAc).

S8: ^{1}H NMR (400 MHz, $CDCI_3$) δ= 8.61 (s, 1H), 7.99 (bs, 1H), 7.53 – 7.48 (m, 3H), 7.31 – 7.28 (m, 2H), 6.60 (s, 1H), 6.08 (s, 1H), 2.59 (s, 3H), 1.41 (s, 3H), 1.40 (s, 3H). ^{13}C NMR (101 MHz, $CDCI_3$) δ= 144.10, 142.47, 141.24, 134.61, 130.77, 129.51, 129.44, 129.39, 127.91, 127.80, 125.95, 123.90, 122.97, 117.72, 15.14, 14.82, 14.48.

1b was synthesized as described previously in probe synthesis (Michel et al., 2012). (43 mg, 0.12 mmol) of compound **S8** was employed along with 1 equivalent of $Pd(OAc)_2$ for the synthesis. The product was isolated with a good yield (%85) as a violet powder.

1b: ^{1}H NMR (400 MHz, $CDCI_3$) δ= 9.22 (s, 1H), 8.24 (s, 1H), 7.58 – 7.54 (m, 3H), 7.39 – 7.36 (m, 2H), 6.08 (s, 1H), 2.54 (s, 3H), 1.71 (s, 3H), 1.59 (s, 3H), 1.43 (s, 3H). ^{13}C NMR (101 MHz, $CDCI_3$) δ= 184.62, 160.23, 146.50, 144.69, 144.67, 142.26, 141.67, 141.58, 134.71, 133.83, 133.46, 129.48, 129.44, 128.10, 127.97, 123.32, 119.97, 29.83, 23.00, 15.08, 14.84.

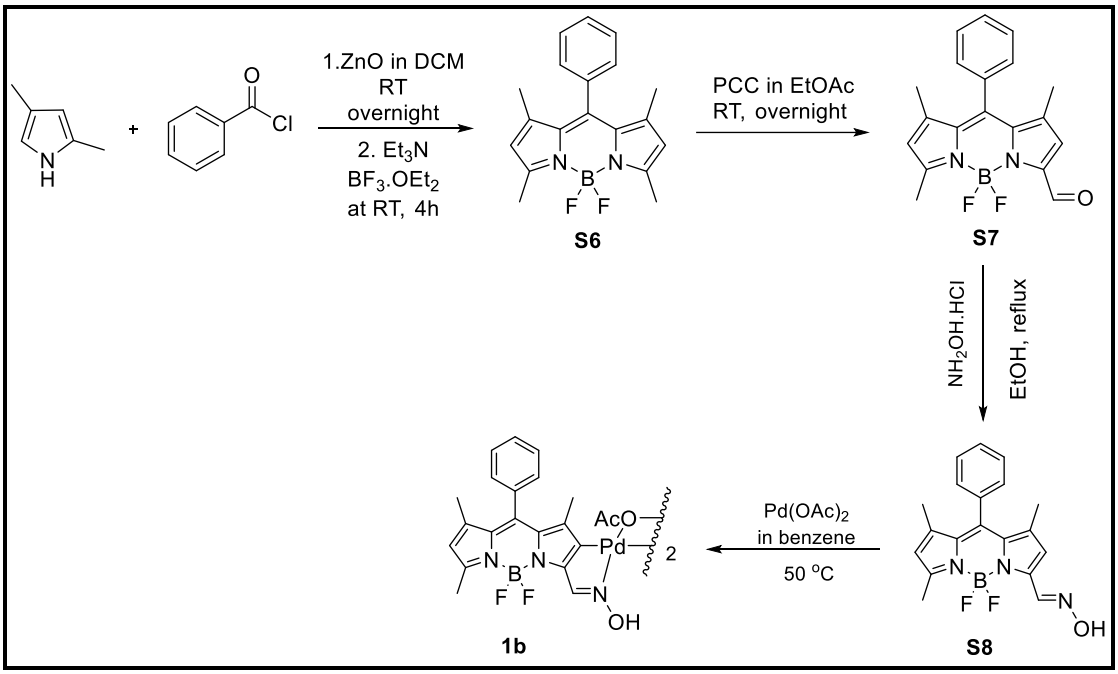

Figure 3.3. Synthesis of **1b**.

3.7.3. Synthesis of the Probes 1c and 1d

(1.67 mL, 16.2 mmol) 2,4-dimethylpyrrole and (0.64 mL, 8.1 mmol) chloroacetyl chloride were dissolved in 100 mL dry DCM. The reaction mixture was stirred at 50 °C under an argon atmosphere for 90 minutes. After removing the solvent under reduced pressure, the residue was dissolved %5 DCM in 200 mL toluene. 5.5 mL Et_3N was added to the solution and stirred at RT for 30 minutes under air. 7 mL $BF_3.OEt_2$ was added to the solution, and the reaction mixture was stirred at 50 °C, for 90 minutes. The solvent was removed, the residue was dissolved with EtOAc, the organic layer was washed with water, and dried with Na_2SO_4. The solvent was evaporated, and the product was purified with column chromatography using hexane-EtOAc (10:1) to yield **S9** (%73) as dark orange crystals (Rosenthal and Lippard, 2010).

S9: ^{1}H NMR (400 MHz, $CDCl_3$) δ= 6.06 (s, 2H), 4.81 (s, 2H), 2.58 (s, 12H).

(468 mg, 1.6 mmol) **S9** was dissolved in 50 mL DCM. (332 mg, 2.4 mmol) K_2CO_3 and (200 mg, 2.4 mmol) dimethylamine hydrochloride were added to the solution and stirred overnight at RT. After completion of the reaction, the solution was filtered with a short pad of celite, and the solvent was removed. The product was purified with column

chromatography using DCM-MeOH (10:1) to afford **S10** (%60) as a dark orange solid. The Rf value is 0.35 (10 DCM: 1 MeOH).

S10: ^{1}H NMR (400 MHz, $CDCI_3$) δ= 6.49 (s, 1H), 6.10 (s, 1H), 3.90 (s, 2H), 2.60 (s, 3H), 2.52 (s, 3H), 2.45 (s, 3H), 2.43 (s, 9H). ^{13}C NMR (101 MHz, $CDCI_3$) δ= 154.95, 154.59, 142.30, 141.87, 140.80, 132.43, 131.81, 121.72, 119.96, 56.71, 46.18, 17.64, 17.47, 16.58, 14.61.

(32 mg, 0.1 mmol) of **S10** was dissolved in 6 mL benzene. To this solution, (22.5 mg, 0.1 mmol) $Pd(OAc)_2$ was added and sonicated for 1 minute. The reaction mixture was stirred at 50 °C for 14 hours in the dark. The reaction mixture was cooled to RT and crystallized with n-hexane. Formed crystals were dissolved with DCM and purified with column chromatography using DCM-MeOH (20:1) eluent system. Probe **1c** was obtained with a good yield (%90) as a red powder, and the Rf value is 0.7 (10 DCM: 1 MeOH) (Michel et al., 2012).

1c: ^{1}H NMR (400 MHz, $CDCI_3$) δ= 5.98 (s, 1H), 3.74 (d, J = 16.7 Hz, 1H), 3.62 (d, J = 16.7 Hz, 1H), 2.92 (s, 3H), 2.56 (s, 3H), 2.42 (s, 3H), 2.40 – 2.36 (m, 9H), 2.01 (s, 3H). ^{13}C NMR (101 MHz, $CDCI_3$) δ= 181.80, 161.86, 151.92, 142.89, 140.14, 140.00 132.54, 132.04, 124.18, 120.45, 65.33, 53.84, 51.81, 23.93, 17.55, 16.68, 15.57, 14.39.

The purified product was dissolved in a saturated solution of LiCI in acetone. The reaction solution was stirred at RT for 4 hours. Then, the solvent was evaporated, and the product crystallized with n-hexane: $CHCI_3$. The product (**1d**) was isolated qualitatively as a red powder (Michel et al., 2012).

1d: ^{1}H NMR (400 MHz, $CDCI_3$) δ= 6.00 (s, 1H), 4.00 (s, 2H), 2.87 (s, 6H), 2.58 (s, 3H), 2.51 (s, 3H), 2.44 (s, 3H), 2.39 (s, 3H). ^{13}C NMR (101 MHz, $(CD_3)_2SO$) δ= 164.42, 148.10, 145.37, 139.57, 138.40, 132.41, 130.48, 121.66, 119.42, 63.87, 51.44, 41.70, 17.41, 16.80, 16.26, 13.76.

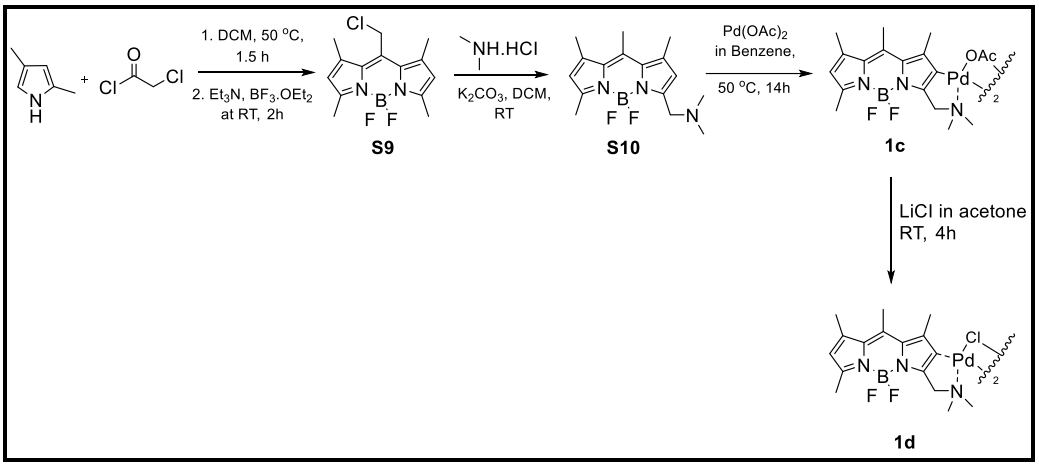

Figure 3.4. Synthesis of **1c** and **1d**

3.7.4. Synthesis of the Probe 1e

S7 (0.66 mmol, 223 mg) and 2-aminothiophenol (0.66 mmol, 82.6 mg) were dissolved in 10 mL dimethylformamide. Iodine, dissolved in 2 mL of dimethylformamide (0.33 mmol, 83.8 mg), was added. After stirring at 100 °C for 1 hour, it was washed with 10% $Na_2S_2O_3$ solution and extracted with DCM. The organic residue was dried with Na_2SO_4, and the solvent was removed under vacuum. The mixture was purified by column chromatography using 200-400 mesh silica gel. The column was initially eluted with a 15 Hexane: 10 DCM), then the gradient was gradually adjusted to a 2 Hexane: 3 DCM). The desired product (**S11**) was obtained with a good yield (219 mg, %75) as a dark red powder, and the Rf value is 0.55 (2 DCM: 1Hexane), (Li et al., 2006).

S11: ^{1}H NMR (400 MHz, $CDCI_3$) δ= 8.02 (dd, J = 8.1, 2.5 Hz, 1H), 7.86 (dd, J = 8.0, 1.7 Hz, 1H), 7.46 – 7.39 (m, 4H), 7.34 – 7.29 (m, 1H), 7.27 – 7.24 (m, 2H), 7.00 (s, 1H), 6.05 (s, 1H), 2.59 (s, 3H), 1.38 (s, 3H), 1.36 (s, 3H). ^{13}C NMR (101 MHz, $CDCI_3$) δ= 161.34, 158.73, 153.15, 146.91, 144.61, 143.04, 140.26, 137.19, 136.98, 134.66, 133.87, 133.34, 132.16, 129.50, 128.01, 126.33, 125.58, 123.80, 123.53, 123.37, 121.59, 118.66, 115.40, 15.37, 14.81, 14.51. HRMS (ESI) calculated: $C_{25}H_{21}BF_2N_3S^+$ [M + H^+]: 444.1512; founded: 444.1555.

S11 (0.23 mmol, 103 mg) and $Pd(OAc)_2$ (0.25 mmol) were dissolved in 7 mL of benzene. The mixture was kept in an ultrasonic homogenizer for 1 min, wrapped with foil the reaction flask to protect it from light, and the reaction mixture was stirred at 50 °C

overnight under an argon atmosphere. The reaction mixture was cooled to room temperature and crystallized with n-hexane. In the 2nd step of the reaction, the crystals were dissolved in 10 mL of acetone saturated with lithium chloride and protected from light, stirred under argon for 4 h at room temperature. At the end of the experiment, the mixture was filtered through a short pad of celite. The filtrate was concentrated under vacuum (Michel et al., 2012). The remaining solid was dissolved in 14 mL of dry DCM 0.23 mmol (1 eq.) of pyridine was added and stirred at room temperature for 4 h. At the end of the experiment, the solvent was removed under vacuum, and the remaining solid crystallized with the help of n-hexane. The desired product (**1e**) was purified with column chromatography by using DCM: MeOH eluting system (94,6 mg, %62) as dark blue powder (Morstein et al., 2020).

1e: ^{1}H NMR (400 MHz, $CDCI_3$) δ= 9.73 (d, J = 8.6 Hz, 1H), 8.92 (d, J = 5.0 Hz, 2H), 7.82 – 7.74 (m, 2H), 7.57 – 7.53 (m, 1H), 7.44 – 7.33 (m, 6H), 7.25 – 7.23 (m, 2H), 6.10 (s, 1H), 2.64 (s, 3H), 1.33 (s, 3H), 0.46 (s, 3H). ^{13}C NMR (101 MHz, $CDCI_3$) δ= 165.79, 160.51, 157.79, 153.90, 151.18, 150.60, 146.85, 141.63, 140.65, 138.40, 137.57, 134.97, 134.51, 134.49, 134.05, 133.72, 133.69, 129.39, 129.27, 128.00, 127.64, 126.06, 125.66, 124.23, 123.65, 121.48, 15.33, 14.98, 13.01. HRMS (ESI) calculated: $C_{27}H_{22}BF_2N_4PdS^+$ $[M – CI – Pyr + MeCN]^+$: 589.0661; founded: 589.0688.

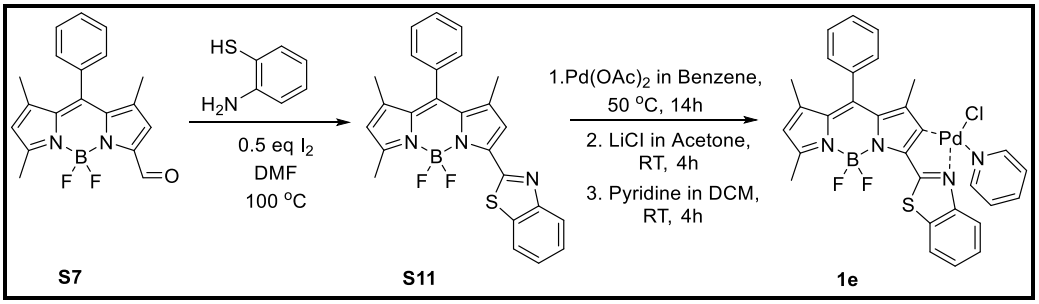

Figure 3.5. Synthesis of **1e**

CHAPTER 4

RESULTS AND DISCUSSION

In this study, five Pd complexes with a BODIPY skeleton were synthesized for the fluorescent detection of CO. The spectroscopic properties of these compounds and their interactions with carbon monoxide gas were systematically examined and analyzed. Additionally, the responsiveness of these compounds to CO gas within living cells was investigated. The structures of the probes and the products formed upon interaction with CO were elucidated using HRMS and NMR spectroscopy.

4.1. Reaction of the Probes with CO

As a standard procedure, a probe concentration of 0.1 mmol was dissolved in 10 mL of $CHCl_3$ and 0.5 mL of H_2O. CO gas was bubbled through this solution, and a color change in the solution indicated the completion of the reaction. The products formed as a result of the reaction, which was checked with TLC, were isolated and characterized.

Building upon findings from a 2012 literature study (Michel et al.), Pd metal was coordinated with an identical ligand group at the 2-position of the BODIPY core to investigate its interaction with CO gas. Interestingly, no demetallation product was detected when **1a** was exposed to CO gas under standard conditions. The carboxylated product (**1aa**) was isolated with a 78% yield (Figure 4.1.), and its structure was determined using ^{1}H, ^{13}C NMR, and HRMS analysis. Furthermore, spectroscopic measurements aligned well with the characteristics of the synthesized product.

1aa: ^{1}H NMR (400 MHz, $CDCI_3$) δ= 11.13 (s, 1H), 7.96 (s, 1H), 7.56 – 7.47 (m, 3H), 7.33 – 7.30 (m, 1H), 7.20 (dd, J = 16.8, 7.8 Hz, 2H), 7.10 – 7.06 (m, 1H), 3.84 (s, 2H), 2.58 (s, 3H), 2.53 (s, 6H), 2.36 – 2.28 (m, 5H), 1.32 (s, 3H), 1.27 (s, 3H), 1.00 (t, 3H). ^{13}C NMR (101 MHz, $CDCI_3$) δ= 162.65, 158.15, 141.40, 135.52, 135.17, 133.35, 133.13, 132.71, 131.57, 129.90, 129.31, 129.10, 128.50, 128.40, 128.34, 128.22, 128.14, 127.69, 126.57, 62.65, 45.90, 29.93, 18.89, 17.24, 14.65, 14.31, 11.97, 8.59. HRMS (ESI) calculated: $C_{31}H_{35}BF_2N_3O_2^+$ [M+H$^+$]: 530.2785; founded: 530.2748.

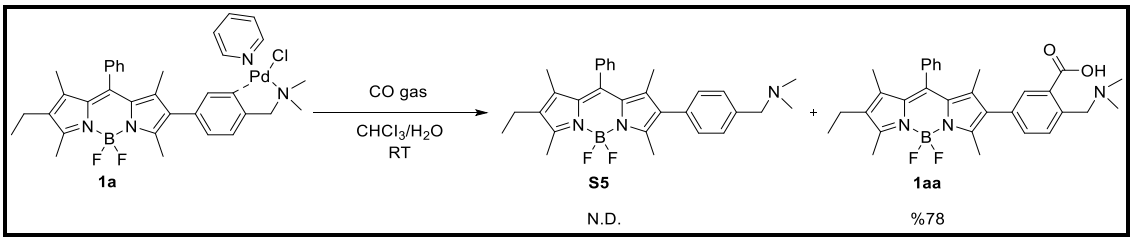

Figure 4.1. Reaction with carbon monoxide gas of the probe **1a**.

Fluorescence in molecules tends to decrease as heavy metal atoms are positioned closer to the fluorophore group. In light of this phenomenon, to investigate this effect and the probe's responsiveness to CO gas., Pd metal was directly attached to the BODIPY core. Based on this conceptual framework, **1b** was synthesized. The results demonstrated

that, at the conclusion of the reaction, no carboxylated product was obtained; instead, the demetallation product was successfully synthesized with a yield of 91% (Figure 4.2.).

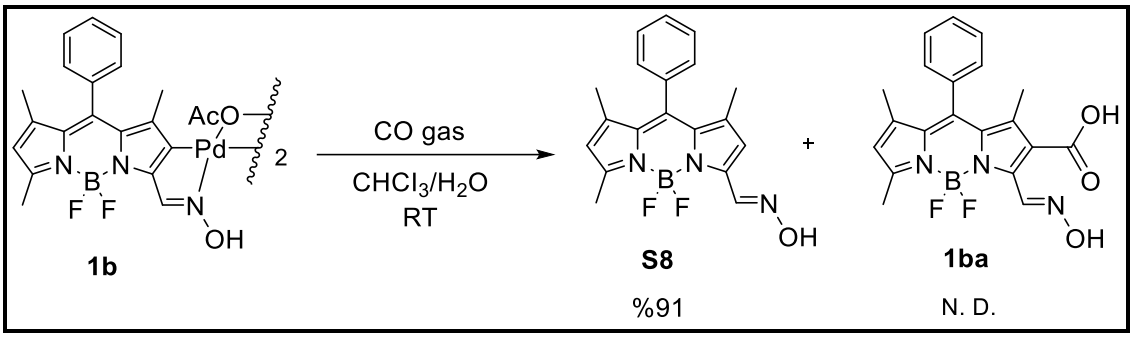

Figure 4.2. Reaction with carbon monoxide gas of the probe **1b**.

In the next step, the environment surrounding the nitrogen group bound to the Pd metal was modified. Following the approach outlined in the 2012 research (Michel et al.), we incorporated two methyl groups attached to the nitrogen in our study. Simultaneously, the ligands coordinated to palladium were modified, and the effects of various ligands were investigated. In the presence of the acetate ligand (**1c**), the CO reaction resulted in a 63% yield of the carboxylated product (**1ca**) and a 26% yield of the demetallated product (**S10**), (Figure 4.3.)

1ca: ^{1}H NMR (400 MHz, $CDCl_3$) δ= 6.23 (s, 1H), 4.21 (s, 2H), 2.78 (s, 3H), 2.69 (s, 3H), 2.59 (s, 6H), 2.55 (s, 3H), 2.47 (s, 3H). ^{13}C NMR (101 MHz, $CDCl_3$) δ= 160.08, 153.79, 147.66, 146.26, 144.91, 142.18, 134.83, 134.81, 131.16, 124.31, 53.98, 42.89, 29.85, 18.10, 17.73, 15.16, 15.01.

In the subsequent phase of the study, the ligand coordinated to the palladium center underwent modifications to assess its impact on the carbonylation reaction. Specifically, compound **1c** was subjected to treatment with acetone saturated with LiCl, which facilitated the substitution of the acetate group with a chlorine atom. Notably, the carbonylation reaction of compound **1d** resulted exclusively in the formation of the demetallation product, yielding an 80% success rate (Figure 4.3.). This outcome underscores the critical role that ligands bound to palladium play in mediating the reactivity of the molecule with CO.

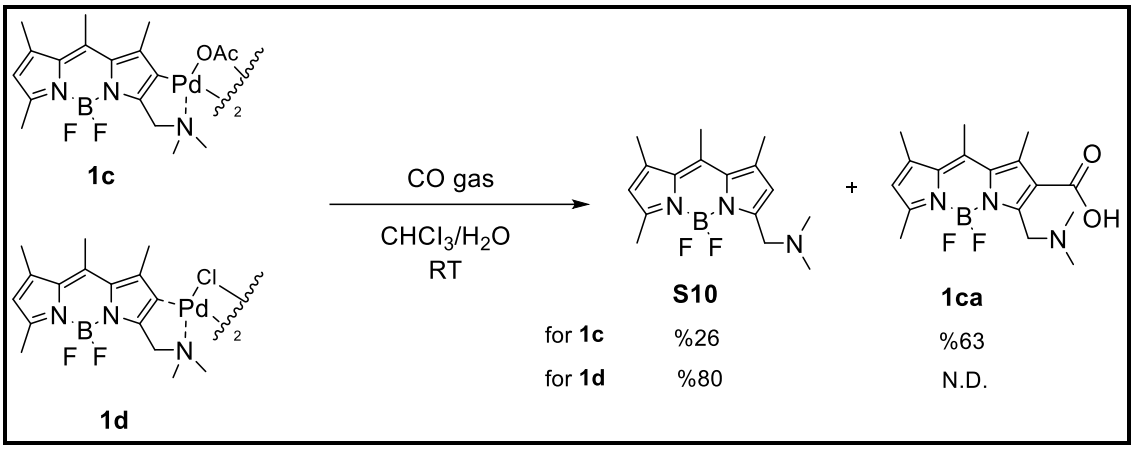

Figure 4.3. Reaction with carbon monoxide gas of the probe **1c** and **1d**.

Finally, the aminothiophenol group was conjugated to the 3-position of the BODIPY, and palladium was subsequently linked to this group and the BODIPY core **(1e)**. As a result of the standard reaction of this molecule with CO gas, no carboxylated product was detected; however, a demetallation product (**S11**) was isolated with an 85% yield (Figure 4.4.). The presence of the demetallation product was confirmed through thin-layer chromatography (TLC) and spectroscopic analyses.

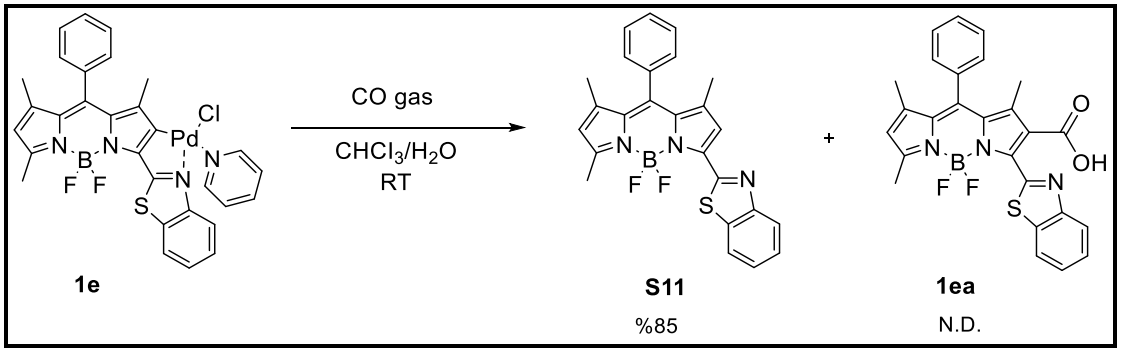

Figure 4.4. Reaction with carbon monoxide gas of the probe **1e**.

4.2. Spectroscopic Investigations of the Probe 1a

The spectroscopic properties of compound **1a** were systematically investigated, drawing inspiration from the work of Chang (Michel et al., 2012). In Chang's study, the group located at the meso position of BODIPY was attached to the 2 position, which

aimed to compare in our research (Çevik Eren et al., 2022). It was anticipated that the probe would exhibit fluorescence due to the distance between the metal atom and the fluorophore group. However, a key objective was to identify a solvent system that would suppress fluorescence. Through various tests, it was discovered that the optimal solvent system for the probe was PBS/ACN.

After finding the solvent system, measurements were conducted to evaluate the probe's performance in different aqueous systems and identify the most suitable environment for its optimal functionality. The studies revealed that the probe exhibits optimal performance in 8PBS/2ACN.

The investigation centered on the spectroscopic properties of probe **1a** with respect to CO utilizing ultraviolet and fluorescence spectroscopy. In the absence of CO, the probe exhibited absorption at the characteristic wavelength of the BODIPY fluorophore at 517 nm (Figure 4.5.a). The analysis revealed that the probe did not demonstrate any fluorescence when excited at wavelengths of 460 nm or 510 nm. However, after the addition of CO, a slight blue shift in the absorbance was observed; the new absorption peak was at 503 nm, and the solution became visibly fluorescent at 537 nm when excited at 460 nm (Figure 4.5.b).

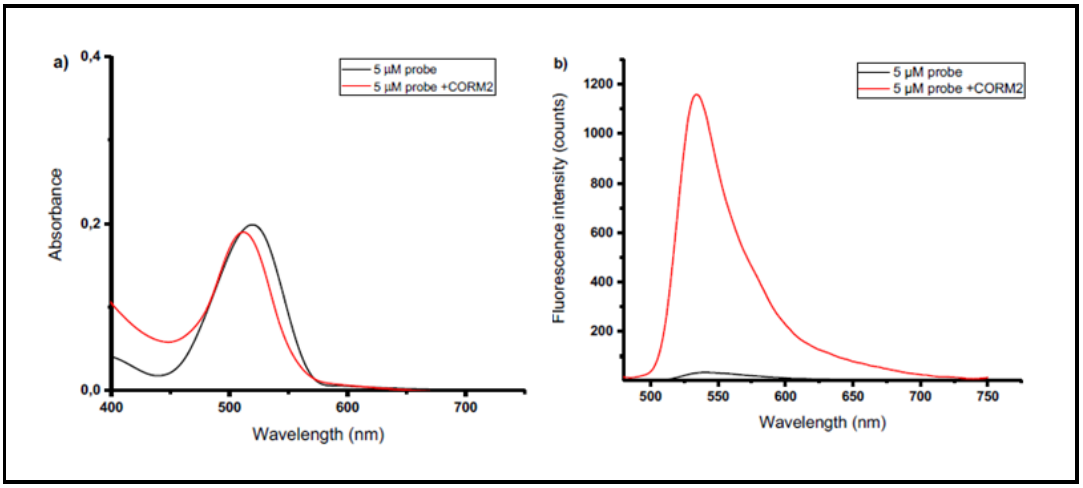

Figure 4.5. a) Absorbance and b) fluorescence spectra of **1a** (5 µM) in the absence and presence of CORM-2 (250 µM) in 0.01 M PBS/CH_3CN (pH 7.4, v/v,8:2), (λ_{ex}: 460 nm).

A titration experiment was conducted by gradually adding CORM-2 to the probe solution over a concentration range from 0 to 100 eq for 2 hours, and a linear increase in probe fluorescence intensity was observed (Figure 4.6.).

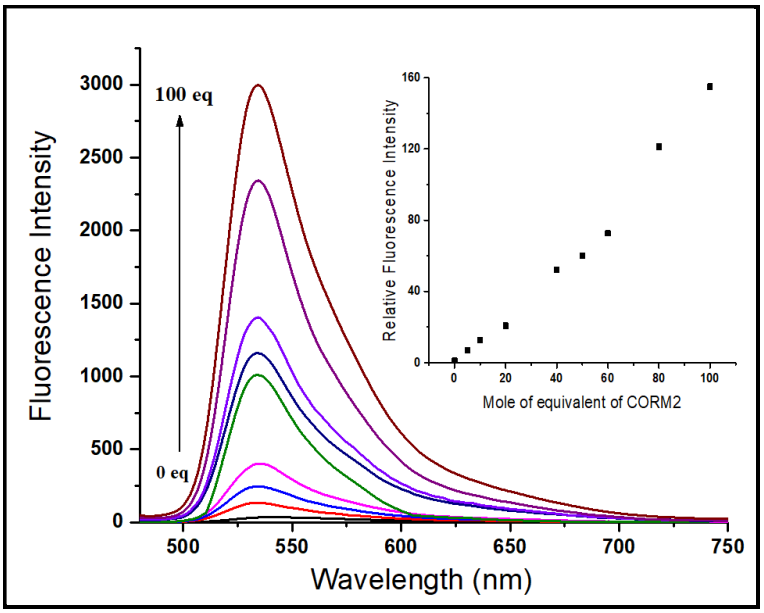

Figure 4.6. Fluorescence spectra of **1a** (5 μM) in the presence of increasing amount of CORM-2 (0-500 μM) in 0.01 M PBS/CH_3CN (pH 7.4, v/v,8:2), (λ_{ex}: 460 nm). Inset: Calibration curve.

Next, the probe's variation in fluorescence intensity over time at a fixed CORM-2 concentration was investigated. It was determined that the fluorescence intensity increased by more than 60-fold over 120 minutes, after which the solution reached saturation (Figure 4.7.).

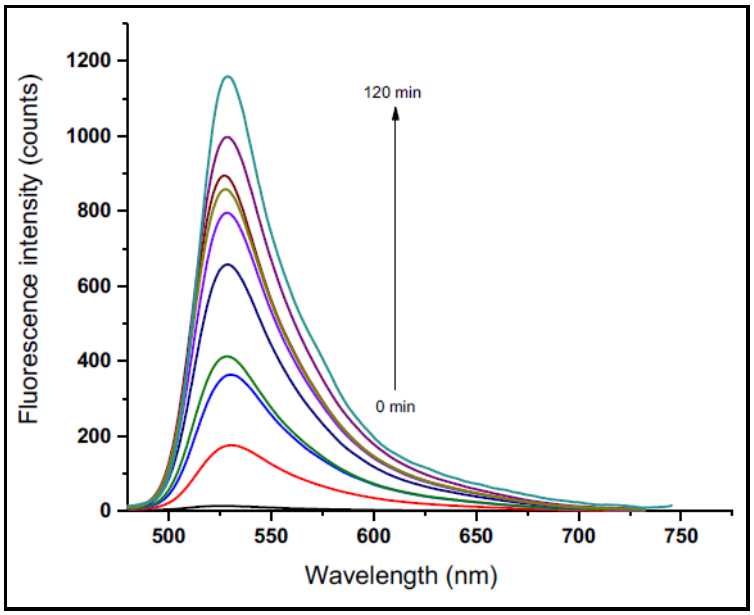

Figure 4.7. Reaction time profiles of **1a** (5 μM) in the presence of CORM-2 (50 eq) in 0.01 M PBS/CH_3CN (pH 7.4, v/v, 8:2), (λ_{ex}: 460 nm).

The probe's selectivity was investigated in the presence of biologically relevant analytes and reactive oxygen species commonly found in living cells. The probe exhibited no response to any species other than CO, demonstrating its selectivity for CO in the presence of these biologically relevant species (Figure 4.8).

Measurements were conducted at various pH levels to ascertain the probe's ideal operational pH and to compare it with the physiological pH environment. **1a** exhibited fluorescence across a pH range of 4 to 9, with optimal performance observed at physiological pH. Sensitivity was reduced under both acidic and basic conditions (Figure 4.9.).

In the next step, the quantum yields of the probe and the product formed due to its reaction with CO gas were calculated. The fluorescence quantum yields of **1a** and **1aa** were found according to the general procedure. As expected, quantum yields were found to be $\Phi_{F(\mathbf{1a})} = 0.035$ and $\Phi_{F(\mathbf{1aa})} = 0.862$ (Figure 4.10.).

For the detection limit determination, fluorescence titration data of the probe in the absence and presence of CORM-2 (0.1 μM- 1.0 μM) were collected. The fluorescence intensity and CORM-2 concentration showed a good linear relationship with $R^2 = 0.9927$ (Figure 4.11.), and the detection limit was calculated to be 263 nM.

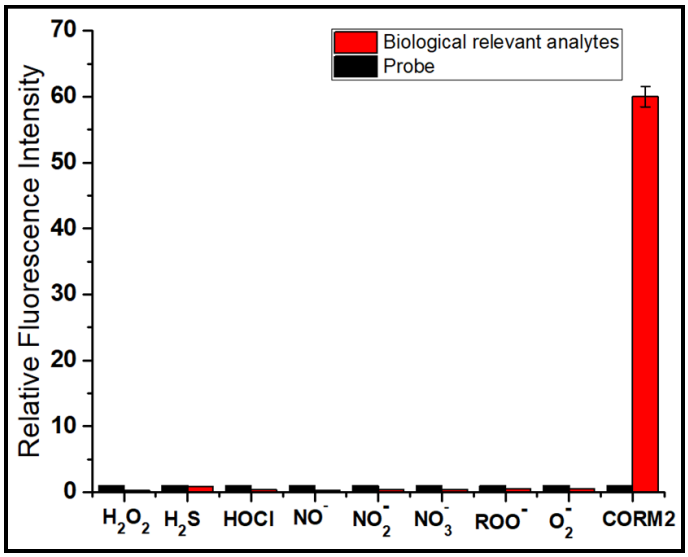

Figure 4.8. Fluorescence intensities of **1a** (5 μM) towards other biologically relevant analytes and reactive oxygen species (50 eq) along with CORM-2 in 0.01 M PBS/CH_3CN (pH 7.4, v/v, 8:2) (λ_{ex}: 460 nm).

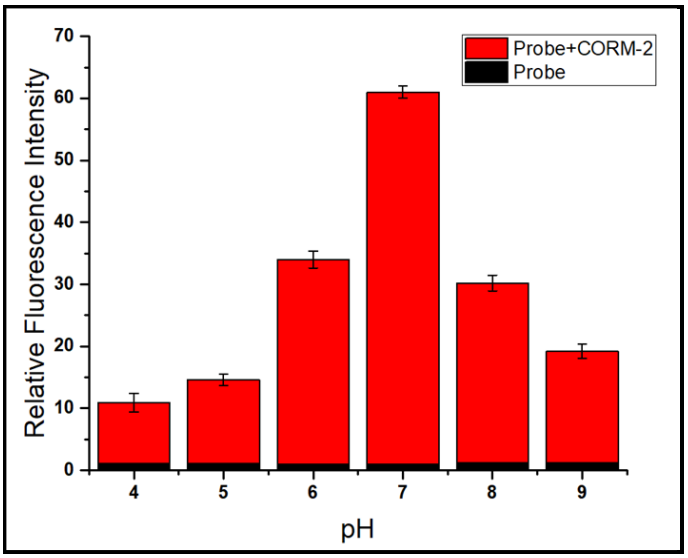

Figure 4.9. Performance of **1a** (5 μM) with CORM-2 (50 eq) at various pH levels in 0.01 M PBS/CH_3CN (pH 7.4, v/v, 8:2), (λ_{ex}: 460 nm).

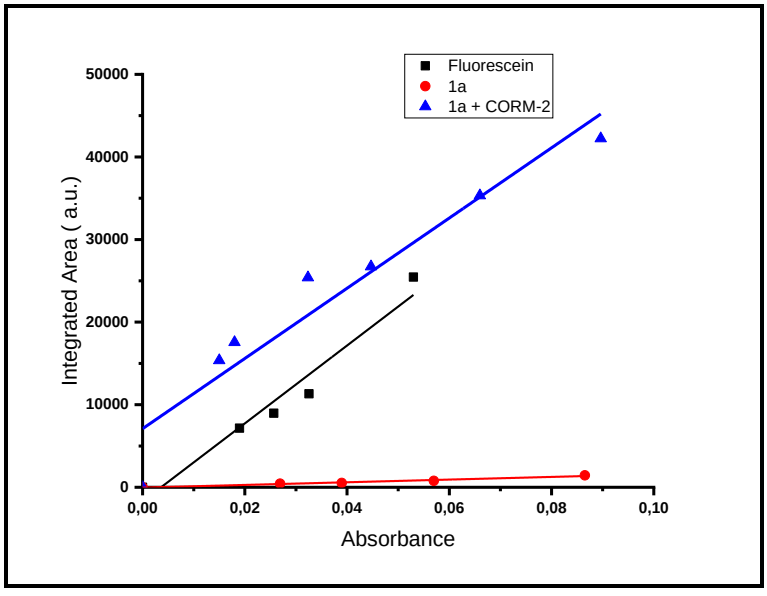

Figure 4.10. The quantum yield plot and relative fluorescence intensities are used to calculate quantum yields using fluorescein as a reference.

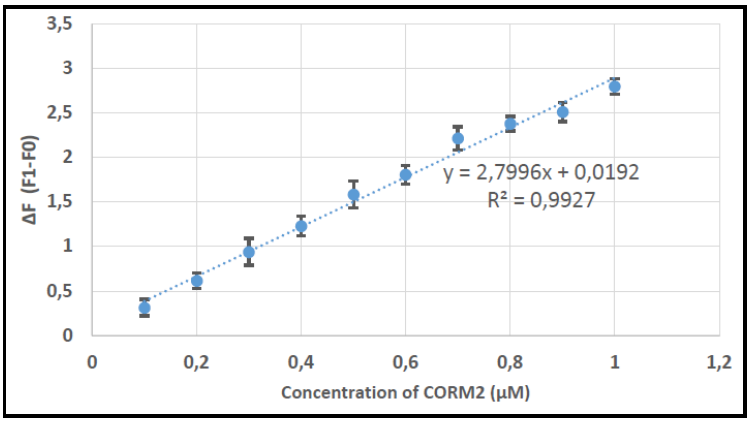

Figure 4.11. Fluorescence changes of **1a** with the addition of CORM-2 at increasing concentrations in 0.01 M PBS/CH_3CN (pH 7.4, v/v, 8:2), (λ_{ex}: 460 nm).

Building upon the encouraging results obtained from our spectroscopic measurements, we conducted a detailed investigation into the probe's sensitivity to CO within a living cell environment. The experimental procedure began with the incubation of A549 cells in a solution of CORM-2 at a concentration of 120 μM for a precise duration of 20 minutes. This initial step was followed by a secondary incubation of the cells with **1a** at a concentration of 4 μM for an additional 20 minutes, allowing ample time for the probe to interact with its target. To further elucidate the cellular architecture, DAPI staining was employed for 10 minutes, effectively labeling the nuclei of the cells and providing a clear contrast against the background. Upon examining the fluorescence, an intriguing outcome was observed: cells that were treated solely with **1a** exhibited no significant fluorescence, suggesting a lack of interaction or detection. In contrast, cells that received a dual treatment of both **1a** and CORM-2 showcased a striking and distinct fluorescence signal (Figure 4.12). These compelling results affirm that **1a** possesses the remarkable ability to penetrate the cell membrane and successfully detect CO in living organisms, highlighting its potential for future applications in biomedical research.

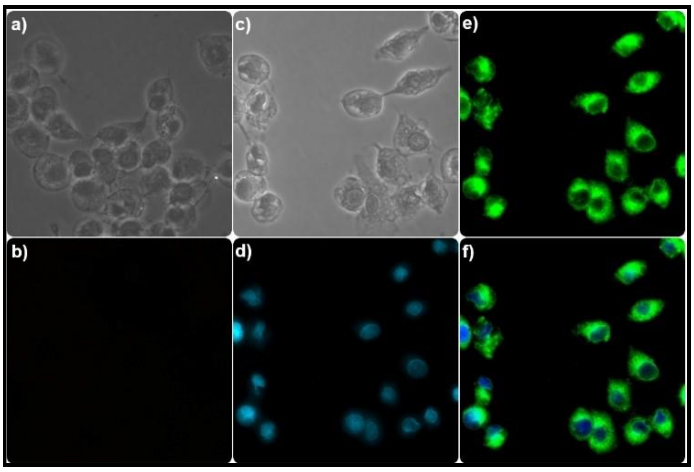

Figure 4.12. Fluorescence images of A549 cells. (a) Bright-field image of A549 cells treated with only **1a** (4 μM); (b) fluorescence image of cells treated with only **1a** (4 μM) (control); (c) bright field image of A549 cells treated with **1a** (4 μM) and CORM-2 (120 μM); (d, e) fluorescence image of (c); (f) merged images of frames (d and e). (λ_{ex}:460 nm), scale bar: 100 μm.

4.3. Spectroscopic Investigations of the Probe 1b

Through UV-visible and fluorescence spectroscopy, the spectroscopic properties of 1b were examined in both the absence and presence of CO. A series of solvent systems were evaluated to determine the optimal environment for **1b**, ultimately identifying a PBS-ethanol solvent mixture as the most effective system. The absorbance measurements indicated a prominent peak at 574 nm. Furthermore, upon interaction with CORM-2, a new peak emerged at 525 nm, demonstrating a blue shift (Figure 4.13).

To assess the fluorescent properties of **1b**, excitation wavelengths of 460, 500, 540, and 560 nm were employed. As expected, no fluorescence intensity was detected. Upon interaction with CORM-2, **1b** exhibits high fluorescence intensity, with an emission wavelength in 540 nm when excited at 500 nm (Figure 4.14).

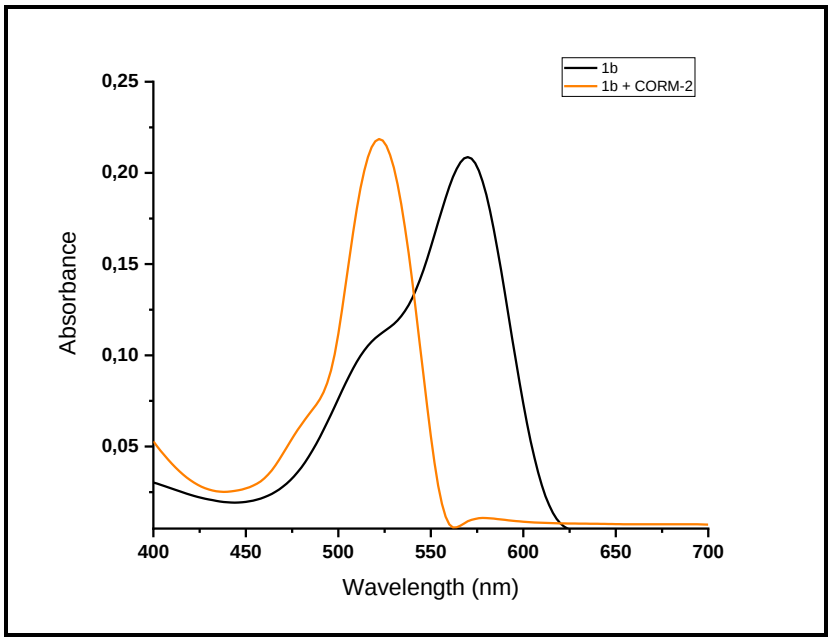

Figure 4.13. Absorbance spectra of **1b** (5 μM) in the absence and presence of CORM-2 in 0.01 M PBS/EtOH (pH 7.4, v/v, 1:1).

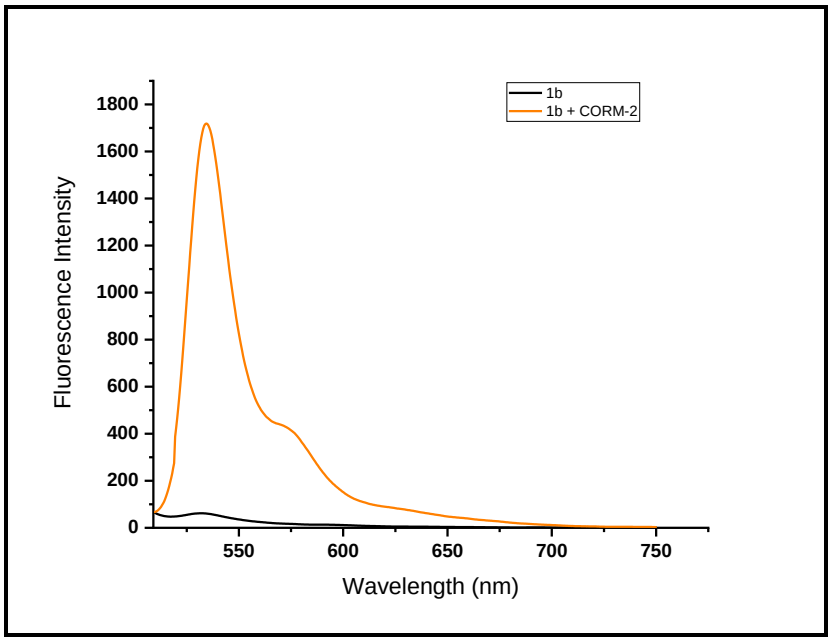

Figure 4.14. Fluorescence spectra of **1b** (5 μM) in the absence and presence of 40 eq. CORM-2 in 0.01 M PBS/EtOH (pH 7.4, v/v, 1:1), (λ_{ex}: 500 nm).

Experiments were conducted to determine the optimal water concentration for the effective interaction between **1b** and CORM-2. Consequently, the 1PBS/1EtOH system

was identified as the optimal solvent environment for **1b**'s interaction with CORM-2, yielding a 28-fold increase in fluorescence intensity (Figure 4.15.).

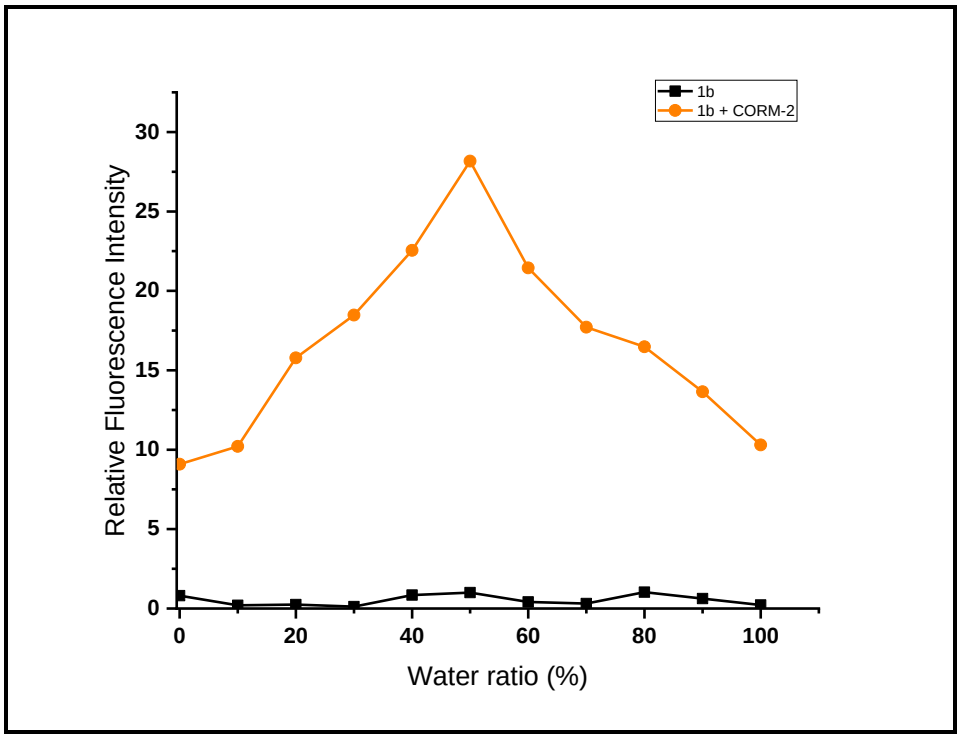

Figure 4.15. Fluorescence performance of **1b** (5 μM) at increasing water ratios with CORM-2 (40 eq.) in 0.01 M PBS/EtOH (pH 7.4 v/v, 1:1), (λ_{ex}: 500 nm).

In the next step, systematic titration of **1b** with CORM-2 was performed. Fluorescence measurements taken at increasing concentrations of CORM-2 indicated that **1b** reached saturation at 40 equivalents of CORM-2 (Figure 4.16.).

Time-dependent fluorescence measurements taken at a constant concentration of CORM-2 revealed that **1b** responded rapidly, reaching maximum fluorescence intensity within 45 minutes, followed by a gradual decrease in intensity over a period (Figure 4.17.).

The fluorescence behavior of **1b** was also investigated under similar conditions in the presence of other biological analytes and reactive oxygen species. Surprisingly, **1b** responded to almost all of them with varying intensities, and the probe exhibited significantly higher fluorescence intensity in response to H_2S than CORM-2 (Figure 4.18.).

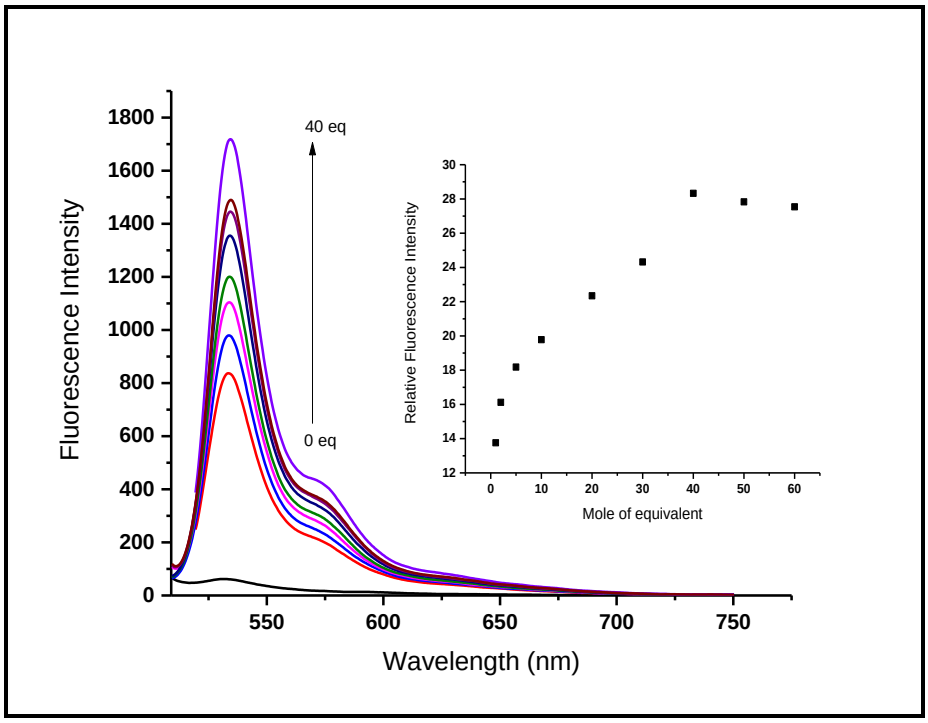

Figure 4.16. Fluorescence spectra of **1b** (5 μM) in the presence of the increasing amount of CORM-2 (0-40 eq.) in 0.01 M PBS/EtOH (pH 7.4, v/v,1:1), (λ_{ex}: 500 nm).

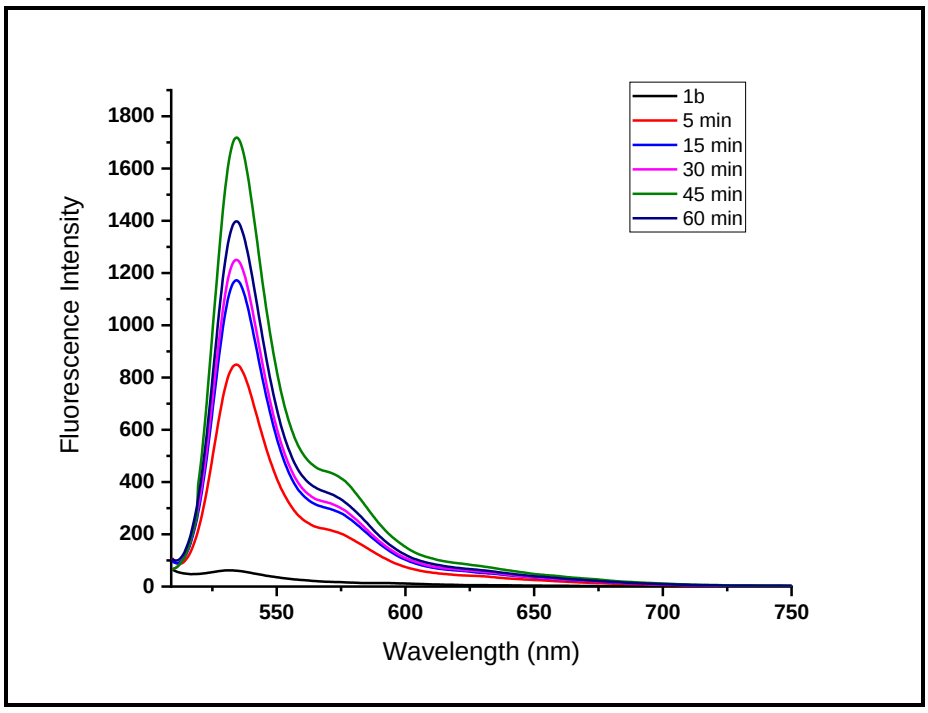

Figure 4.17. Reaction time profiles of **1b** (5 μM) in the presence of CORM-2 (40 eq.) in 0.01 M PBS/EtOH (pH 7.4, v/v,1:1), (λ_{ex}: 500 nm).

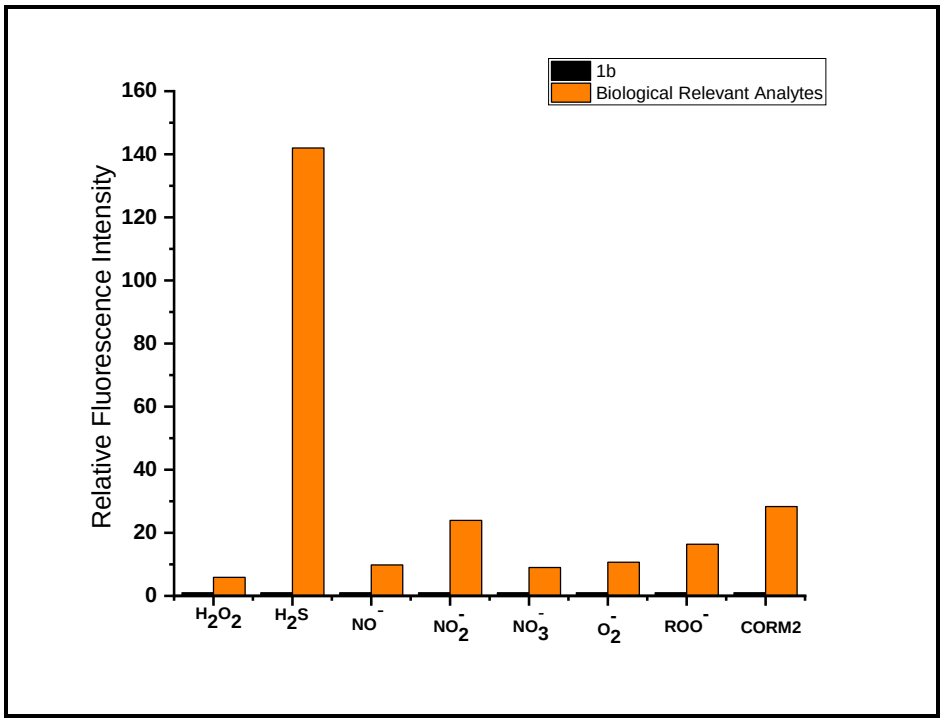

Figure 4.18. Fluorescence intensities of **1b** (5 μM) towards other biologically relevant analytes and reactive oxygen species (40 eq) along with CORM-2 in 0.01 M PBS/EtOH (pH 7.4, v/v, 1:1), (λ_{ex}: 500 nm).

The photostability of **1b** was examined in a 0.01 M PBS/Ethanol system (1:1). Absorbance measurements were taken over 7 hours at 1-hour intervals (Figure 4.19.), and the degradation rate was calculated as 0.002 min^{-1} (Figure 4.20.). The calculated half-life of 5.8 h suggests that this probe exhibits moderate photostability.

The detection limit was calculated according to the general procedure. Under the specified conditions, fluorescence intensities of **1b** were measured across CORM-2 concentrations ranging from 0.1 to 1 μM, and the results were subsequently plotted. A good linear relationship between fluorescence intensity and CORM-2 concentration was established, yielding an R^2 value of 0.9971 (Figure 4.21.). Based on the calculation from the formula, the detection limit was determined to be 279 nM.

Following the methodology applied to the previous probe, the quantum yield of **1b** was also calculated. The results calculated from the formula are as expected ($\Phi_{F(1b)}$=0,0932, $\Phi_{F(1b + CORM\text{-}2)}$ =0.927).

Additionally, the interaction of **1b** with CO gas is visually distinguishable to the naked eye and under UV illumination. While the probe solution is purple under daylight, the solution color turns orange when it interacts with CO. Under UV, no fluorescence was

observed in the probe solution, while the solution interacted with CO showing highly green fluorescence (Figure 4.22.).

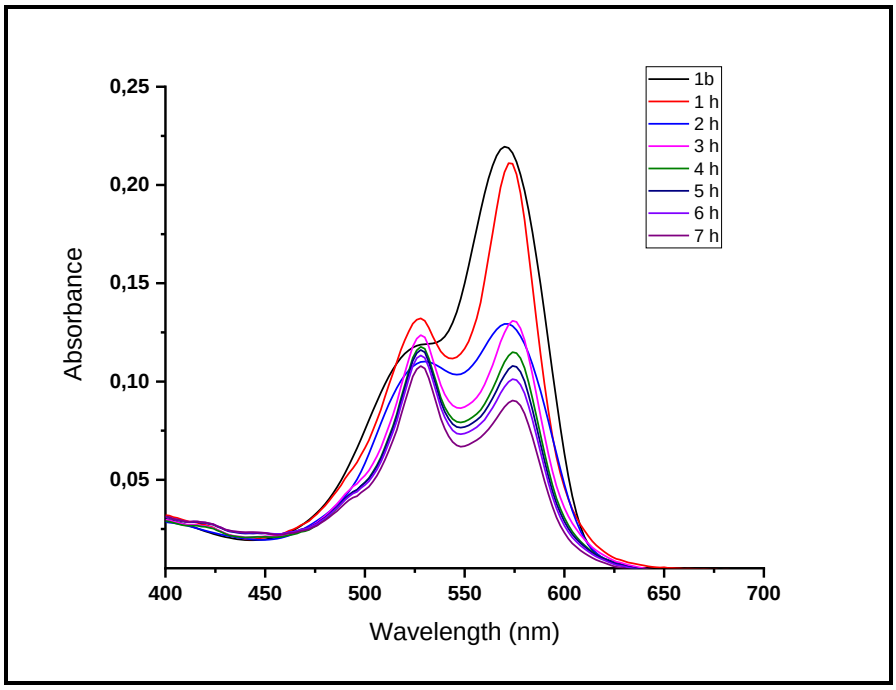

Figure 4.19. Absorbance change of **1b** over time under green led.

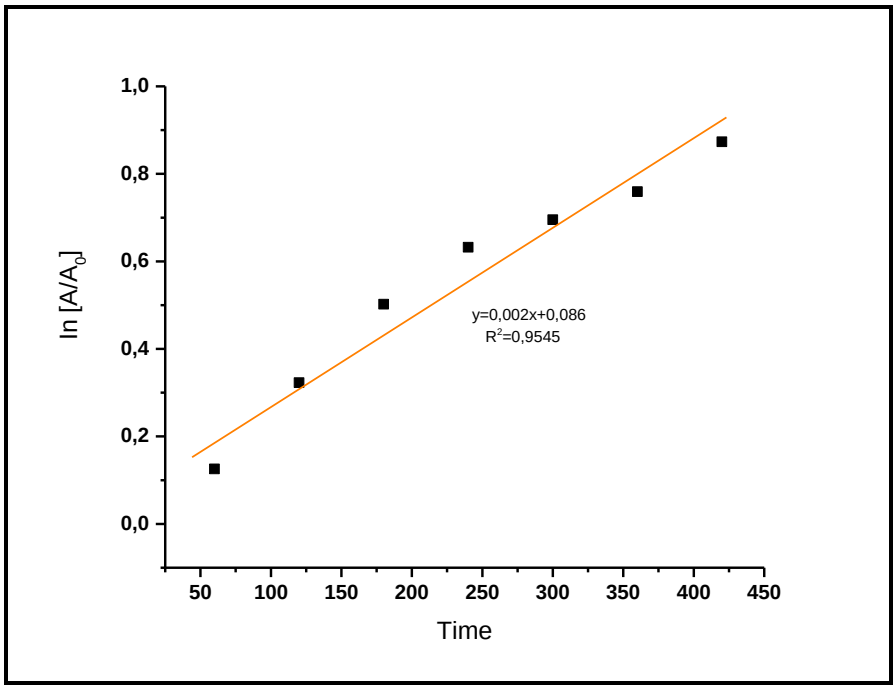

Figure 4.20. ln (A_t/A_0)/time graphic of **1b**.

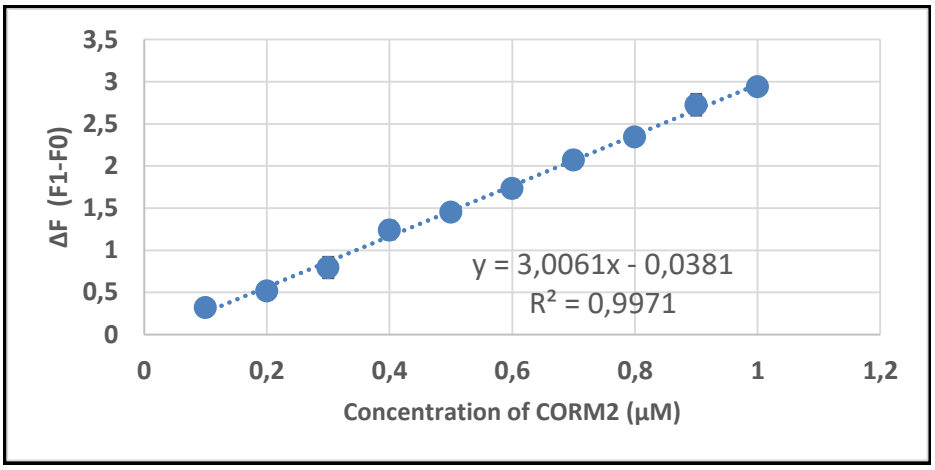

Figure 4.21. Fluorescence changes of **1b** with the addition of CORM-2 at increasing concentrations in 0.01 M PBS/EtOH (pH 7.4, v/v, 1:1), (λ_{ex}: 500 nm).

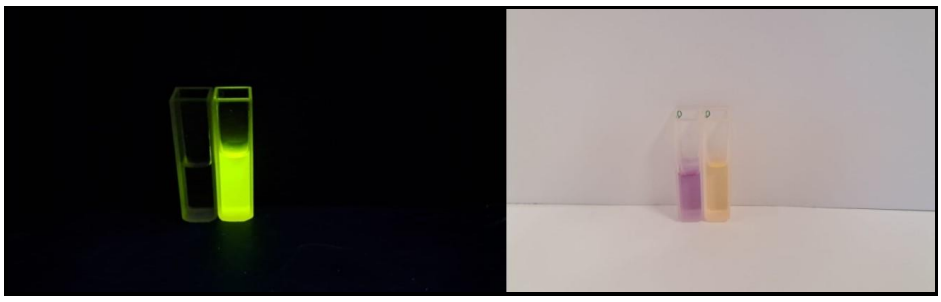

Figure 4.22. **1b** photographs in UV (left) and daylight (right) in the absence (left ones) and presence (right ones) of CORM-2.

Following standard procedures, filter paper impregnated with the **1b** solution was exposed to CO gas within a closed container. The effect of CO gas on the probe was clearly observed with the naked eye under both UV light and daylight (Figure 4.23). The green fluorescence of the filter paper exposed to CO gas is distinctly visible under UV light, while the same paper appears pale orange in daylight.

Experiments were conducted to investigate the response of 1**b** to CO within living cells. The goal of these studies was to evaluate **1b**'s selectivity, sensitivity, and potential for real-time detection of CO in a biologically relevant environment. Initially, a 1 µM solution of **1b** was applied to the living cells, followed by a 20-minute incubation period. This allowed **1b** to permeate the cellular environment and interact adequately with intracellular components before further analysis. Afterward, the cells were washed three times with a PBS solution and then incubated with a 100 µM maleimide solution for

another 20 minutes. This step was performed to eliminate any potential interference from sulfur-containing species. Following three additional washes with PBS solution, the cells were incubated in PBS that had been pre-saturated with CO gas for 20 minutes. Almost no fluorescence was observed in the cells treated with **1b** alone; however, green fluorescence emerged in the nuclei of the CO-treated cells (Figure 4.24.). These results demonstrate that the dye effectively facilitates the detection of CO within living cells.

Figure 4.23. Filter papers impregnated **1b** photographs in UV (left) and daylight (right) in the absence (left ones) and presence (right ones) of CO.

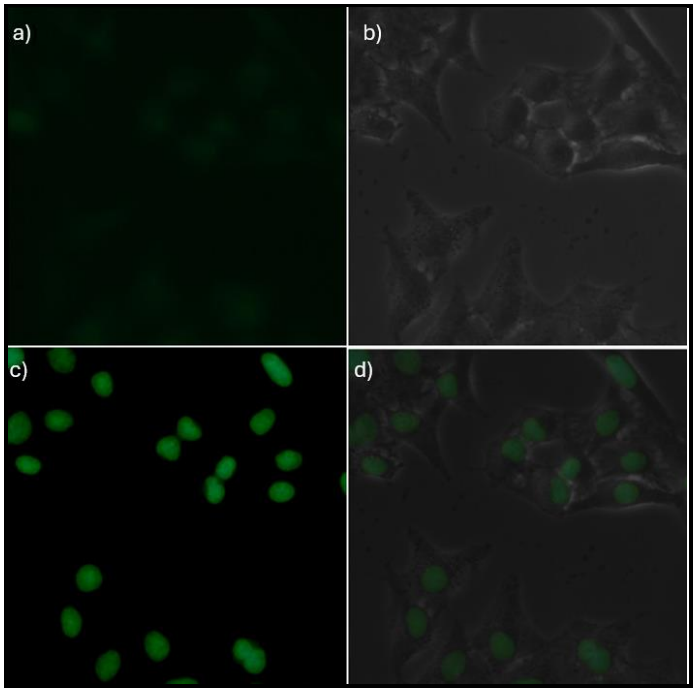

Figure 4.24. Fluorescence images of A549 cells. (a) fluorescence image of cells treated with only **1b** (1 μM) (control); (b) bright field image of cells treated with **1b** (1 μM) in CO environment; (c) fluorescence image of cells treated with **1b** (1 μM) in CO environment; (d) merged images of frames (b and c). (λ_{ex}:500 nm), scale bar: 100 μm.

4.4. Spectroscopic Investigations of the Probe 1c

At this stage of the thesis, a comprehensive analysis of **1c**'s spectroscopic properties has been conducted. This analysis included a detailed investigation of its selectivity when exposed to various analytes, its stability over time, and its potential applicability for cellular studies. Experiments focused on different water-miscible organic solvents to identify the optimal solvent system for maximizing the probe's sensitivity to CO. DMF was found to be the most effective choice, significantly enhancing the probe's performance. Additionally, a systematic approach was employed to vary the proportions of water and DMF. It was revealed that **1c** achieves its highest performance level when placed in a completely buffered solution (Figure 4.25.). This finding underscores the importance of solvent selection in optimizing the probe's efficacy for future applications.

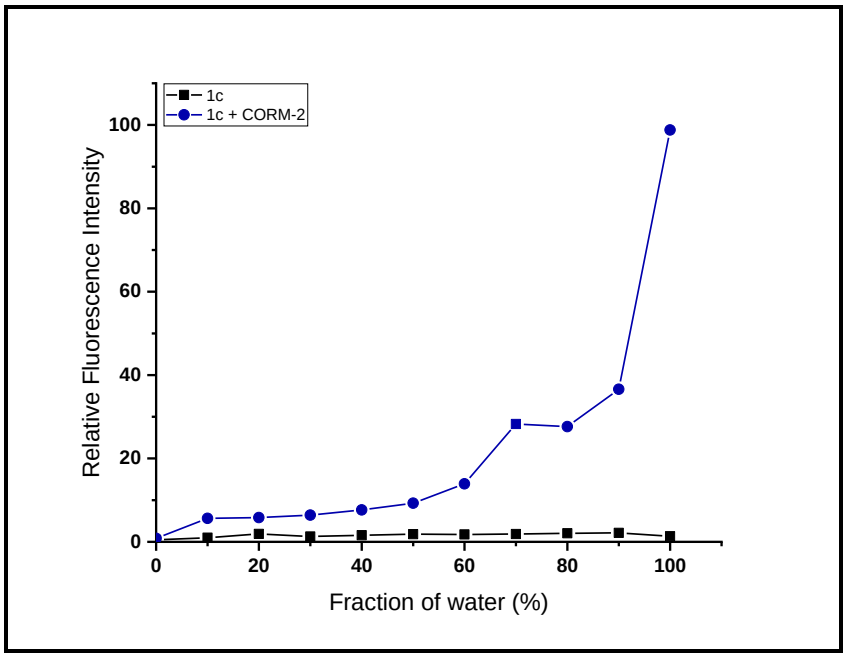

Figure 4.25. Fluorescence performance of **1c** (5 μM) at increasing water ratios with CORM-2 (5 eq.) in 0.01 M PBS/DMF (pH 7.4), (λ_{ex}: 460 nm).

The UV measurements for **1c** demonstrated a single absorption peak at 520 nm. Notably, the introduction of CORM-2 caused a blueshift in this absorbance peak, resulting in a shift to 480 nm (Figure 4.26.). Additionally, no fluorescence emission was observed when **1c** was excited at 520 nm in the designated solvent system. However, upon the addition of CORM-2 to **1c** and exciting the solvent at 460 nm, a new

fluorescence peak was identified at 502 nm, accompanied by a significant increase in fluorescence intensity, quantified at 98-fold (Figure 4.27.).

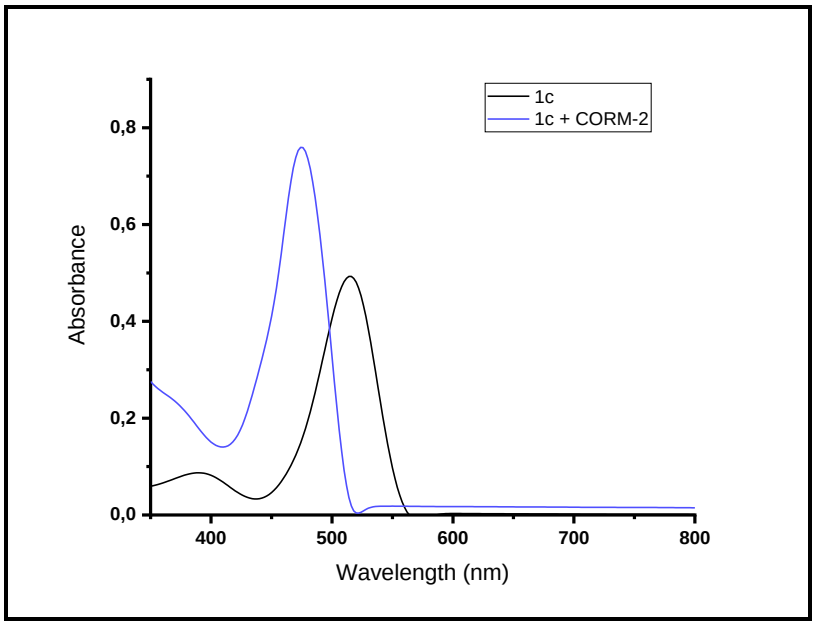

Figure 4.26. Absorbance spectra of **1c** (5 μM) in the absence and presence of CORM-2 (5 eq.) in 0.01 M PBS (pH 7.4).

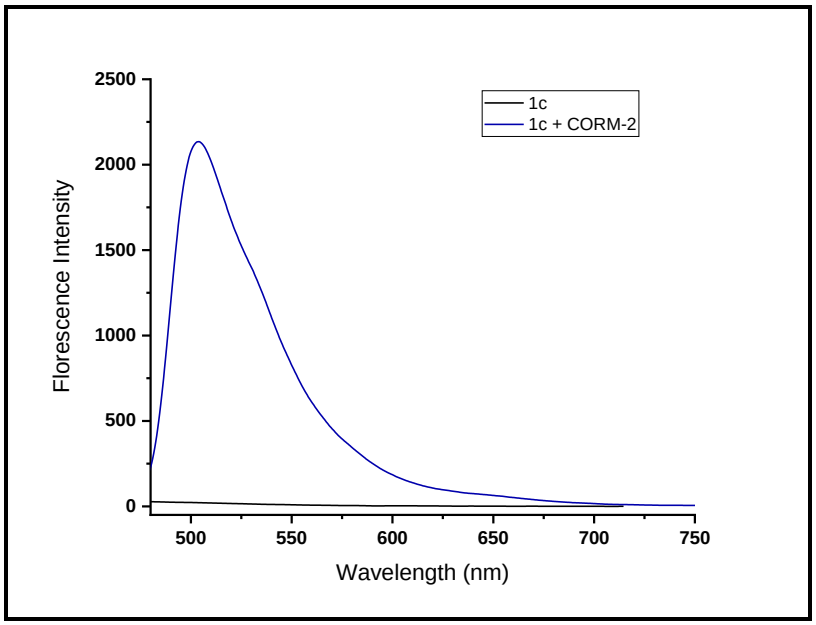

Figure 4.27. Emission spectra of **1c** (5 μM) in the absence and presence of CORM-2 (5 eq.) in 0.01 M PBS (pH 7.4), (λ_{ex}: 460 nm).

During the subsequent research phase, a comprehensive investigation was conducted to assess the influence of pH on compound **1c**. This study aimed to determine how variations in pH levels could impact the behavior and effectiveness of **1c**. The findings revealed that under acidic conditions, **1c** exhibited structural degradation, resulting in fluorescence. This result suggests that **1c** becomes unstable at pH values below 5. Conversely, **1c** demonstrated maximum fluorescence at physiological pH when exposed to CORM-2. It is worth noting that no structural changes were observed under basic conditions, and no significant fluorescence was detected in the presence of CORM-2 at higher pH levels (Figure 4.28.).

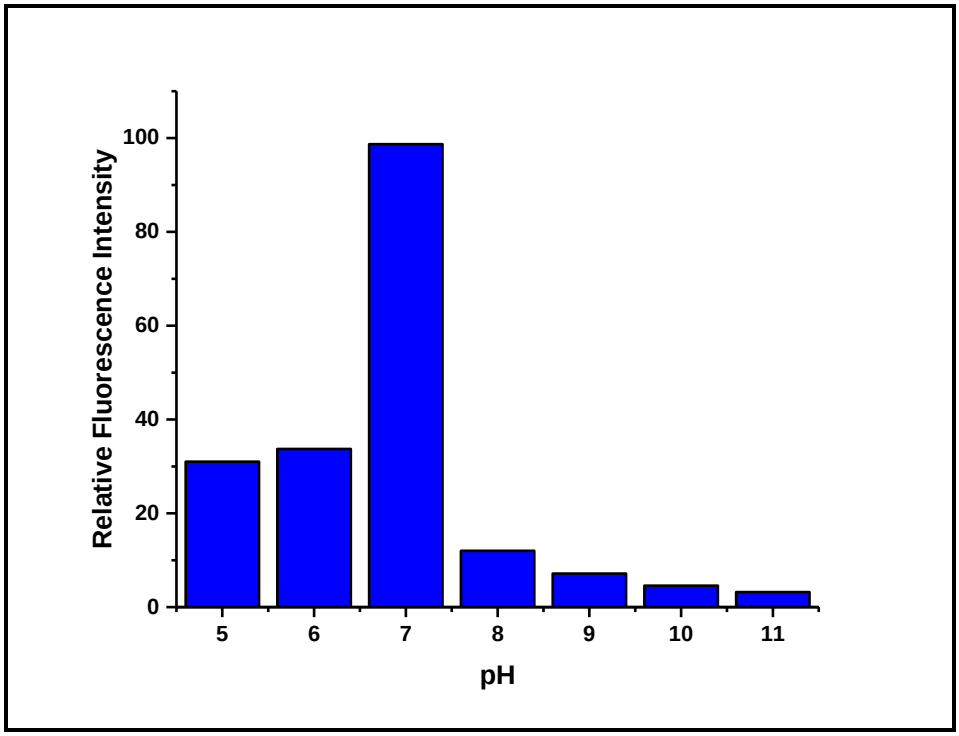

Figure 4.28. Effect of pH on the **1c** (5μM) in the presence of CORM-2 (5 eq.) in 0.01 M PBS (pH 7.4), (λ_{ex}: 460 nm).

The findings were extended using a systematic titration of CORM-2 molecules. Figure 4.29 shows that increasing molar equivalents of CORM-2 (from 0 to 60) caused an increase in the fluorescence signal of **1c**. No significant change in fluorescence intensity was observed after adding five equivalents of CORM-2, indicating that the probe had reached saturation.

In the next step, the time-dependent fluorescence changes of **1c** in the presence of 5 eq CORM-2 were measured. Negligible changes in fluorescence intensity were

observed after 5 minutes, with the probe reaching maximum intensity within 45 minutes (Figure 4.30.).

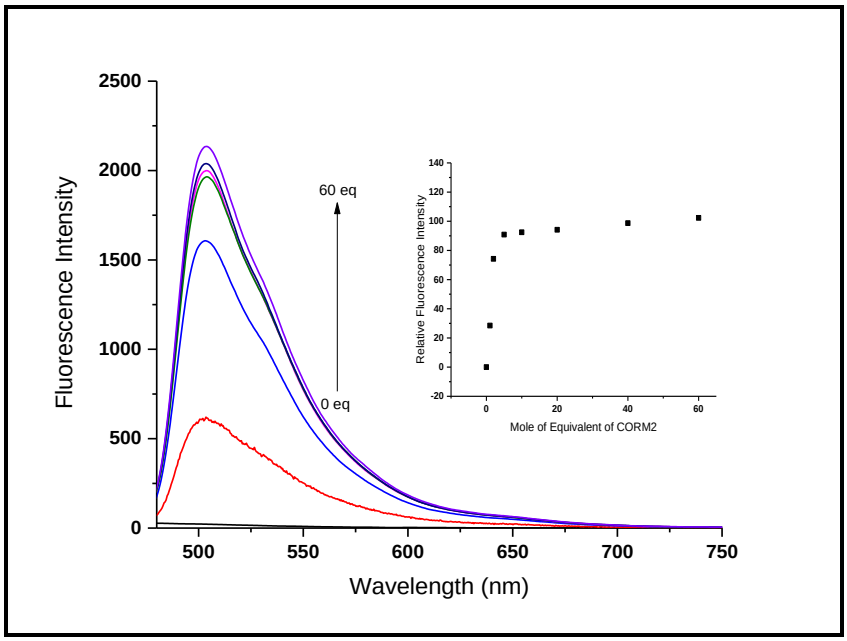

Figure 4.29. Emission spectra of **1c** (5 μM) with increasing amount CORM-2 in 0.01 M PBS (pH 7.4), (λ_{ex}: 460 nm).

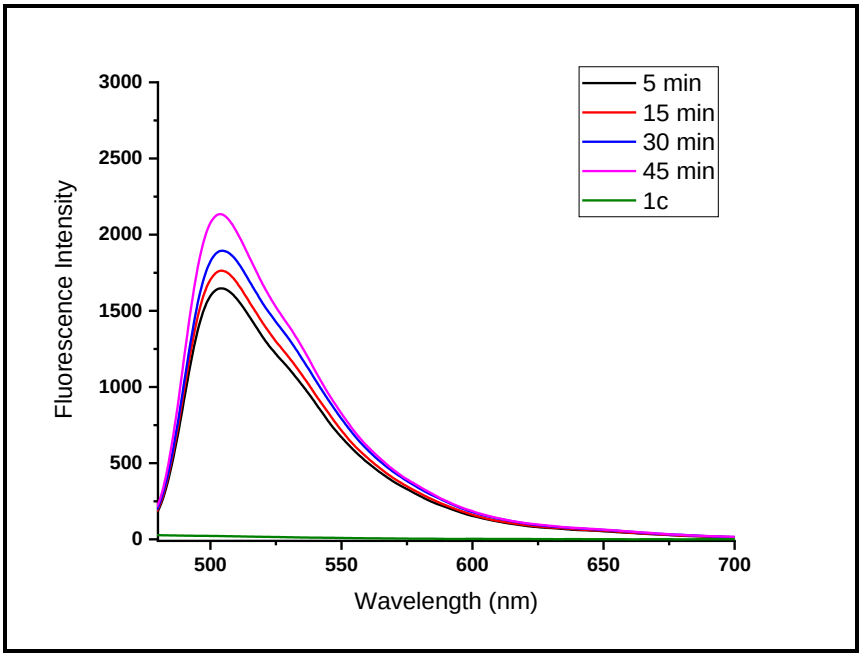

Figure 4.30. Reaction time profiles of **1c** (5 μM) in the presence of CORM-2 (5eq.) in 0.01 M PBS (pH 7.4), (λ_{ex}: 460 nm).

When the selectivity of **1c** with metal species was examined, it was observed that it gave some response to mercury compared to other metals, but this response was insignificant compared to CORM-2 (Figure 4.31.).

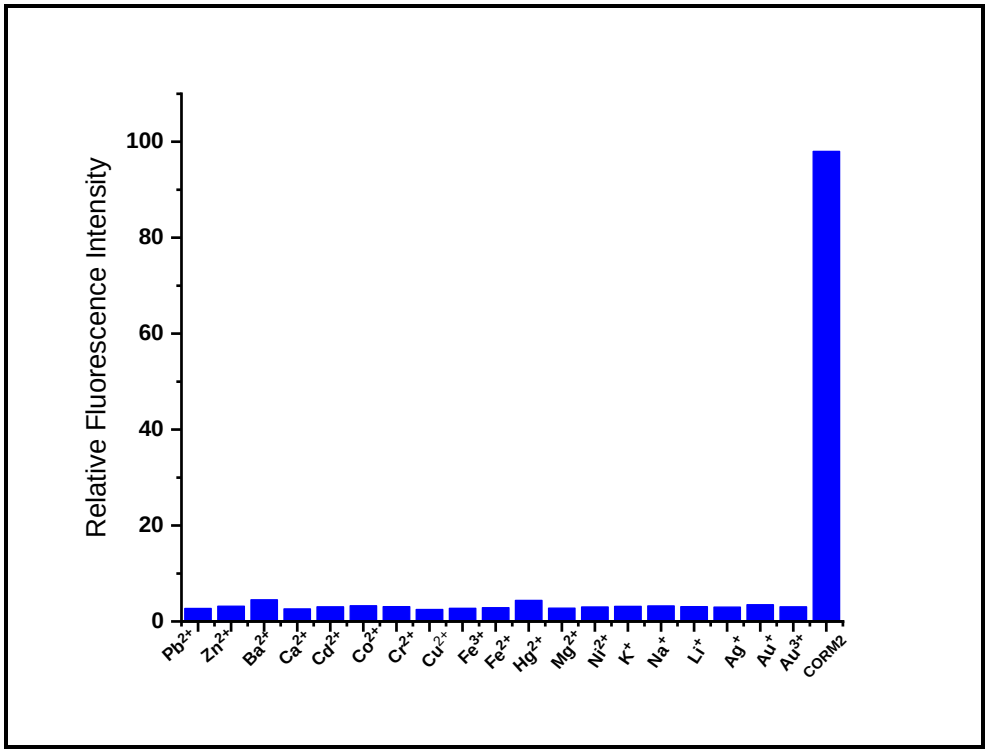

Figure 4.31. Fluorescence intensity of **1c** (5 μM) in the presence of CORM-2 and other metal ions (5 eq.) in 0.01 M PBS (pH 7.4), (λ_{ex}: 460 nm).

Selectivity tests were conducted on biologically relevant analytes and reactive oxygen species, providing initial data for future cell experiments. The results indicated that compound **1c** exhibited a measurable response to sulfur-containing species, particularly hydrogen sulfide (H_2S) (Figure 4.32.). The findings revealed that the probe displayed limited selectivity for CO, emphasizing the necessity for further modifications prior to proceeding with cell studies.

The detection limit of **1c** was calculated from the fluorescence titration data. Figure 4.33. illustrates the change in fluorescence signal ($\Delta F = F_1 - F_0$) as a function of CORM-2 concentration. The graph demonstrates a linear correlation between CORM-2 concentration and the fluorescence signal change, represented by the equation y=2.3424x + 0.3028. The R^2 value of 0.9754 indicates the goodness of fit of the linear regression model to the data points. As R^2 approaches 1, the accuracy of the model improves, suggesting that the model closely represents the data. This high value signifies a strong

relationship between CORM-2 concentration and fluorescence intensity, confirming that the model provides an excellent fit to the observed data. Furthermore, the LOD was calculated to be 442 nM.

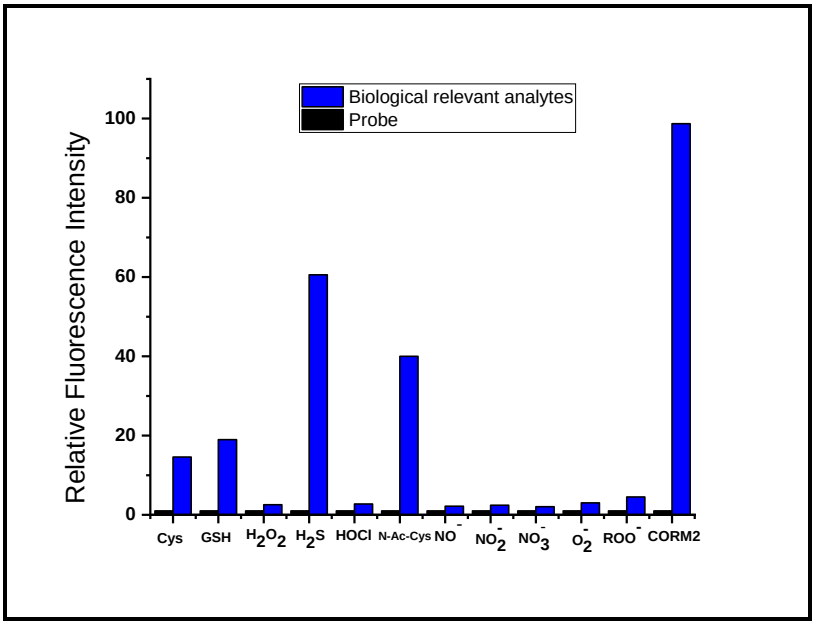

Figure 4.32. Fluorescence responses of **1c** (5 μM) in the presence of biologically relevant analytes, reactive oxygen species, and CORM-2 (5 eq.) in 0.01 M PBS (pH 7.4), (λ_{ex}: 460 nm).

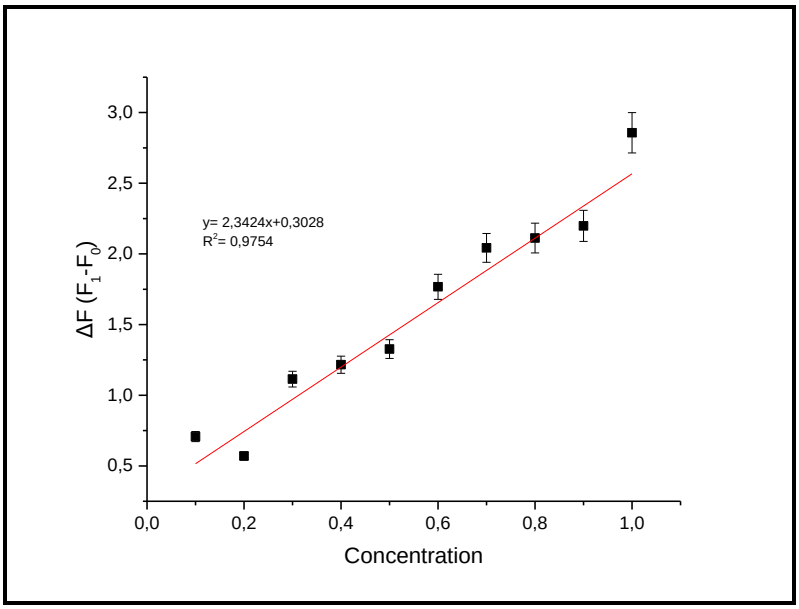

Figure 4.33. Fluorescence changes of **1c** (5 μM) upon addition of CORM-2 (0.1 to 1 μM) in 0.01 M PBS (pH 7.4), (λ_{ex}: 460 nm).

The quantum yield of **1c** was determined relative to the reference, consistent with the methodology employed in previous calculations (Michel et al., 2012). The results obtained from the formulation yielded a value of 0.0217 for **1c** and 0.94 for the CORM-2 added version, aligning with the expected outcomes.

To assess the photostability of **1c**, it was exposed to green light, and absorbance values were recorded at regular time intervals (Figure 4.34.). The degradation rate, determined from the slope of the graph, was calculated to be 0.017 min^{-1} (Figure 4.35.). The half-life was calculated as 40.8 minutes, indicating that the probe has limited resistance to light exposure.

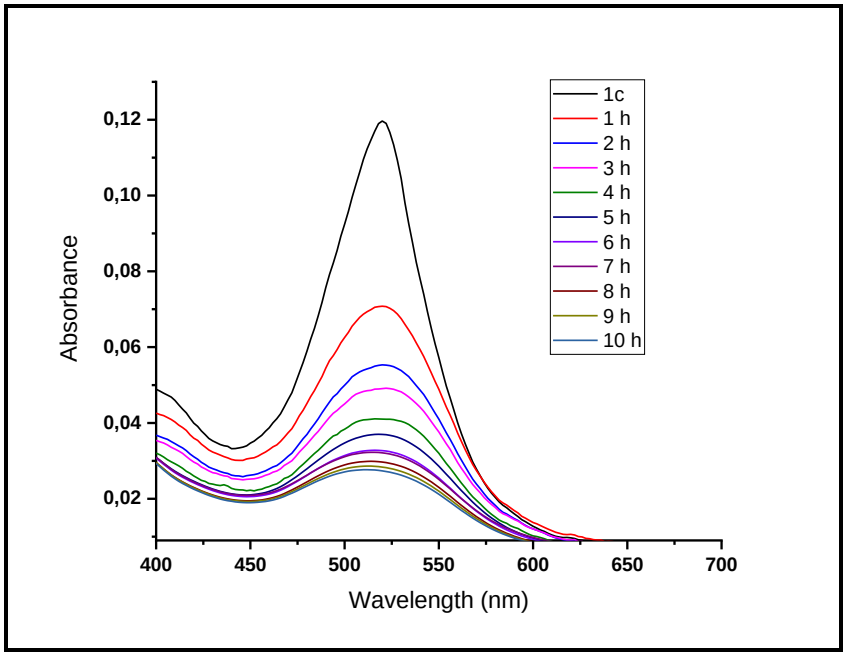

Figure 4.34. Absorbance change of **1c** over time under green led.

Under daylight, **1c** exhibited a pale pink hue. However, upon CO exposure, its color shifted to pale yellow. This observable color change indicates that **1c** enables the visual detection of CO gas, suggesting its potential as an effective naked-eye sensor for CO monitoring. Furthermore, while **1c** solution displays no fluorescence under UV light, exposure to CO induces a green fluorescence (Figure 4.36).

In the filter paper tests, no clear difference was seen in daylight, while the distinction under UV was slightly more noticeable (Figure 4.37).

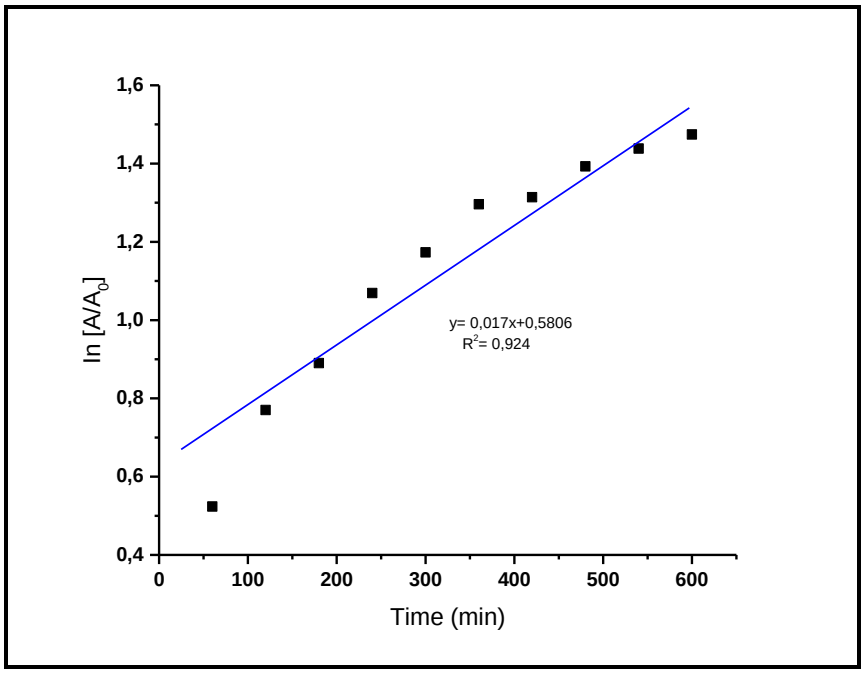

Figure 4.35. ln (A_t/A_0)/time graphic of **1c**.

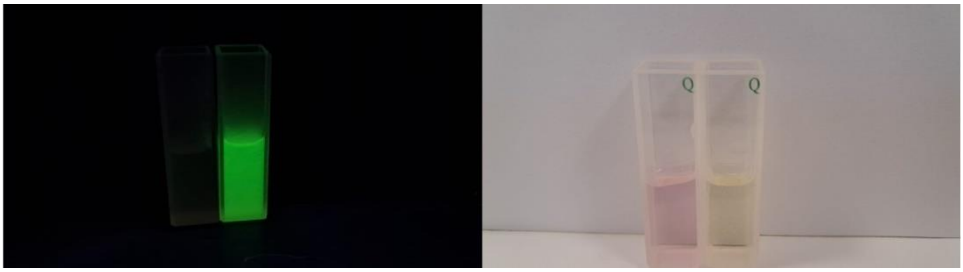

Figure 4.36. **1c** photographs in UV (left) and daylight (right) in the absence (left ones) and presence (right ones) of CORM-2.

Figure 4.37. Filter papers impregnated **1c** photographs in UV (left) and daylight (right) in the absence (left ones) and presence (right ones) of CO.

In cell studies involving compound **1c**, A549 cells were initially treated with the probe, followed by a 20-minute incubation period. After this, the cells were washed three times with PBS solution and then incubated with a 100 μM maleimide solution for an additional 20 minutes to eliminate any potential sulfur-containing species. Following three more washes with PBS, the cells were incubated with PBS that had been pre-saturated with CO for another 20 minutes. Fluorescence microscopy imaging revealed negligible fluorescence in the control cells that were treated with **1c** alone. However, surprising green fluorescence was observed in the nuclei of the cells in the CO environment (Figure 4.38.). These results indicate that **1c** can penetrate living cells and can be used for real-time detection of CO.

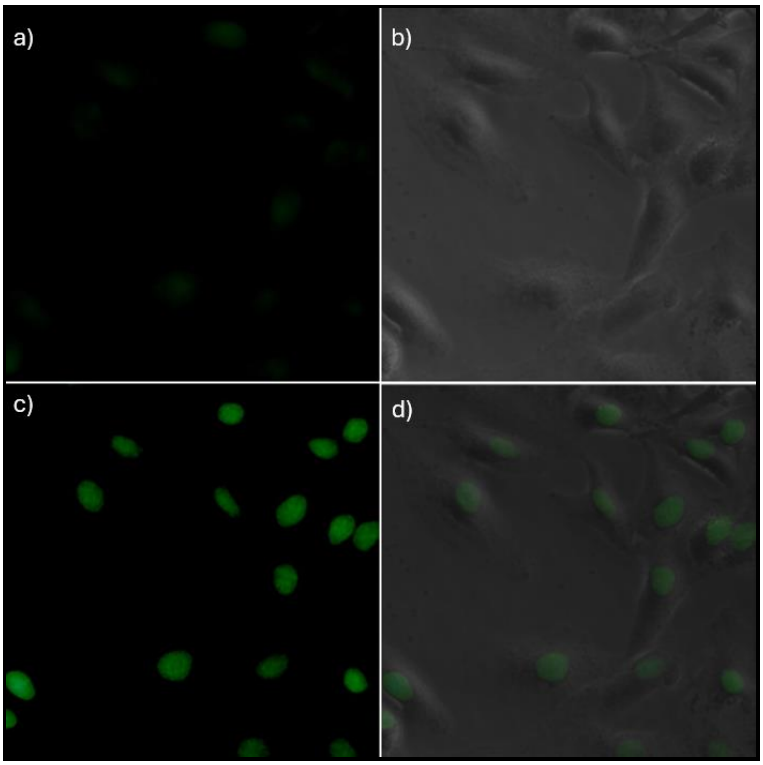

Figure 4.38. Fluorescence images of A549 cells. (a) fluorescence image of cells treated with only **1c** (1 μM) (control); (b) bright field image of cells treated with **1c** (1 μM) in CO environment; (c) fluorescence image of cells treated with **1c** (1 μM) in CO environment; (d) merged images of frames (b and c). (λ_{ex}:460 nm), scale bar: 100 μm.

4.5. Spectroscopic Investigations of the Probe 1d

The spectroscopic characteristics of **1d**, which was synthesized using a saturated lithium chloride solution in acetone, were investigated as a continuation of the study on compound **1c**. The initial phase of this research focused on evaluating the optical properties of **1d** across various solvent systems utilizing UV-visible and fluorescence spectroscopy. Notably, the PBS/EtOH system demonstrated the highest fluorescence intensity and proved to be particularly effective for compound **1d**. During the absorbance measurements of **1d**, a distinct absorption peak was identified at 502 nm. Additionally, the introduction of CORM-2 to **1d** resulted in a red shift of the absorption, culminating in a single peak at 508 nm (Figure 4.39.).

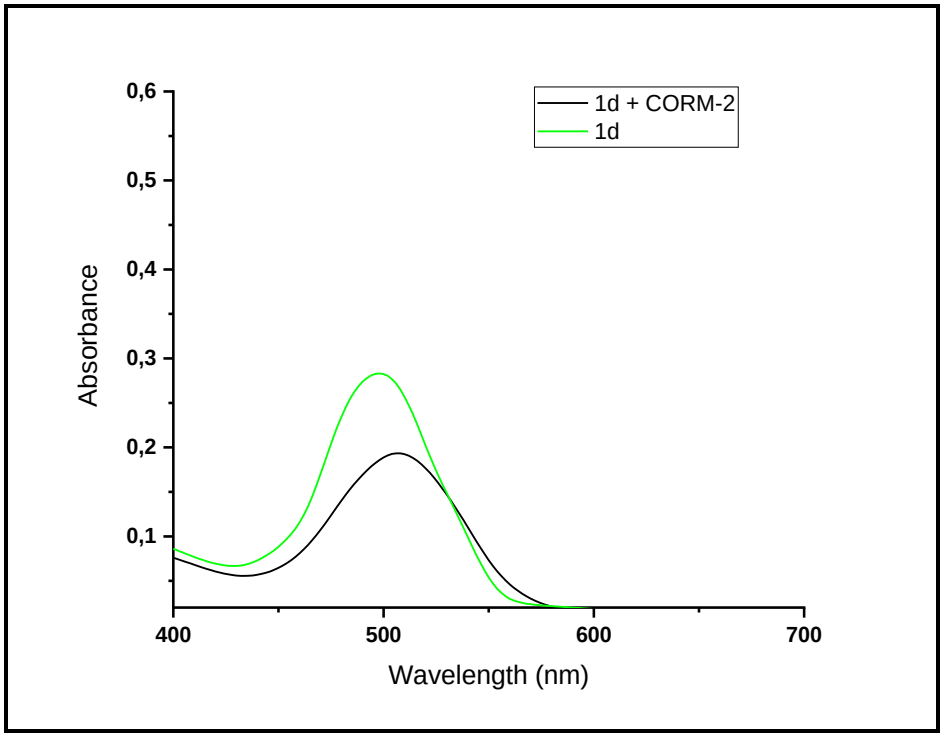

Figure 4.39. Absorbance spectra of **1d** (5 μM) in the absence and presence of 2eq. CORM-2 in 0.01 M PBS/EtOH (pH 7.4, v/v, 9:1).

The fluorescence behavior of **1d** was investigated in the presence and absence of CORM-2. Upon excitation at 460 nm, **1d** exhibited a minor fluorescence peak at 505 nm. In an optimized solvent system, a 5-fold enhancement in fluorescence intensity was observed following the interaction of **1d** with CORM-2. (Figure 4.40.).

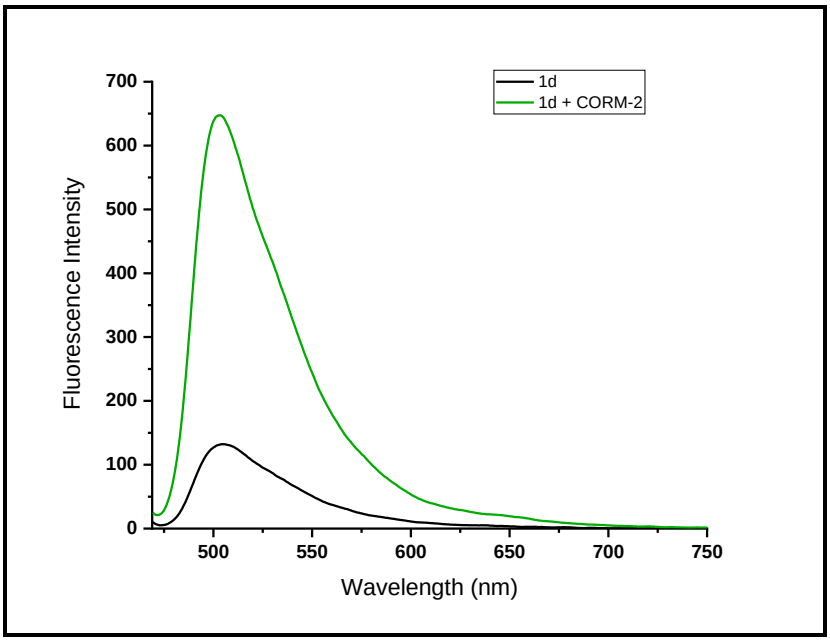

Figure 4.40. Fluorescence spectra of **1d** (5 μM) in the absence and presence of 2 eq. CORM-2 in 0.01 M PBS/EtOH (pH 7.4, v/v, 9:1), (λ_{ex}: 460 nm).

To identify the optimal aqueous system for **1d**, measurements were conducted in the presence of CORM-2 in solutions with varying water content, ranging from 0% to 100%. Figure 4.41. shows that the best system for **1d** is 9PBS/1EtOH.

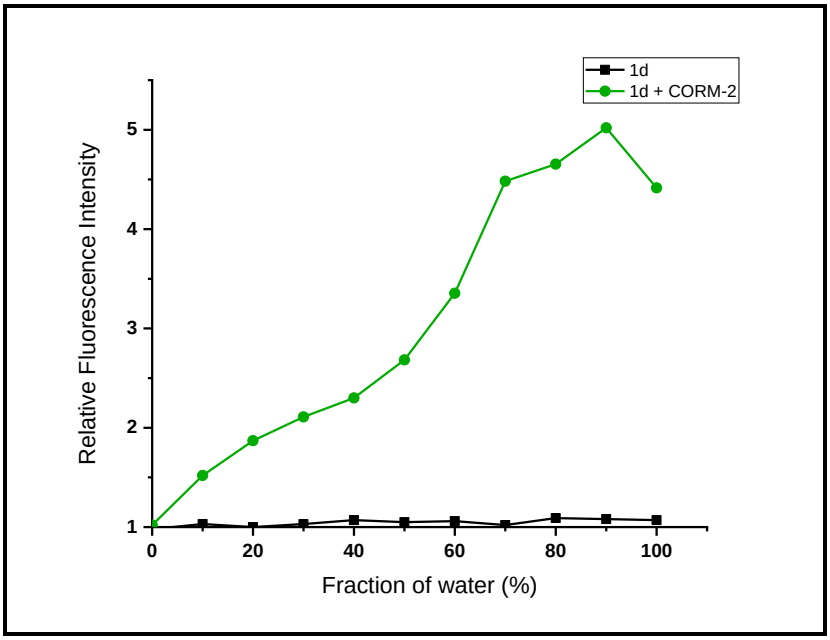

Figure 4.41. Effect of water fraction on fluorescence intensity of **1d** (5 μM) in the presence and absence of CORM-2 (2 eq.) in 0.01 M PBS/EtOH (pH 7.4, v/v, 9:1), (λ_{ex}: 460 nm).

In the subsequent phase of the study, a comprehensive analysis was conducted to assess the impact of pH on the **1d**. This stage aimed to elucidate the effects of varying pH levels on the behavior and functionality of **1d**. The findings indicated that **1d** displayed significantly higher fluorescence intensity in acidic pH conditions compared to neutral or basic environments. This observation suggests that **1d** undergoes protonation in acidic conditions, leading to a depalladation process along with structural or electronic modifications that enhance its fluorescence. In contrast, the fluorescence intensity of **1d**, both independently and in the presence of CORM-2, was notably diminished in basic environments. Given the significance of these observations for biological research, it is essential for such probes to demonstrate optimal functionality at physiological pH levels. Ensuring effective performance near neutral pH is crucial for their practical application in biological systems, as most cellular environments maintain pH values around 7. Notably, **1d** exhibited maximum fluorescence intensity at pH 7, highlighting its optimal performance under physiological conditions (Figure 4.42.).

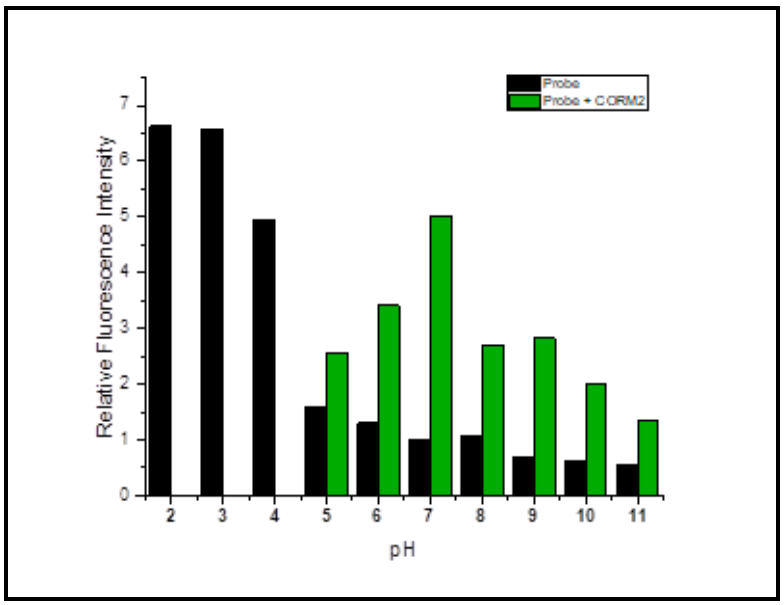

Figure 4.42. Effect of pH on **1d** (5 μM) in the presence and absence of CORM-2 (2 eq.) in 0.01 M PBS/EtOH (pH 7.4, v/v, 9:1), (λ_{ex}: 460 nm).

Next, **1d** was systematically titrated with CORM-2 to ascertain the concentration that yielded optimal findings. It was observed that **1d** exhibited maximum fluorescence intensity at a concentration corresponding to 2 equivalents of CORM-2 (Figure 4.43.). A

slight decrease in fluorescence intensity was noted at higher CORM-2 concentrations, and titration was not extended beyond 25 equivalents.

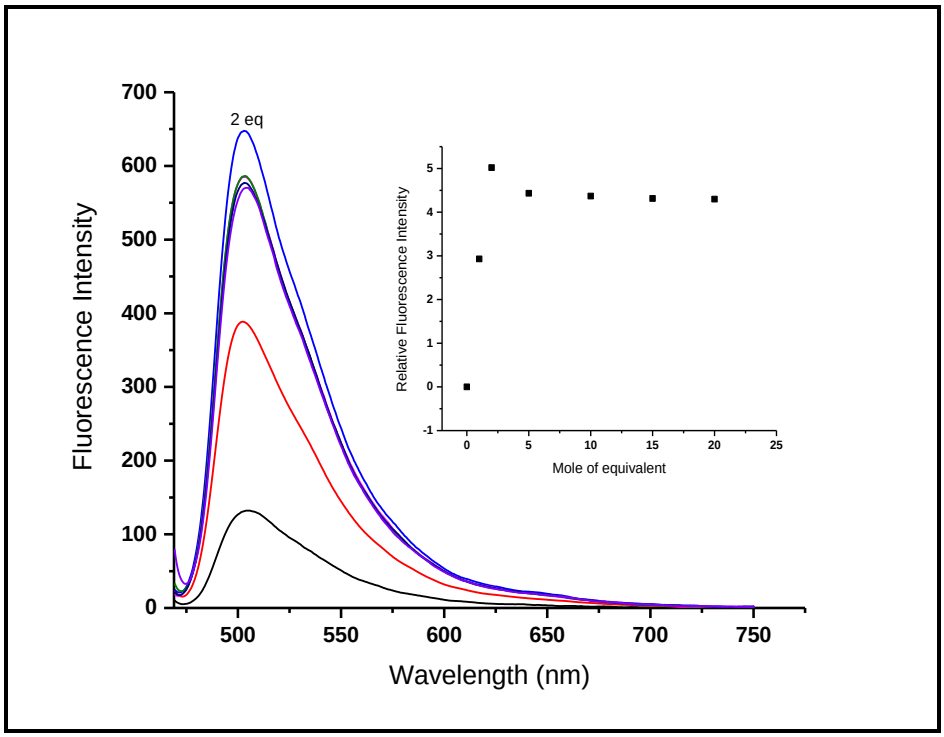

Figure 4.43. Fluorescence spectra of **1d** (5 μM) in the presence of the increasing amount of CORM-2 (0-25 eq) in 0.01 M PBS/EtOH (pH 7.4, v/v,9:1), (λ_{ex}: 460 nm).

A time-dependent titration of **1d** was carried out at a constant CORM-2 concentration to assess the temporal response of the probe. Measurements conducted from 0 to 45 minutes revealed that **1d** exhibited optimal fluorescence intensity at the 5-minute mark, with subsequent minutes showing diminished intensity (Figure 4.44.).

Under optimal conditions, the probe's selectivity and specificity towards various metal ions were measured. Fortunately, **1d** exhibited no significant response to metal ions other than CORM-2 (Figure 4.45.).

The selectivity of **1d** was assessed using biologically relevant analytes and reactive oxygen species to evaluate its specificity in a broader physiological context. Like its predecessor probe, **1d** also showed positive results against sulfur-containing analytes, particularly H_2S, almost as much as CORM-2 (Figure 4.46.).

The detection limit was calculated from the fluorescence titration data. The figure 4.47. illustrates the change in fluorescence signal ($\Delta F = F_1 - F_0$) relative to the concentration of CORM-2. It shows a solid linear relationship between the CORM-2

concentration and the fluorescence signal change, expressed by the equation y=2,41685x+ 0,09613. The R^2 value, which is 0.98533, reflects the accuracy of the linear regression model; closer to 1 means a better fit. Hence, this high value suggests a solid correlation between CORM-2 concentration and fluorescence intensity, confirming the model's reliability. The LOD was found to be 245 nM, as previously calculated methods.

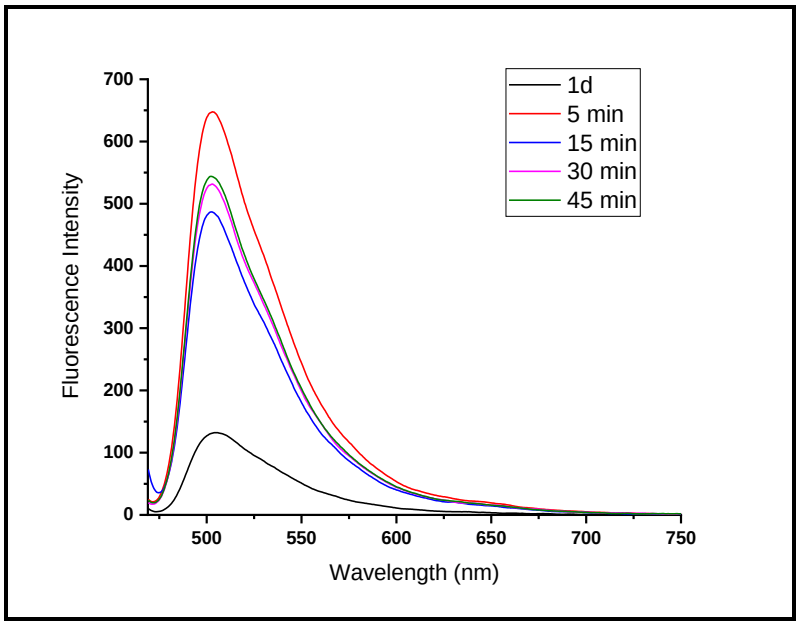

Figure 4.44. Reaction time profiles of **1d** (5 μM) in the presence of CORM-2 (2 eq.) in 0.01 M PBS/EtOH (pH 7.4, v/v,9:1), (λ_{ex}: 460 nm).

According to the general procedure, the quantum efficiency of **1d** was measured at 0.089, while the CORM-added version exhibited a significantly higher quantum efficiency of 0.74.

The sharp difference in the colors of the probe's solution in the absence and presence of CORM-2 is sufficient to use it as an eye-detectable sensor. While the probe solution exhibits no fluorescence under UV light, adding the CORM-2 induces a green fluorescence that is clearly visible to the naked eye (Figure 4.48.).

In filter paper tests, the filter paper impregnated with **1d** solution changed from light pink to light yellow when exposed to a CO gas atmosphere. This change is significantly more pronounced under UV light, where the filter paper exposed to CO gas exhibits a distinct green fluorescence while the probe solution remains non-fluorescent (Figure 4.49.).

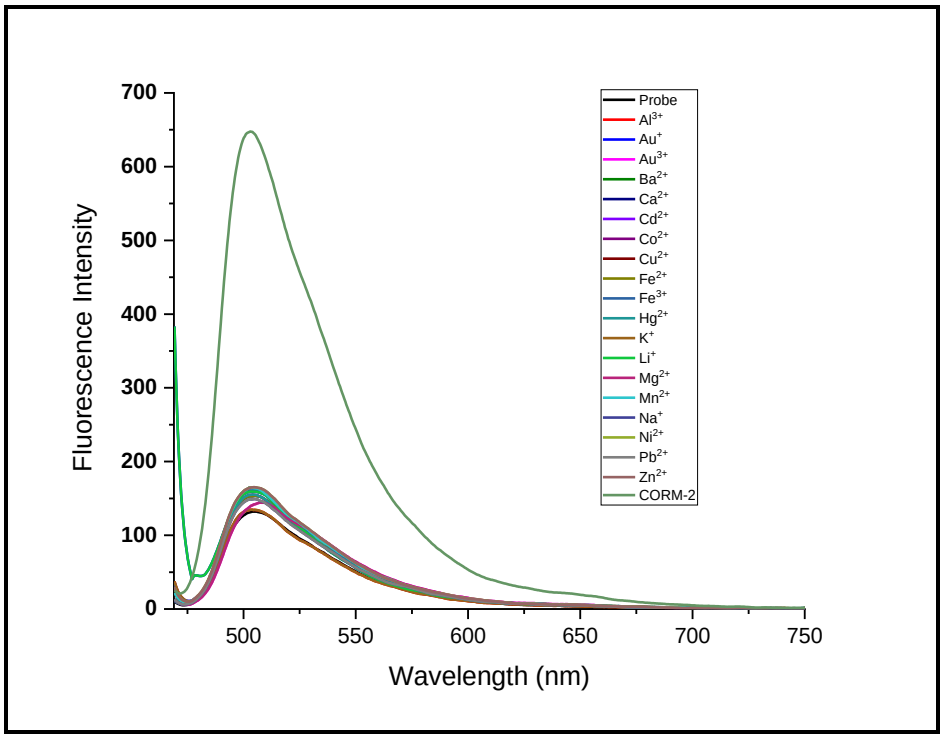

Figure 4.45. Fluorescence intensity of **1d** (5 μM) in the presence of CORM-2 and other metal ions (2 eq.) in 0.01 M PBS/EtOH (pH 7.4, v/v,9:1), (λ_{ex}: 460 nm).

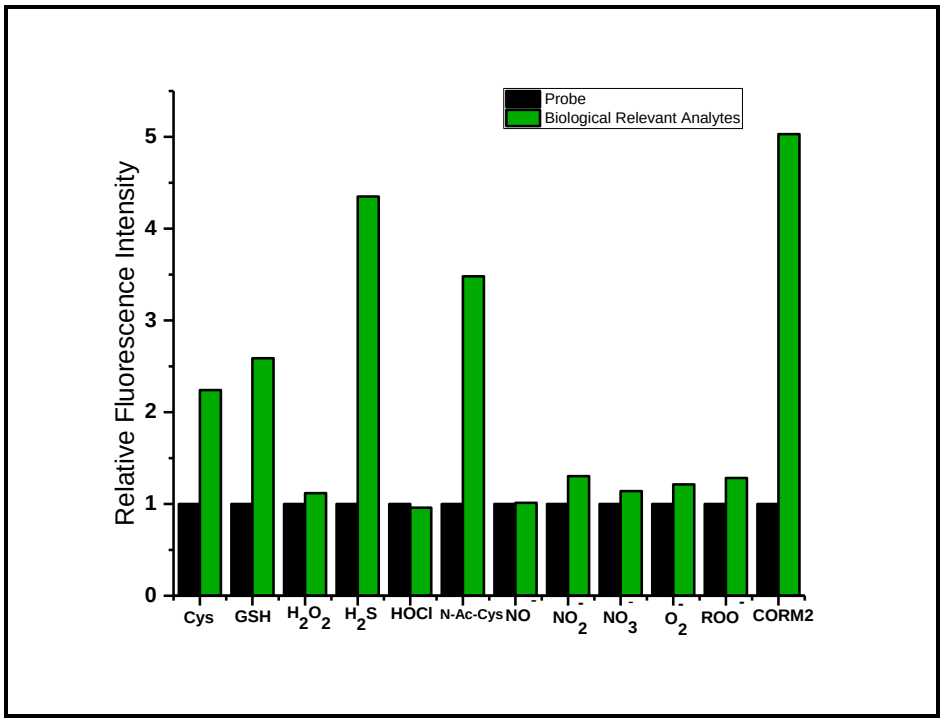

Figure 4.46. Fluorescence intensity of **1d** (5 μM) in the presence of biologically relevant analytes, reactive oxygen species, and CORM-2 (2eq.) in 0.01 M PBS/EtOH (pH 7.4, v/v,9:1), (λ_{ex}: 460 nm).

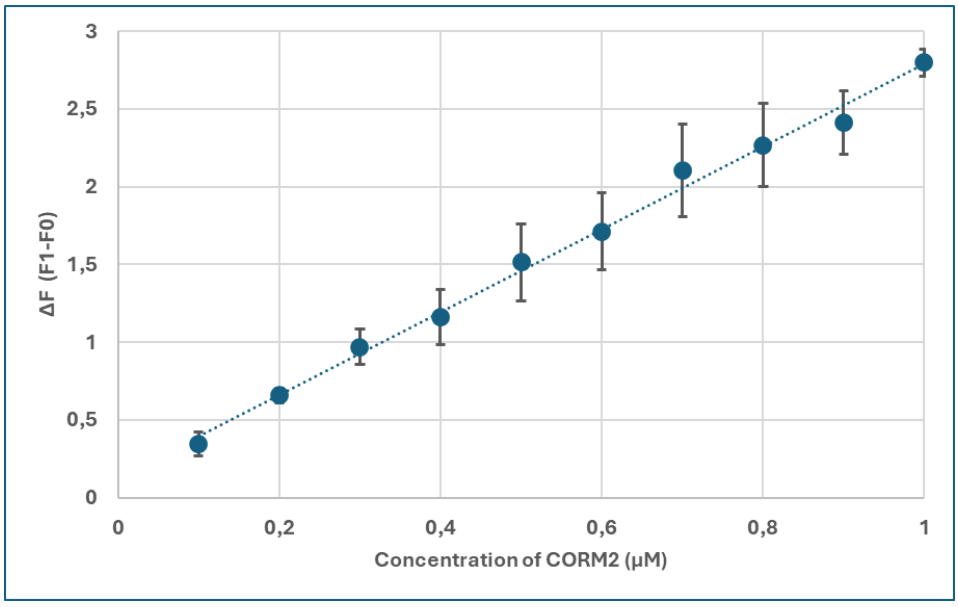

Figure 4.47. Fluorescence changes of **1d** (5 μM) upon the addition of CORM-2 (0.1 to 1 equiv.) in PBS/EtOH (pH 7.4, v/v, 9:1), (λ_{ex}:460 nm).

Figure 4.48. **1d** photographs in UV (left) and daylight (right) in the absence (left ones) and presence (right ones) of CORM-2.

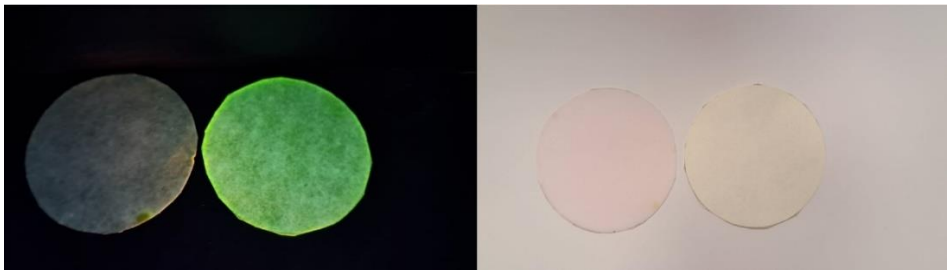

Figure 4.49. Filter papers impregnated **1d** photographs in UV (left) and daylight (right) in the absence (left ones) and presence (right ones) of CO.

In the conducted cell studies, A549 cells were initially treated with compound **1d** and incubated for a duration of 20 minutes. Following this treatment, the cells were subjected to three washes with PBS solution. Subsequently, they were treated with a 100 μM maleimide solution for an additional 20 minutes to remove any potential sulfur-containing species. After three further washes with PBS, the cells were incubated in a PBS solution saturated with CO gas for an additional 20 minutes. Upon completion of three additional washes with PBS, images of the cells were obtained using a fluorescence microscope. No fluorescence was detected in control cells; however, green fluorescence was observed in the nuclei of the cells exposed to the CO environment (Figure 4.50.). These findings indicate that **1d** is cell-permeable and facilitates the real-time detection of CO within living cells.

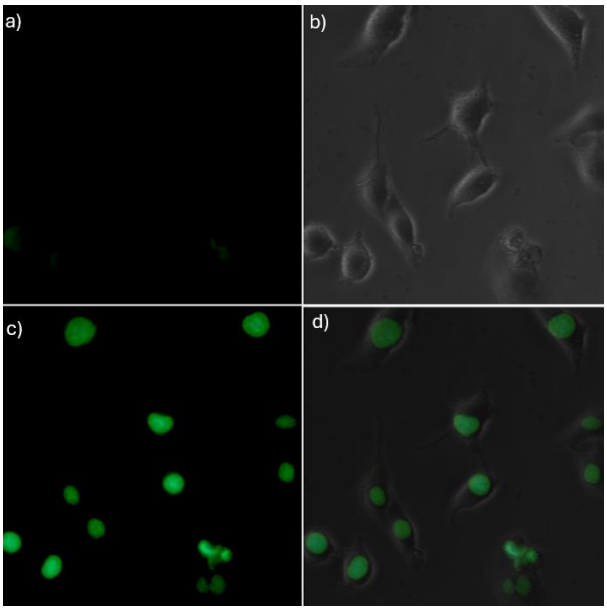

Figure 4.50. Fluorescence images of A549 cells. (a) fluorescence image of cells treated with only **1d** (1 μM) (control); (b) bright field image of cells treated with **1d** (1 μM) in CO environment; (c) fluorescence image of cells treated with **1d** (1 μM) in CO environment; (d) merged images of frames (b and c). (λ_{ex}:460 nm), scale bar: 100 μm.

To determine the degradation time of **1d**, time-dependent absorbance measurements were taken under the green light following the standard procedure. Measurements were taken every hour for 7 hours (Figure 4.51.), and the k_{deg} value was found from the slope of the graph ($3x10^{-4}$) of $\ln(A_t/A_0)$ versus time (Figure 4.52.). The half-life of **1d** was calculated to be 38.5 hours, indicating a high resistance to

photodegradation. This extended half-life under continuous light exposure suggests that the probe possesses significant photostability, making it suitable for applications requiring prolonged light exposure without rapid degradation.

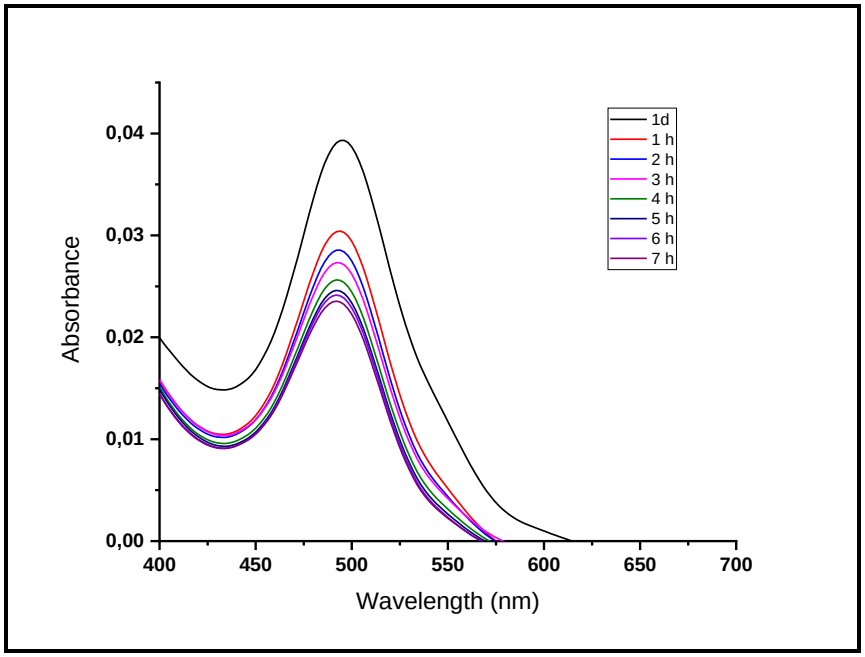

Figure 4.51. Absorbance change of **1d** over time under green led.

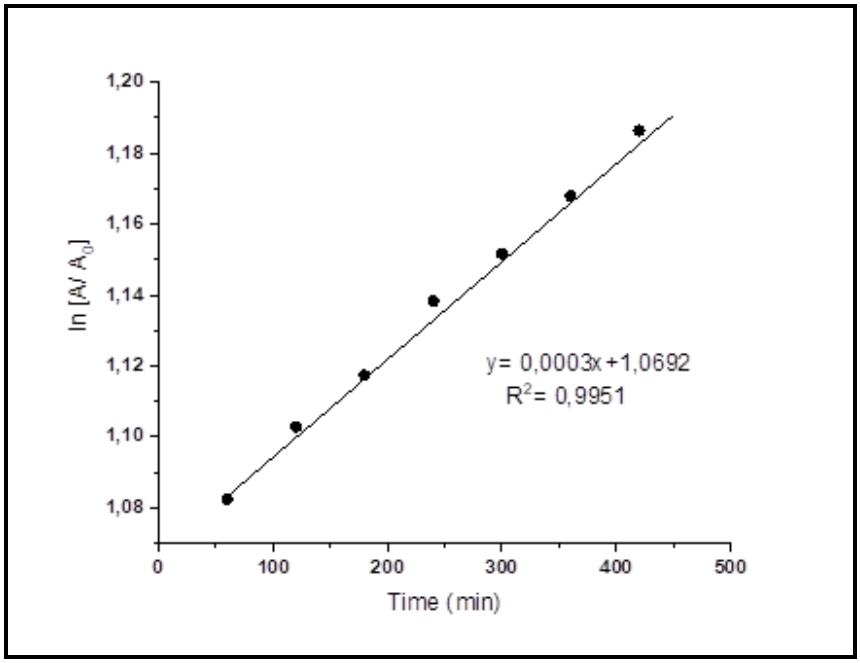

Figure 4.52. ln (A_t/A_0)/time graphic of **1d**.

4.6. Spectroscopic Investigations of the Probe 1e

In this section of the thesis, the spectroscopic properties of **1e** were investigated. First, measurements were conducted to identify the most effective solvent system for detecting CO. The highest fluorescent intensity was achieved using a 0.01 M PBS and DMF solvent system, which was visible to the naked eye. Subsequently, different ratios of the PBS-DMF system were studied. The optimal results were obtained with a 0.01 M PBS/DMF mixture at a volume ratio of 8:2 (Figure 4.53.).

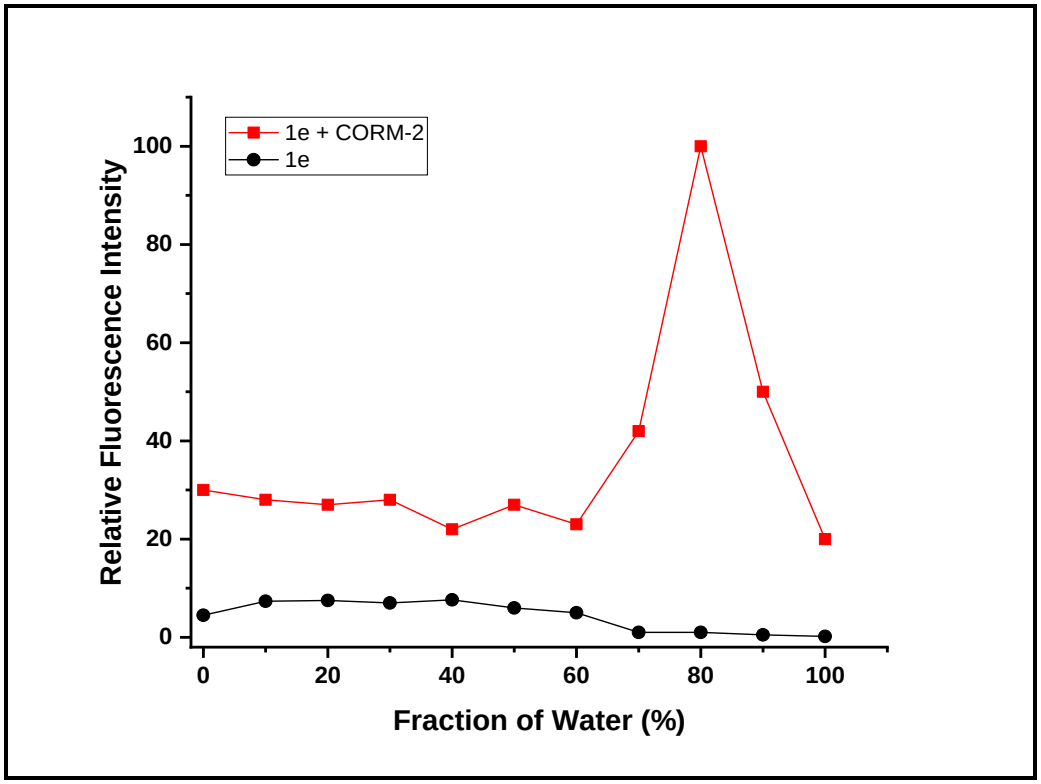

Figure 4.53. Effect of the fraction of water on the interaction of **1e** (5 μM) with CORM-2 (50 μM) in 0.01M PBS/DMF (pH 7.4), (λ_{ex}: 520 nm).

The ongoing investigations focused on evaluating the optical behavior of compound **1e** in response to the addition of CORM-2 molecules, which serve as a source of exogenous CO that releases 0.7 moles of CO per mole at a temperature of 37°C (Motterlini et al., 2002). The absorption and emission spectra of the probe, both in the absence and presence of CO, are illustrated in Figure 4.54. In the absence of CO, **1e** demonstrated a single absorption band at 620 nm. However, upon the introduction of

CORM-2, there was a noticeable decrease in the intensity of the 620 nm band, accompanied by the emergence of a new absorption band at 540 nm. The observations at this wavelength correlate with the **S11** molecule, thereby confirming that the reaction leads to depalladation.

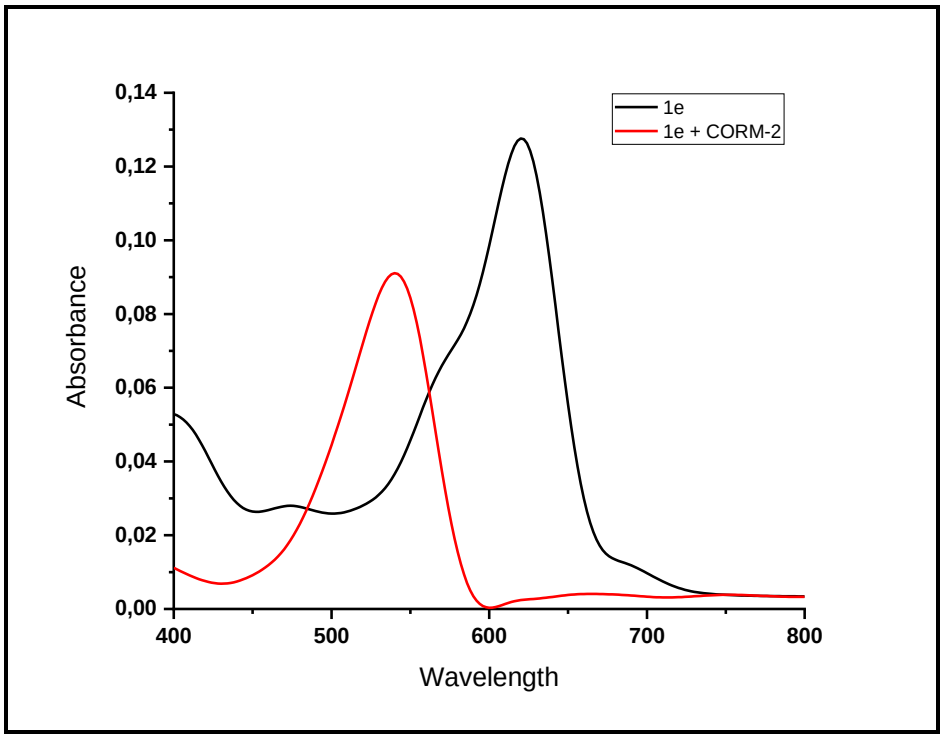

Figure 4.54. Absorbance spectra of **1e** (5 μM) in the absence and presence of 50 eq. CORM-2 in 0.01M PBS/DMF (pH 7.4, v/v, 8:2).

Although the probe has no fluorescence properties, adding 50 equivalents of CORM-2 resulted in a new fluorescence peak at 563 nm (Figure 4.55.). This result is consistent with the characteristics of the **S11** molecule and demonstrates that the probe is sensitive to CO gas.

The next step involved investigating the effect of pH on probe **1e**. Measurements taken across a pH range of 2 to 13 indicated that **1e** performed reliably between pH 3 and 9. The optimal operating pH was found to be 7, which closely aligns with physiological pH (Figure 4.56.). Based on these findings, it is anticipated that the probe will function with maximum efficiency in studies involving living cells.

The investigations continued with a systematic titration of CORM-2 molecules. To examine the change in fluorescence intensity as a function of increasing CORM-2 concentration, measurements were conducted by incrementally increasing the

concentration from 1 equivalent to 80 equivalents (Figure 4.57.). It was found that the fluorescence intensity peaked at 80 equivalents of CORM-2, after which it began to quench at higher concentrations. Additionally, an analysis of the reaction time profile indicated that **1e** reached saturation at 75 minutes, with no further changes in its response observed beyond this point (Figure 4.58.).

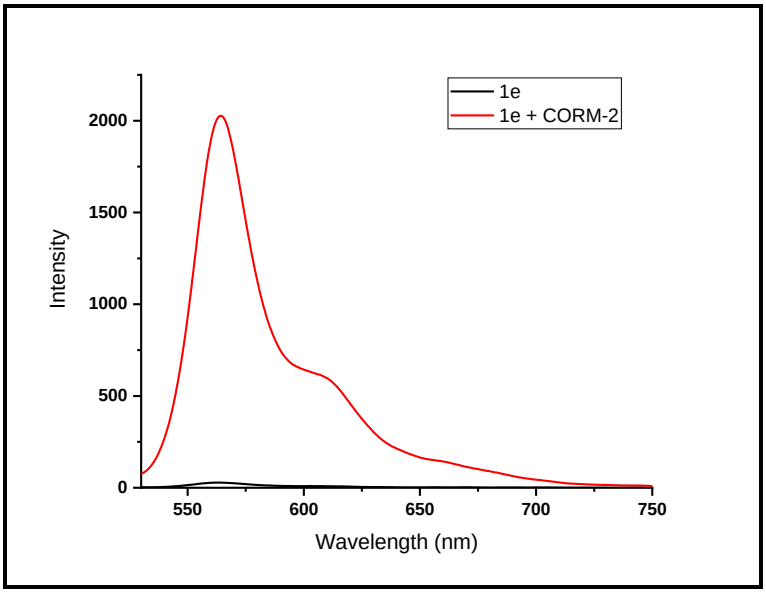

Figure 4.55. Fluorescence spectra of **1e** (5 μM) in the absence and presence of 50 eq. CORM-2 in 0.01 M PBS/DMF (pH 7.4, v/v, 8:2), (λ_{ex}: 520 nm).

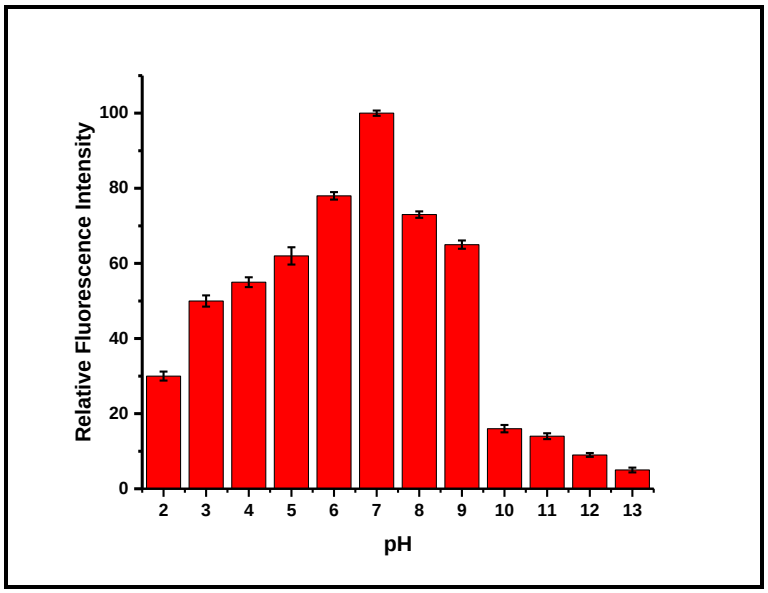

Figure 4.56. Effect of pH on the response of **1e** (5 μM) toward CORM-2 (250 μM, 50 eq.) in 0.01 M PBS/DMF (pH 7.4, v/v, 8:2), (λ_{ex}: 520 nm).

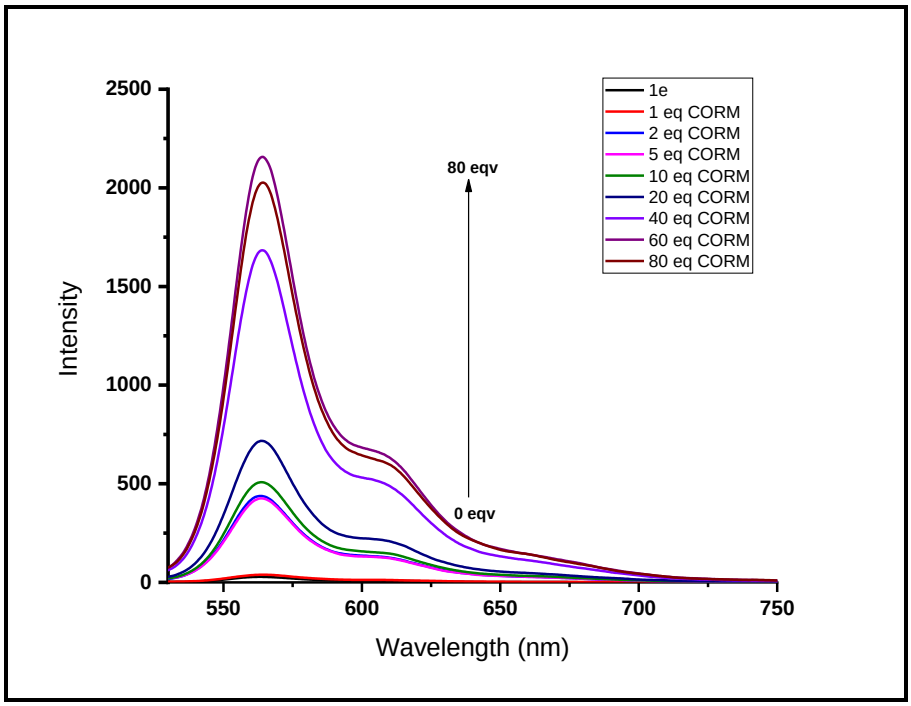

Figure 4.57. Fluorescence intensity of **1e** (5 μM) in the presence of increasing amount of CORM-2 in 0.01 M PBS/DMF (pH 7.4, v/v,8:2), (λ_{ex}: 520 nm).

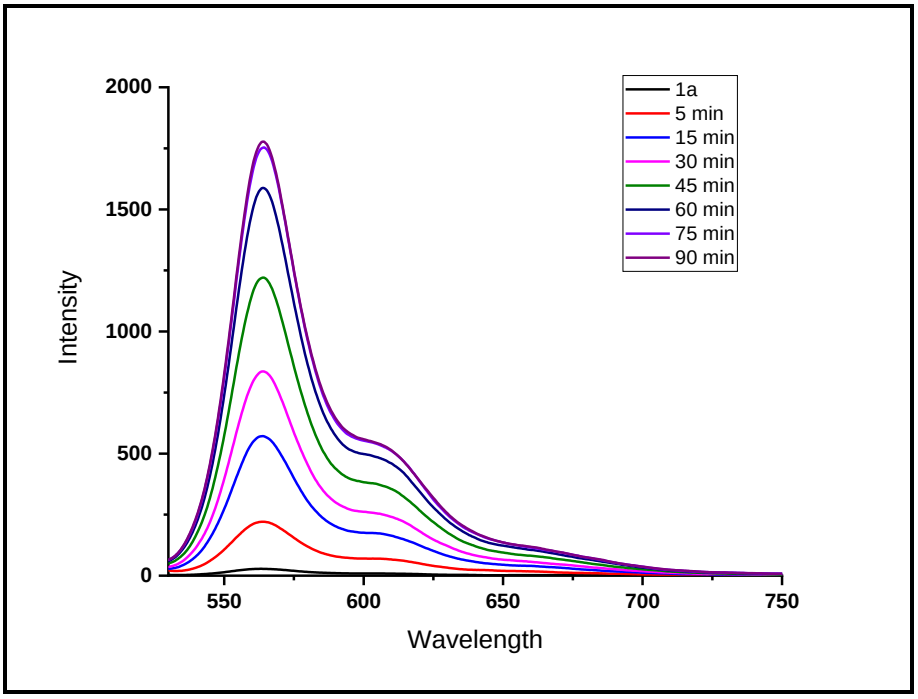

Figure 4.58. Reaction time profiles of **1e** (5 μM) in the presence of CORM-2 (80 eq) in 0.01 M PBS/DMF (pH 7.4, v/v,8:2), (λ_{ex}: 520 nm).

The detection limit was calculated from the fluorescence titration data. To determine the standard deviation, 10 separate stock samples of **1e** (5.0 μM) were prepared and treated at 37 °C for 75 minutes, and the emission intensities of these samples were measured consecutively in the absence of CORM-2. Then, the fluorescence emission intensities of **1e** (5.0 μM) were recorded after 75 minutes of incubation with CORM-2 (0.1 – 1 μM) at 37 °C. A good linear relationship between the fluorescence intensity and CORM-2 concentration was obtained with $R^2 = 0.9874$ (Figure 4.59.). The detection limit was measured to be 187 nM.

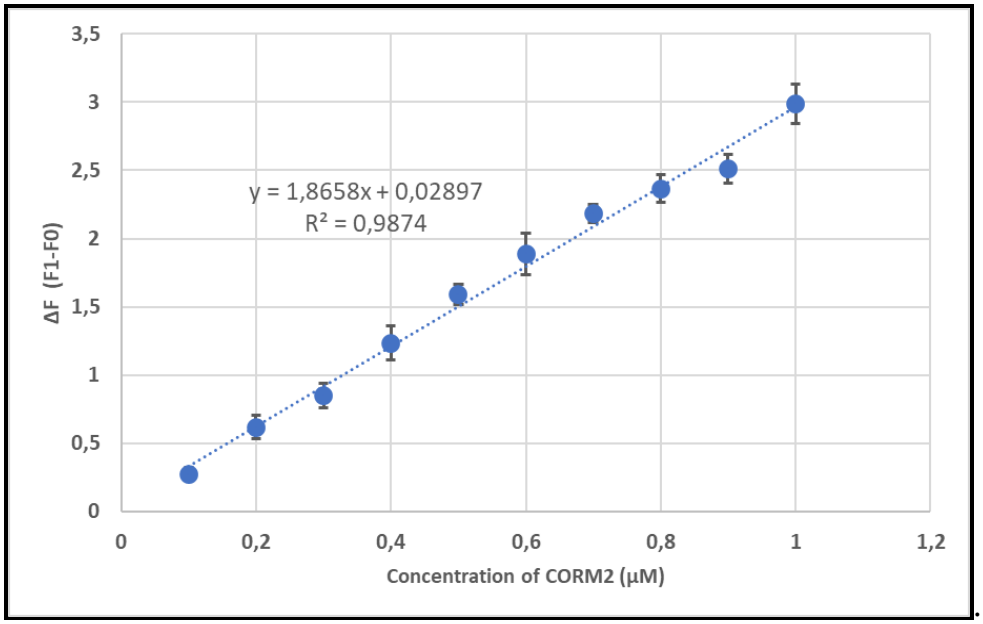

Figure 4.59. Fluorescence changes of **1e** (5 μM) upon the addition of CORM-2 (0.1 to 1 μM) in 0.01 M PBS/DMF (pH 7.4, v/v, 8:2), (λ_{ex}: 520 nm).

The reactivity of **1e** was investigated against various biological analytes, reactive oxygen species, and sulfur-containing species. As expected, **1e** did not exhibit a response to any analytes other than CO (Figure 4.60.). This high specificity ensures that **1e** can reliably distinguish CO from other potential interfering species in biological environments.

During the evaluation of **1e**'s selectivity towards metal ions, it was observed that it exhibited a limited reaction towards gold metals. However, this sensitivity was not interpreted as a significant value when compared with CO (Figure 4.61.).

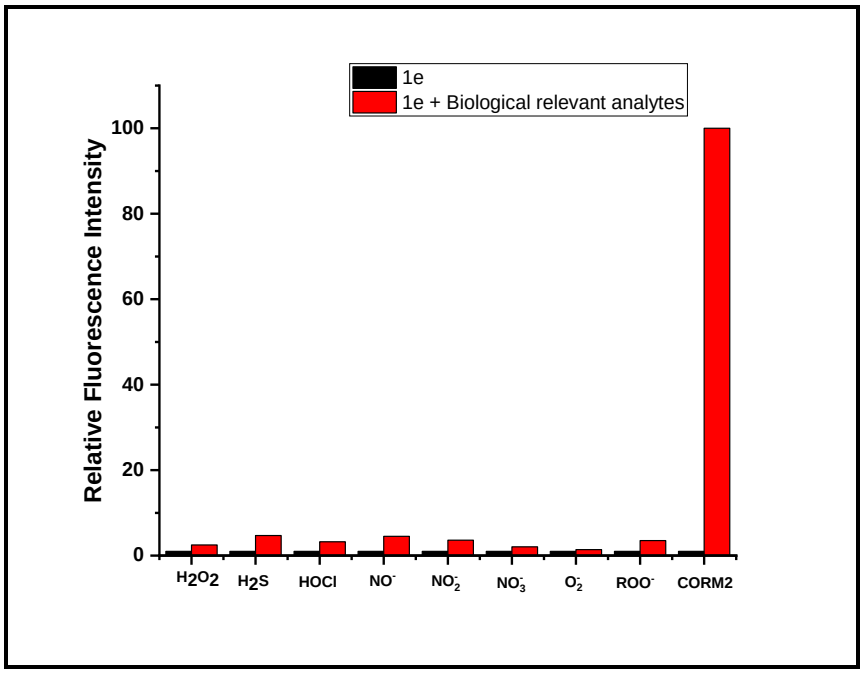

Figure 4.60. Bar graph notation of fluorescence intensities of **1e** (5 μM) with reactive oxygen species and CORM-2 (250 μM, 50 eq.) in 0.01M PBS/DMF (pH 7.4, v/v, 8:2), (λ_{ex}: 520 nm).

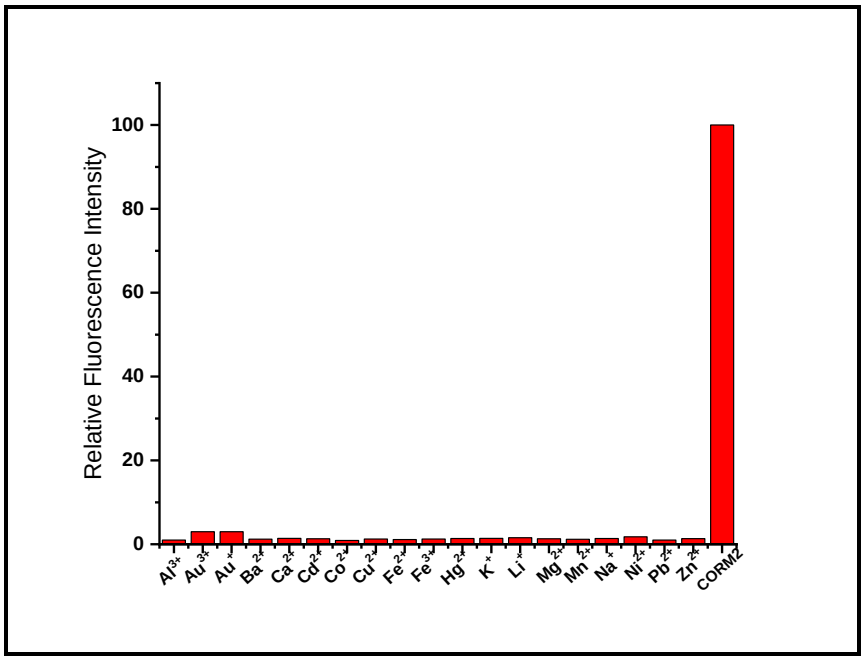

Figure 4.61. Bar graph notation of fluorescence intensities of **1e** (5 μM) with metal species and CORM-2 (250 μM, 50 eq.) in 0.01 M PBS/DMF (pH 7.4, v/v, 8:2), (λ_{ex}: 520 nm).

Quantum yields of **1e** were determined according to standard procedures. The calculated value of the probe from the formulation was 0.0295; upon the addition of CORM-2, this value increased to 0.845, as anticipated.

Under daylight, the probe solution appears light blue, whereas the CORM-2 treated solution shifts to light pink. This distinct color change further underscores **1e**'s suitability as a visual indicator for CO. Additionally, under UV light, the probe solution with added CORM-2 exhibited a distinct yellow fluorescence, whereas the probe solution alone showed no fluorescence (Figure 4.62.).

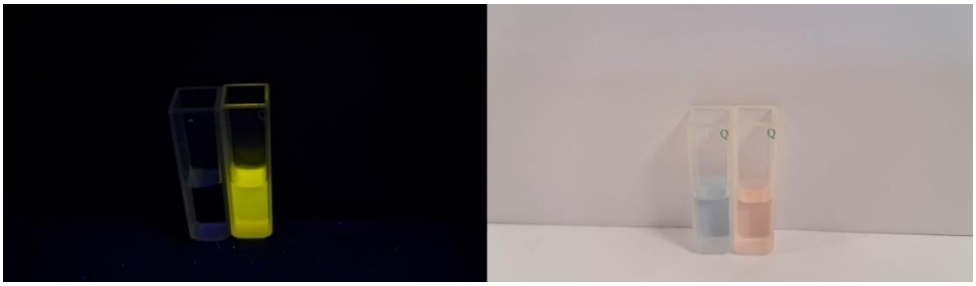

Figure 4.62. **1e** photographs in UV (left) and daylight (right) in the absence (left ones) and presence (right ones) of CORM-2.

In the filter paper test, while the distinction between the two papers is not pronounced in daylight, the yellow fluorescence of the filter paper exposed to CO gas is distinctly visible under the UV lamp (Figure 4.63.).

Figure 4.63. Filter papers impregnated **1e** photographs in UV (left) and daylight (right) in the absence (left ones) and presence (right ones) of CO.

Cell studies involving **1e** were conducted in accordance with standard protocols. The concentration of **1e** was maintained at 4 μM, while CORM-2 was utilized at a concentration of 120 μM. Remarkably, red fluorescence was observed in control cells containing only **1e**, whereas cells treated with CORM-2 exhibited yellow fluorescence

(Figure 4.64.). The red fluorescence in the control cells is thought to result from the cell culture medium. In contrast, the distinct fluorescence observed in the CORM-2 treated cells confirms **1e**'s capability to detect real-time CO within living cells and demonstrates its effective permeation of the cell membrane.

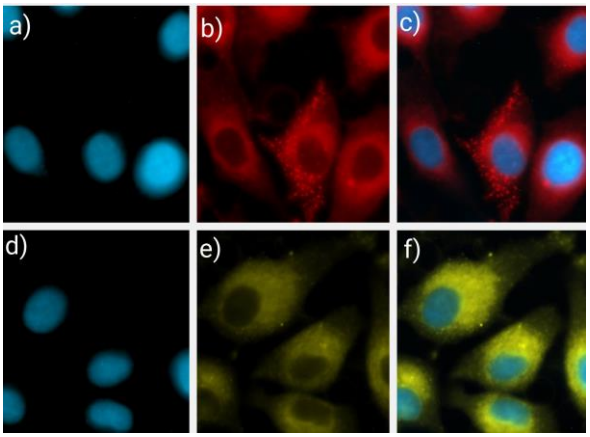

Figure 4.64. Fluorescence images of human lung adenocarcinoma cells (A549). (a) Fluorescence image of A549 cells treated with DAPI (control); (b) fluorescence image of cells treated with only **1e** (4 μM); (c) merged images of frames (a and b); (d, e) fluorescence field image of A549 cells treated with **1e** (4 μM) and CORM-2 (120μM); (f) merged images of frames (d and e). (λ_{ex}: 480 nm)

To assess the photostability of **1e**, absorbance measurements were conducted at 5-minute intervals under illumination with a red LED (Figure 4.65.). The degradation rate constant of **1e** was determined to be $36x10^{-4}$ from the slope of the $\ln(A_t/A_0)$ versus the time plot (Figure 4.66.). The probe's half-life was measured as 192.5 minutes, indicating a considerable resistance to photodegradation and thus demonstrating its photostability under red LED light exposure.

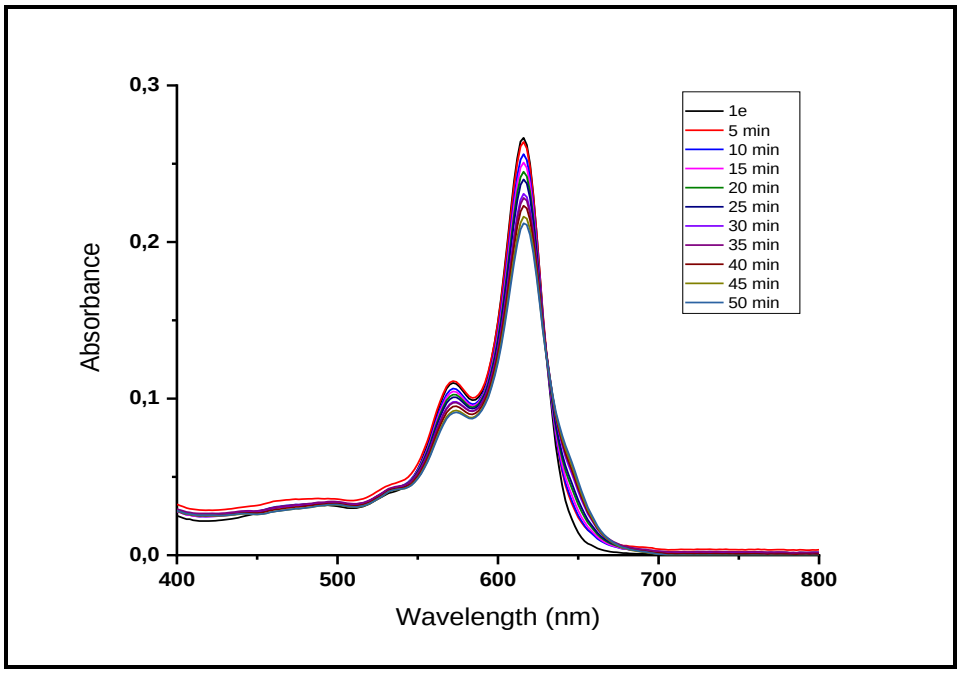

Figure 4.65. Absorbance change of **1e** over time under red led.

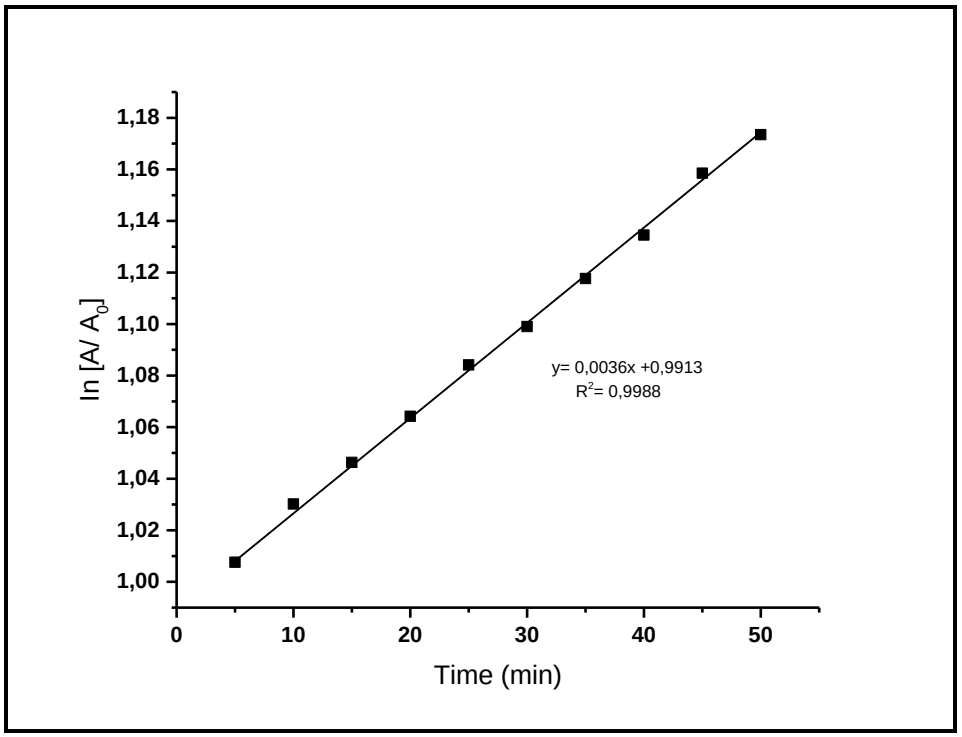

Figure 4.66. ln (A_t/A_0)/time graphic of **1e**.

CHAPTER 5

CONCLUSION

Five distinct Pd complexes of BODIPY have been synthesized, with four of these being the first documented instances of Pd attachment at the 2-position of BODIPY in the relevant literature. Comprehensive studies were conducted to explore the reactions of these complexes with CO gas, as well as their interactions in the presence of CORM. In addition, analytical measurements and cellular studies were performed. During the experiments, two products resulting from the complex reactions with CO gas were exclusively observed in the reaction involving complex **1c**. In contrast, complexes **1b**, **1d**, and **1e** exclusively yielded the depalladation product, while complex **1a** produced only the carboxylation product.

In a detailed comparison of the probes, probe **1e** stood out with the highest level of fluorescent enhancement. This probe not only demonstrated exceptional selectivity but also boasted a low detection limit and a high quantum yield while demonstrating moderate stability. These attributes are collectively positioned **1e** as the most effective option among the tested probes. On the other hand, probe **1a** also showed commendable performance in detecting CO. While it exhibited a slightly lower fluorescent enhancement and a higher detection limit compared to **1e**, its remarkable selectivity for CO reinforced its efficacy in targeted applications. This combination of strengths makes both probes valuable in their respective capabilities. (Table 5.1.).

Table 5.1. Comparison of the Probes

Probes	**Quantum Yields**	**Turn-on Ratio**	**Det. Limit**	**$t_{1/2}$**	**Selectivity**
1a	0.035-0.86	60-fold	263 nM	-	good
1b	0.093-0.92	28-fold	279 nM	5.8 h	H_2S
1c	0.021-0.94	98-fold	442 nM	0.68 h	H_2S
1d	0.089-0.74	5-fold	245 nM	38.5 h	H_2S
1e	0.029-0.84	100-fold	187 nM	3.2 h	good

Probe **1b** showcased impressive characteristics, including a high quantum yield, a favorable detection limit, a moderate half-life, and an acceptable turn-on ratio. However, its selectivity was a notable drawback, as it also responded to H_2S, limiting its effectiveness. Additionally, probe **1c** exhibited remarkable quantum yield and significant fluorescence enhancement when exposed to CO. Despite these strengths, its overall performance was hindered by a high detection limit, lack of stability, and low selectivity. When probe **1d** was evaluated, it stood out for its exceptional stability, but it had poor fluorescence enhancement, selectivity, and quantum efficiency. Despite these varied limitations among the individual probes, a silver lining emerged: all five probes demonstrated positive outcomes in cellular studies, successfully responding selectively and sensitively to CO within living cells. This highlighted their potential applicability and importance in biological environments (Table 5.1.).

This novel approach involves the direct coordination of palladium at the 2-position of the BODIPY skeleton, marking the first instance where the influence of heavy atoms on fluorescence has been thoroughly examined. In this innovative configuration, the palladium atom is positioned extremely close to the BODIPY fluorophore group, leading to lower quantum yields than those reported in prior studies. Remarkably, the probes created through this technique exhibited a complete lack of fluorescence, a finding that was further corroborated through rigorous cell experiments, underscoring the complexities and nuances of heavy atom interactions in fluorescence-based applications.

Furthermore, a novel approach has been devised for the synthesis of Pd complexes that feature BODIPY ligands. This innovative method not only facilitates the creation of these unique compounds, which are poised to serve as effective catalysts in various chemical reactions, but it also highlights the distinctive properties of the BODIPY ligand. Due to its vibrant fluorescence, the BODIPY component can function as a visual indicator during reactions, allowing researchers to monitor and analyze the processes in real-time. This dual functionality enhances the utility of these palladium complexes in both catalysis and experimental observation.

REFERENCES

Bai, C.; Zhang, J.; Qin, Y.; Meng, Q.; Yao, J.; Huang, H.; Wei, B.; Li, R.; Zhang, L.; Miao, H.; Qu, C.; Qiao, R. Strategy for Detecting Carbon Monoxide: Cu^{2+}-Assisted Fluorescent Probe and Its Applications in Biological Imaging. *Anal. Chem.* **2022**, *94* (32), 11298–11306. DOI: 10.1021/acs.analchem.2c01948.

Bay, H. W.; Blurton, K. F.; Sedlak, J. M.; Valentine, A. M. Electrochemical Technique for the Measurement of Carbon Monoxide. *Anal. Chem.* **1974**, *46* (12), 1837–1839. DOI: 10.1021/ac60348a001.

Biswas, B.; Venkateswarulu, M.; Sinha, S.; Girdhar, K.; Ghosh, S.; Chatterjee, S.; Mondal, P.; Ghosh, S. Long Range Emissive Water-Soluble Fluorogenic Molecular Platform for Imaging Carbon Monoxide in Live Cells. *ACS Appl. Bio Mater.* **2019**, *2* (12), 5427–5433. DOI: 10.1021/acsabm.9b00736.

Blurton, K. F.; Sedlak, J. M. The Electro-Oxidation of Carbon Monoxide on Platinum. *J. Electrochem. Soc.* **1974**, *121*, 1315. DOI: 10.1149/1.2401677.

Cinelli, M. A.; Li, H.; Pensa, A. V.; Kang, S.; Roman, L. J.; Martásek, P.; Poulos, T. L.; Silverman, R. B. Phenyl Ether- and Aniline-Containing 2-Aminoquinolines as Potent and Selective Inhibitors of Neuronal Nitric Oxide Synthase. *J. Med. Chem.* **2015**, *58* (21), 8694–8712. DOI: 10.1021/acs.jmedchem.5b01330.

Chen, C.; He, J.; Xu, D.; Tan, X.; Zhou, X.; Wang, X. Study of Nano-Au-Assembled Amperometric CO Gas Sensor. *Sens. Actuators, B* **2005**, *107* (2), 866–871. DOI: 10.1016/j.snb.2004.12.037.

Chen, J.; Gan, Y.; Hong, S.; Yin, G.; Zhou, L.; Wang, C.; Fu, Y.; Li, H.; Yin, P. A Novel Red Emission Fluorescent Probe for Monitoring Carbon Monoxide in Living Cells and Zebrafish. *Anal. Methods* **2021**, *13* (25), 2871–2877. DOI: 10.1039/D1AY00704A.

Coburn, R. F.; Williams, W. J.; White, P.; Kahn, S. B. The Production of Carbon Monoxide from Hemoglobin *In Vivo*. *J. Clin. Invest.* **1967**, *46* (3), 346–356. DOI: 10.1172/JCI105536.

Courbat, J.; Pascu, M.; Gutmacher, D.; Briand, D.; Wöllenstein, J.; Hoefer, U.; Severin, K.; de Rooij, N. F. A Colorimetric CO Sensor for Fire Detection. *Procedia Eng.* **2011**, *25*, 1329–1332. DOI: 10.1016/j.proeng.2011.12.328.

Çevik Eren, M; Eren, A; Dartar, S; Tütüncü, B. B; Emrullahoğlu, M. A Cyclopalladated BODIPY Construct as a Fluorescent Probe for Carbon Monoxide. *Eur. J. Inorg. Chem.* **2022**, *2022* (14), e202200093. DOI: 10.1002/ejic.202200093.

Das, B.; Lohar, S.; Patra, A.; Ahmmed, E.; Mandal, S. K.; Bhakta, J. N.; Dhara, K.; Chattopadhyay, P. A Naphthalimide-Based Fluorescence "Turn-On" Chemosensor for Highly Selective Detection of Carbon Monoxide: Imaging Applications in Living Cells. *New J. Chem.* **2018,** *42* (16), 13497–13502. DOI: 10.1039/C8NJ02552E.

Dhara, K.; Lohar, S.; Patra, A.; Roy, P.; Saha, S. K.; Sadhukhan, G. C.; Chattopadhyay, P. A New Lysosome-Targetable Turn-On Fluorogenic Probe for Carbon Monoxide Imaging in Living Cells. *Anal. Chem.* **2018**, *90* (4), 2933–2938. DOI: 10.1021/acs.analchem.7b05331.

Du, F.; Qu, Y.; Li, M.; Tan, X. Mitochondria-Targetable Ratiometric Fluorescence Probe for Carbon Monoxide Based on Naphthalimide Derivatives. *Anal. Bioanal. Chem.* **2021**, *413*, 1395–1403. DOI: 10.1007/s00216-020-03103-8.

Esteban, J.; Ros-Lis, J.; Martínez-Máñez, R.; Marcos, M. D.; Moragues, M.; Soto, J.; Sancenón, F. Sensitive and Selective Chromogenic Sensing of Carbon Monoxide by Using Binuclear Rhodium Complexes. *Angew. Chem., Int. Ed.* **2010**, *49* (28), 4934–4937. DOI: 10.1002/anie.201001344.

Faizan, M.; Muhammad, N.; Niazi, K. U. K.; Hu, Y.; Wang, Y.; Wu, Y.; Sun, H.; Liu, R.; Dong, W.; Zhang, W.; Gao, Z. CO-Releasing Materials: An Emphasis on

Therapeutic Implications, as Release and Subsequent Cytotoxicity Are the Part of Therapy. *Materials* **2019**, *12* (10), 1643. DOI: 10.3390/ma12101643.

Fang, X.; Zhang, Z.; Qi, Y.; Yue, B.; Yu, J.; Yang, H.; Yu, H. High-Performance Recognition, Cell-Imaging, and Efficient Removal of Carbon Monoxide toward a Palladium-Mediated Fluorescent Sensing Platform. *Anal. Chem.* **2023**, *95* (30), 11518–11525. DOI: 10.1021/acs.analchem.3c02050.

Fang, X.; Cui, L.; Yu, H.; Qi, Y. Fe(III)-Based Fluorescent Probe for High-Performance Recognition, Test Strip Analysis, and Cell Imaging of Carbon Monoxide. *Anal. Chem.* **2024**, *96* (28), 11588–11594. DOI: 10.1021/acs.analchem.4c02438.

Feng, S.; Liu, D.; Feng, W.; Feng, G. Allyl Fluorescein Ethers as Promising Fluorescent Probes for Carbon Monoxide Imaging in Living Cells. *Anal. Chem.* **2017**, *89* (6), 3754–3760. DOI: 10.1021/acs.analchem.7b00135.

Fu, G.-Q.; Xia, Y.-S.; Jiang, W.-L.; Wang, W.-X.; Tan, Z.-K.; Guo, K.-Y.; Mao, G.-J.; Li, C.-Y. A Novel Precipitating-Fluorochrome-Based Fluorescent Probe for Monitoring Carbon Monoxide During Drug-Induced Liver Injury. *Talanta* **2022**, *243*, 123398. DOI: 10.1016/j.talanta.2022.123398.

Ha, Y.; Sim, J.; Lee, Y.; Suh, M. Insertable Fast-Response Amperometric NO/CO Dual Microsensor: Study of Neurovascular Coupling During Acutely Induced Seizures of Rat Brain Cortex. *Anal. Chem.* **2016**, *88* (5), 2563–2569. DOI: 10.1021/acs.analchem.5b04288.

Itou, M.; Araki, Y.; Ito, O.; Kido, H. Carbon Monoxide Ligand-Exchange Reaction of Triruthenium Cluster Complexes Induced by Photosensitized Electron Transfer: A New Type of Photoactive CO Color Sensor. *Inorg. Chem.* **2006**, *45* (16), 6114–6116. DOI: 10.1021/ic060751n.

Lee, Y.; Kim, J. Simultaneous Electrochemical Detection of Nitric Oxide and Carbon Monoxide Generated from Mouse Kidney Organ Tissues. *Anal. Chem.* **2007**, *79* (20), 7669–7675. DOI: 10.1021/ac070814z.

Li, S.; Yang, K.; Zeng, J.; Ding, Y.; Cheng, D.; He, L. Golgi-Targeting Fluorescent Probe for Monitoring CO-Releasing Molecule-3 In Vitro and In Vivo. *ACS Omega* **2022**, *7* (11), 9929–9935. DOI: 10.1021/acsomega.2c00422.

Li, S.-J.; Zhou, D.-Y.; Li, Y.-F.; Yang, B.; Ou-Yang, J.; Jie, J.; Liu, J.; Li, C.-Y. Mitochondria-Targeted Near-Infrared Fluorescent Probe for the Detection of Carbon Monoxide In Vivo. *Talanta* **2018**, *188*, 691–700. DOI: 10.1016/j.talanta.2018.06.046.

Li, Y.; Wang, Y.-L.; Wang, J.-Y. A Simple Iodine-Promoted Synthesis of 2-Substituted Benzothiazoles by Condensation of Aldehydes with 2-Aminothiophenol. *Chem. Lett.* **2006**, *35* (4), 460–461. DOI: 10.1246/cl.2006.460.

Li, Y.; Wang, X.; Yang, J.; Xie, X.; Li, M.; Niu, J.; Tong, L.; Tang, B. Fluorescent Probe Based on Azobenzene-Cyclopalladium for the Selective Imaging of Endogenous Carbon Monoxide under Hypoxia Conditions. *Anal. Chem.* **2016**, *88* (22), 11154–11159. DOI: 10.1021/acs.analchem.6b03376.

Lower, S. K.; El-Sayed, M. A. *Chem. Rev.* **1966**, *66* (2), 199–241. DOI: 10.1021/cr60240a004.

Madea, D.; Martínek, M.; Muchová, L.; Váňa, J.; Vítek, L.; Klán, P. Structural Modifications of Nile Red Carbon Monoxide Fluorescent Probe: Sensing Mechanism and Applications. *J. Org. Chem.* **2020**, *85* (5), 3473–3489. DOI: 10.1021/acs.joc.9b03217.

Michel, B. W.; Lippert, A. R.; Chang, C. J. A Reaction-Based Fluorescent Probe for Selective Imaging of Carbon Monoxide in Living Cells Using a Palladium-Mediated Carbonylation. *J. Am. Chem. Soc.* **2012**, *134* (38), 15668–15671. DOI: 10.1021/ja307017b.

Moragues, M. E.; Esteban, J.; Ros-Lis, J. V.; Martínez-Máñez, R.; Marcos, M. D.; Martínez, M.; Soto, J.; Sancenón, F. Sensitive and Selective Chromogenic Sensing of Carbon Monoxide via Reversible Axial CO Coordination in

Binuclear Rhodium Complexes. *J. Am. Chem. Soc.* **2011**, *133* (39), 15762–15772. DOI: 10.1021/ja206251r.

Moragues, M. E.; Toscani, A.; Sancenón, F.; Martínez-Máñez, R.; White, A. J. P.; Wilton-Ely, J. D. E. T. A Chromo-Fluorogenic Synthetic "Canary" for CO Detection Based on a Pyrenylvinyl Ruthenium(II) Complex. *J. Am. Chem. Soc.* **2014**, *136* (34), 11930–11933. DOI: 10.1021/ja507014a.

Morstein, J.; Höfler, D.; Ueno, K.; Jurss, J. W.; Walvoord, R. R.; Bruemmer, K. J.; Rezgui, S. P.; Brewer, T. F.; Saitoe, M.; Michel, B. W.; Chang, C. J. Ligand-Directed Approach to Activity-Based Sensing: Developing Palladacycle Fluorescent Probes That Enable Endogenous Carbon Monoxide Detection. *J. Am. Chem. Soc.* **2020**, *142* (37), 15917–15930. DOI: 10.1021/jacs.0c06405.

Park, S. S.; Kim, J.; Lee, Y. Improved Electrochemical Microsensor for the Real-Time Simultaneous Analysis of Endogenous Nitric Oxide and Carbon Monoxide Generation. *Anal. Chem.* **2012**, *84* (3), 1792–1796. DOI: 10.1021/ac2031628.

Park, S. S.; Hong, M.; Ha, Y.; Sim, J.; Jhon, G.-J.; Lee, Y.; Suh, M. The Real-Time *In Vivo* Electrochemical Measurement of Nitric Oxide and Carbon Monoxide Release upon Direct Epidural Electrical Stimulation of the Rat Neocortex. *Analyst* **2015**, *140* (10), 3415–3421. DOI: 10.1039/C5AN00122F.

Ramos-Torres, Á.; Avellanal-Zaballa, E.; Prieto-Castañeda, A.; García-Garrido, F.; Bañuelos, J.; Agarrabeitia, A. R.; Ortiz, M. J. FormylBODIPYs by PCC-Promoted Selective Oxidation of α-MethylBODIPYs. Synthetic Versatility and Applications. *Org. Lett.* **2019**, *21* (12), 4563–4566. DOI: 10.1021/acs.orglett.9b01465.

Robson, J. A.; Kubánková, M.; Bond, T.; Hendley, R. A.; White, A. J. P.; Kuimova, M. K.; Wilton-Ely, J. D. E. T. Simultaneous Detection of Carbon Monoxide and Viscosity Changes in Cells. *Angew. Chem., Int. Ed.* **2020**, *59*, 21431. DOI: 10.1002/anie.202007965.

Rosenthal, J.; Lippard, S. J. Direct Detection of Nitroxyl in Aqueous Solution Using a Tripodal Copper(II) BODIPY Complex. *J. Am. Chem. Soc.* **2010**, *132* (16), 5536–5537. DOI: 10.1021/ja909148v.

Saha, S. K.; Saha, N. C. A New Naphthalimide-Pd(II) Complex as a Light-Up Fluorescent Chemosensor for Selective Detection of Carbon Monoxide in Aqueous Medium. *Inorg. Chim. Acta* **2021**, *517*, 120204. DOI: 10.1016/j.ica.2020.120204.

Sakla, R.; Ghosh, A.; Kumar, V.; Kanika; Das, P.; Sharma, P. K.; Khan, R.; Jose, D. A. Light Activated Simultaneous Release and Recognition of Biological Signaling Molecule Carbon Monoxide (CO). *Methods* **2023**, *210*, 44–51. DOI: 10.1016/j.ymeth.2023.01.003.

Sarkar, A.; Fouzder, C.; Chakraborty, S.; Ahmmed, E.; Kundu, R.; Dam, S.; Chattopadhyay, P.; Dhara, K. A Nuclear-Localized Naphthalimide-Based Fluorescent Light-Up Probe for Selective Detection of Carbon Monoxide in Living Cells. *Chem. Res. Toxicol.* **2020**, *33* (2), 651–656. DOI: 10.1021/acs.chemrestox.9b00462.

Sarkar, A.; Hansda, S.; Dutta, T.; Ghoshal, S.; Mukhopadhyay, S.; Sarkar, P.; Mandal, S. K.; Saha, N. C.; Chattopadhyay, P.; Dhara, K. Endoplasmic Reticulum-Targeted Fluorescent Probes for Metal-Free Tracking of Carbon Monoxide in Living Cells. *Sens. Actuators B Chem.* **2023**, *393*, 134150. DOI: 10.1016/j.snb.2023.134150.

Sedlak, J. M.; Blurton, K. F. The Electrochemical Reactions of Carbon Monoxide, Nitric Oxide, and Nitrogen Dioxide at Gold Electrodes. *J. Electrochem. Soc.* **1976**, *123*, 1476. DOI: 10.1149/1.2132622.

Seto, H.; Kondo, T.; Yuasa, M. Sensitive and Selective Electrochemical Detection of Carbon Monoxide in Saline at a Pt-Ru/Nafion/MnO_2-Modified Electrode. *Anal. Sci.* **2012**, *28* (2), 115–120. DOI: 10.2116/analsci.28.115.

Steinberg, M. H. In *Wintrobe's Clinical Hematology;* Lippincott Williams & Wilkins, 2014; Chapter 35.

Takagi, T.; Uchiyama, K.; Naito, Y. The Therapeutic Potential of Carbon Monoxide for Inflammatory Bowel Disease. *Digestion* **2015**, *91* (1), 13–18. DOI: 10.1159/000368765.

Tang, J.; Zhang, P.; Li, Z.; Zhang, Y.; Chen, H.; Li, X.; Wei, C. A Simple Ratiometric Fluorescent Probe for Two-Photon Imaging of Carbon Monoxide in Living Cells and Zebrafish. *Bioorg. Chem.* **2023**, *135*, 106489. DOI: 10.1016/j.bioorg.2023.106489.

Toscani, A.; Marín-Hernández, C.; Moragues, M. E.; Sancenón, F.; Dingwall, P.; Brown, N. J.; Martínez-Máñez, R.; White, A. J. P.; Wilton-Ely, J. D. E. T. Ruthenium(II) and Osmium(II) Vinyl Complexes as Highly Sensitive and Selective Chromogenic and Fluorogenic Probes for the Sensing of Carbon Monoxide in Air. *Chem. Eur. J.* **2015**, *21* (41), 14529–14538. DOI: 10.1002/chem.201501843.

Toscani, A.; Marín-Hernández, C.; Robson, J. A.; Chua, E.; Dingwall, P.; White, A. J. P.; Sancenón, F.; de la Torre, C.; Martínez-Máñez, R.; Wilton-Ely, J. D. E. T. Highly Sensitive and Selective Molecular Probes for Chromo-Fluorogenic Sensing of Carbon Monoxide in Air, Aqueous Solution and Cells. *Chem. Eur. J.* **2019**, *25* (9), 2069–2074. DOI: 10.1002/chem.201806005.

Treibs, A.; Kreuzer, F.-H. Difluorboryl-Komplexe von Di- und Tripyrrylmethenen. *Justus Liebigs Ann. Chem.* **1968**, *718* (1), 208–223. DOI: 10.1002/jlac.19687180119.

Tsceng, K.-I.; Yang, M.-C. Platinum Electrodes Modified by Tin for Electrochemical CO Sensors. *J. Electrochem. Soc.* **2003**, *150*, H156. DOI: 10.1149/1.1576774.

Untereiner, A. A.; Wu, L.; Wang, R. *Gasotransmitters: Physiology and Pathophysiology;* Hermann, A., Sitdikova, G. F., Weiger, T. M., Eds.; Springer, 2012, Chapter 2. DOI: 10.1007/978-3-642-30338-8_2.

Wang, J.; Karpus, J.; Zhao, B. S.; Luo, Z.; Chen, P. R.; He, C. A Selective Fluorescent Probe for Carbon Monoxide Imaging in Living Cells. *Angew. Chem., Int. Ed.* **2012**, *51* (38), 9652–9656. DOI: 10.1002/anie.201203684.

Wang, X.; Wang, Y.; Kim, H. P.; Nakahira, K.; Ryter, S. W.; Choi, A. M. K. Carbon Monoxide Protects against Hyperoxia-Induced Endothelial Cell Apoptosis by Inhibiting Reactive Oxygen Species Formation. *J. Biol. Chem.* **2007**, *282* (3), 1718–1726. DOI: 10.1074/jbc.M607610200.

Wilkinson, L. J. Carbon Monoxide—The Silent Killer. In *Molecules of Death*, Imperial College Press: London, 2007; pp 37–46.

Xiao, Z.-Y.; Tu, B.-L.; Hua, S.-H.; Wang, F.; Tang, L.-J.; Dong, W.-R.; Jiang, J.-H. Near-Infrared Fluorogenic Imaging of Carbon Monoxide in Live Cells Using Palladium-Mediated Carbonylation. *Chem. Commun.* **2024**, *60* (11), 1420–1423. DOI: 10.1039/D3CC04523D.

Xu, H.; Zong, S.; Xu, H.; Tang, X.; Li, Z. Detection and Imaging of Carbon Monoxide Releasing Molecule-2 in HeLa Cells and Zebrafish Using a Metal-Free Near-Infrared Fluorescent Off–On Probe. *Spectrochim. Acta A Mol. Biomol. Spectrosc.* **2022**, *272*, 120964. DOI: 10.1016/j.saa.2022.120964.

Yan, J.-w.; Zhu, J.-y.; Tan, Q.-f.; Zhou, L.-f.; Yao, P.-f.; Lu, Y.-t.; Tan, J.-h.; Zhang, L. Development of a Colorimetric and NIR Fluorescent Dual Probe for Carbon Monoxide. *RSC Adv.* **2016**, *6* (70), 65373–65376. DOI: 10.1039/C6RA14409H.

Yue, L.; Tang, Y.; Huang, H.; Song, W.; Lin, W. A Fluorogenic Probe for Detecting CO with the Potential Integration of Diagnosis and Therapy (IDT) for Cancer. *Sens. Actuators B Chem.* **2021**, *344*, 130245. DOI: 10.1016/j.snb.2021.130245.

Zaromb, S.; Stetter, J. R.; O'Gorman, D. Determination of Carbon Monoxide in Air by Dynamic Coulometry. *J. Electroanal. Chem. Interfacial Electrochem.* **1983**, *148* (2), 279–287. DOI: 10.1016/S0022-0728(83)80403-3.

Zhao, L.; Chen, R.; Jia, C.; Liu, J.; Liu, G.; Cheng, T. BODIPY-Based OFF-ON Fluorescent Probe for Endogenous Carbon Monoxide Imaging in Living Cells. *J. Fluoresc.* **2024**, *34* (4), 1793–1799. DOI: 10.1007/s10895-023-03403-z.

Zhu, B.; Xing, X.; Kim, J.; Rha, H.; Liu, C.; Zhang, Q.; Zeng, L.; Lan, M.; Kim, J. S. Endogenous CO Imaging in Bacterial Pneumonia with a NIR Fluorescent Probe. *Biomaterials* **2024**, *304*, 122419. DOI: 10.1016/j.biomaterials.2023.122419.

APPENDIX A

^{1}H NMR AND ^{13}C NMR SPECTRUMS OF THE COMPOUNDS

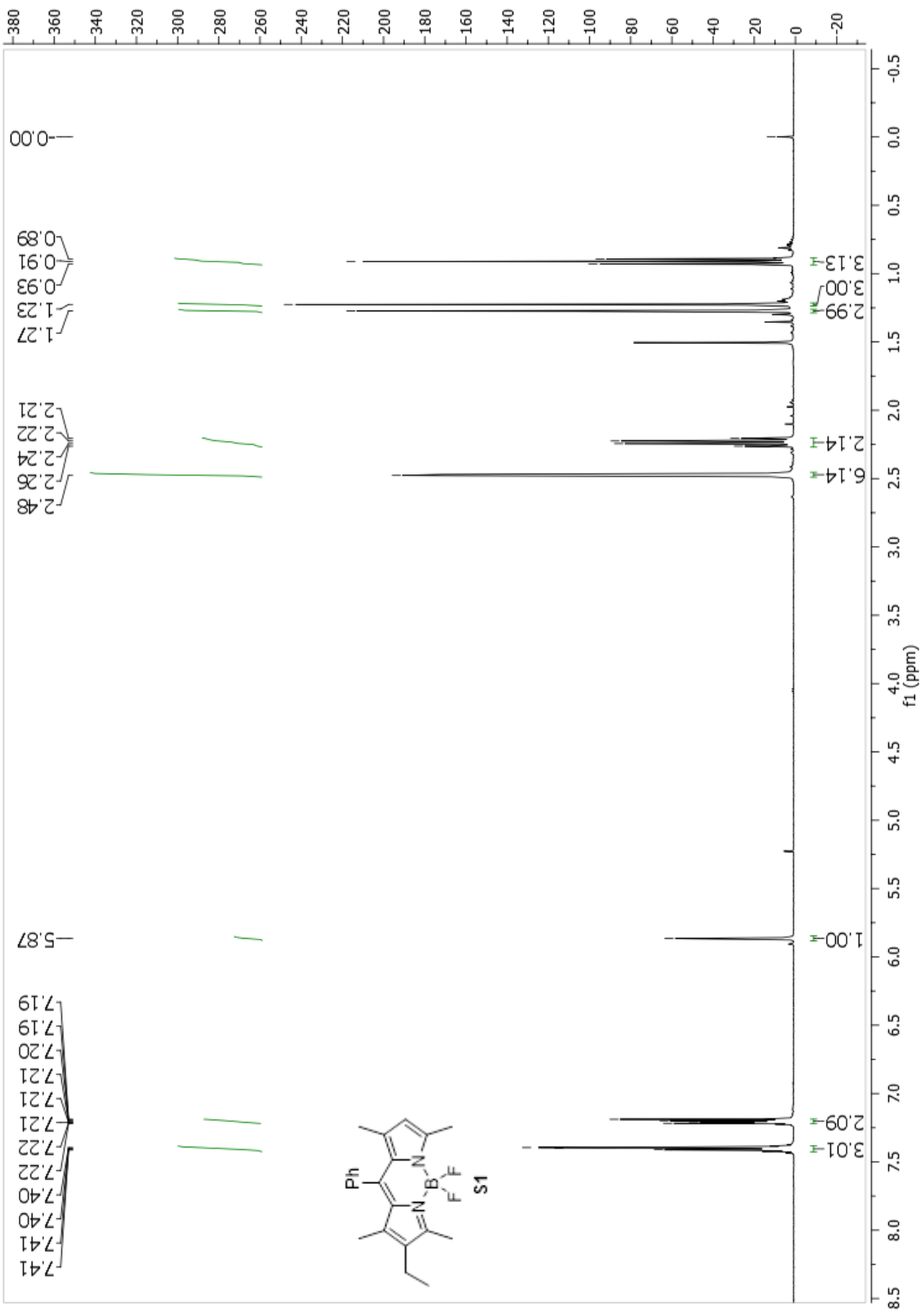
7.41
7.41
7.40
7.40
7.22
7.22
7.21
7.21
7.21
7.20
7.19
7.19
5.87
2.48
2.36
2.24
2.22
2.21
1.27
1.23
0.93
0.91
0.89
0.00
3.01
2.09
1.00
6.14
2.14
3.00
2.99
3.13
Ph
S1
f1 (ppm)

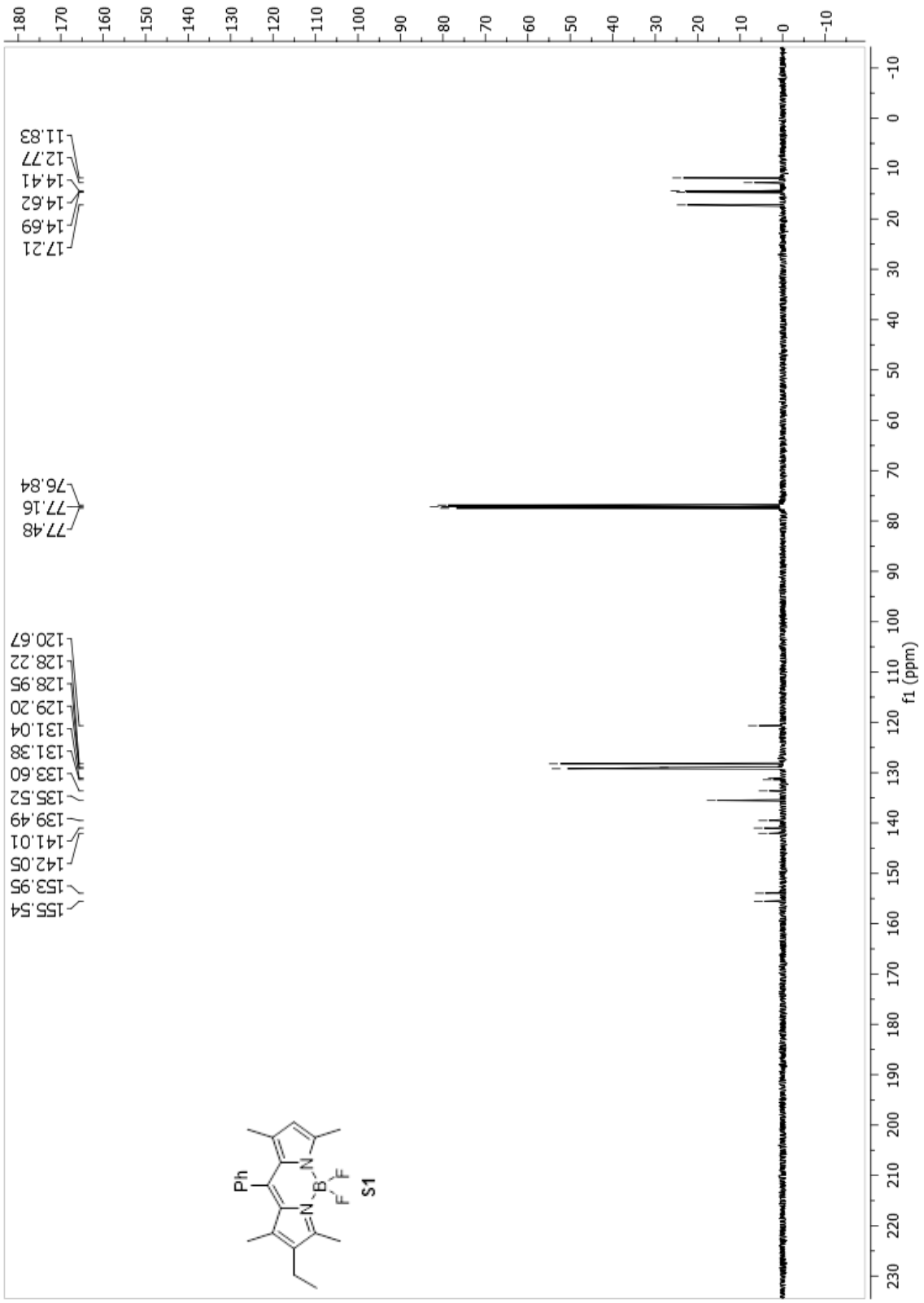
155.54
153.95
142.05
141.01
139.49
135.52
133.60
131.38
131.04
129.20
128.95
128.22
120.67
77.48
77.16
76.84
17.21
14.69
14.62
14.41
12.77
11.83
f1 (ppm)
Ph
S1

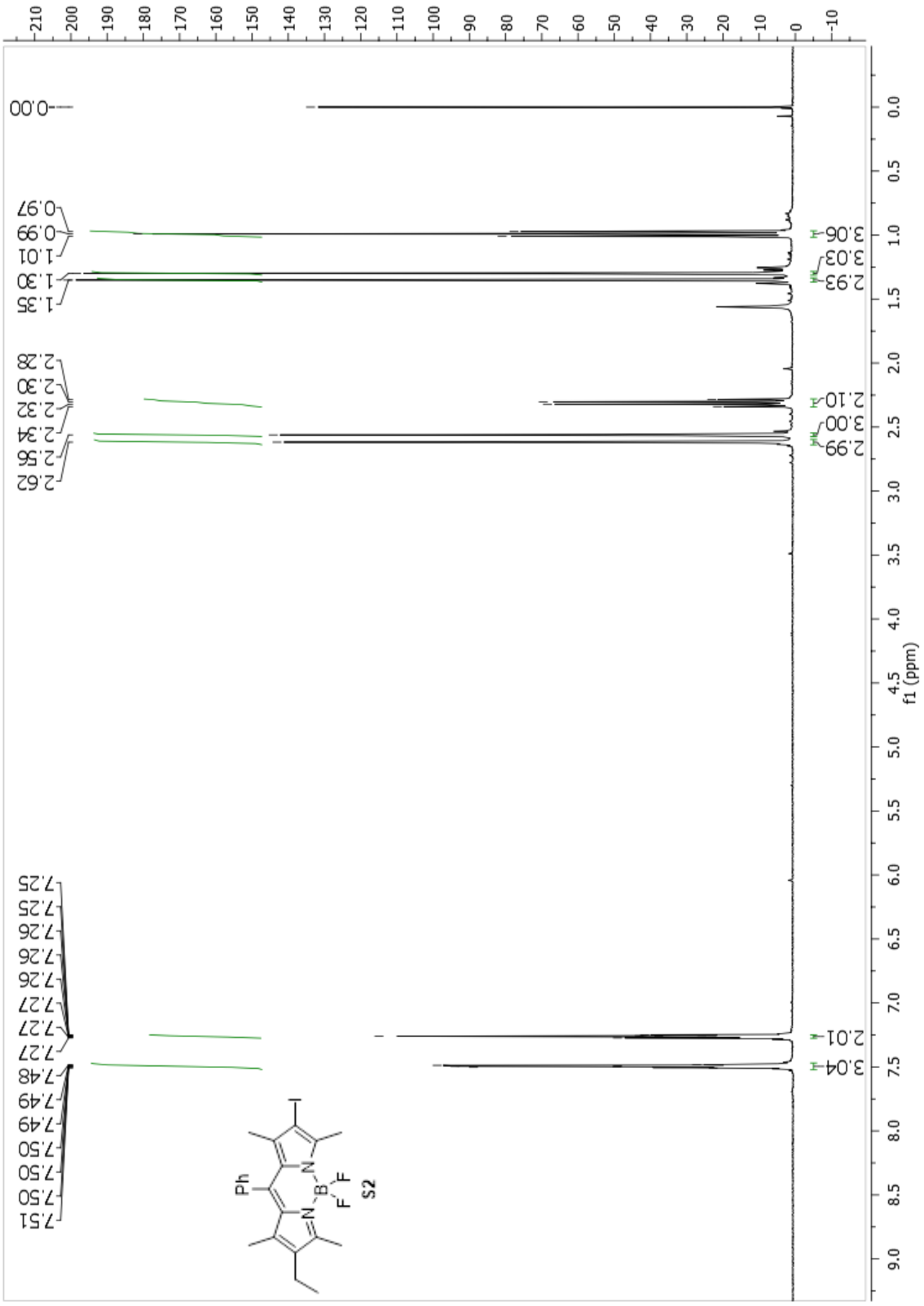
S2
f1 (ppm)

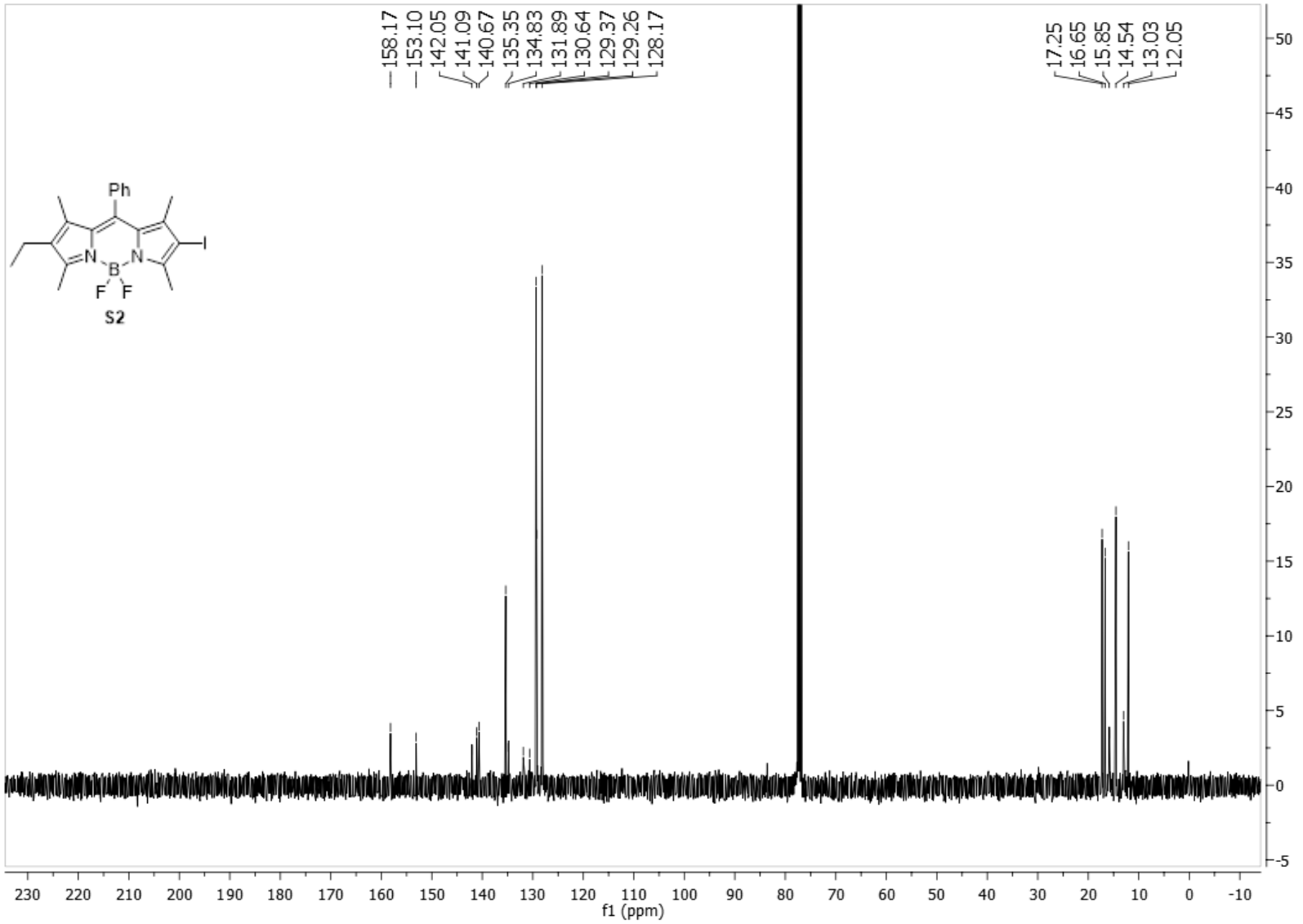
158.17
153.10
142.05
141.09
140.67
135.35
134.83
131.89
130.64
129.37
129.26
128.17
17.25
16.65
15.85
14.54
13.03
12.05
Ph
N
B
N
F
F
I
S2
f1 (ppm)

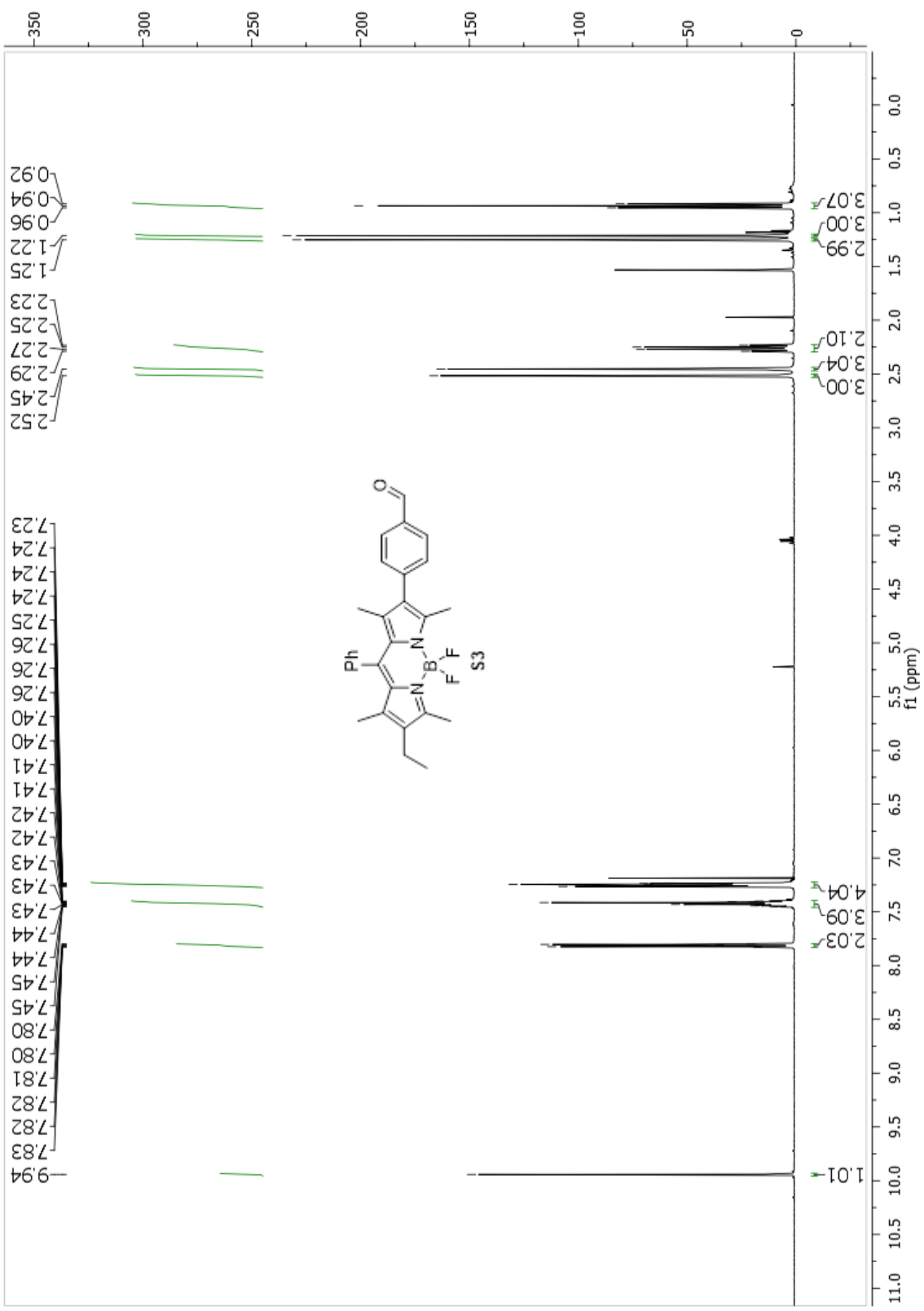
Ph
B
F
F
S3
f1 (ppm)

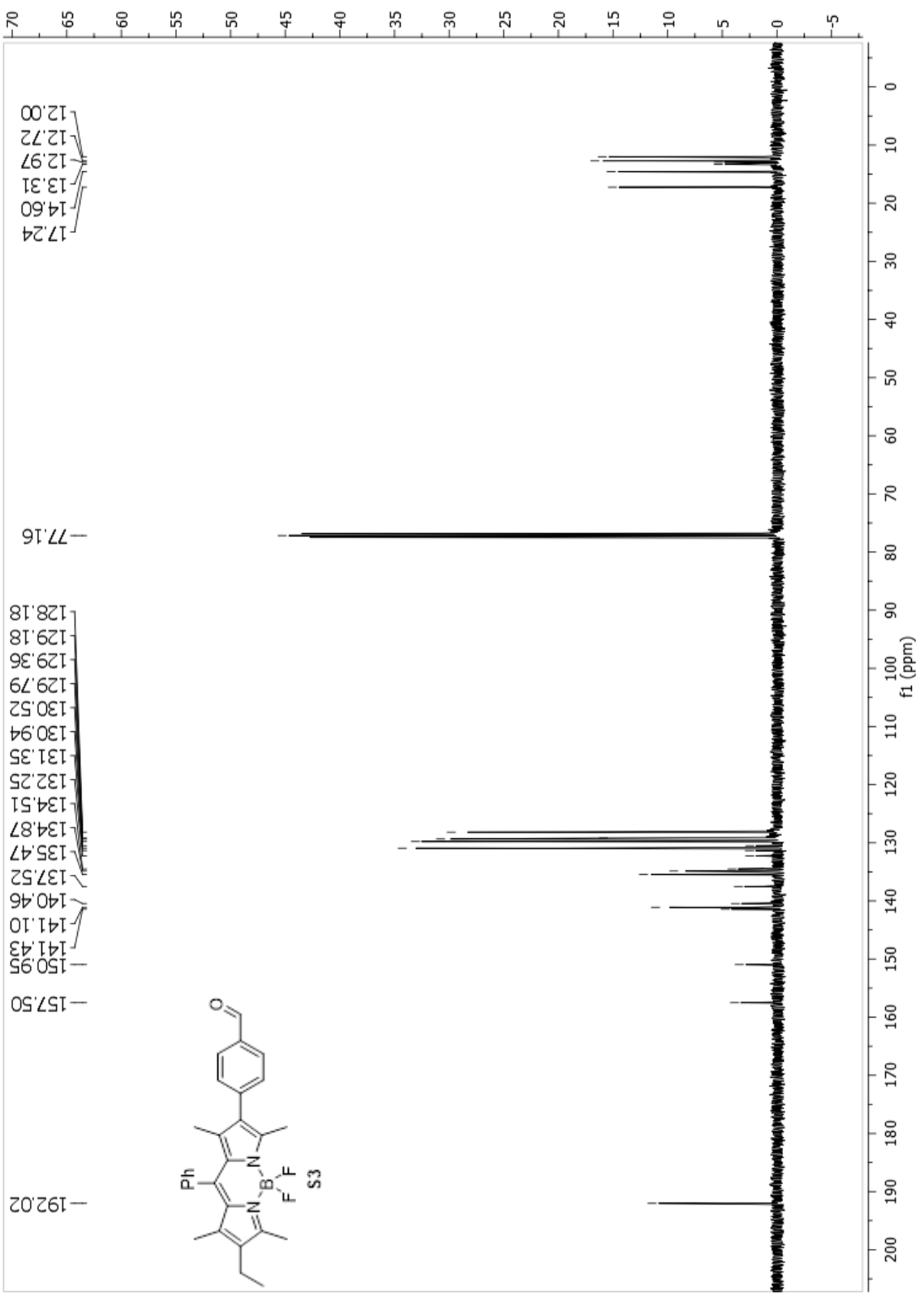
192.02
157.50
150.95
141.43
141.10
140.46
137.52
135.47
134.87
134.51
132.25
131.35
130.94
130.52
129.79
129.36
129.18
128.18
77.16
17.24
14.60
13.31
12.97
12.72
12.00
Ph
F
F
S3
f1 (ppm)

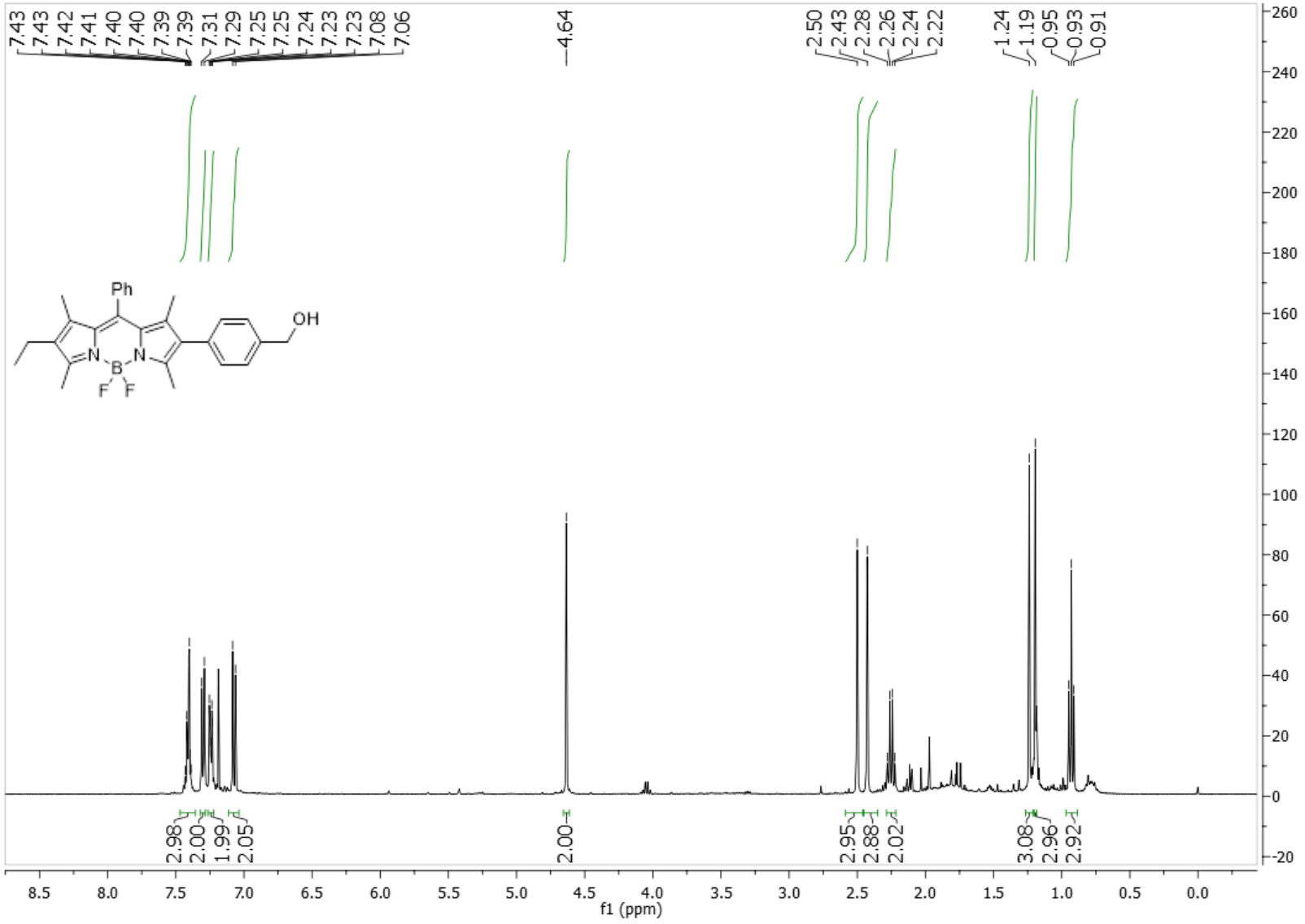
7.43
7.43
7.42
7.41
7.40
7.40
7.39
7.39
7.31
7.29
7.25
7.25
7.24
7.23
7.23
7.08
7.06
4.64
2.50
2.43
2.28
2.26
2.24
2.22
1.24
1.19
0.95
0.93
0.91
Ph
OH
N
B
N
F
F
2.98
2.00
1.99
2.05
2.00
2.95
2.88
2.02
3.08
2.96
2.92
f1 (ppm)

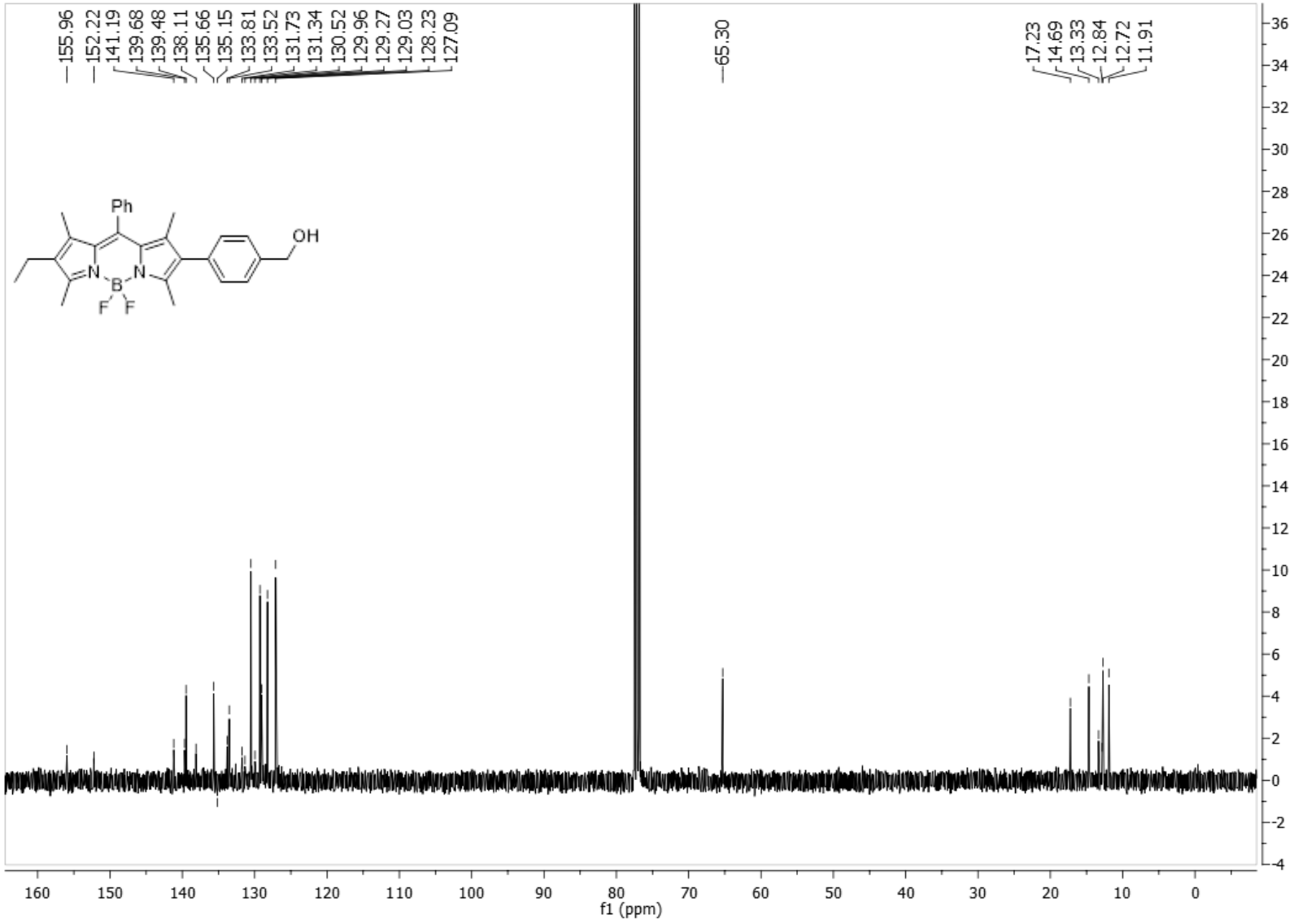
155.96
152.22
141.19
139.68
139.48
138.11
135.66
135.15
133.81
133.52
131.73
131.34
130.52
129.96
129.27
129.03
128.23
127.09
65.30
17.23
14.69
13.33
12.84
12.72
11.91
Ph
OH
N
B
N
F
F
160
150
140
130
120
110
100
90
80
70
60
50
40
30
20
10
0
f1 (ppm)
36
34
32
30
28
26
24
22
20
18
16
14
12
10
8
6
4
2
0
-2
-4

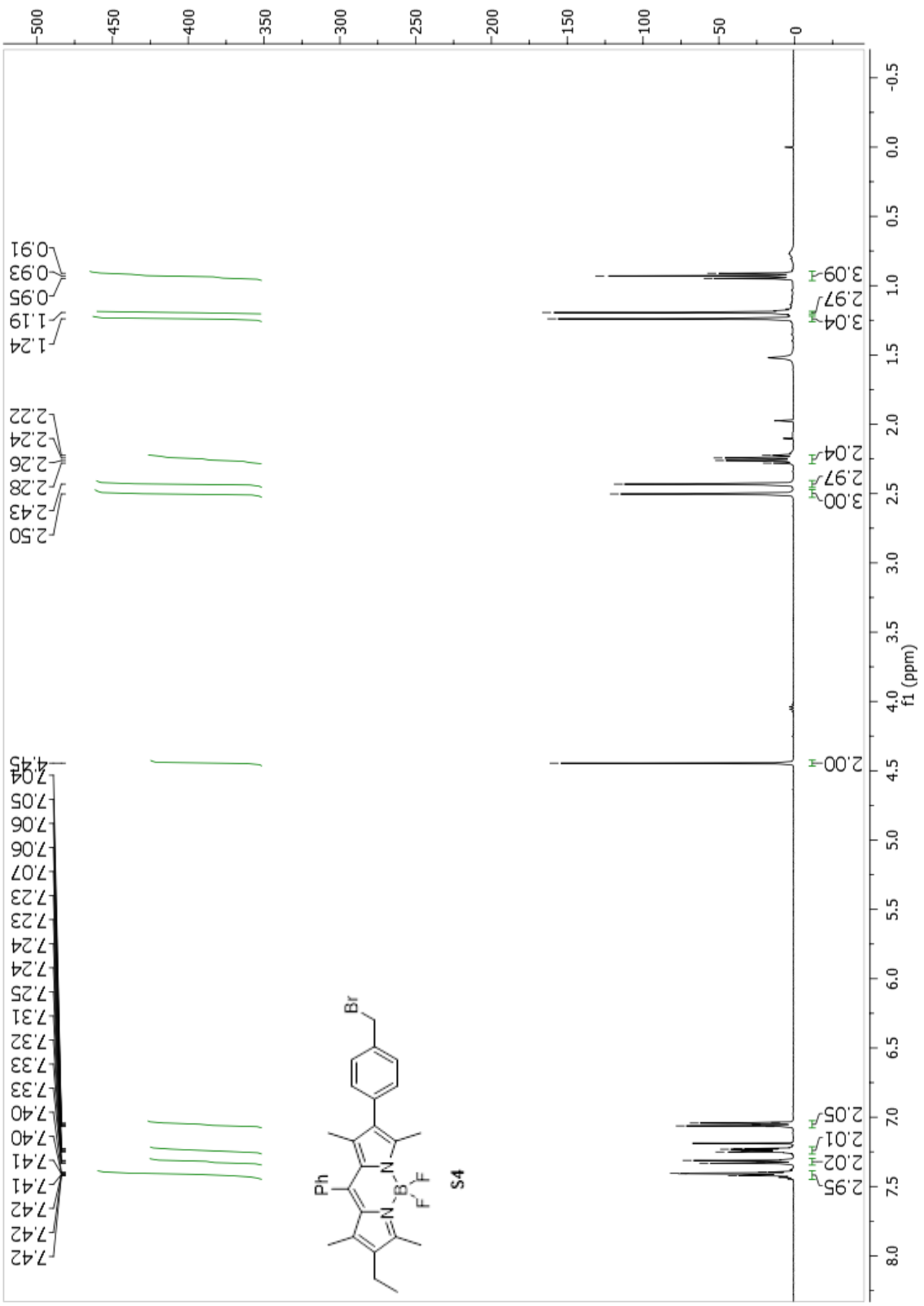
Br
Ph
N
B
F
F
S4
f1 (ppm)

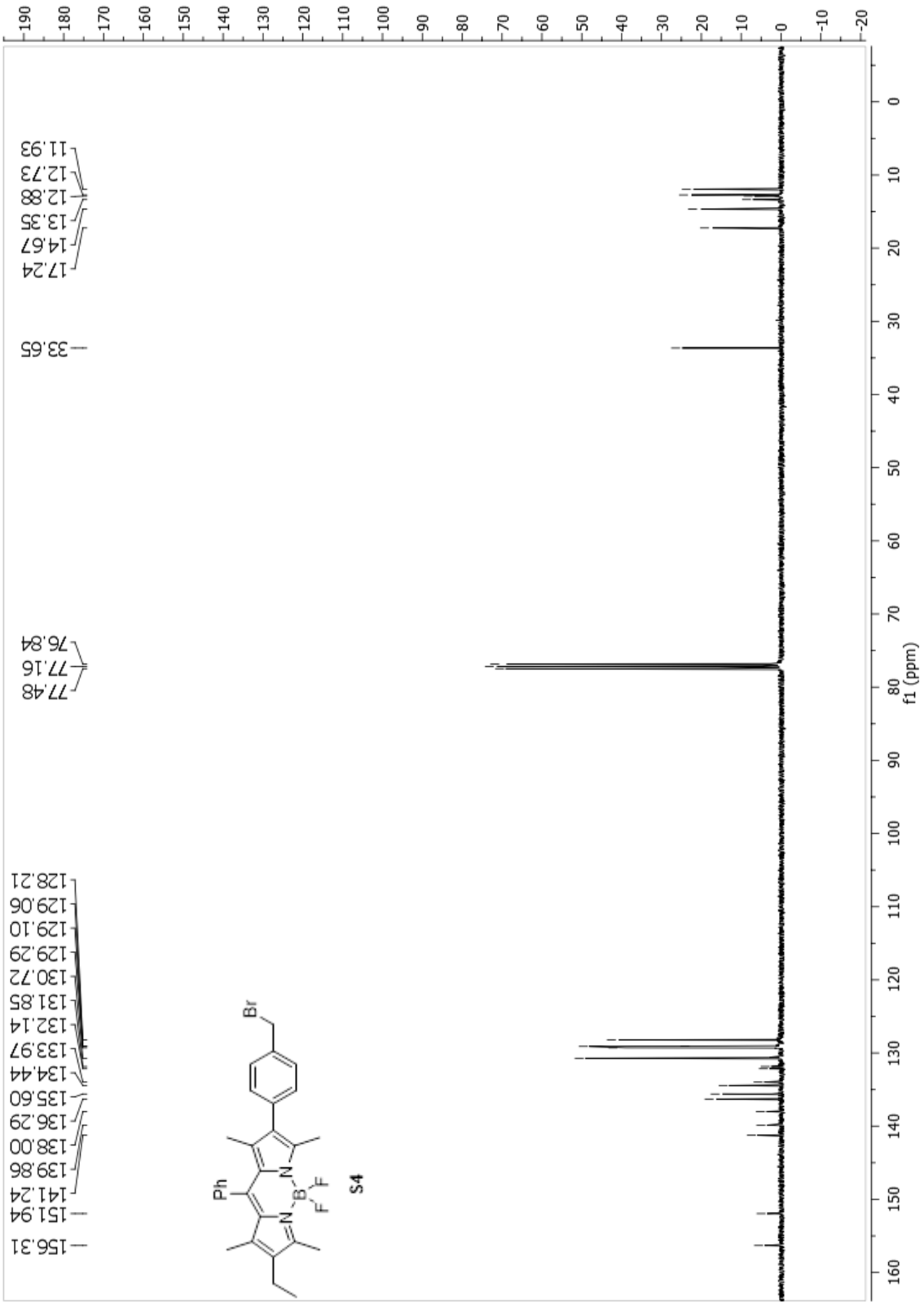
Br
Ph
N
B
F
F
S4
156.31
151.94
141.24
139.86
138.00
136.29
135.60
134.44
133.97
132.14
131.85
130.72
129.29
129.10
129.06
128.21
77.48
77.16
76.84
33.65
17.24
14.67
13.35
12.88
12.73
11.93
f1 (ppm)

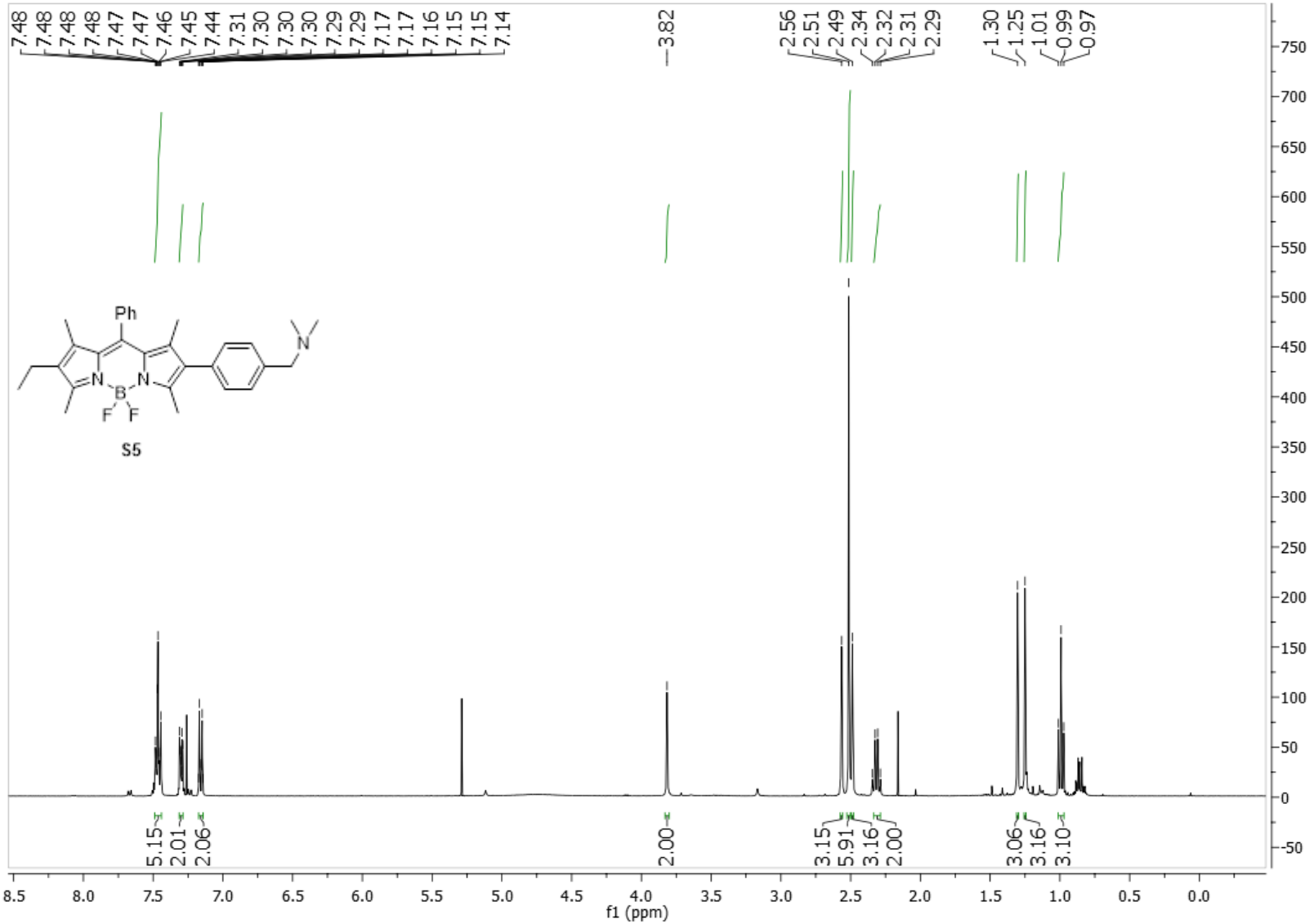
7.48
7.48
7.48
7.48
7.47
7.47
7.46
7.45
7.44
7.31
7.30
7.30
7.30
7.29
7.29
7.17
7.17
7.16
7.15
7.15
7.14
3.82
2.56
2.51
2.49
2.34
2.32
2.31
2.29
1.30
1.25
1.01
0.99
0.97
Ph
N
N
B
F
F
N
S5
5.15
2.01
2.06
2.00
3.15
5.91
3.16
2.00
3.06
3.16
3.10
f1 (ppm)

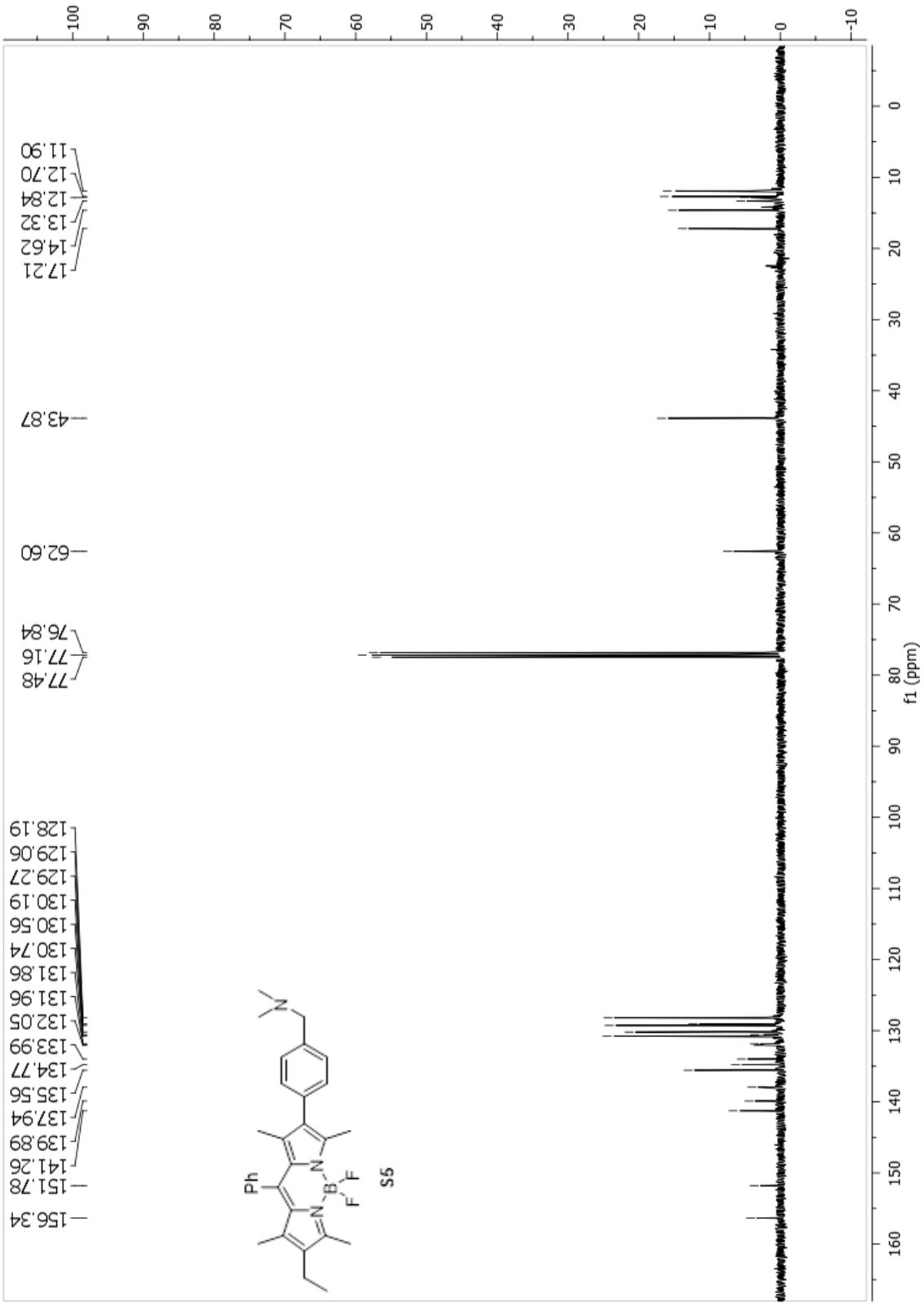
156.34
151.78
141.26
139.89
137.94
135.56
134.77
133.99
132.05
131.96
131.86
130.74
130.56
130.19
129.27
129.06
128.19
77.48
77.16
76.84
62.60
43.87
17.21
14.62
13.32
12.84
12.70
11.90
Ph
S5
f1 (ppm)

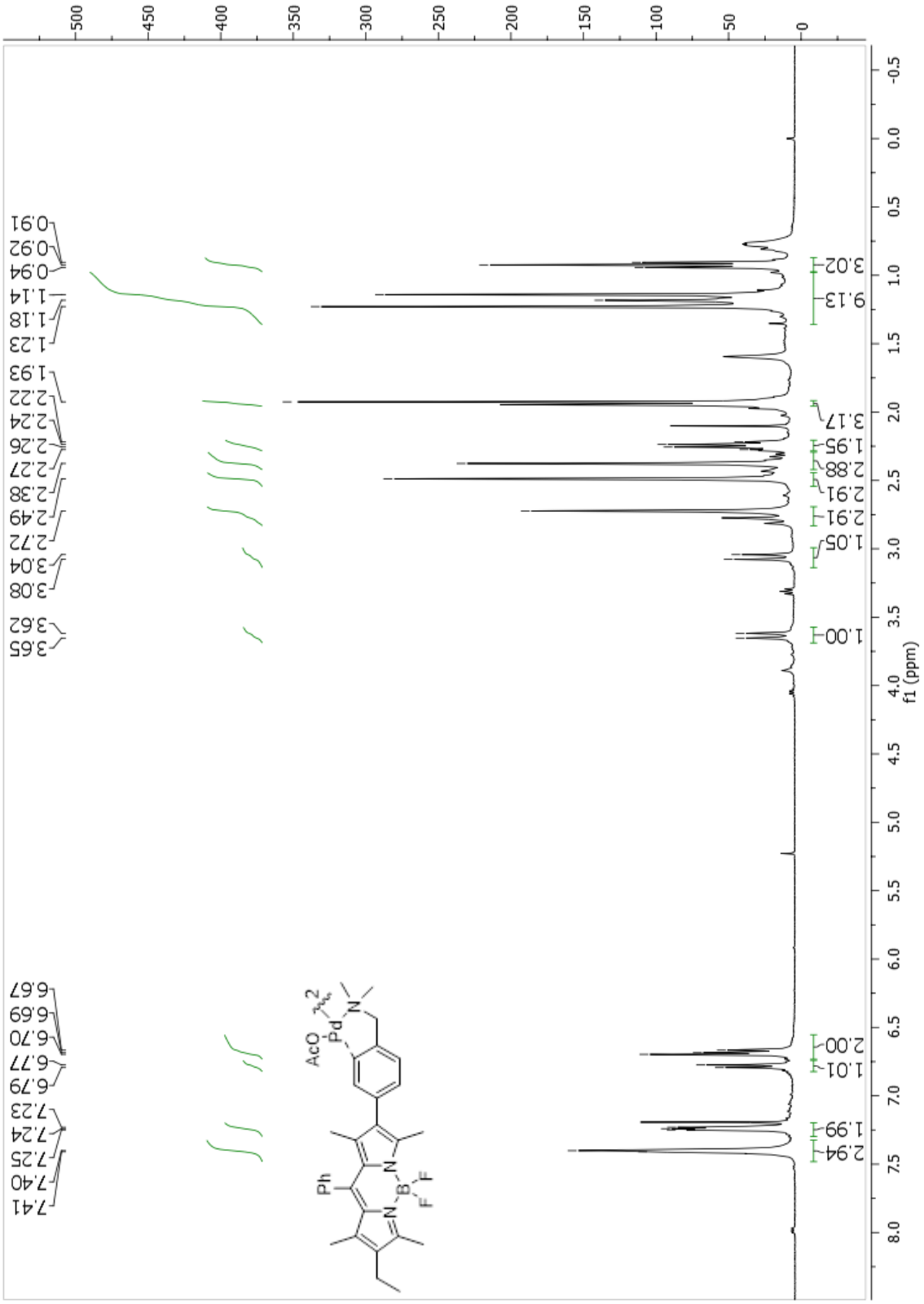
f1 (ppm)
AcO
Pd
Ph
B
F
F
N
N
N
0.91
0.92
0.94
1.14
1.18
1.23
1.93
2.22
2.24
2.26
2.27
2.38
2.49
2.72
3.04
3.08
3.62
3.65
6.67
6.69
6.70
6.77
6.79
7.23
7.24
7.25
7.40
7.41
3.02
9.13
3.17
1.95
2.88
2.91
2.91
1.05
1.00
2.00
1.01
1.99
2.94

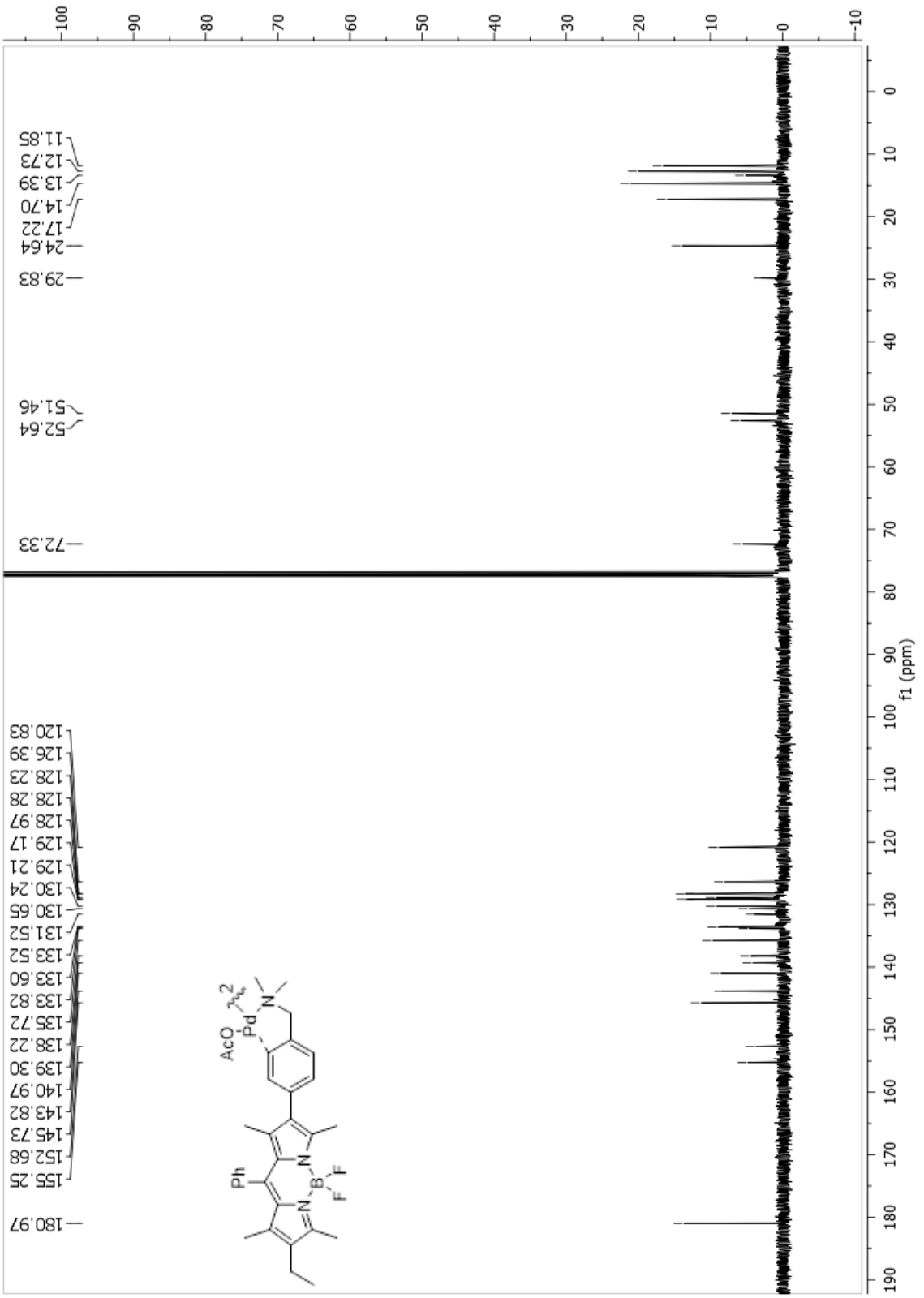
180.97
155.25
152.68
145.73
143.82
140.97
139.30
138.22
135.72
133.82
133.60
133.52
131.52
130.65
130.24
129.21
129.17
128.97
128.28
128.23
126.39
120.83
72.33
52.64
51.46
29.83
24.64
17.22
14.70
13.39
12.73
11.85
f1 (ppm)

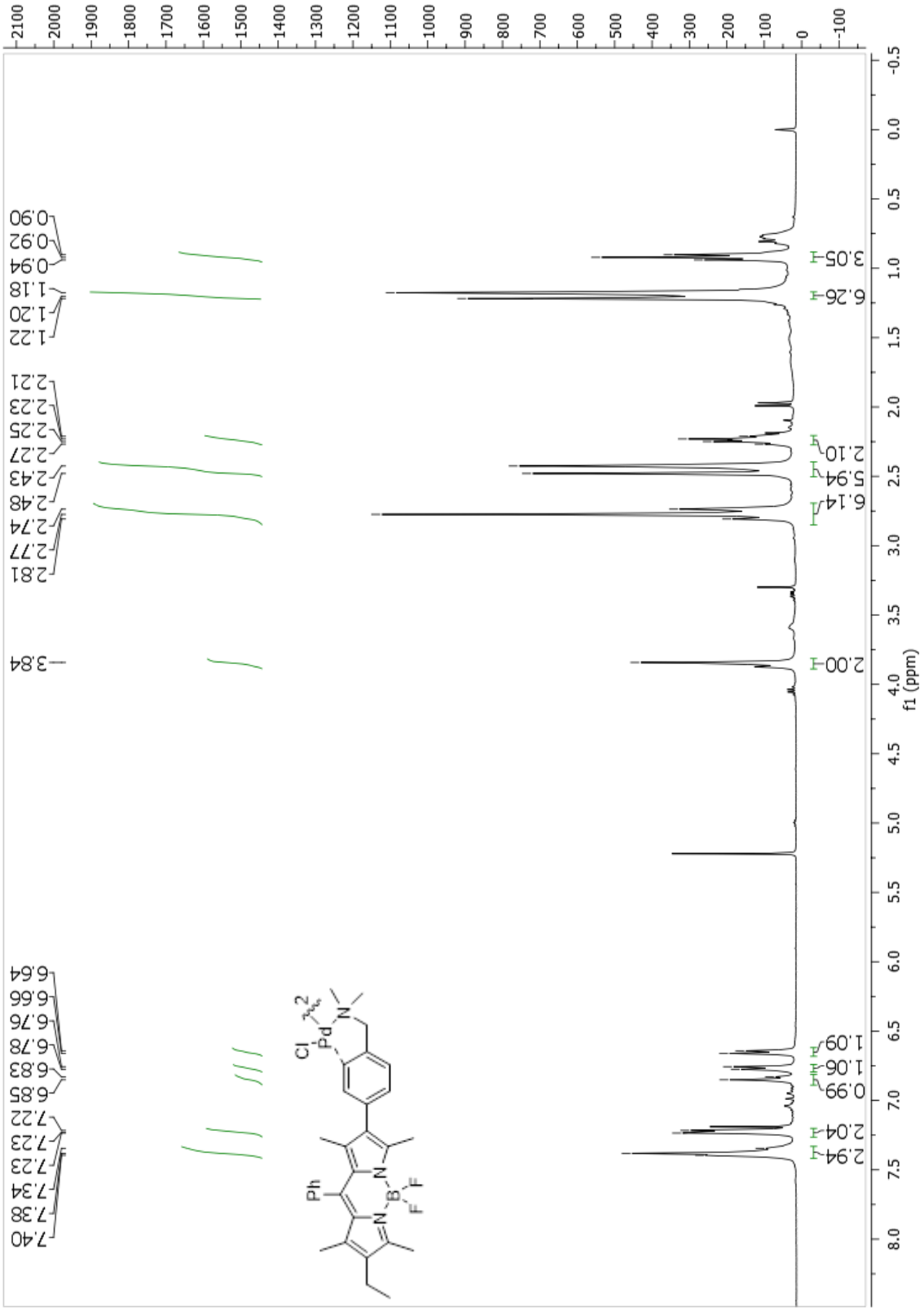
7.40
7.38
7.34
7.23
7.23
7.22
6.85
6.83
6.78
6.76
6.66
6.64
3.84
2.81
2.77
2.74
2.48
2.43
2.27
2.25
2.23
2.21
1.22
1.20
1.18
0.94
0.92
0.90
2.94
2.04
0.99
1.06
1.09
2.00
6.14
5.94
2.10
6.26
3.05
f1 (ppm)

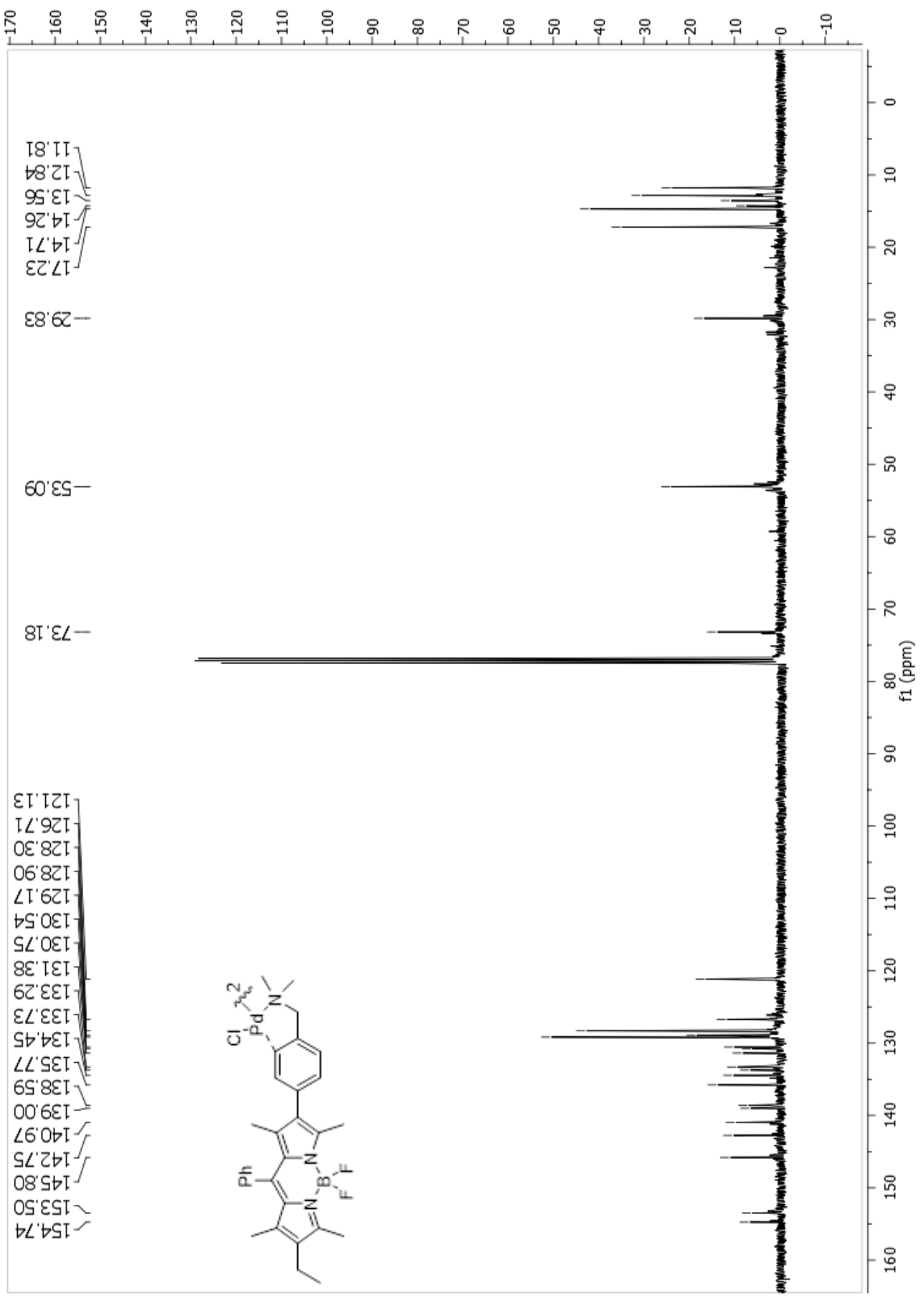
11.81
12.84
13.56
14.26
14.71
17.23
29.83
53.09
73.18
121.13
126.71
128.30
128.90
129.17
130.54
130.75
131.38
133.29
133.73
134.45
135.77
138.59
139.00
140.97
142.75
145.80
153.50
154.74
Cl
Pd
N
Ph
N
B
F
F
f1 (ppm)

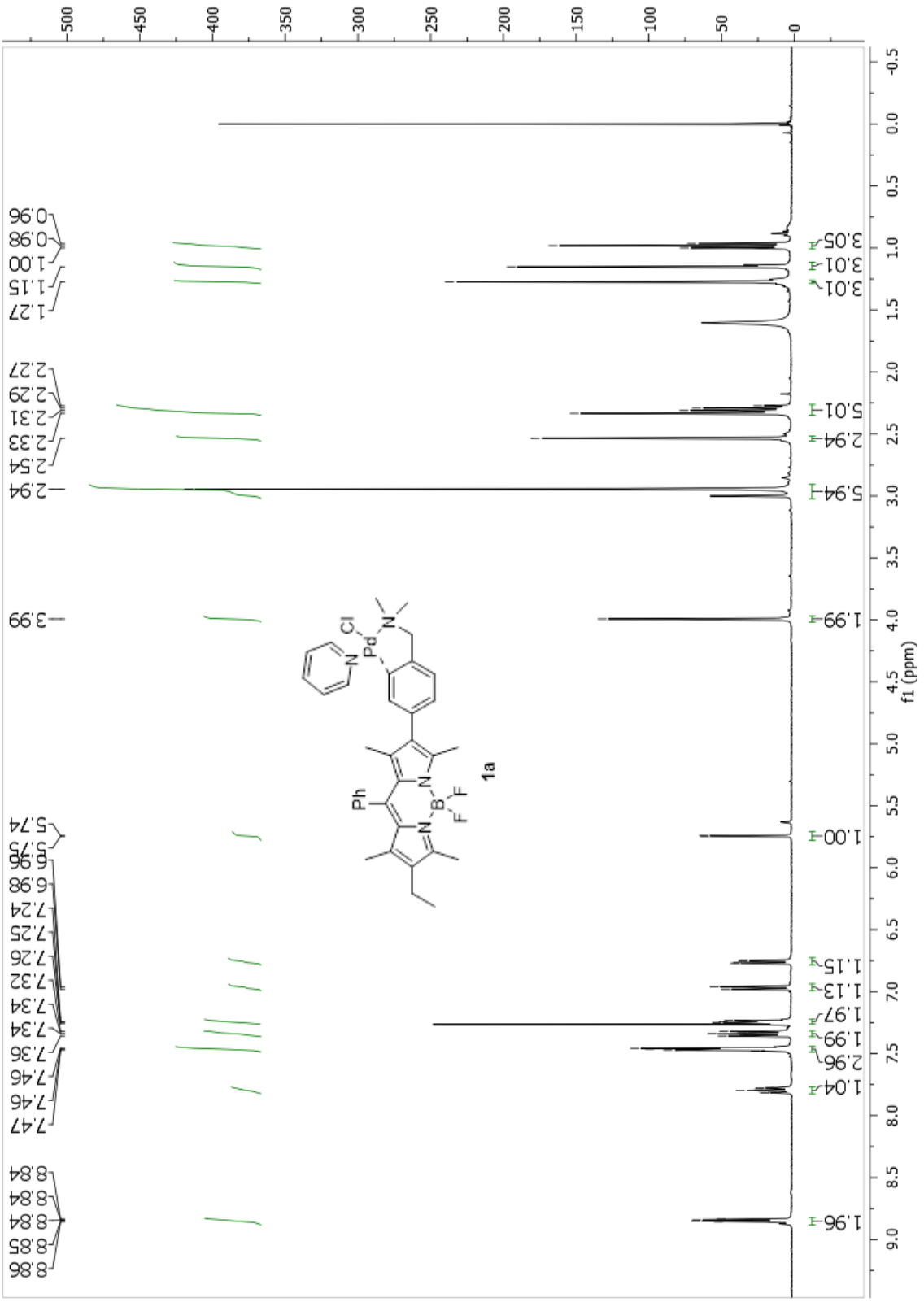
8.86
8.85
8.84
8.84
8.84
7.47
7.46
7.46
7.36
7.34
7.34
7.32
7.26
7.25
7.24
6.98
6.96
5.75
5.74
3.99
2.94
2.54
2.33
2.31
2.29
2.27
1.27
1.15
1.00
0.98
0.96
1.96
1.04
2.96
1.99
1.97
1.13
1.15
1.00
1.99
5.94
2.94
5.01
3.01
3.01
3.05
f1 (ppm)
Ph
Cl
Pd
N
B
F
F
1a

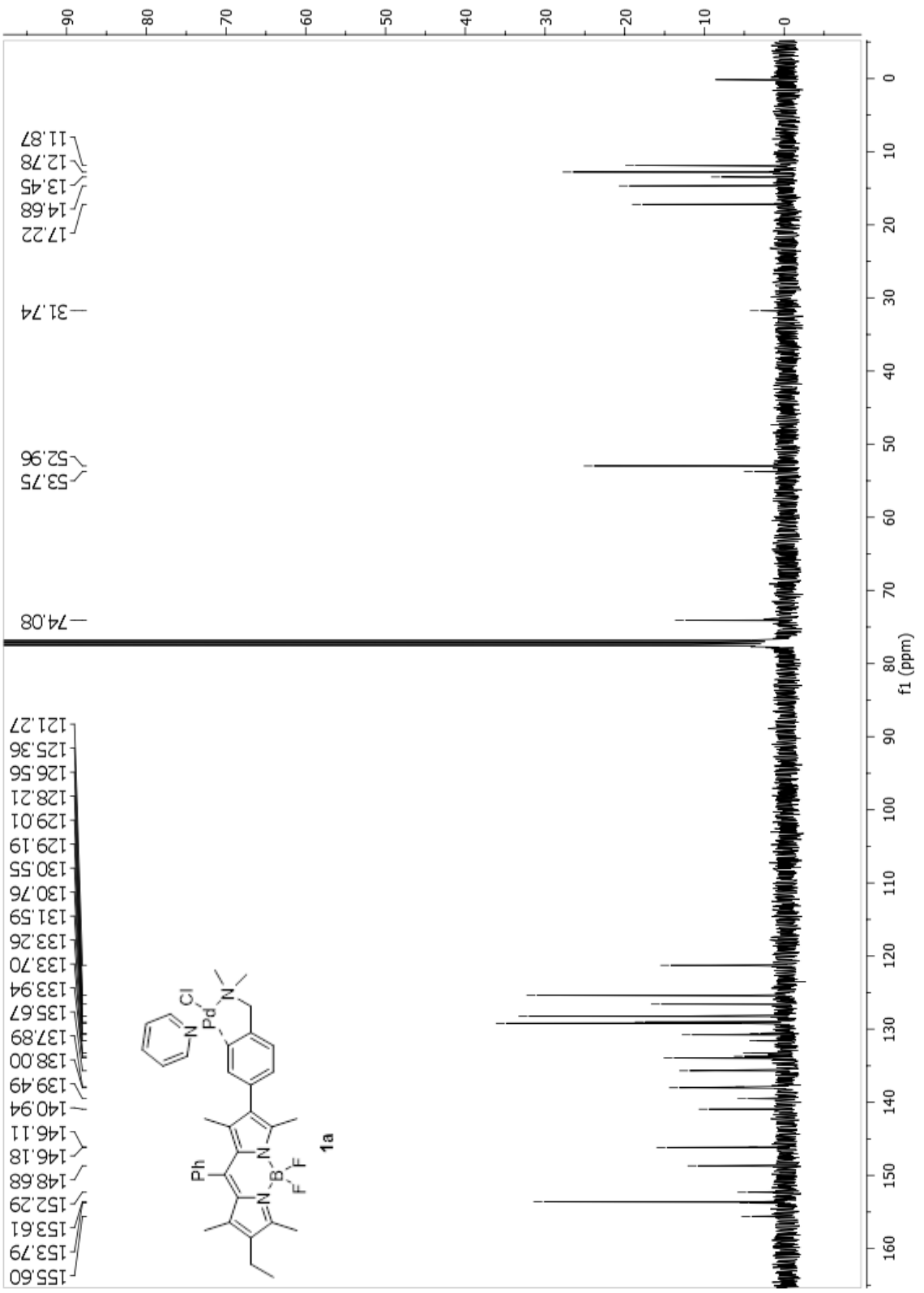
155.60
153.79
153.61
152.29
148.68
146.18
146.11
140.94
139.49
138.00
137.89
135.67
133.94
133.70
133.26
131.59
130.76
130.55
129.19
129.01
128.21
126.56
125.36
121.27
74.08
53.75
52.96
31.74
17.22
14.68
13.45
12.78
11.87
Ph
Cl
Pd
N
B
F
F
1a
f1 (ppm)

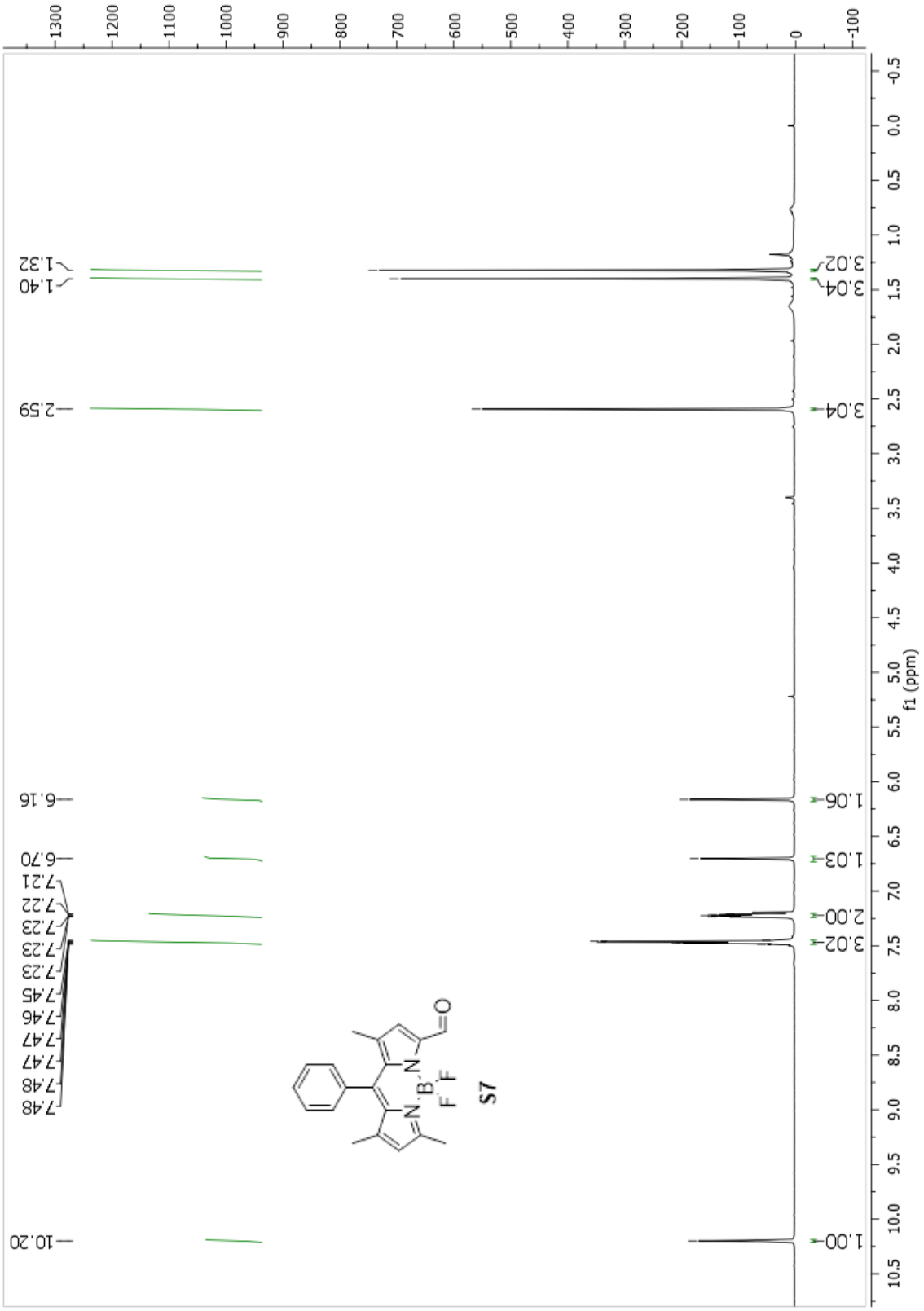
10.20
7.48
7.48
7.47
7.47
7.46
7.45
7.23
7.23
7.22
7.21
6.70
6.16
2.59
1.40
1.32
1.00
3.02
2.00
1.03
1.06
3.04
3.04
3.02
S7
f1 (ppm)

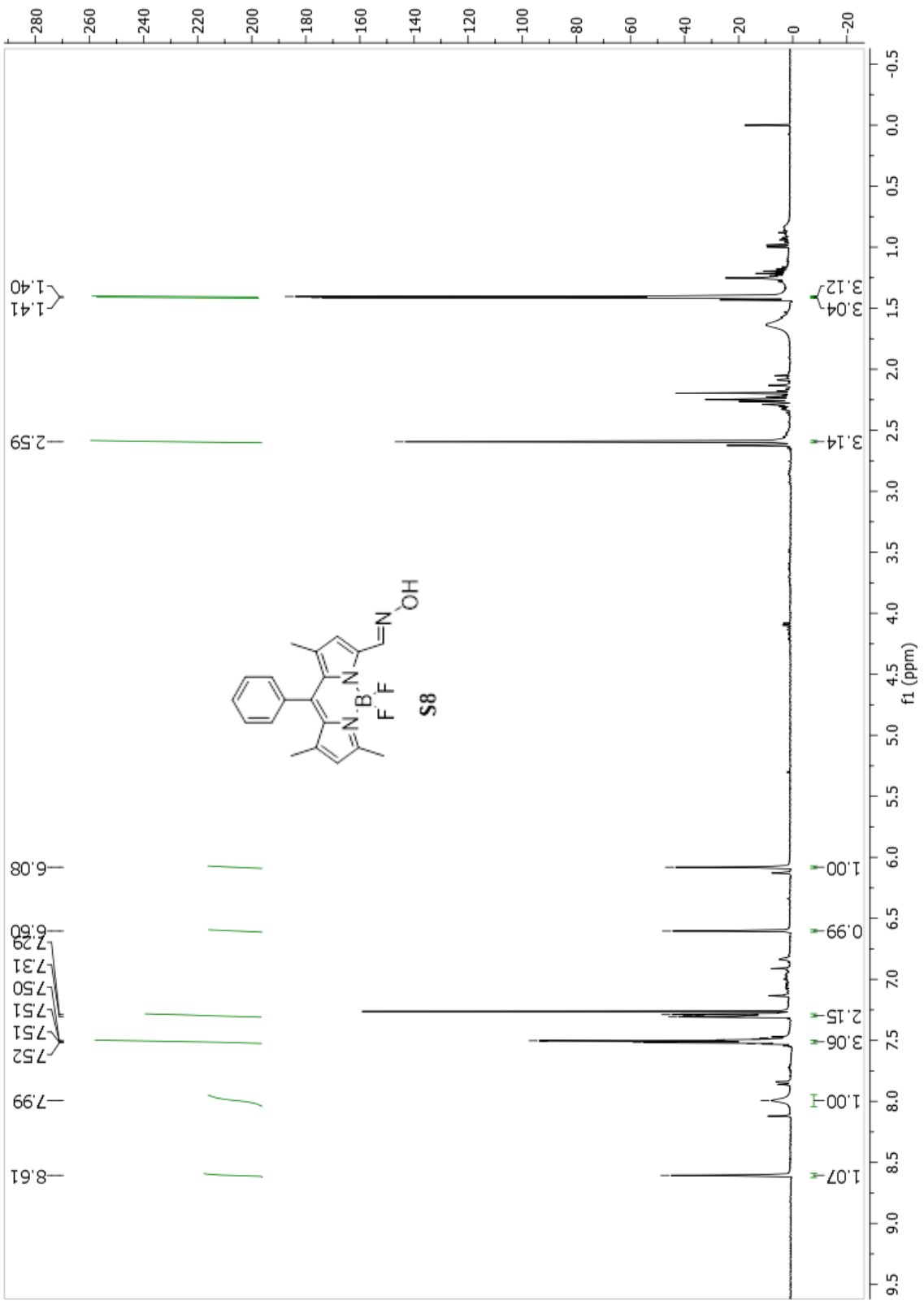
S8
f1 (ppm)

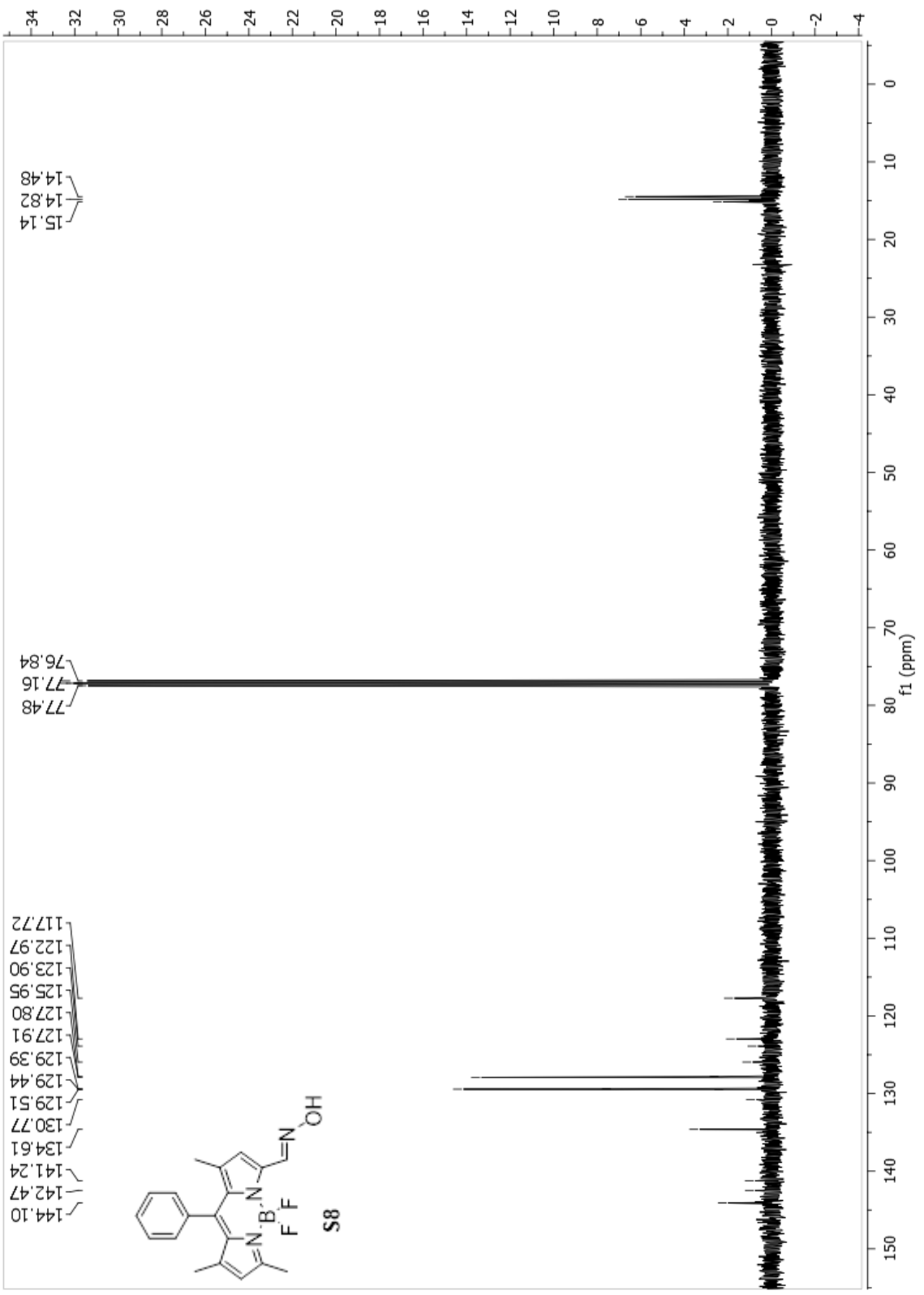
144.10
142.47
141.24
134.61
130.77
129.51
129.44
129.39
127.91
127.80
125.95
123.90
122.97
117.72
77.48
77.16
76.84
15.14
14.82
14.48
f1 (ppm)
S8

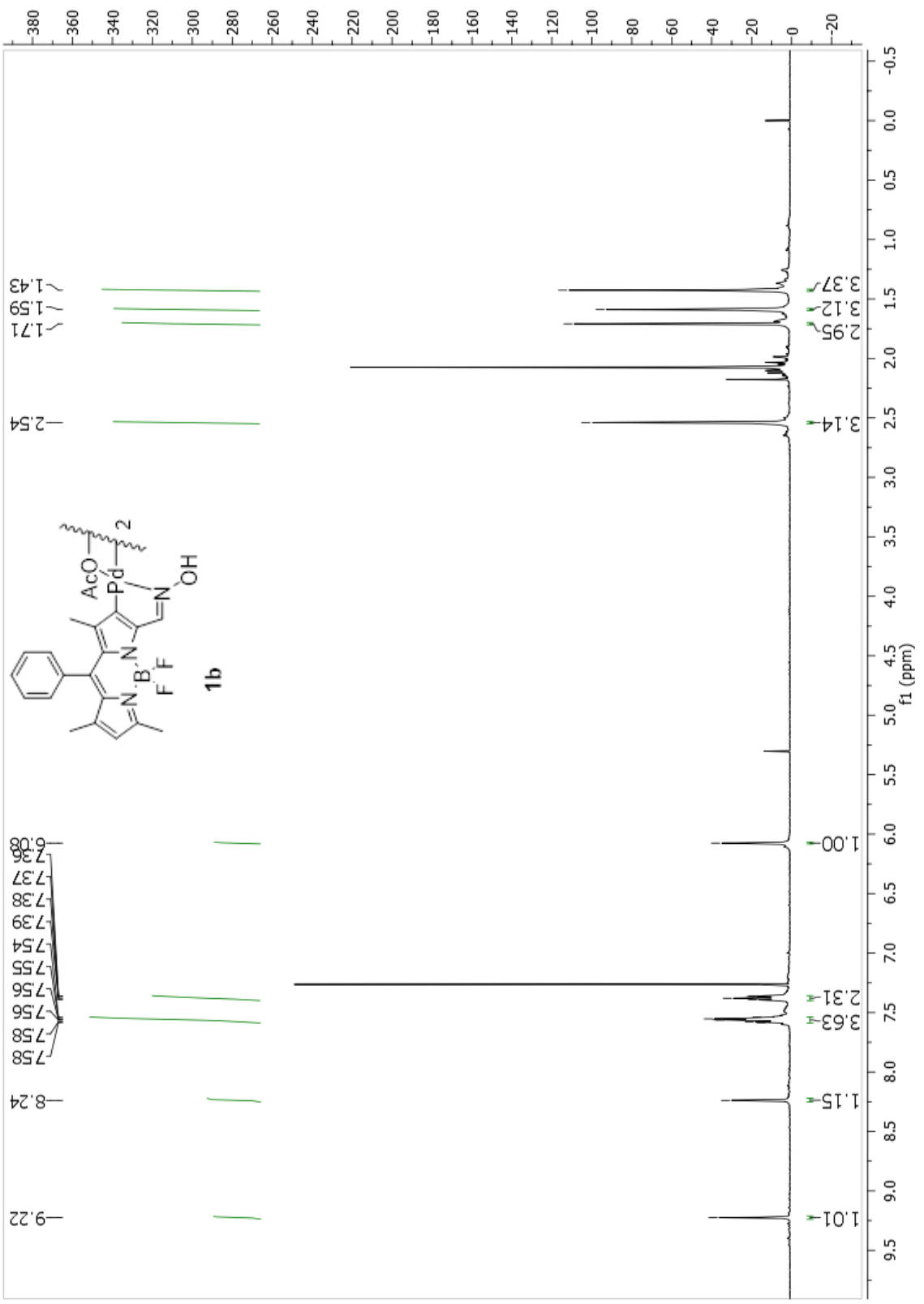
1b
AcO
Pd
2
N
B
F
F
OH
9.22
8.24
7.58
7.58
7.56
7.56
7.55
7.54
7.39
7.38
7.37
7.36
6.08
2.54
1.71
1.59
1.43
1.01
1.15
3.63
2.31
1.00
3.14
2.95
3.12
3.37
f1 (ppm)

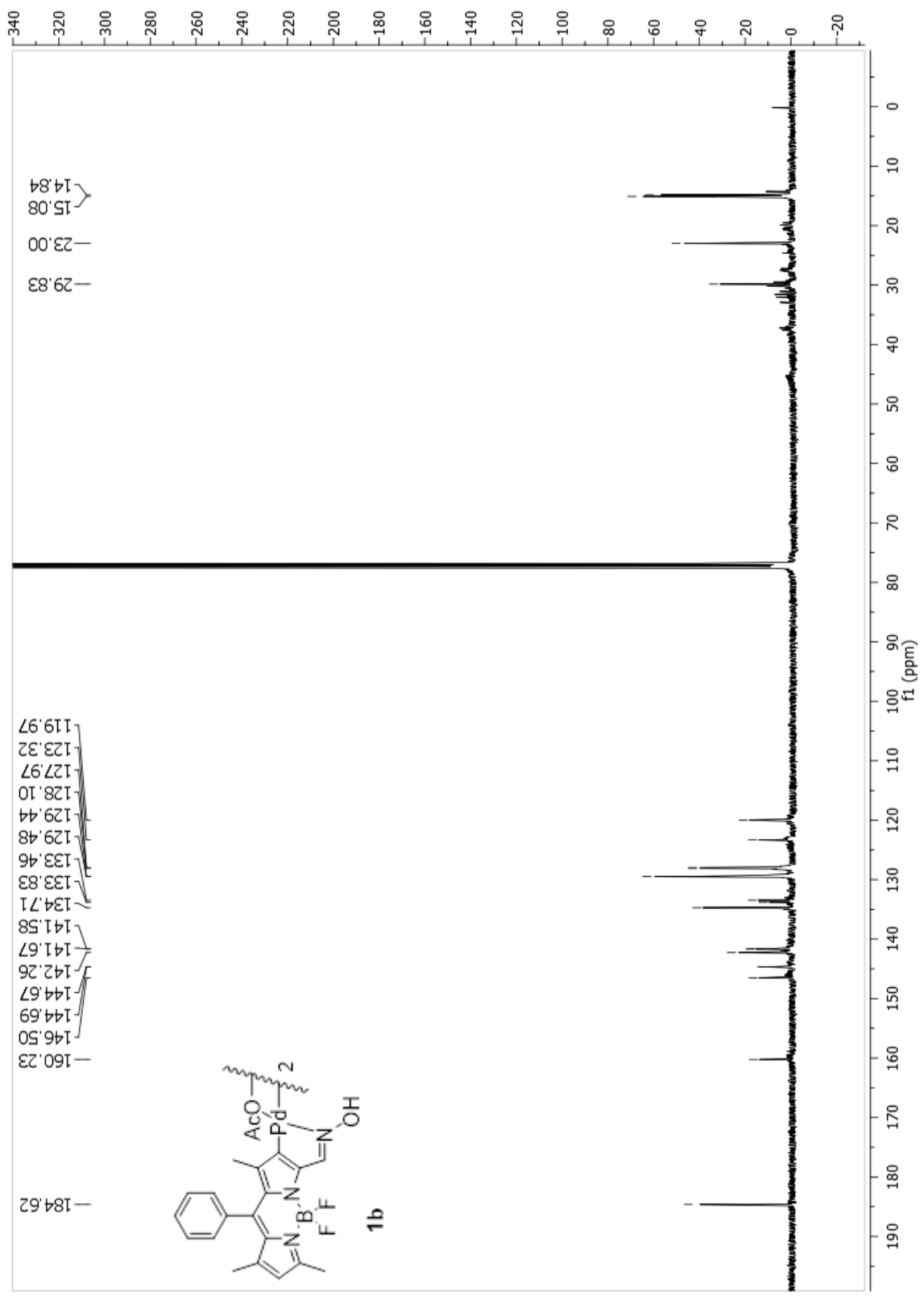
184.62
160.23
146.50
144.69
144.67
142.26
141.67
141.58
134.71
133.83
133.46
129.48
129.44
128.10
127.97
123.32
119.97
29.83
23.00
15.08
14.84
f1 (ppm)
1b

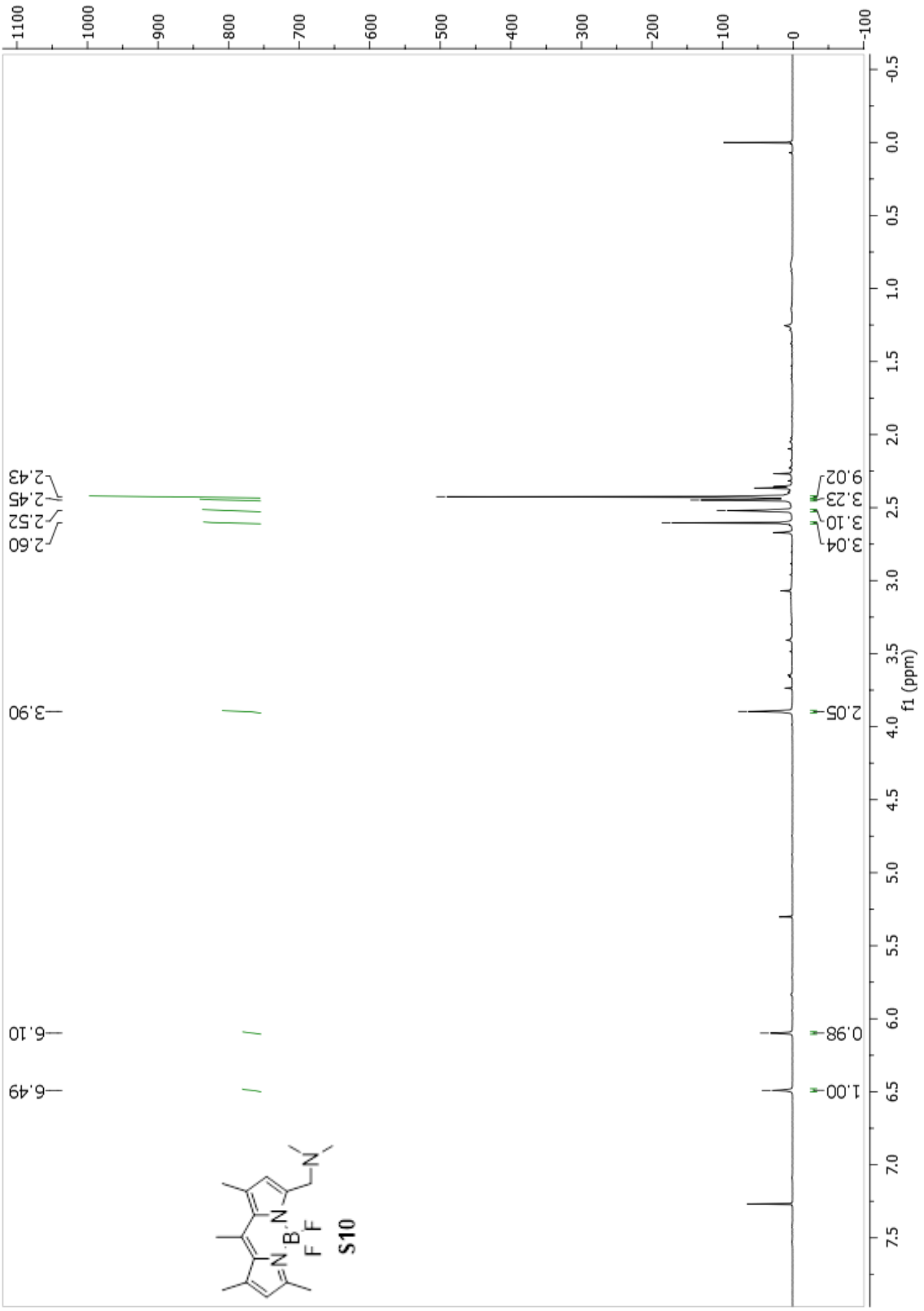
S10
f1 (ppm)
9.02
3.23
3.10
3.04
2.05
1.00
0.98
2.60
2.52
2.45
2.43
3.90
6.49
6.10

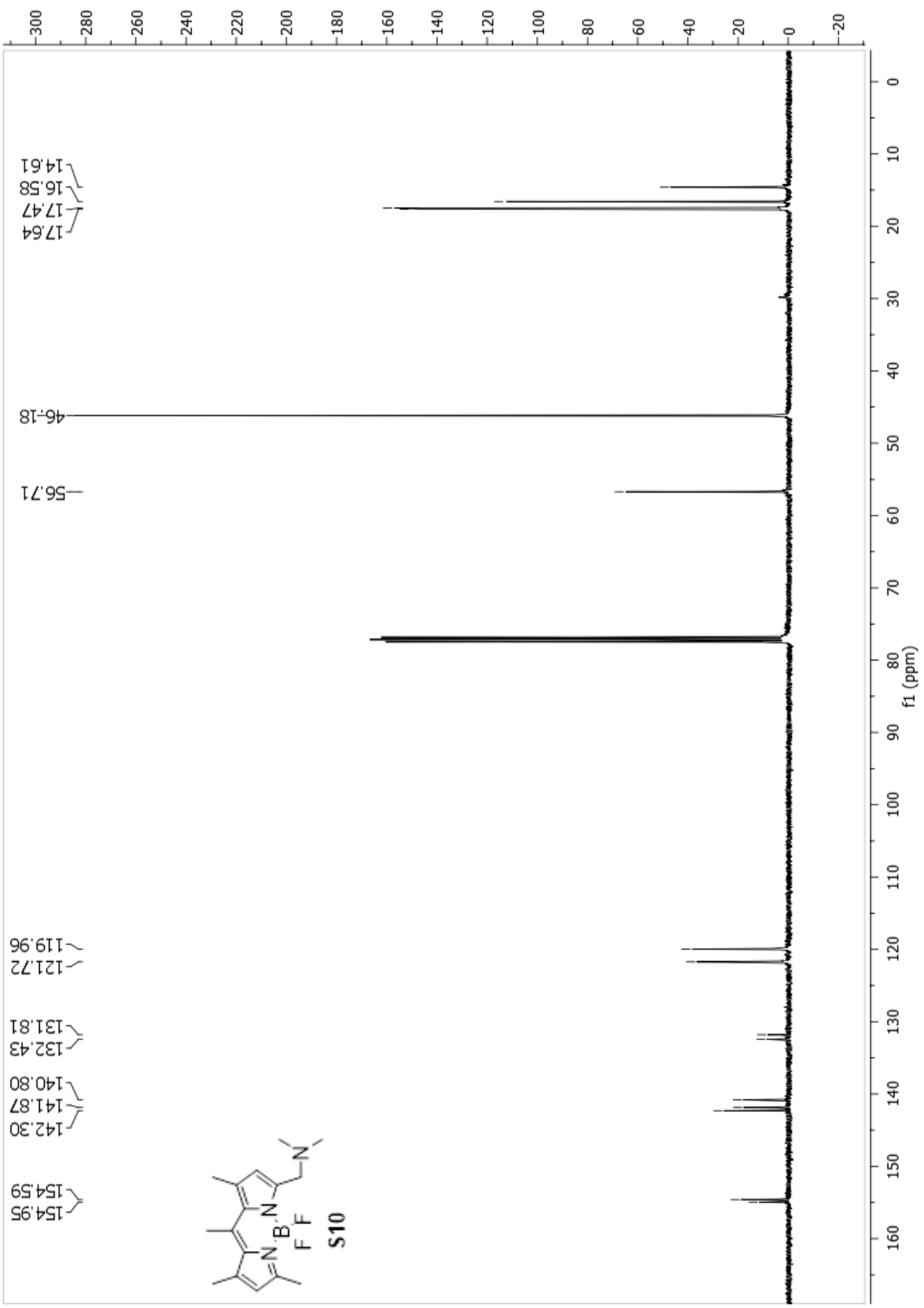
154.95
154.59
142.30
141.87
140.80
132.43
131.81
121.72
119.96
56.71
46.18
17.64
17.47
16.58
14.61
S10
f1 (ppm)

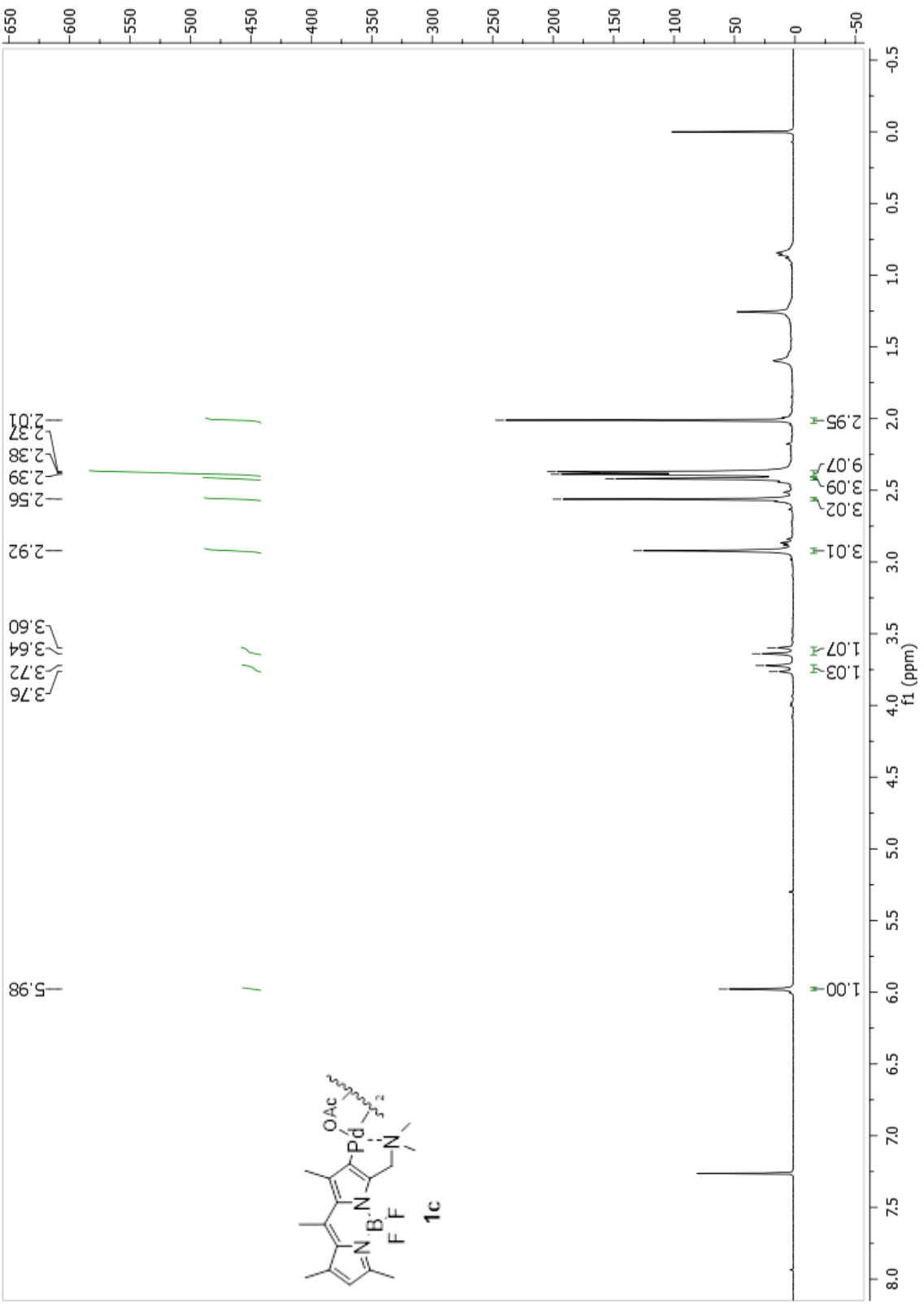
1c
OAc
Pd
N
B
F
F
5.98
3.76
3.72
3.64
3.60
2.92
2.56
2.39
2.38
2.37
2.01
1.00
1.07
1.03
3.01
3.02
3.09
9.07
2.95
f1 (ppm)

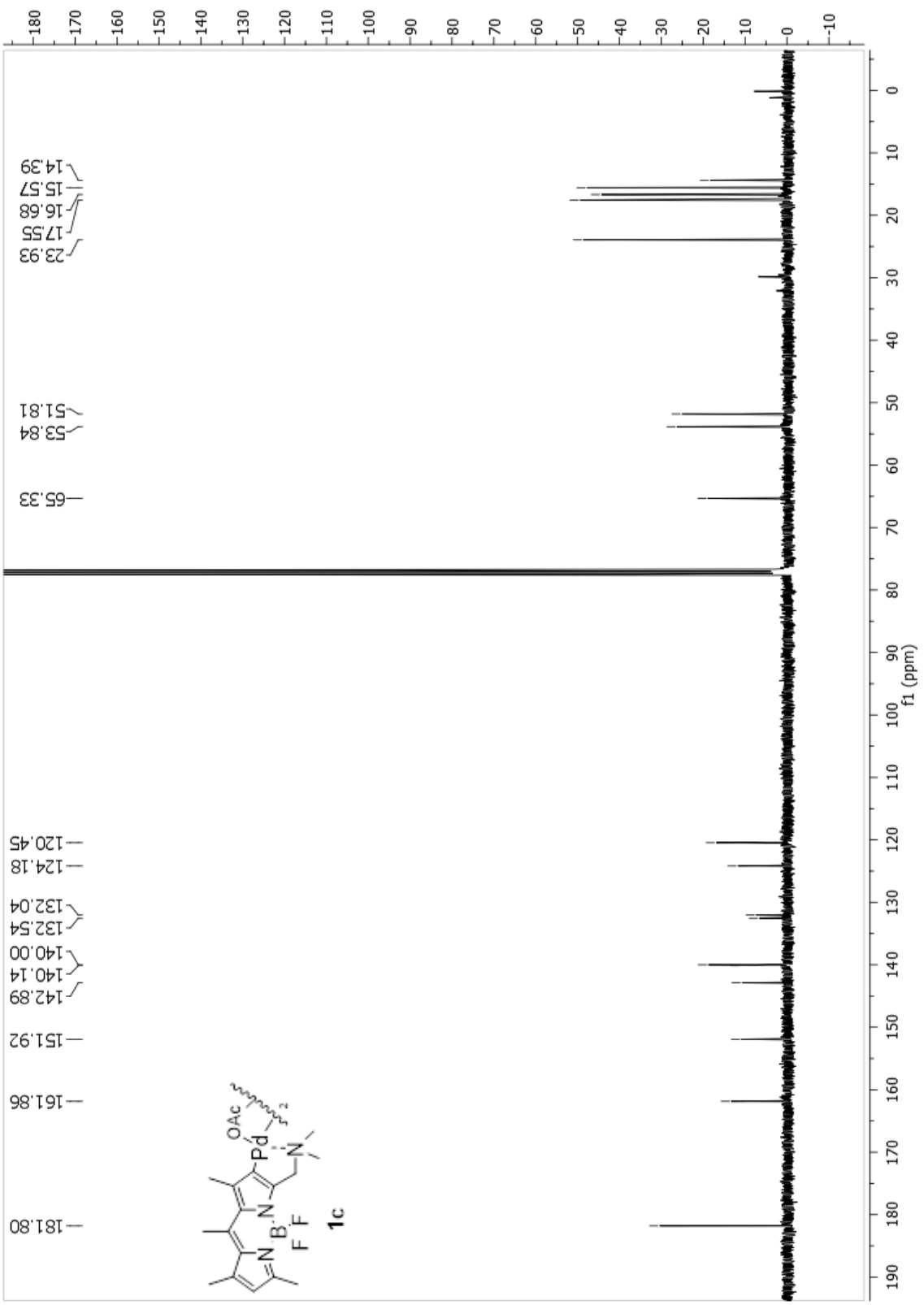
14.39
15.57
16.68
17.55
23.93
51.81
53.84
65.33
120.45
124.18
132.04
132.54
140.00
140.14
142.89
151.92
161.86
181.80
f1 (ppm)
1c

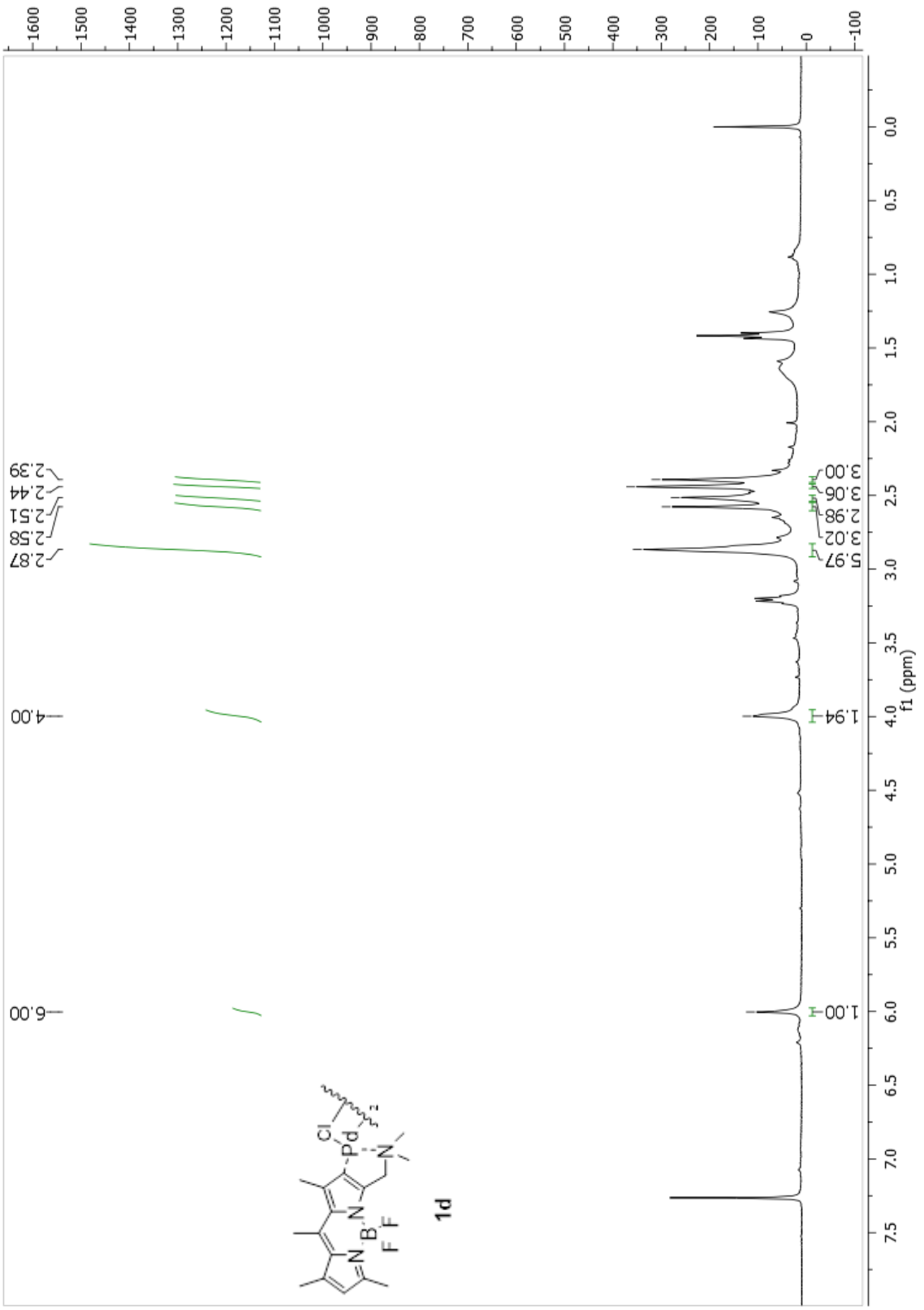
1d
6.00
4.00
1.94
1.00
2.87
2.58
2.51
2.44
2.39
5.97
3.02
2.98
3.06
3.00
f1 (ppm)

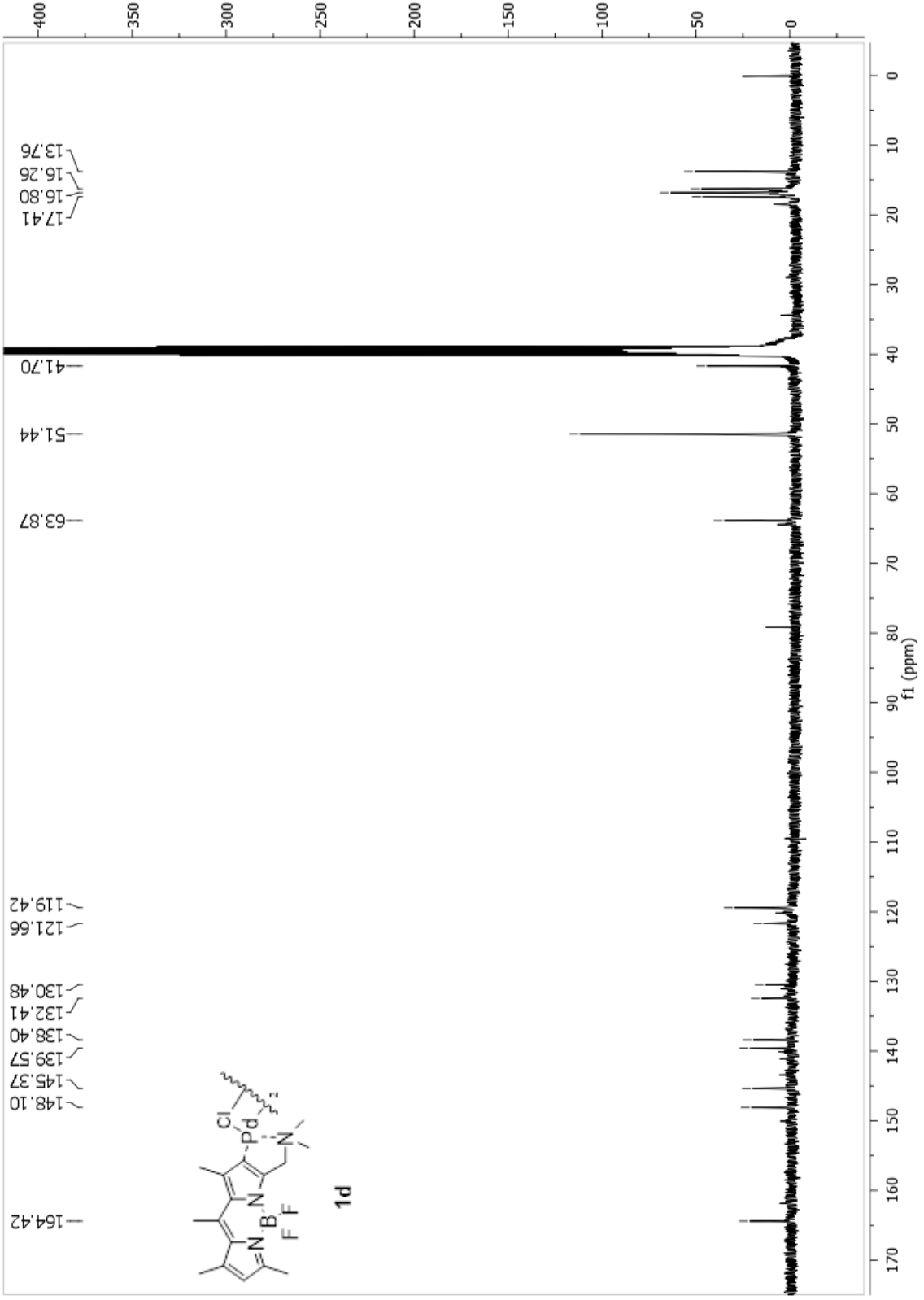
17.41
16.80
16.26
13.76
41.70
51.44
63.87
119.42
121.66
130.48
132.41
138.40
139.57
145.37
148.10
164.42
1d
f1 (ppm)

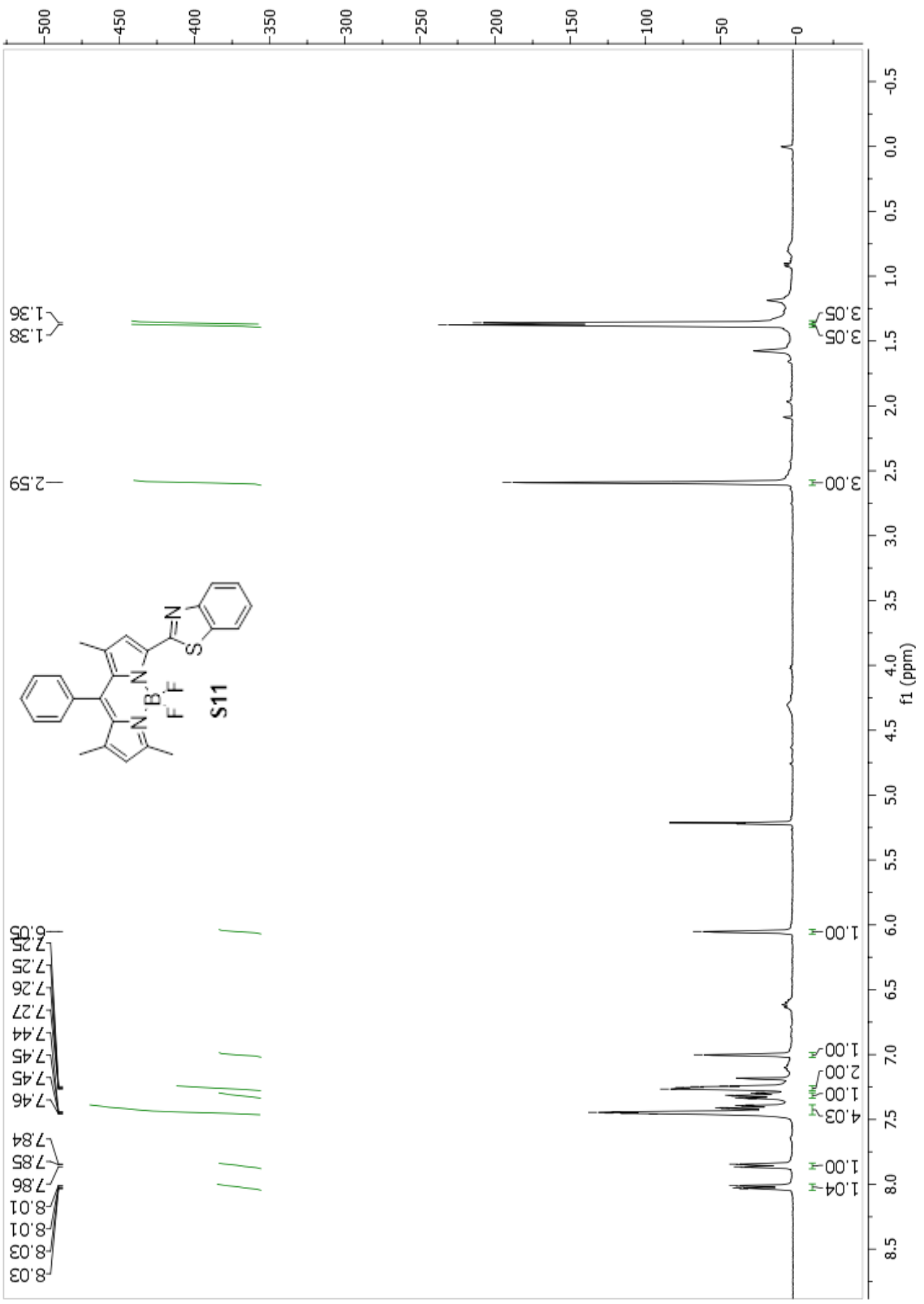
S11
f1 (ppm)

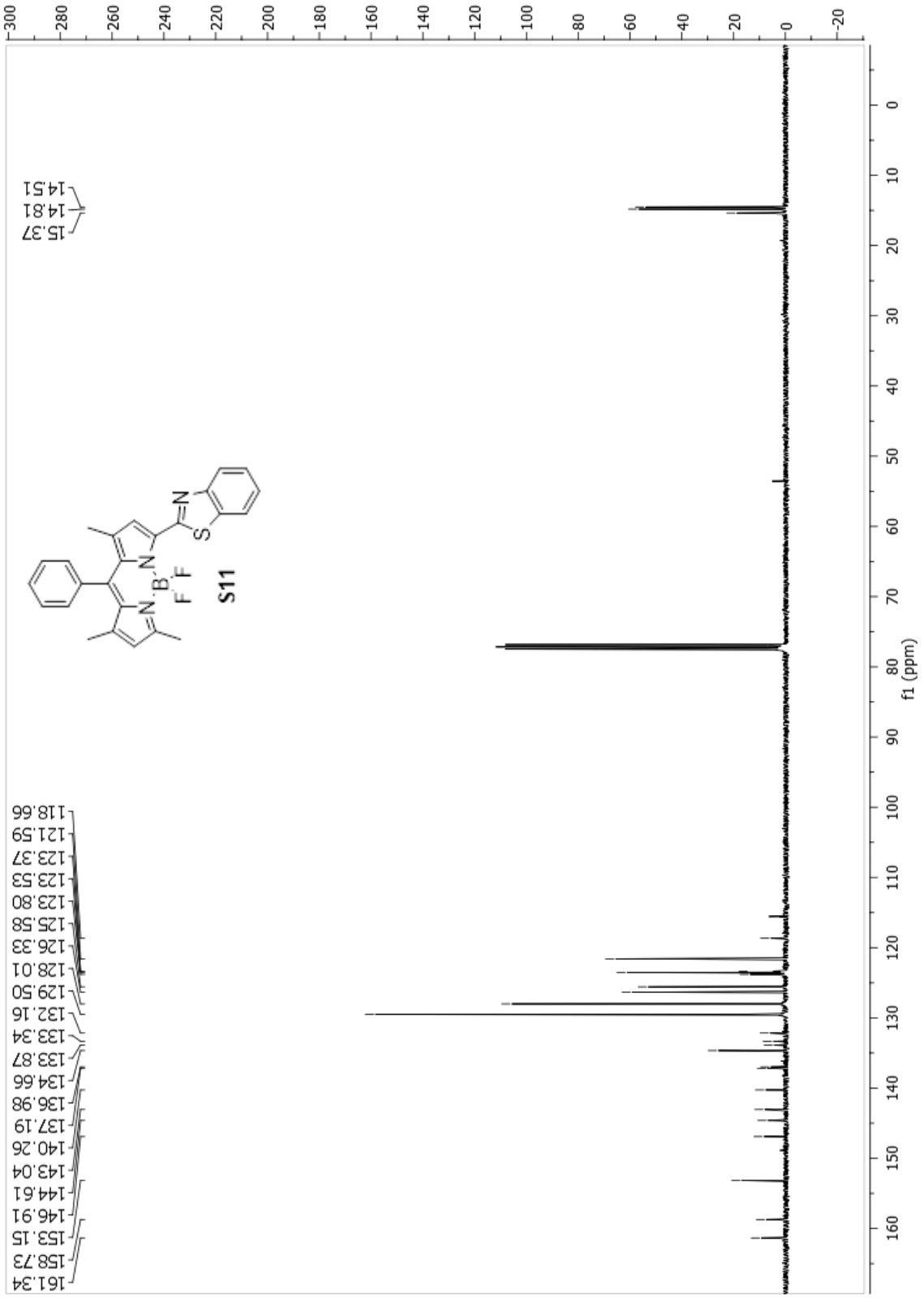
S11
f1 (ppm)

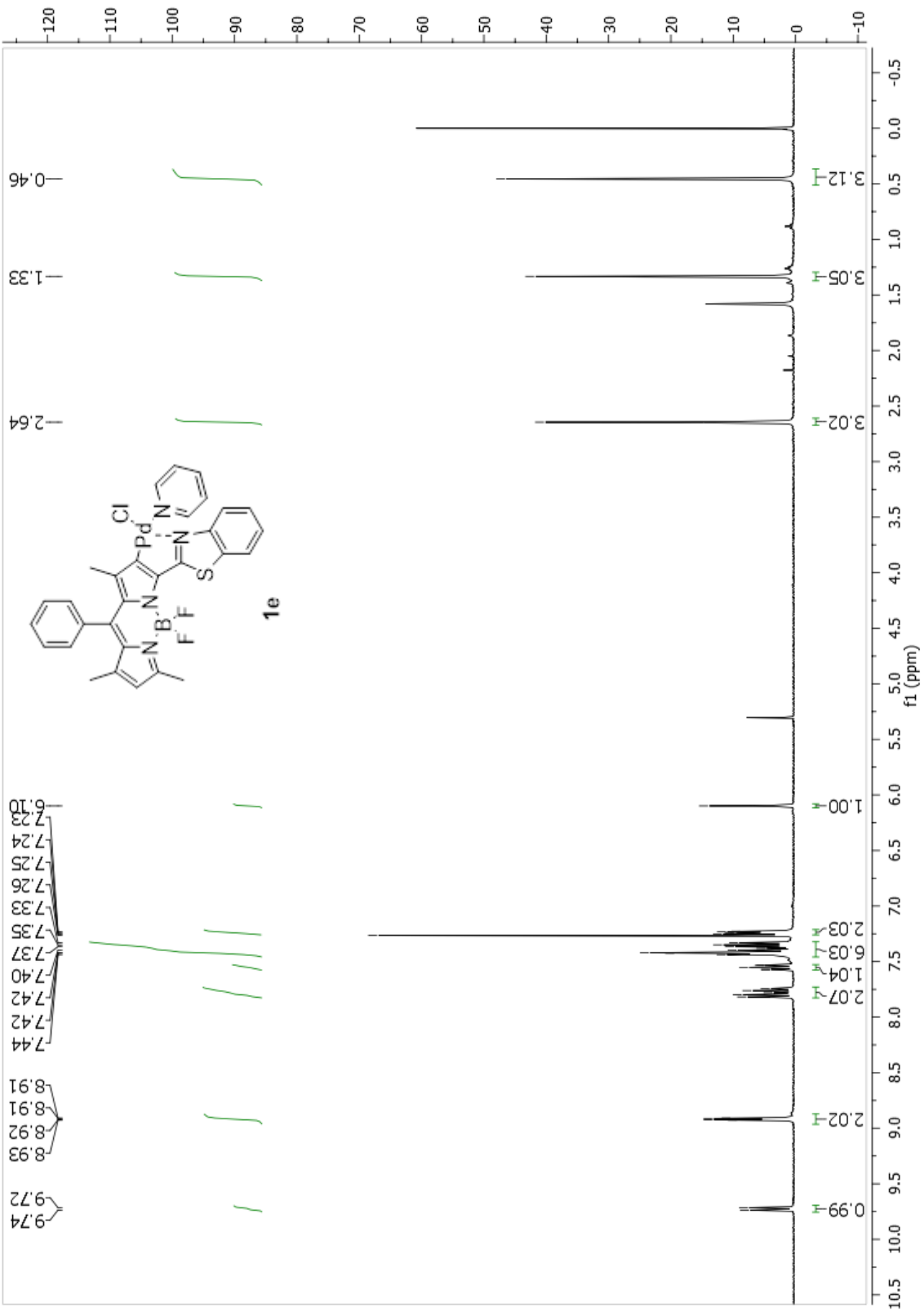
9.74
9.72
8.93
8.92
8.91
8.91
7.44
7.42
7.42
7.40
7.37
7.35
7.33
7.26
7.25
7.24
7.23
6.10
2.64
1.33
0.46
0.99
2.02
2.07
1.04
6.03
2.03
1.00
3.02
3.05
3.12
f1 (ppm)
1e

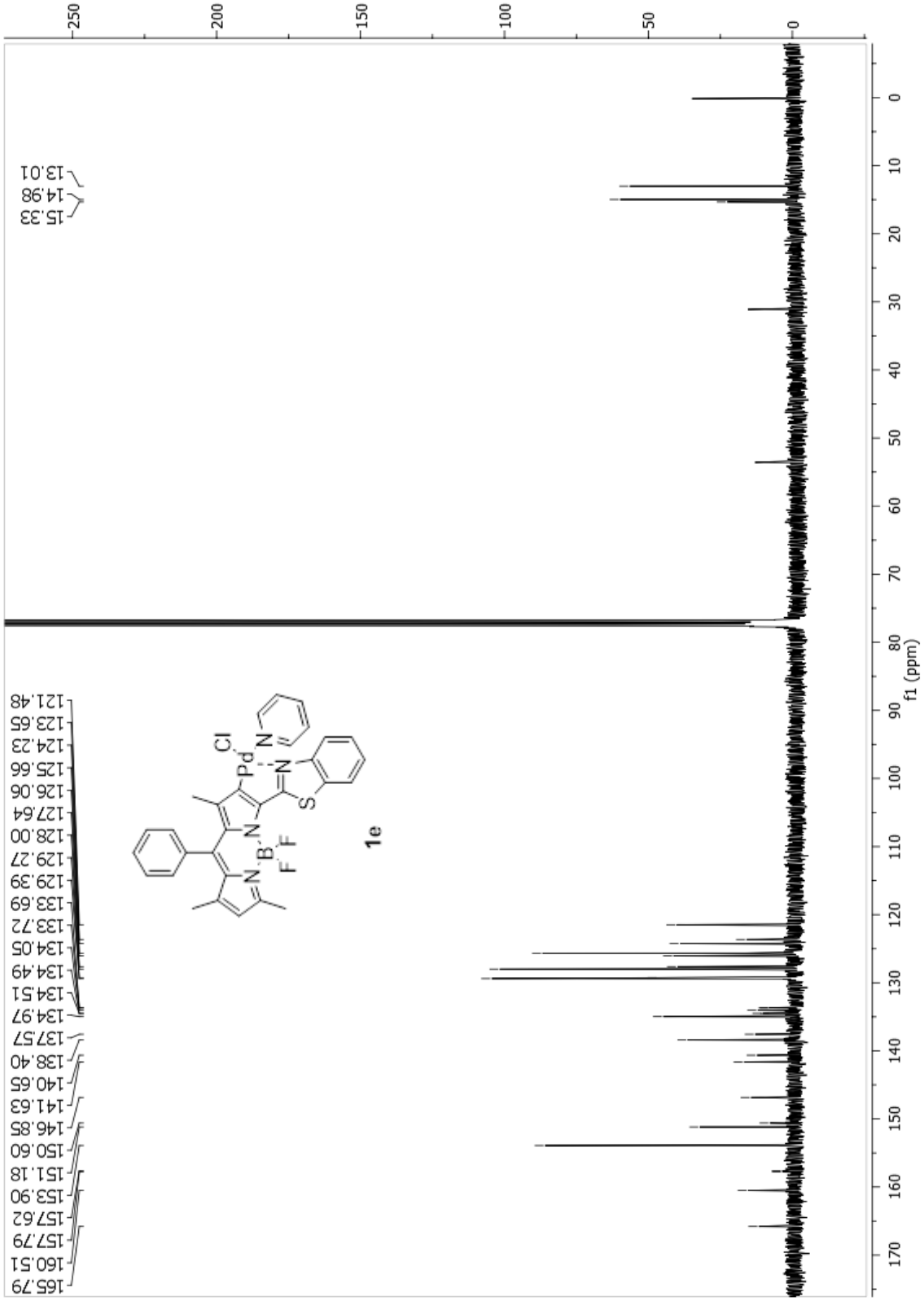
15.33
14.98
13.01
121.48
123.65
124.23
125.66
126.06
127.64
128.00
129.27
129.39
133.69
133.72
134.05
134.49
134.51
134.97
137.57
138.40
140.65
141.63
146.85
150.60
151.18
153.90
157.62
157.79
160.51
165.79
1e
f1 (ppm)

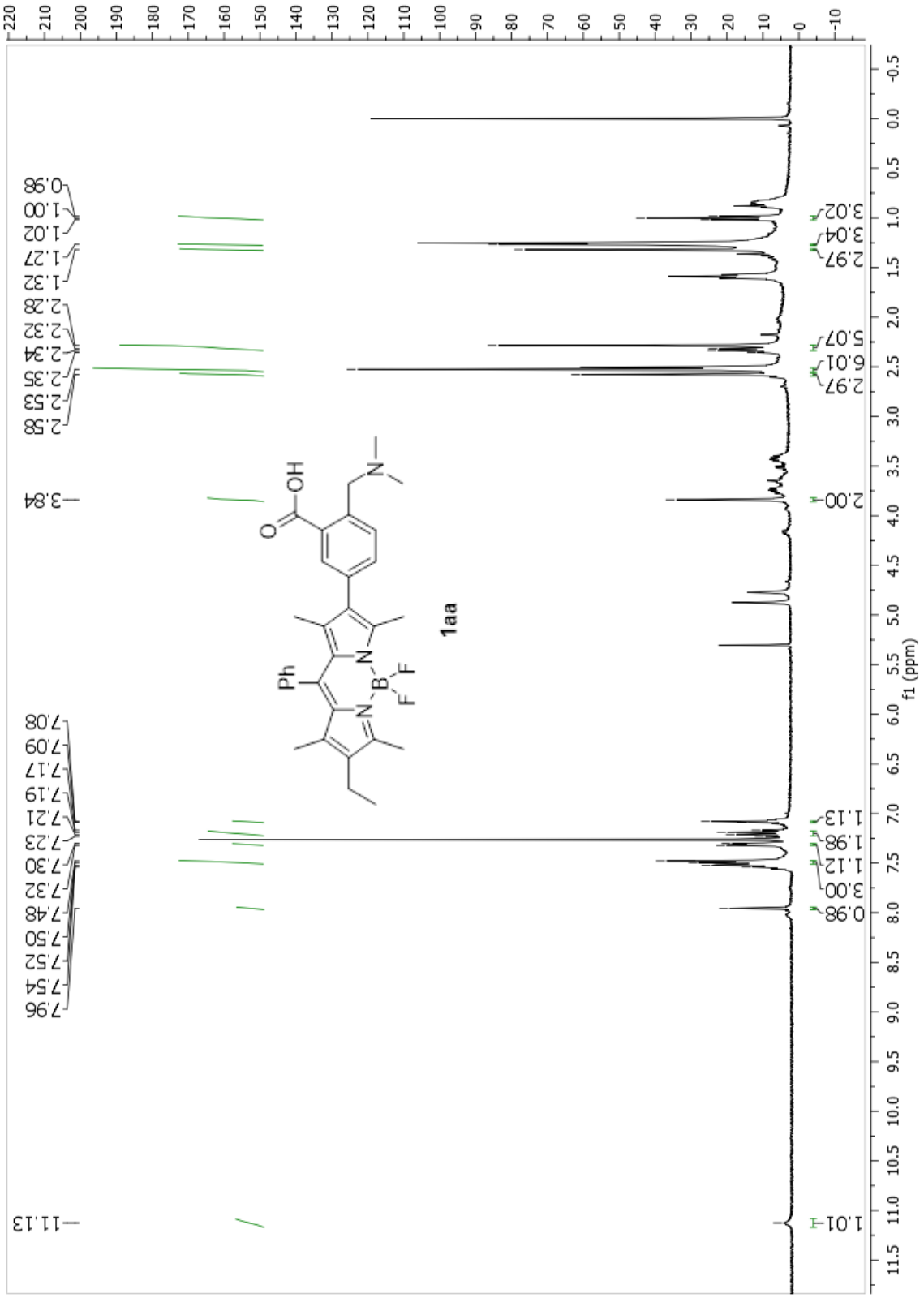
1aa
f1 (ppm)

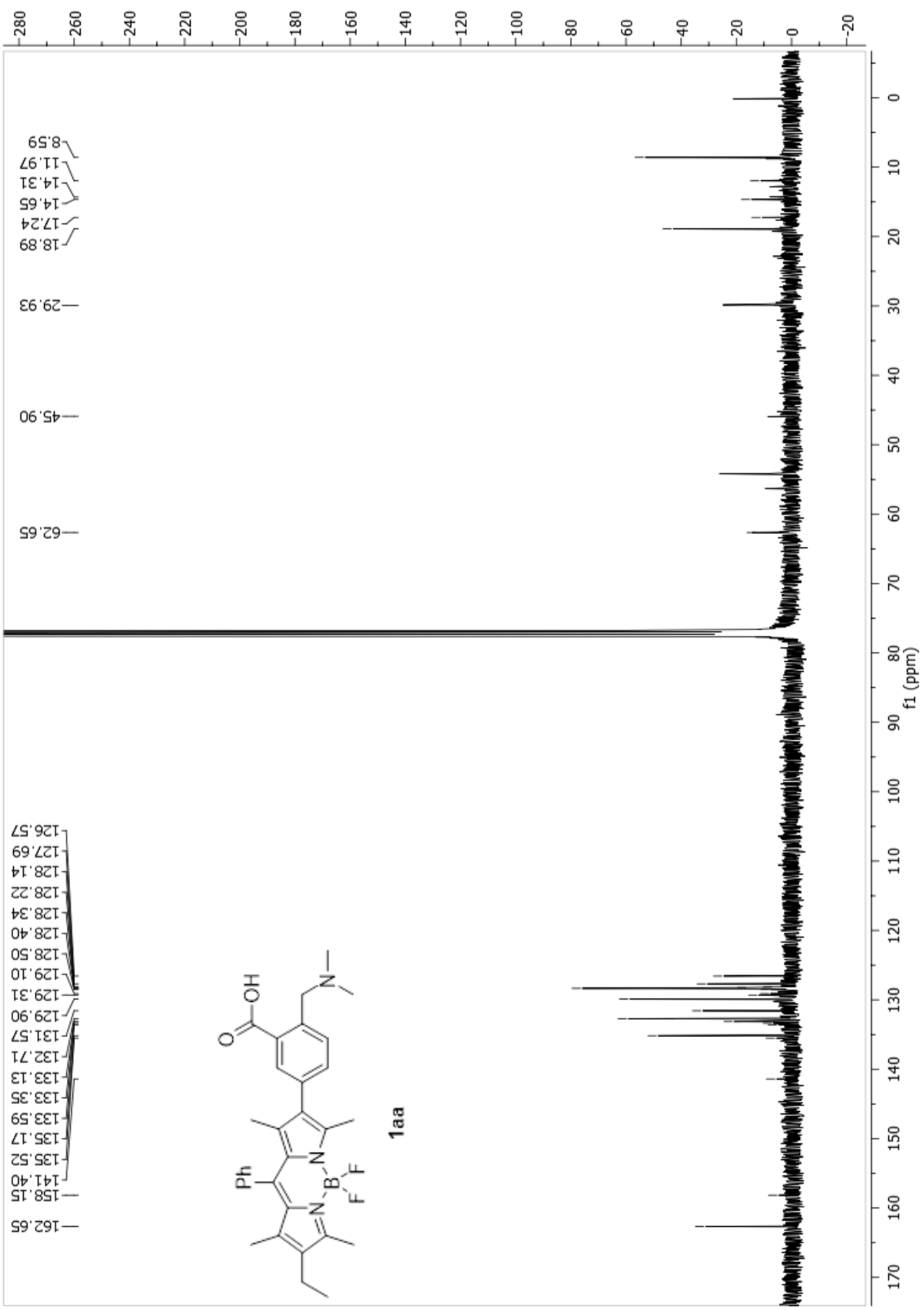
8.59
11.97
14.31
14.65
17.24
18.89
29.93
45.90
62.65
126.57
127.69
128.14
128.22
128.34
128.40
128.50
129.10
129.31
129.90
131.57
132.71
133.13
133.35
133.59
135.17
135.52
141.40
158.15
162.65
Ph
O
OH
N
B
F
F
1aa
f1 (ppm)

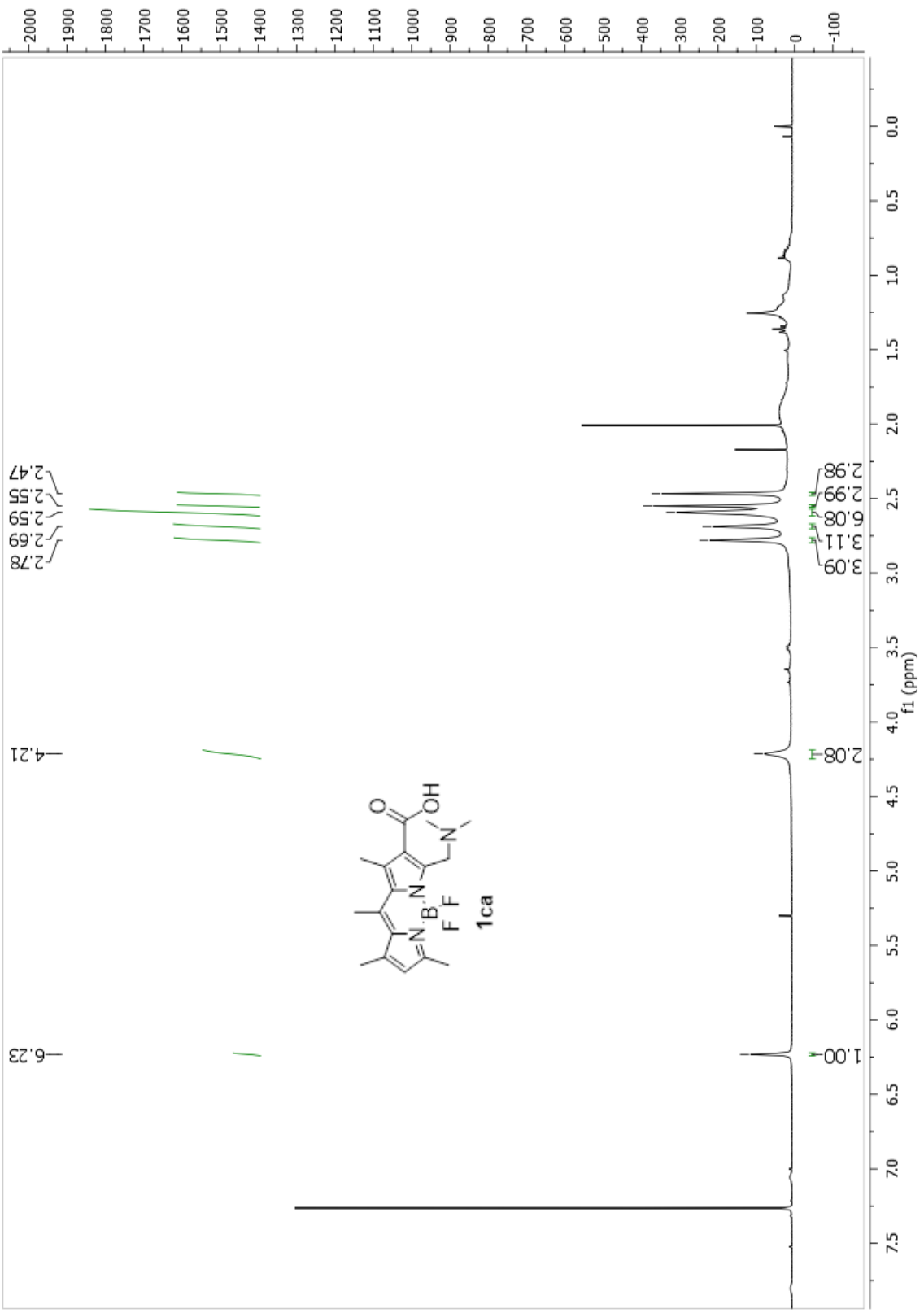
6.23
4.21
2.78
2.69
2.59
2.55
2.47
3.09
3.11
6.08
2.99
2.98
2.08
1.00
1ca
f1 (ppm)

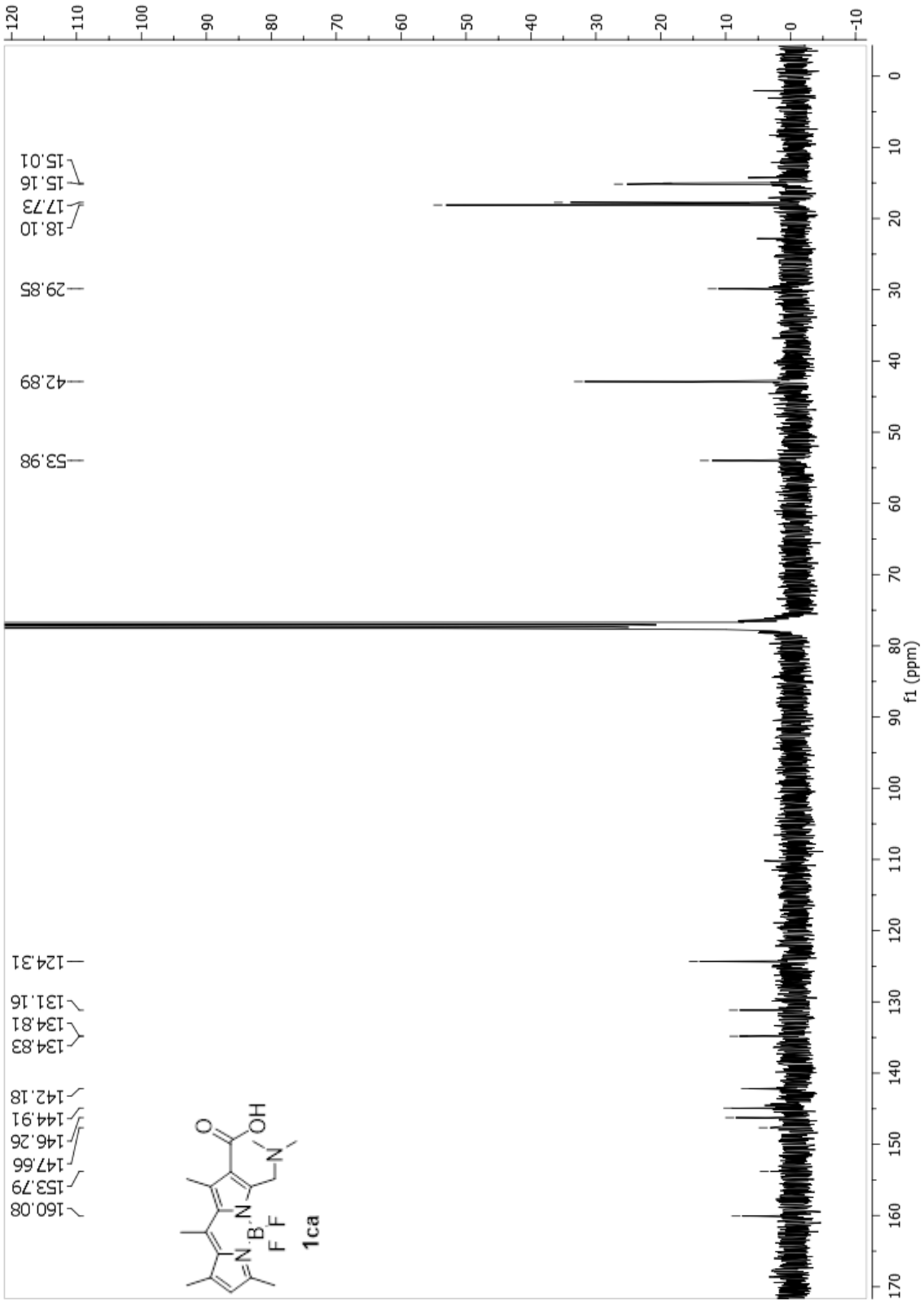
15.01
15.16
17.73
18.10
29.85
42.89
53.98
124.31
131.16
134.81
134.83
142.18
144.91
146.26
147.66
153.79
160.08
1ca
f1 (ppm)

APPENDIX B

HRMS OF THE COMPOUNDS

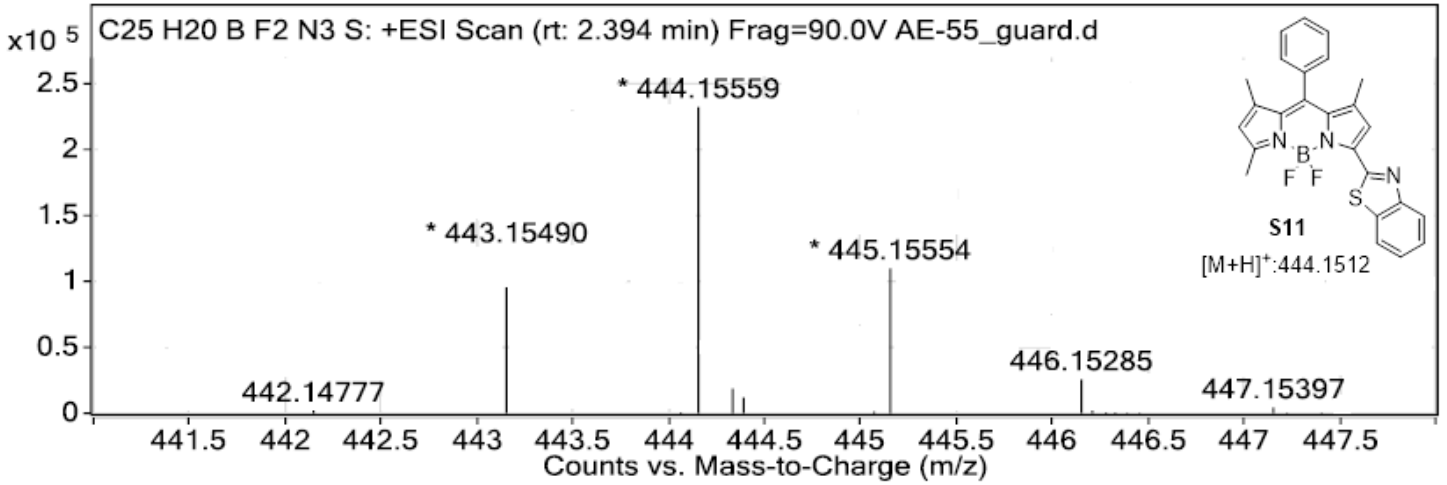
x10 5
C25 H20 B F2 N3 S: +ESI Scan (rt: 2.394 min) Frag=90.0V AE-55_guard.d
* 444.15559
* 443.15490
* 445.15554
442.14777
446.15285
447.15397
S11
[M+H]+:444.1512
Counts vs. Mass-to-Charge (m/z)

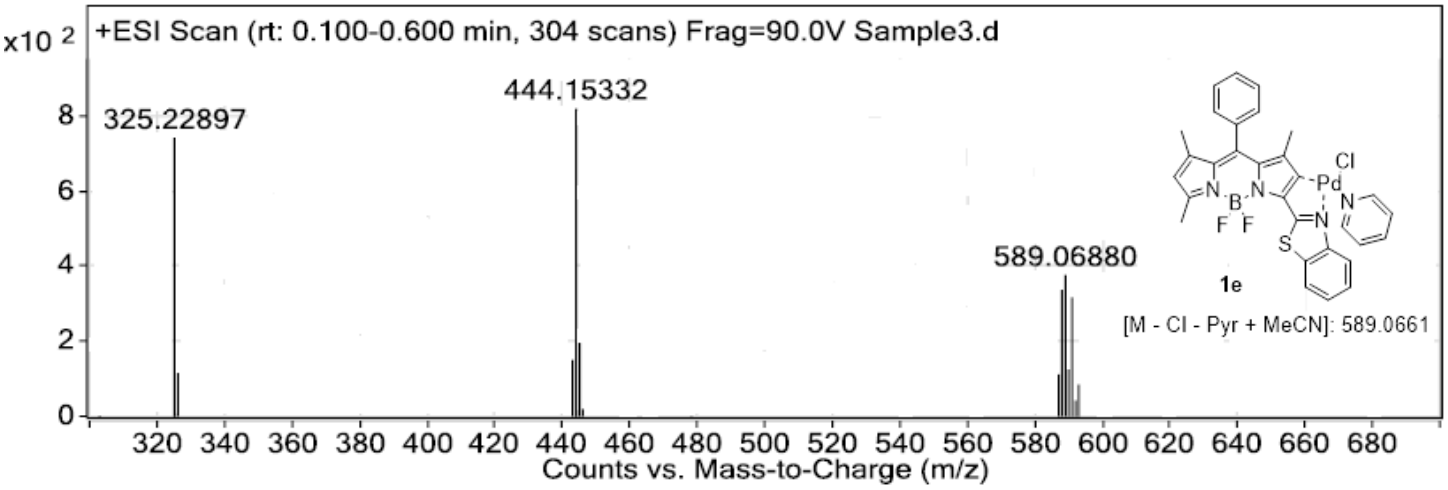
x10 2
+ESI Scan (rt: 0.100-0.600 min, 304 scans) Frag=90.0V Sample3.d
325.22897
444.15332
589.06880
1e
[M - Cl - Pyr + MeCN]: 589.0661
Counts vs. Mass-to-Charge (m/z)

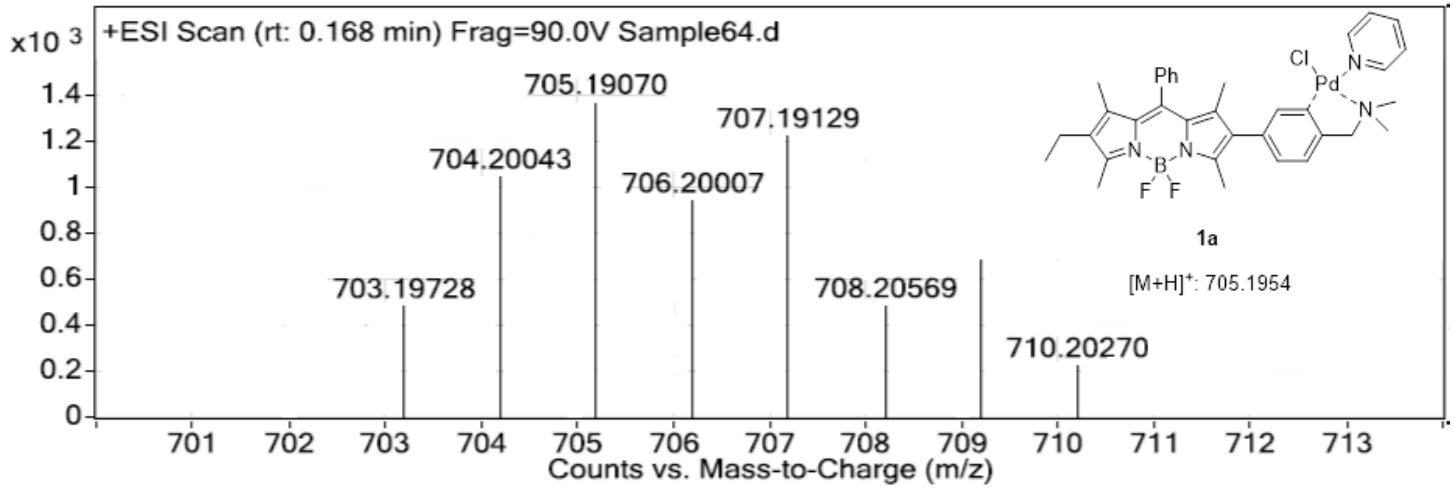
x10 3
+ESI Scan (rt: 0.168 min) Frag=90.0V Sample64.d
705.19070
707.19129
704.20043
706.20007
703.19728
708.20569
710.20270
1a
[M+H]+: 705.1954
Counts vs. Mass-to-Charge (m/z)

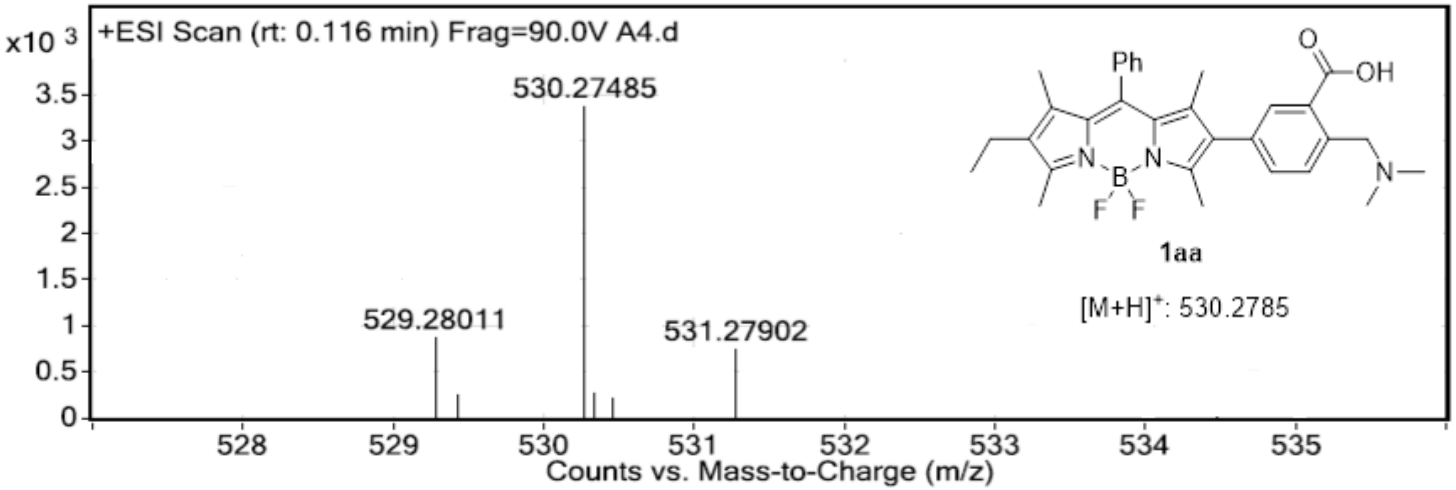
x10 3
+ESI Scan (rt: 0.116 min) Frag=90.0V A4.d
530.27485
529.28011
531.27902
1aa
[M+H]+: 530.2785
Counts vs. Mass-to-Charge (m/z)

CURRICULUM VITAE

Education

2010 – 2014 BS, Dokuz Eylül University, Chemistry Department

2015 – 2018 MS, İzmir Institute of Technology, Chemistry Department

2018 – 2024 PhD, İzmir Institute of Technology, Chemistry Department

Experience

2018 - … Research Assistant, İzmir Institute of Technology, Chemistry Department

Thesis

Palladium-catalyzed cross-coupling reactions of alkenyl epoxides and organoboronic acid esters (Ref No. 10184907, 2018)

Design and Synthesis of BODIPY-Based Palladacycles for the Detection of Carbon Monoxide (Ref No. 10695353, 2025)

Projects

Rhodium-Catalyzed Reactions of Alkenyl Oxirane with Organoborons: In The 4- Aril Or 4- Alkenil Substituted Allyl Alcohols Synthesis, Regio, and Selective a Method (114Z228)

Publications

Çevik Eren, M; Eren, A; Dartar, S; Tütüncü, B. B; Emrullahoğlu, M. A Cyclopalladated BODIPY Construct as a Fluorescent Probe for Carbon Monoxide. *Eur. J. Inorg. Chem.* **2022**, *2022* (14), e202200093. DOI: 10.1002/ejic.202200093.

Çevik Eren, M; Eren, A; Dartar, S; Kaya, B. U; Üçüncü, M; Varlikli, C; Karakaya, H. Ç; Emrullahoğlu, M. A Reaction-Based Scenario for Fluorescence Probing of Au(III) Ions in Human Cells and Plants. *Org. Biomol. Chem.* **2023**, *21* (39), 7880–7885. DOI: 10.1039/D3OB01081C.